Probing the Properties of Zn Complexes for the Cleavage of Phosphate Diesters and the Influence of Non-covalent Assembly

The University of Sheffield – Department of Chemistry

June 2015

Zeyed Abdulkarim

Submitted to the University of Sheffield in part-fulfilment of the requirements for the degree of

Doctor of Philosophy

Declaration

The work presented in this thesis was undertaken at the University of Sheffield between July 2011 and June 2015 under the supervision of Professor N. H. Williams. Unless otherwise stated, it is the work of the author and has not been submitted in whole or part for any other degree at this or any other institution.

June 2015

Zeyed Abdulkarim

Department of Chemistry
University of Sheffield
Dainton Building
Brook Hill
Sheffield
S3 7HF

To mum and dad

Jag kan inte tacka er tillräckligt

Acknowledgements

This is the hard part…how do I thank everyone without turning this into a chapter in and of itself?

I would like to express my deepest gratitude and thanks to my supervisor, Professor Nick Williams, who has been nothing short of excellent in his supervision. In these years I've learnt so much because you allowed me to work independently while still always being available for discussions despite a busy schedule. All I can say is, thank you.

I would also like to thank Professor Roger Strömberg at Karolinska Institutet in Stockholm for his help and support and without whom I probably would not have moved to Sheffield.

A special thanks to the oldest Post Doc in the department Prof. Em. Charles Stirling for being an inspiration and a walking encyclopedia of chemistry (as well as being a patron of the solvent fairies).

Thanks to Dr. Barbara Ciani for her help with the peptide coiled-coils and useful general discussions.

I would also like to thank Dr. Simon Webb and Dr. Andrew Booth at The University of Manchester for their help with the membrane based project as well as Dr. Guoqiang Feng at Wuhan University for kindly providing the oxazole-bridged complexes.

Now for the thanks to the long list of friends and colleagues that I owe so much.

Iain and Zoe who took me to my first Uni-Arms meal ever and convinced me that Sheffield was the right place to do my PhD. Dr. Barlow, though you've left our lab your spirit still lingers in the form of flap jacks (or digestives) occasional appearing next to the microwave. I'm constantly reminded of you whenever I see a cyclist and instinctively think "I hope he doesn't fall and land on his elbow". Le Manu, mon ami français, mon premiere "housemate" à Sheffield et mon colocataire au cours de PhosChemRec. Je veux te dire merci pour tout, venir en Suède à nouveau?

Jackson, Lex and Premma…where do I start with you? Taking me to my first veggie English breakfast, taking me to IKEA when I got homesick (and no, I don't know who comes up with the names for IKEA products), taking me to Chatsworths muddy field, the numerous movie nights, almost driving me to the east coast, helping me move the excessive amounts of IKEA furniture out of my flat (including Malkolm the office chair that was undeservedly plagued with a terrible reputation)…the list goes on. You are the reason that I felt less home sick in Sheffield. Thanks for trying (sometimes unsuccessfully) to take my mind of work.

Dawn, for getting me what must have been a 20 pound watermelon by train from Stockport…that is a gift that has yet to be topped. Claire for making me very manly birthday hats, Ashlie (sorry for the unintentional slap) and a fail compilation video for indicating the commencement of a Friday afternoon. Jonny, Dan(dy), Andy, Edeson and the other

Harrity/Jones people that occasionally popped into our lab. Esther and Ash for the centertainment trips when chemistry wasn't behaving and Mickey Walker (MFW) for helping me reach my feeder ambitions.

All the past and present E-floor and E81 people over the years, Almahdi, Nate, Mohammed, Adel, Will, Moody, Crisitina, Taurino, Li, Jack, Mark T, Dave and all the project students that I've had the opportunity to work with/teach over the years, it has been as much a learning experience for me as I hope it was for you.

All the lads and lasses of the golden (green) team Exeter: PJ, Jarman, Hiwa, Scott, Caroline, Hannah, Sascha, Tom, Nath and Killeen. All the people from the Wednesday footy…oh…the memories of all the failed (sometimes successful) attempts on goal that often led to rummaging around in the Goodwin shrubbery. The three musketeers Pete, Nick and Dan. Thanks for all the work that you do in stores and the work that you don't do on the pitch. I was considering getting each one of you a gift card for a hip replacement but then I remembered the beauty of free healthcare that is the NHS, so just pop down to the clinic, no rush.

A special thanks to Dr. Craig Robertson and Will Cullen for their help with the plate reader experiments.

Thanks to Simon and Sharon for their help with the mass spectrometric analysis. Rob, Keith, Jenny, Mel, Stephen, Sharon, Richard as well as Louise, Rachel, Brittany, Denise and Elaine for the work that they do…when you do something right people will think that you've done nothing.

All the people/trainers at Wicker Camp and the uni club, in particular Mick, Trix, Pooley, Daz, James, Jimbob, Chris, LJ, Helene, Bear, Pete, Sam, Wayne, Mani and Adam. The blood, sweat and thai liniment, somehow I've missed it while being stuck in thesis writing.

All the people in the PhosChemRec ITN for organising the conferences and the friendly atmosphere of scientific exchange. The people at Novum, Malgo, Dmytro, Håkan, Jyoti and in particular Martina, Margarita and Alice for all chemical/instrumental predicaments that we endured together.

My friends that I rarely get to see, CK, Bobo, Linda, Jonas, Martina, Alex, Martin, Thao, Jonathan and Tobias. Not forgetting the old gang Fredrik, Filip and Sebastian. I know I've been pretty terrible at finding time to meet up but hopefully I'll see you more now.

Anyone that I've forgotten to thank is automatically invited to my birthday meal (it is not as exclusive as it sounds).

Lastly, Mum and Dad, Ziko, Isrig, Dawi as well as my extended family who have been supportive throughout. Thank you for encouraging me through these years as you've always done, you are the home to which I always long to return.

Abstract

The design of artificial catalysts to hydrolyse phosphate diesters under mild conditions remains extremely challenging. In particular, dissecting and quantifying the interactions that lead to efficient catalysis has yet to be achieved fully to allow the complete understanding of current catalysts. Furthermore, the use of weak, supramolecular interactions to influence and control the activity of these catalysts remains a challenge, despite the central role that these interactions play in natural systems.

This work focuses on catalysing the hydrolysis of DNA- and RNA-like substrates with mono- and dinuclear zinc complexes. Particular attention is given to quantifying the effect of varying structural features on kinetic activity and to study the impact of organic groups that affect the microenvironment and potential assembly of these complexes.

The activity of a series of dinuclear zinc complexes is separated into ground and transition state effects to understand the impact of changing peripheral ligand substituents in cleaving RNA-like substrates. The presence of amino functionalities (NH_2 and NHMe) in the vicinity of the metal ions resulted in a 30-fold increase in ground state binding and 40 to 130-fold increase in transition state stabilisation compared to the parent complex. The role of headgroup is explored, and an unexpected sensitivity to reversible inhibition by carbon dioxide discovered.

To introduce aggregation of mononuclear complexes through non-covalent interactions, ligands with hydrophobic anchors were synthesised so that they could be embedded into vesicles. No evidence for an increase in activity through aggregation was observed, but a medium effect in cationic vesicles enhanced the activity of the catalytic centre by more than an order of magnitude ($3.6 \pm 0.4\ M^{-1}\ s^{-1}$) relative to the reactivity in more polar aqueous environment ($0.16 \pm 0.01\ M^{-1}\ s^{-1}$).

More specific structural organisation of the same zinc complex was attempted through the conjugation of peptides that were designed to assemble into dimers, but the observed activity reflected that of the monomeric species. Structural characterisation suggested that although the peptides did form the anticipated secondary structure, intermolecular association did not occur to an appreciable extent.

Finally, the effect of varying the structures of alcohol and oxime nucleophiles covalently incorporated into zinc complexes was explored. The introduction of methyl groups close to the nucleophilic centre led to significant changes in solution properties, but approximately 3-fold lower reactivity towards DNA-like substrates.

Abbreviations

µL	Microlitres
µM	Micromolar
Abs	Absorbance
BNPP	bis(4-nitrophenyl)phosphate
CD	Circular Dichroism
$CHCl_3$	Chloroform
CHES	N-Cyclohexyl-2-aminoethanesulfonic acid
d	doublet
DCM	Dichloromethane
DIPEA	Diisopropylethyl amine
DMDODA	Dimethyldioctadecyl ammonium chloride
DMF	Dimethyl formamide
DMP	Dimethyl phosphate
DNA	Deoxyribonucleic acid
EPPS	N-(2-hydroxyethyl)piperazine-N'-(3-propanesulfonic acid)
ES	Electrospray
Et_3N	Triethylamine
EtOAc	Ethyl acetate
H_2O	Water
HBTU	*N,N,N',N'*-Tetramethyl-*O*-(1*H*-benzotriazol-1-yl)uronium hexafluorophosphate
HCl	Hydrochloric acid
H_2SO_4	Sulphuric acid
HEPES	2-[4-(2-hydroxyethyl)piperazine-1-yl]ethanesulfonic acid
HPLC	High Performance Liquid Chromatography
HPNPP	2-hydroxypropyl 4-nitrophenyl phosphate
HRMS	High resolution mass spectrometry
IR	Infrared
KIE	Kinetic Isotope Effect
LG	Leaving Group
m	multiplet
MeOH	Methanol
MPNPP	Methyl 4-nitrophenyl phosphate
$MgSO_4$	Magnesium sulphate
MS	Mass Spectrometry
$Np^*{}_2P$	bis-3-(4-carboxyphenyl)neopentyl phosphate
Np_2P	Dineopentyl phosphate
NaOH	Sodium hydroxide
Na_2SO_4	Sodium sulphate
nm	Nanometer
NMR	Nuclear Magnetic Resonance
Nuc	Nucleophile
q	quartet
RNA	Ribonucleic acid
s	singlet
SKIE	Solvent Kinetic Isotope Effect
SPPS	Solid Phase Peptide Synthesis
t	triplet
TACN	Triazacyclononane
tBDMS	*tert*-Butyldimethyl silyl
tBDPS	*tert*-Butyldiphenyl silyl
TFA	Trifluoroacetic acid
TFAA	Trifluoroacetic anhydride
THF	Tetrahydrofuran
TLC	Thin Layer Chromatography
TS	Transition State
UpU	2',5' uridine dinucleoside monophosphate
UV/Vis	Ultra-violet/Visible

List of contents

Chapter 1 - Introduction

1.1 - Phosphates in nature

Phosphates are prolific in nature, and used in a variety of biochemical processes and structures ranging from the cell membranes (phospholipids), cell signaling and protein regulation through phosphorylation to chemical energy molecules (adenosine triphosphate, ATP), see Figure 1.1. These molecules are of great importance in living organisms although one could argue that the most vital task performed by phosphates is the storage of genetic information in the biopolymers of DNA and RNA.

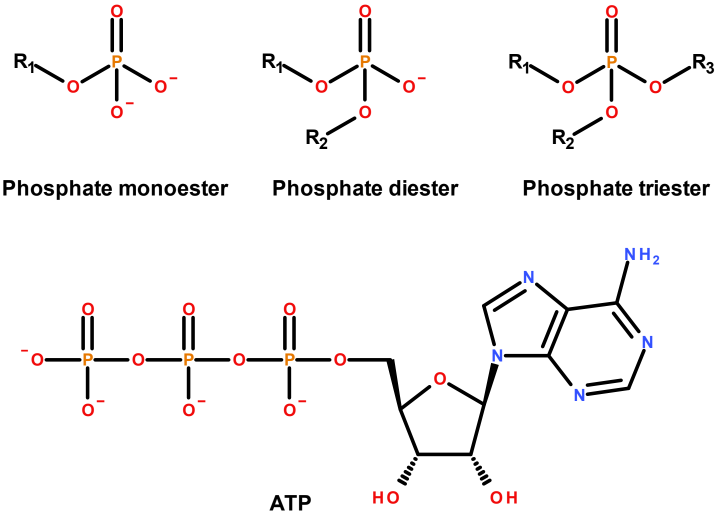

Phosphate monoester Phosphate diester Phosphate triester

ATP

Figure 1.1. The structure of mono-, di- and triesters as well as ATP. R_1, R_2 and R_3 represent various substituents.

The DNA and RNA backbone consists of a polyanionic phosphate diester polymer linked through the 3'- and 5'-OH of nucleosides, see Figure 1.2.

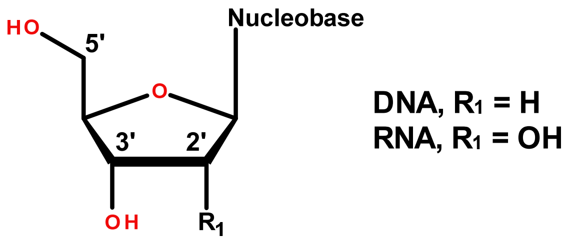

Figure 1.2. An illustrative structure of a nucleoside.

The reason for the prevalence of phosphates in nature has been at the core of decades of research into the chemistry of these molecules.[1,2] It has been argued by Westheimer that other functionalities (carboxyl ester, amides etc.) could be used for the same task of forming the RNA/DNA backbone but that the phosphate possesses superior qualities.

A potential functionality that can be used as a genetic information bearer is required to be divalent, for connectivity, to allow the formation of single stranded biopolymer as well as maintaining a charge at neutral pH. The ionisable functionality should have a pK_a that is lower than 4 or higher than 10 to ensure that the moiety is essentially fully protonated or deprotonated under neutral conditions (phosphate diester $pK_a \approx 2$).

The charge of the phosphates is believed to play an important role in keeping the phosphate biopolymers within the cell. It has been hypothesised that the earliest forms of life began to appear from the primordial mixture of compounds only when molecules became adsorbed on surfaces or compartmentalised in cell-like structures.[3–5] This would allow for sufficiently high concentrations of biomolecules to accumulate for complex chemical reactions to become feasible. These structures would most likely have been primitive analogues of the lipophilic cell membranes found in all living organisms today.The compartmentalisation of charged moieties within lipophilic structures is heavily reliant on the charge-lipophile repulsion.[6] The lack of charge or polar character would allow for relatively easy diffusion across the lipophilic barrier and therefore reduces the capacity to concentrate complex species.

The trivalent linker molecule citrate seems to fulfill these requirements but it is far less stable to hydrolysis than the phosphate diester. The stability of the phosphate diester to nucleophilic attack has been associated with the negative charge that is in close proximity to the electrophilic phosphorous center. The neutralisation of the charge on phosphate diester, illustrated by a triester, leads to a significant increase in reactivity (typically 4 to 5 orders of magnitude in water), consistent with this explanation. It has been suggested that molecules that feature negatively charged moieties in the vicinity of the hydrolysable bond could be stabilised by a similar mechanism. The hydrolysis of phosphates (and esters/amides) proceeds through a mechanism involving a nucleophilic attack on the electrophilic carbonyl/phosphate. The charged species must be held in close enough proximity to the vulnerable electrophilic center to effectively shield it from incoming nucleophilic attacks by negatively charged species.

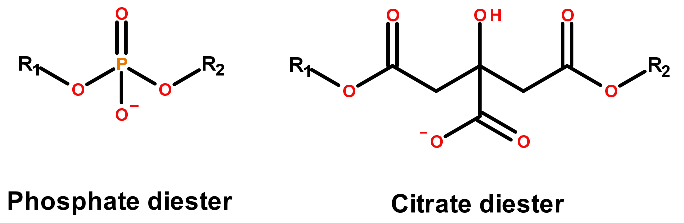

Figure 1.3. The structures of phosphate and citrate diesters show the difference in the proximity of the anionic species to the electrophilic centers (phosphorous or carbonyl). R_1 and R_2 represent various substituents.

The hydrolysis of phosphates is particularly disfavored due to the high local charge concentration at the phosphorous center. The negatively charged moiety in citrate is relatively distant from the hydrolysable bond, see Figure 1.3, so the electrostatic repulsion of the incoming nucleophile is likely to be less effective.

The main conclusion that is to be taken from this comparison of potential chemical functionalities for DNA/RNA is that the phosphate diester moiety is better suited to perform the tasks for which it has been employed than any other functionality.

1.1.1 - DNA and its model compounds

Deoxyribonucleic acid (DNA) is a biopolymer linked through phosphate diesters that are very stable to hydrolysis at the P-O bond, see Figure 1.4. The stability of the phosphate diester bond to spontaneous hydrolysis at neutral pH and 25 °C makes monitoring the reaction under these conditions impossible, which has prompted the use of elevated temperatures (up to 250 °C) in order to accelerate the reaction.This stability is a desirable property to preserve the genetic information but there are other bonds in DNA that cause strand breakage/degradation that are more labile.

Common degradations seen in DNA are the deamination of nucleobases or the depurination/depyrimidination processes,[7] see Figure 1.5, and are counteracted by repair mechanisms *in vivo*. These reactions occur under physiological conditions but become even more prevalent at high temperatures.

The dinucleoside monophosphate TpT has been reported to have rate constants for the decomposition that exceed the rate constants for the hydrolysis of phosphate diesters by

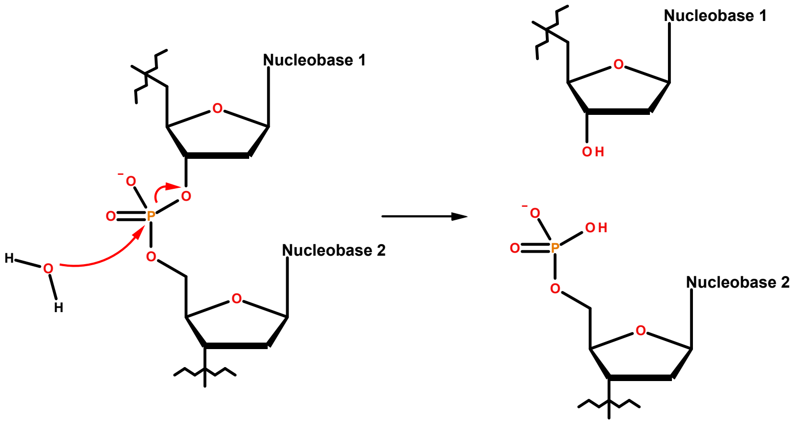

Figure 1.4. The hydrolysis of the phosphate backbone of DNA.

5 orders of magnitude.[8] This renders DNA unsuitable as a candidate for the study of phosphate diester hydrolysis when uncatalysed. The cleavage and formation of the phosphate diester bond is an essential biochemical process for the transcription and repair of DNA and RNA. The repair process for DNA would have to involve breaking of the phosphate ester bond followed by insertion of a new nucleoside which would be unfeasible if left uncatalysed. The phosphates diesters are subject to enzymatic catalysis that efficiently accelerates the hydrolysis.

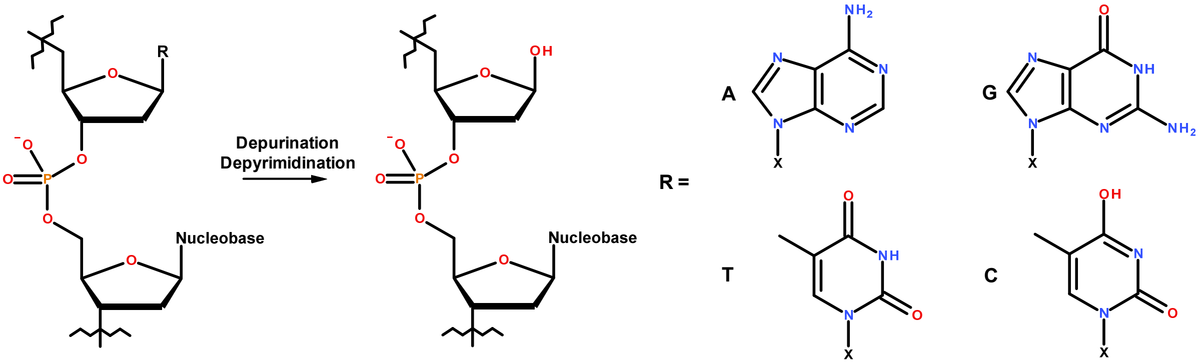

Figure 1.5. The depyrination and depyrimidination process for DNA.

The lack of reactivity of the phosphate diester bond is efficiently counterbalanced by the remarkable rate accelerations (10^{17}-fold) reducing the half-life under physiological conditions from millions of years to milliseconds.[8,9] These remarkable rate accelerations (provided by for example staphylococcal nuclease[9]) are not uncommon for enzymes.[8] This makes the hydrolysis of phosphate diesters an excellent reaction to study, not just to understand the chemistry of phosphates but more generally, to understand the structures and interactions that are responsible for such remarkable rate accelerations.

The rate of spontaneous hydrolysis of DNA under neutral conditions and at 25 °C was extrapolated from high temperature experiments using the model compound dimethyl phosphate (DMP) that eliminates the problems associated with the deoxyribose nucleobases. The main mechanism involved in the hydrolysis was the C-O bond breakage (> 99 %) as opposed to the targeted P-O bond (< 1 %), see Figure 1.6. The reported half-life was 1.3 × 10^5 years for the C-O bond breakage[10] which indicates that the upper limit for the half-life of the P-O bond breakage is 2.2 × 10^6 years.

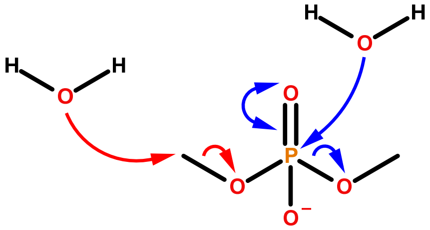

Figure 1.6. The hydrolysis of DMP through competing mechanisms of C-O (red) and P-O (blue) bond breakage.

More appropriate model compounds that sterically preclude C-O bond breakage, see Figure 1.7, were used by Williams *et al.* to study phosphate diester hydrolysis at high temperatures.[8,11] The reported first-order rate constant for the hydrolysis of these substrates at neutral pH and 25 °C was estimated to be 7 × 10^{-16} s^{-1}, which equates to a half-life of 3.1 × 10^7 years.

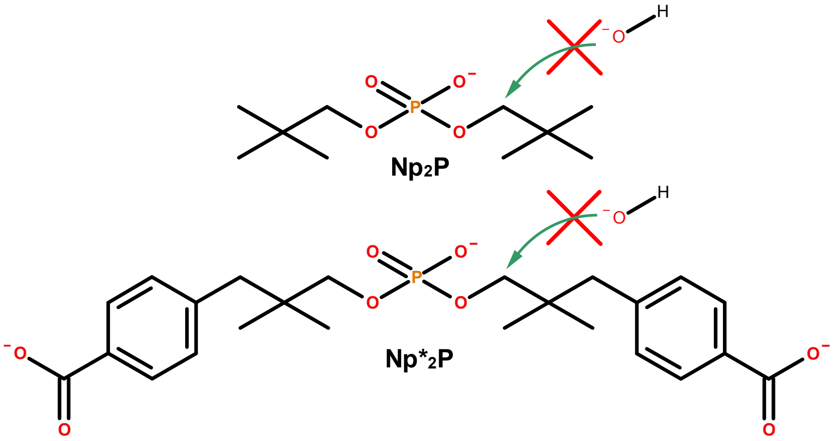

Figure 1.7. The phosphate diesters used for the measurement of P-O bond breakage.

The difference in the rates of spontaneous hydrolysis between the neutral and negatively charged phosphates is indicated in the pH-rate profile for Np_2P and $Np^*{}_2P$, see Figure 1.8.

Figure 1.8. The observed rates at 250 °C versus pH (measured at 25 °C) for Np_2P (squares) and Np^*_2P (circle).[8] Reproduced with permission from Schroeder, G. K., Lad, C., Wyman, P., Williams, N. H. & Wolfenden, R. The time required for water attack at the phosphorus atom of simple phosphodiesters and of DNA. *Proc. Natl. Acad. Sci. U. S. A.* 103, **4052–5 (2006). Copyright (2006) National Academy of Sciences, U.S.A.**

The source of the phosphate diester stability to nucleophilic attack is the negative charge on the phosphate backbone which forms on the non-bridging oxygen under neutral and basic conditions. In order to mimic the neutral form of the substrate Np^*_2P a methylated triester equivalent Np^*_2MeP was used, see Figure 1.9.

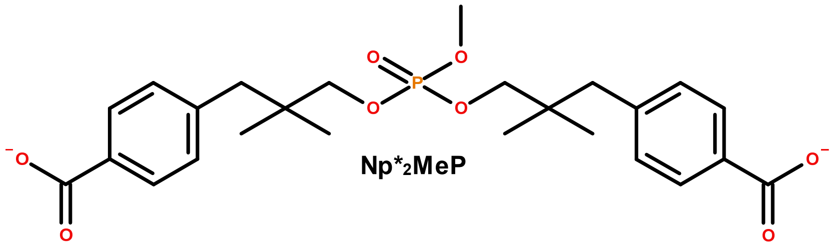

Figure 1.9. The triester Np^*_2MeP was used as a more appropriate model for the neutral form of Np^*_2MeP.

Comparing second-order rate constants for the base-catalysed hydrolysis of Np^*_2P (1.4×10^{-15} M^{-1} s^{-1}) and Np^*_2MeP (1×10^{-6} M^{-1} s^{-1}) show a remarkable 10^9-fold increase in reactivity simply due to the removal of the electrostatic repulsion. The use of a triester as an analogue for the neutral diester hydrolysis could be subject to criticism since the neutral diester (unlike the triester) could participate in proton transfer processes which would render the base-catalysed reaction similar to the water attack on an anionic phosphate. The experimental results for the triester model have been confirmed more recently using computational investigation.[12]

Interestingly the observed pH-rate profile in Figure 1.8 for the hydrolysis of the DNA analogues indicates acid-catalysed (pH < 6), pH-independent (6 < pH < 13) and base-catalysed (pH > 13) hydrolysis.

Given the possible pathways by which the DNA can be degraded, why do we focus on the hydrolysis of the phosphate diester bond which is so difficult? The answer to this lies in the fact that this stable bond is hydrolysed with relative ease by enzymes which indicates that there is a lot of knowledge about catalysis to be gained from studying these reactions.

The stability of the DNA phosphate diester bond makes it a very challenging target for small synthetic molecular complexes that aim to mimic the natural nucleases (see subsequent chapters). The reactivity of these small complexes is insufficient to achieve measurable reactivity over a reasonable time period. The alternative lies in the use of more activated substrates that allows for relatively rapid hydrolysis with small artificial complexes. The most commonly used DNA analogue is bis-(4-nitrophenyl) phosphate (BNPP) which releases 4-nitrophenol (PNP) upon cleavage, see Figure 1.10.

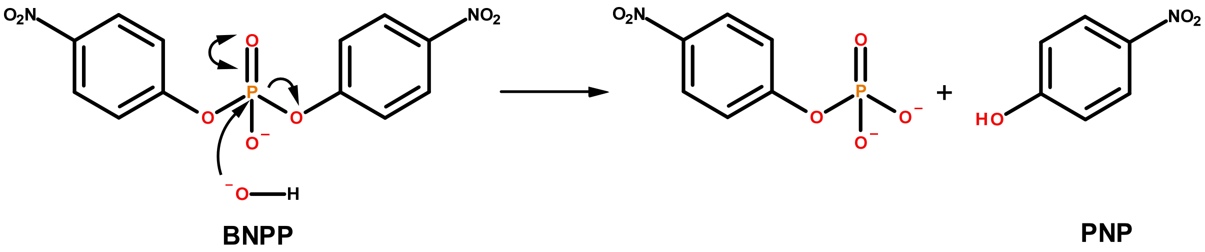

Figure 1.10. The hydrolysis of BNPP.

The PNP allows for easy UV-visible monitoring of the reaction progress at 400 nm which does not overlap with the absorbance maximum of many other molecules used in the kinetic experiments. The increased reactivity of BNPP is due to the relatively acidic PNP (pK_a ≈ 7) which arguably cannot be directly correlated to the alkyl leaving groups of DNA. The BNPP model compound therefore serves as a crude indicator of the activity of nuclease mimics although nuclease-like rates of hydrolysis are yet to be observed for small molecular catalysts. BNPP is widely used as an intermediate solution to the final goal of achieving enough catalytic activity to hydrolyse DNA efficiently. The rate of spontaneous hydrolysis of BNPP has been estimated to be 1.6×10^{-11} s^{-1} at pH 7 and 25 °C.[13,14] Many other phosphate diesters with various leaving groups[15,16] have been reported in literature as DNA analogues but BNPP provides a large amount of accumulated data in the literature for comparison.

1.1.2 - RNA and its model compounds

The study of ribonucleic acid (RNA) and its hydrolysis has been ongoing for over half a century with the earliest studies involving alkaline hydrolysis reported nearly a century ago.[17]

The first detailed investigations regarding the hydrolysis products of RNA indicated the formation of pairs of 2'- and 3'-phosphorylated ribonucleosides.[18–20] This caused confusion as to whether the structure of the native RNA was 2'- or 3'-phosphorylated. The 3'-phosphorylated isomer was later found to be the substrate for enzymes in subsequent reactions which indicated that the native RNA must have been 3'-linked, see Figure 1.11.

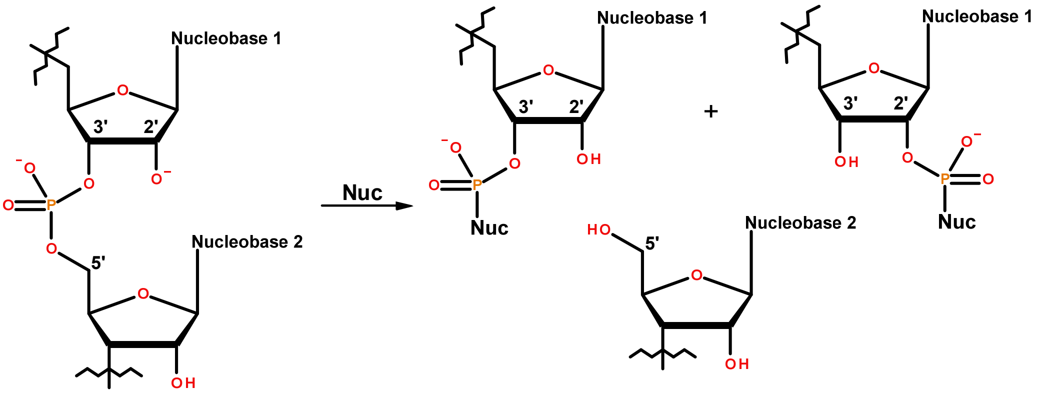

Figure 1.11. The formation of 2'- and 3'-phosphorylated product reported in literature.

The isomers pointed to the existence of a cyclic intermediate in the RNA hydrolysis that could subsequently be hydrolysed to form the two isomers. This revealed the source of the increased alkaline lability of RNA compared to DNA. The 2'-OH acts as an intramolecular nucleophile, see Figure 1.12, which is generally more effective than an intermolecular nucleophile.[21] This means that the hydrolysis of RNA is in fact a transesterification where the nucleophile is an intramolecular alkoxy functionality. The half-life for the phosphate diester bond in RNA at 25 °C and neutral pH has been reported to be in the order of 100 years.[22] The study of RNA and DNA provides a measure for the effectiveness of having an intramolecular nucleophile in the 2'-position. The relative rate acceleration is approximately

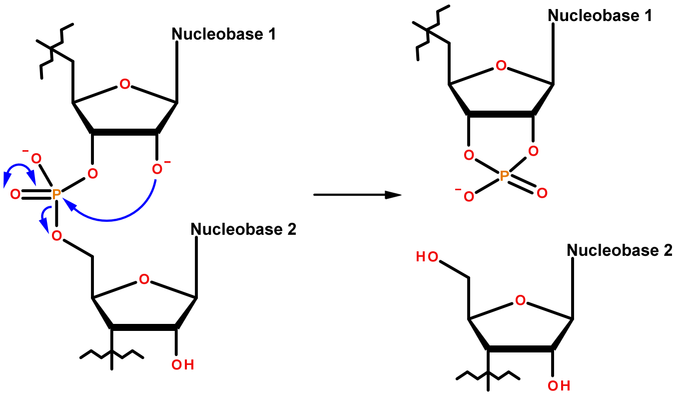

Figure 1.12. The cleavage of RNA by the intramolecular 2'-nucleophile.

10^5-fold although the difference is larger for the base-catalysed than the spontaneous reaction (RNA transesterification has a small pH-independent region at pH ≈ 5).

The mechanism of RNA cleavage was proposed by Westheimer[23] in 1968 where he introduced the notion of pseudo-rotation in pentacoordinate phosphorane intermediates. The mechanism of the RNA cleavage has been extensively studied and reviewed over the years.[24,25]

The departure of the leaving group in RNA cleavage is preceded by the formation of a pentacoordinate phosphorane intermediate. The intermediate adopts the form of a trigonal bipyramid with two longer apical bonds and three shorter equatorial bonds to the phosphorous center, see Figure 1.13. The substituents in the trigonal bipyramid prefer either the apical or equatorial position depending on their inherent chemical properties. Electronegative substituents prefer the apical position (longer P-O bond) and electropositive substituents prefer the equatorial (shorter P-O bond). This implies that the attack by the nucleophile and leaving group departure can only occur through the apical positions. If the intermediate is stable enough the process of pseudo-rotation takes place and isomerisation can occur if the substituents on the phosphorane are of similar acidity. The pseudo-rotation involves the interchange between apical and equatorial substituent which results in a change of configuration, see Figure 1.14

This process is required for the isomerisation of the RNA i.e. the formation of a phosphorane containing a five-membered ring (2',3'-cyclisation) where the 3'-OH of the ribose is initially equatorial and the 2'-OH apical (diapical and diequatorial structures are energetically disfavored). Upon pseudo-rotation the 2'-OH becomes equatorial and 3'-OH apical which upon bond breakage results in isomerisation of the phosphate diester linkage.

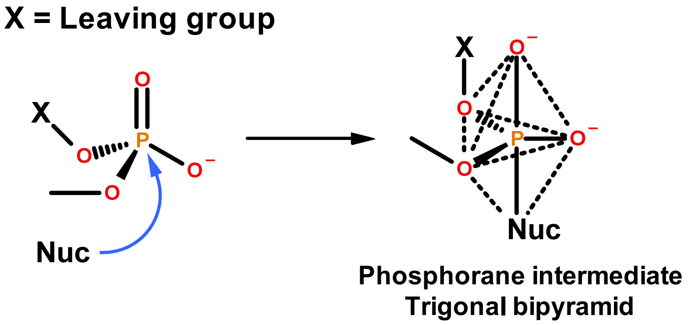

Figure 1.13. The formation of the phosphorane intermediate in phosphate hydrolysis.

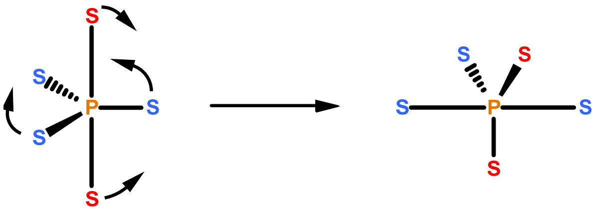

Figure 1.14. The mechanism of pseudo-rotation for the phosphorane intermediate. The substituents are coloured according to their initial position, the apical position (red) and the equatorial position (blue).

The cleavage of the RNA analogue 3’,5’-UpU, see Figure 1.15, revealed that the cleavage reaction is acid (pH < 4) and base (pH > 6) catalysed with a small pH-independent region at pH 5. The corresponding isomerisation reaction between 2’,5’- and 3’,5’-UpU was acid catalysed below and pH-independent above pH 4. Interestingly the isomerisation surpasses the rate of cleavage between pH 3-6 and is 25-fold faster than the corresponding cleavage in the pH-independent region (pH 5).[24,25]

The intramolecular transesterification is proposed to occur through a water-mediated deprotonation of the 2’-OH coupled with a nucleophilic attack by the developing oxyanion on the phosphorous center. It was initially believed that small molecular catalysts generally do not provide enough stabilisation to achieve the interconversion between the two isomeric products (2’- or 3’-phos-phorylated) of the cyclic phosphate.[26]

More recent results[27,28] have proven that a small dinuclear Zn(II) complexes are able to both cleave and isomerise RNA model compounds. Using a phosphonate that precludes the possibility of in-line displacement of a leaving group the observed isomerisation proves that the complex stabilises the pentacoordinate phosphate intermediate sufficiently for this to occur. The stabilising effects of similar dinuclear complexes through Lewis acidic interactions and potential hydrogen bonding will be discussed in subsequent chapters.

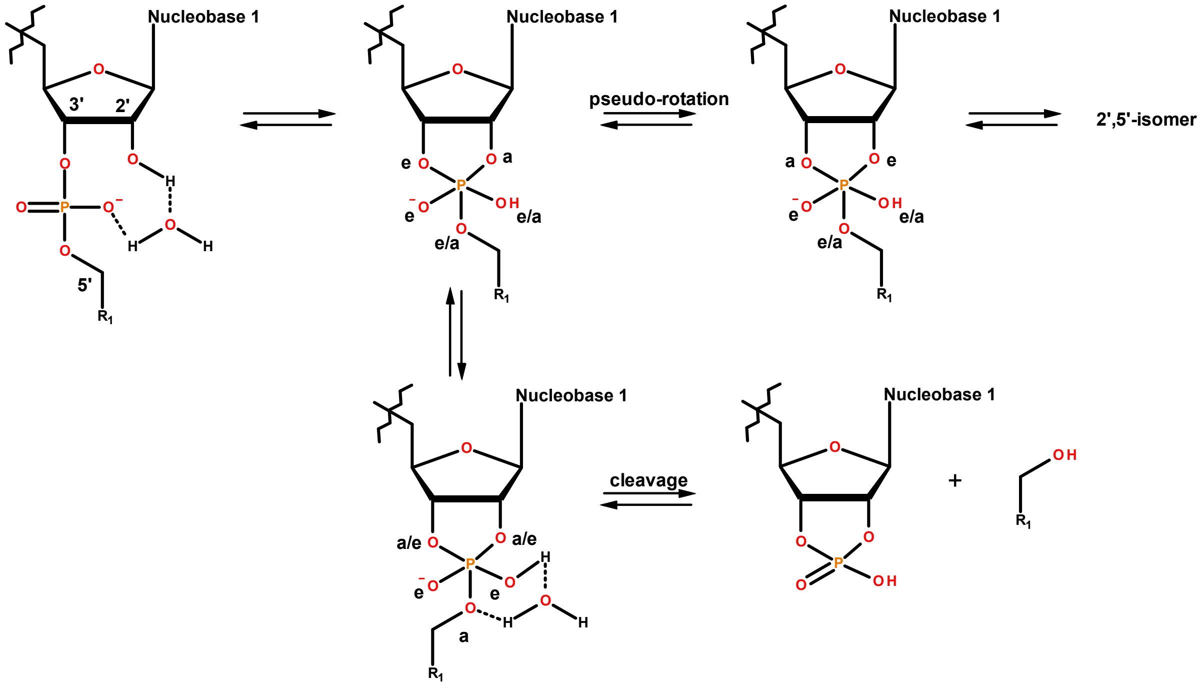

Figure 1.15. The mechanism of the pH-independent transesterification of RNA where the positions of the substituents in the phosphorane are indicated by a (apical) and e (equatorial). R1 represents various substituents.

An RNA analogue, see Figure 1.16, that is commonly used with artificial complexes is 2-hydroxypropyl-(4-nitrophenyl) phosphate, HPNPP, that is 100-fold more reactive than UpU to base catalysed cleavage. HPNPP is subject to the same criticism as BNPP due to the presence of the very good leaving group (PNP). The native RNA (and DNA) lacks good leaving groups that can be conveniently detected (nucleoside) by UV-vis compared to HPNPP (4-nitrophenol).

The extent of the P-O bond fission in the rate limiting transition state varies depending on the leaving group which is confirmed by the Brønsted parameter (β_{LG}) that has been estimated for alkyl (-1.28) and aryl 3'-phosphates (-0.59). The pentacoordinate alkyl phosphorane has a finite life time and the rate limiting step (RLS) is the departure of the leaving group whereas the RLS for the pentacoordinate aryl phosphorane is the formation of the phosphorane. Interestingly, studying the reaction of HPNPP transesterification using kinetic isotope effects (KIE, Chapter 1.4.2) measured at the nucleophilic atom and in the leaving group revealed that the uncatalysed reaction proceeds through a single transition state with little bond fission between the leaving group and phosphorous center.[29] The KIE for the nucleophile indicated that the bond formation to the phosphorous center was the RLS. In the catalysed reaction the transition state was different with greater leaving group bond fission and greater nucleophile bond formation to the phosphorous with the KIE indicating that the leaving group departure had become the RLS.The nucleophilic 2’-OH of HPNPP is more flexible and has a higher pK_a than the corresponding ribose OH in RNA. The advantages of HPNPP paradoxically are also its flaws since it becomes more dissimilar to the native RNA for which the study is intended.

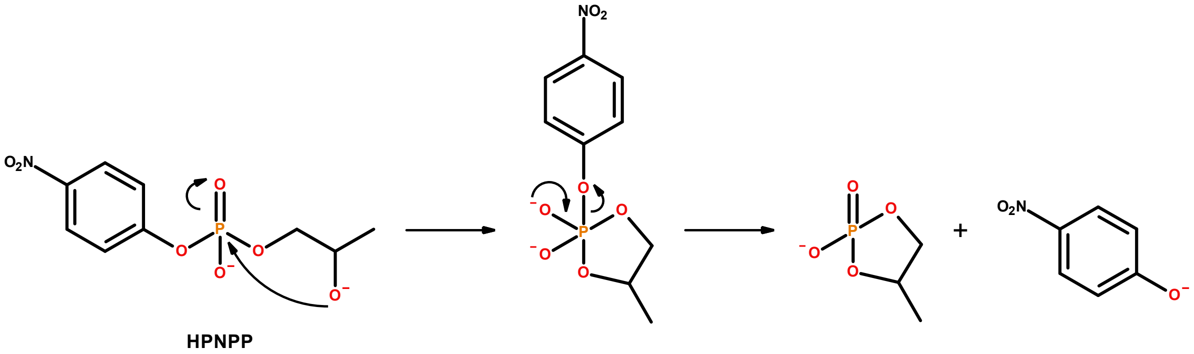

Figure 1.16. The intramolecular transesterification of HPNPP.

A HPNPP analogue that can be used when still greater reactivity is convenient is HPNPPi. The substrate HPNPPi, see Figure 1.17, is a more reactive isomer of HPNPP which contains a primary alcohol as the intramolecular nucleophile. This substrate is approximately 10-fold more reactive than HPNPP and is usually used in conjunction with less efficient catalysts.

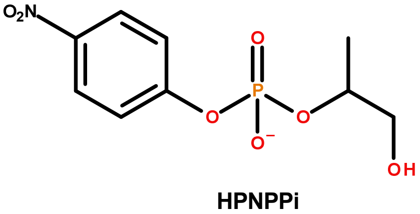

Figure 1.17. The structures and the mechanism for the transesterification of HPNPPi and HPNPP are very similar.

A more RNA like alternative that has been used in literature is UpPNP, see Figure 1.18, that still uses the PNP leaving group but with a ribonucleic 2’-OH nucleophile.[30] The substrate UpU and its equivalent dinucleoside monophosphates offer the advantage of being essentially a dimeric RNA unit and is mainly used with highly reactive complexes.[27] The poorer leaving group in UpU (nucleoside) compared to HPNPP results in the RLS for the uncatalysed reaction being the leaving group departure.

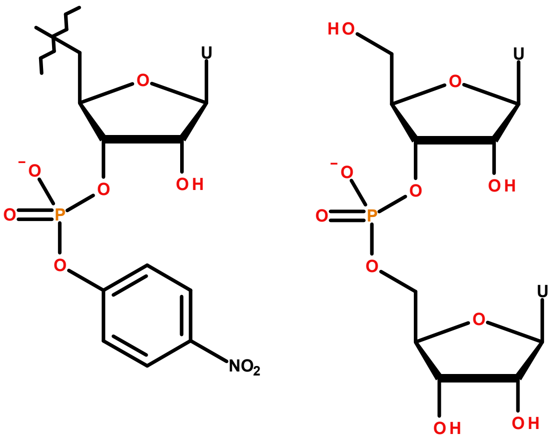

UpPNP UpU

Figure 1.18. The UpPNP and UpU that are commonly used as RNA analogues (U = Uracil).

1.2 - Role of metal ions

Metal ions play an important role[31,32] in the catalytic processes in the active site of many enzymes and are therefore central to the mechanistic investigation and design of artificial catalysts. Although most metal ions do not display remarkable reactivity unless bound to one or multiple ligands, the activity of some metal ions is substantial even in the absence of ligands (e.g. Ce (III)).

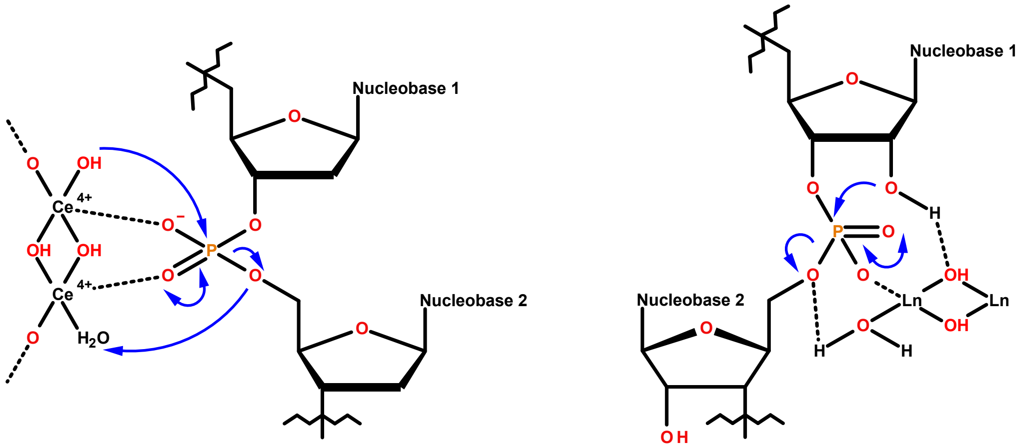

Ce^{4+} - DNA

Ln - RNA
Tm^{3+}/Yb^3

Figure 1.19. The proposed mechanisms for DNA and RNA hydrolysis using Ce(IV) and La(III), respectively.

Among the most reactive metal ions for the catalysis of phosphate diester bond hydrolysis are lanthanides (La(III), Ce(III/IV), Th(IV) etc).[33] The DNA and RNA hydrolysis mechanisms with free lanthanide ions in solution has been proposed to involve metal hydroxide gel structures, see Figure 1.19. Lanthanides are known to form multi-nuclear clusters in solution under physiological conditions even in the absence of ligands. Although lanthanides have proven to be highly effective in promoting the hydrolysis of DNA and RNA[34,35] they are not biologically relevant. Many natural enzymes achieve remarkably high rates using metal cofactors that are moderately reactive in solution or in artificial complexes (Zn(II), Fe(II/III), Mg(II) etc). This demonstrates the inability of the artificial complexes to mimic the interactions in enzyme active sites and ultimately highlights the limited knowledge of these processes.

Many first-row transition metals can be found in the active sites of metalloenzymes that utilise one, two or more metal cofactors (Zn, Cu, Fe etc).[36] The metal nuclei can be seen interplaying cooperatively to achieve the overall catalytic effect: activating the substrate through Lewis acidic interaction with the metal ions, stabilising the transition state structure, lowering the pK_{a} of the nucleophilic moiety in the reaction (intramolecular hydroxyl or metal bound water) and aiding in the departure of the leaving group, see Figure 1.20.

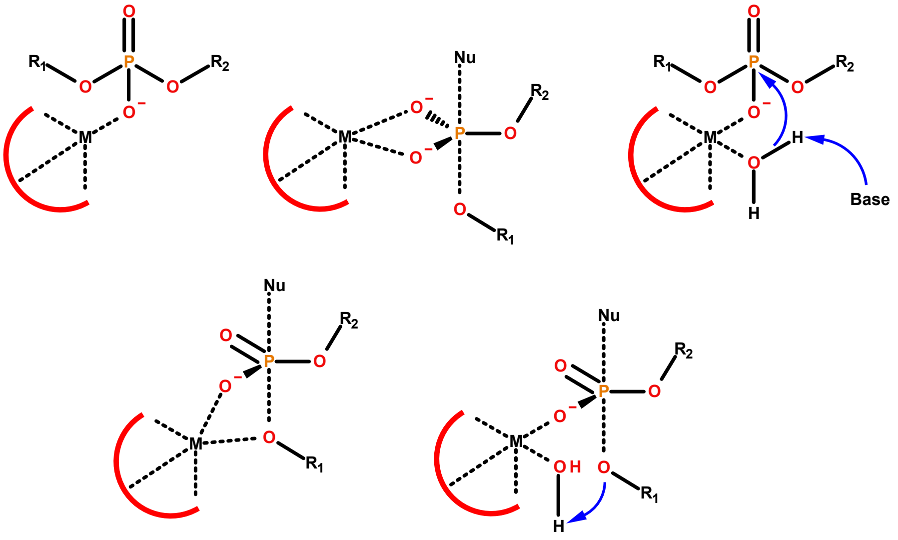

Figure 1.20. The different potential roles of metal ions (M) in catalysis from left to right: Lewis activation, transition state stabilisation, nucleophile activation, leaving group coordination and leaving group protonation.

Magnesium-dependent nucleases are common in nature[37] but Mg(II) itself is a weak Lewis acid and thus cannot efficiently promote the activation and hydrolysis of phosphates in solution,[38] although it has been reported that a Cl$^-$-bridged Mg(II) catalyst was able to cleave DNA.[39]

Zinc has been identified in hundreds of metalloenzymes and several grams of it can be found in the human body. Due to the versatility of Zn(II) and its appearance in many enzymes it has been the focus of many synthetic complexes.[40] It is commonly found in a mononuclear tetrahedral coordination geometry in the active site of enzymes.[41,42] The tetrahedral coordination sphere for Zn(II) in enzymes exhibit a striking preservation of the ligand structural arrangement between different enzyme families.

The three amino acid residues that form the base of the tetrahedron are positioned in a distinct pattern along the sequence. The ligands (L_1, L_2 and L_3) are arranged so that L_1 and L_2 are spaced by 1-3 amino acids and thus form the initial bidentate coordination to the Zn(II). The L_3 ligand is positioned 20-120 amino acids further along the sequence and provides the third coordination to the Zn(II) with some margin for flexibility.[43] One example of this arrangement can be found in carbonic anhydrase II (CAII) that coordinates to Zn(II), see Figure 1.21, by means of His_{94}, His_{96} and His_{119}. There are several examples of this in enzymatic active sites that employ Zn(II) cofactors but also iron and copper.[44]

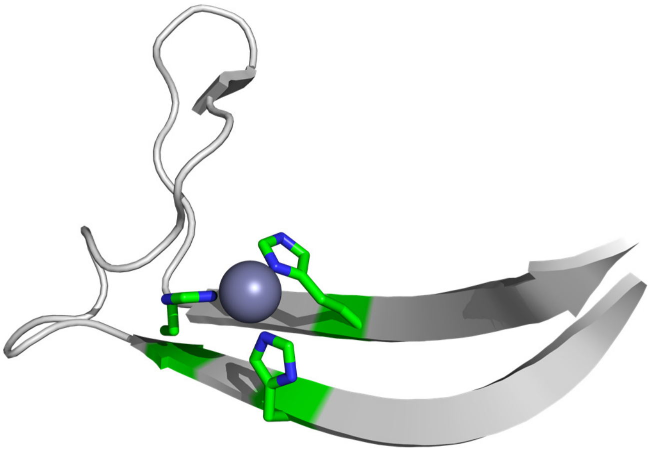

Figure 1.21. The anti parallel β-sheet around the Zn(II) core in the carbonic anhydrase. The sequence displayed here includes Tyr_{88} to Asn_{124} and the ligands are His_{94}, His_{96} and His_{119} (PDB code: 2CBA).[45]

The prevailing coordination geometry in enzymes with a single metal ion cofactor is the tetrahedral arrangement involving three backbone amino acids (usually histidine, cysteine, glutamic acid or aspartic acid) and a fourth coordinated water molecule. Some enzymes, for example prometalloproteinase, have a tetrahedral coordination to 4 amino acids (L_1, L_2, L_3 and Lx) and need to be activated[46,47] in order for water to coordinate, see Figure 1.22.

The metal-bound water is essential for the catalytic activity of many enzymes since Lewis acidic Zn(II) is able to reduce the pK_a of the water to near 7, making the nucleophilic hydroxyl species available at significantly lower pH than would otherwise be possible. Metal ions in catalytic structures have generally been considered to contribute to the hydrolysis rates by providing a general base (hydroxide) near neutral pH.

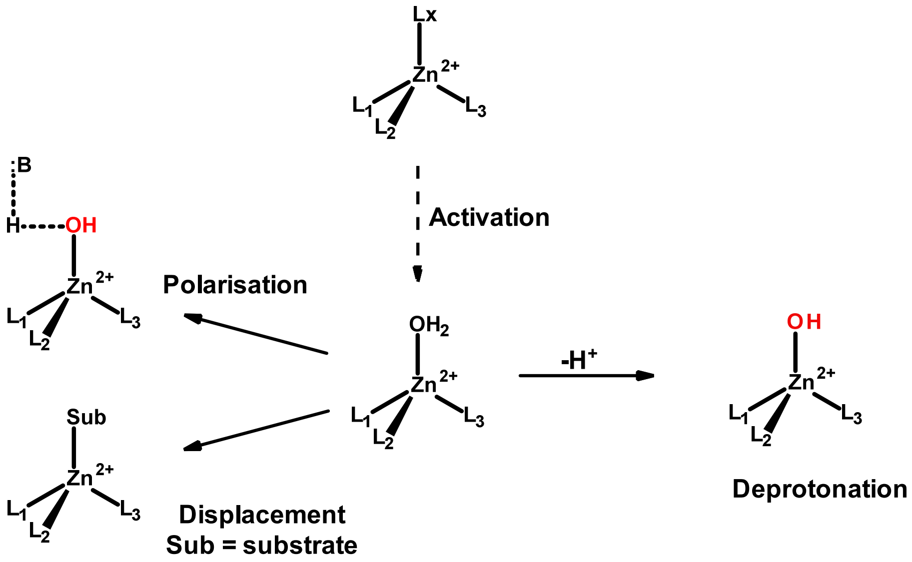

Figure 1.22. The activation of Zn(II) through displacement of the non-aqua ligand L_X followed by various interactions with the Zn(II) bound water.

Interestingly, the increased acidity of the metal bound water has been reported to potentially lead to acid catalysis, as has been reported for Co(III) complexes.[48] Base catalysed transesterification of RNA leads to a dianionic transition state and the release of an alkoxide (β_{LG} = - 1.28) whereas the acid catalysed reaction leads to an alcohol leaving group (β_{LG} = - 0.12). The mechanism of RNA transesterification in the presence of a metal ion is similar to base catalysed transesterification since no intermediate has been observed but the leaving group has been found to depart as an alcohol (β_{LG} = - 0.32). The use of Zn(II) appears to enhance the protonation of the leaving group compared to the buffered pH-independent reaction. The behavior of Zn(II) therefore bears characteristics of both the acid and base catalysed reaction, see Figure 1.23. The potential dual catalytic role of the Zn(II) begs the question of the possibility of simultaneous interaction with multiple metal ions.

The mechanism for the pH-independent spontaneous RNA cleavage, see Figure 1.15, has been suggested as the most appropriate model for the transesterification involving small molecular complexes.[22] It is worth noting it has been reported that dinuclear Zn(II)

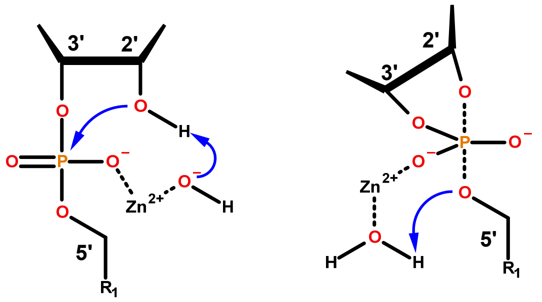

Figure 1.23. The proposed mechanisms for the Zn(II) catalysed transesterification of RNA. The general base catalysis (left) and general acid catalysis (right).

complexes do not use a mechanism involving acid/base catalysis.[30] The small molecular complexes used for the cleavage of RNA or DNA model compounds will be introduced in the subsequent chapters.

Many enzymes have dinuclear arrangements in the active site to allow for cooperative activation and stabilisation of the substrate. The cooperativity between metal ions is central to the roles of many enzymes where multiple metal cofactors interact to achieve the desired catalytic activity. The cooperative role of the metal ions and amino acid residue in enzyme active sites have been reviewed[49,50] and suggests their important role in transition state stabilisation, leaving group activation and nucleophile activation.

The importance of correct positioning of the substrate in the active site prior to the catalysis is essential and might account for some of the discrepancy in reactivity between enzymes and artificial catalysts.

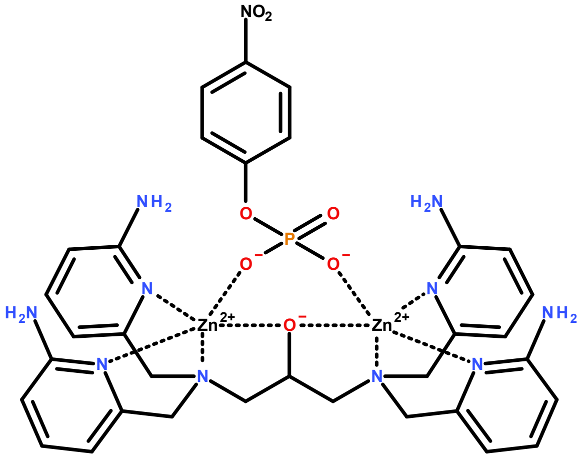

Figure 1.24. The proposed coordination mode of the transition state analogue 4-nitrophenyl phosphate to a dinuclear complex based on x-ray crystallography.[51]

In an artificial dinuclear catalyst for the hydrolysis of phosphate diesters the binding of the substrate is suggested to be through the non-bridging oxygens of the phosphate, see Figure 1.24, leaving very little room for a nucleophile to be activated by the Lewis acidic nuclei.[51] In the case of dinuclear enzyme active sites the substrate is bound in an alternate arrangement that allows for simultaneous nucleophile and leaving group activation. This is illustrated by the structure of a transition state analogue (vanadate, VO_4^{3-}), see Figure 1.25, in the active site of the naturally occurring enzyme phosphodiesterase X. axonopodis nucleotide pyrophosphates/phosphodiesterase (NPP).[37,52,53]

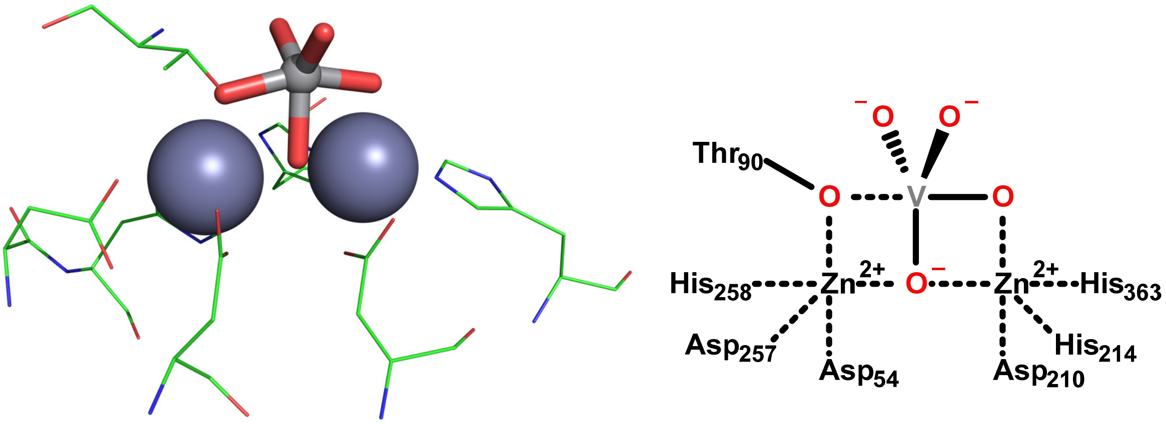

Figure 1.25. The structure of the metal coordination site in enzyme X. axonopodis NPP with bound vandate illustrates the possible interactions in the active site between the dinuclear structure and a phosphate diester in the transition state. Threonine (Thr$_{90}$) represents the nucleophile which held in close proximity of both the Zn(II) and vanadate (PDB code: 2GSO).[45]

Since no artificial catalyst has been successful in achieving all the interactions or rate enhancements seen in enzymes it is clear that there is still a gap in our knowledge of how to replicate the function of these catalysts.

The key to understanding the catalytic rate enhancement provided by enzymes is to study the interactions in their active sites and identify the structural requirements for efficient catalysis.

1.3 - Enzyme catalysis

Enzymes are large biopolymers that function as highly efficient catalysts for most biochemical reactions.[54] The ratio of the size of the enzyme to the size of the active site for most enzymes reveals that the bulk of the structure is not directly involved in the catalysis, see Figure 1.26. The enzyme structure is not efficient with respect to total enzyme residues versus active catalytic residues but the large structure is necessary for other recognition/regulation processes *in vivo*.

The structure of the enzyme functions as a macromolecular scaffold for the appropriate positioning of interacting residues around the active site. The residues involved in the active site are usually widely spaced in the linear protein sequence but become well organised in the active site due to the enzymes secondary and tertiary structure.

The catalytic rates observed in enzymes are due to the well defined structure of the active site that allows for multiple specific interactions with the substrates.

The maximum catalytic efficiencies (k_{cat}/K_M) for most enzymes are relatively similar regardless of the reaction in question since there is an upper limit to the reaction rate. This upper limit is the rate of enzyme-substrate collisions in a solution and depends on the bimolecular diffusion rates of the components (diffusion controlled kinetics). There are many enzymes that reach this limit[54–56] but most enzymes work within a few orders of magnitude of it.

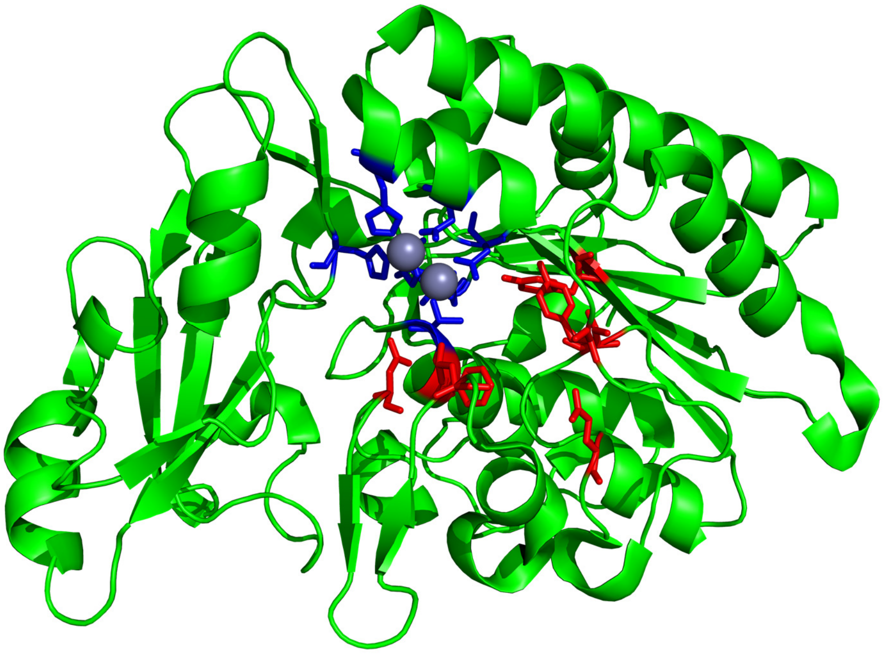

Figure 1.26. The structure of the enzyme X. axonopodis NPP illustrates that the size of the active site is relatively small compared to the overall enzyme structure. The metal coordinated residues (blue) and nucleotide recognising residues (red) have been identified using x-ray crystallography (PDB code: 2GSO).[37,45]

The catalytic efficiency of enzymes will only become as large as is required for a given biological process thus there is no need for diffusion controlled rates for all reactions.[57] For most biological processes the reactions that occur on a milli- to microsecond time scale are sufficiently fast. The effective contribution of an enzyme to the rate of a given reaction can only be appreciated when compared to the rate of the corresponding uncatalysed reaction.

The rates for uncatalysed reactions (k_{uncat}) can differ by many orders of magnitude. The catalytic proficiency ($(k_{\mathrm{cat}}/K_{\mathrm{M}})/k_{\mathrm{uncat}}$) differs significantly for enzyme catalysed reactions since it takes into account the rate for the uncatalysed reaction which provides a more suitable comparison for the work performed by the enzymes.[56] The catalytic proficiency also gives a measure of the formal affinity of the catalyst for the transition state of the substrate which can be compared with transition state analogues.[58] These comparative ratios have revealed a rate acceleration for the enzyme alkaline phosphatase of 10^{27}-fold.[16,53]

The efficiency of an enzyme is characterised by its ability to stabilise the transition state structure of the substrate relative to the ground state and can be related to the dissociation constant of the transition state K_{TS}, see Figure 1.27. The catalyst (C), substrate (S) and catalyst-substrate complex (CS) are in a dynamic equilibrium with K_{M} representing the dissociation constant. k_{uncat} represents the rate at which the unbound substrate (S) reaches the transition state (S*) while k_{cat} represents the same process for the catalyst-bound substrate (CS). The product (P) and the catalyst-product complex (CP) are not considered in this transition state approach. Since $k_{\mathrm{cat}} > k_{\mathrm{uncat}}$, the tightness of substrate binding should correspondingly be ground state < transition state ($K_{\mathrm{M}} > K_{\mathrm{TS}}$).

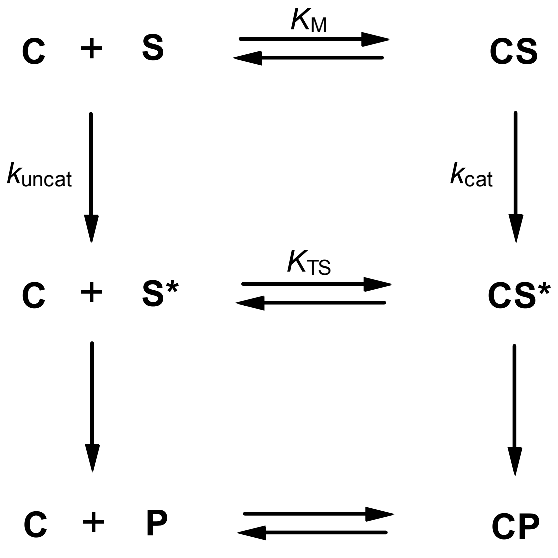

Figure 1.27. The thermodynamic cycle for binding of the substrate to a catalyst in the transition state.

The relationship between the parameters can be described as seen in **Equation 1.1**. An alternative approach is to treat the catalytic proficiency $(k_{cat}/K_M)/k_{uncat}$ as the inverse of K_{TS}.

$$K_{TS} = \frac{k_{cat}K_M}{k_{uncat}} \qquad \text{(Equation 1.1)}$$

The desired properties of a catalyst are to stabilise the transition state better than the ground state since the free energy of activation would otherwise remain unchanged, see Figure 1.28. The differential between the ground state and the transition state equals the free energy of activation (ΔG^{θ}).

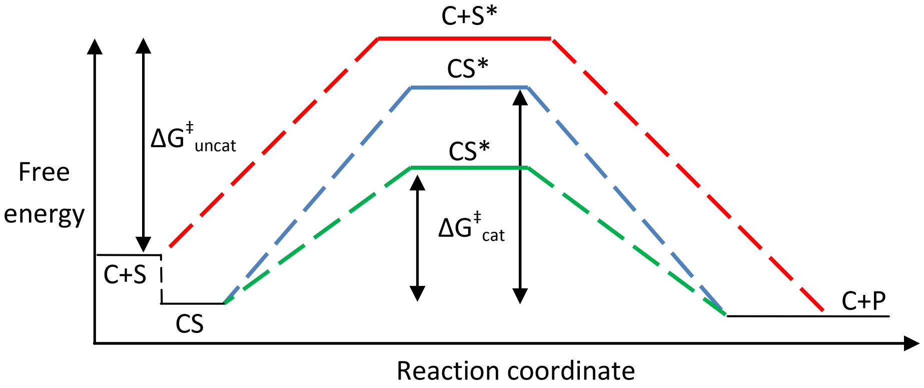

Figure 1.28. The free energy diagrams of the non-catalysed reaction (red) compared to the catalyst-substrate reaction with no differential binding between the ground and transition state (blue). The differential binding between the ground and transition state represents the action of a catalyst (green).

If the binding is identical for the ground state and transition state the there will be no overall reduction in the transition state energy ($\Delta G^{\ddagger}_{uncat} = \Delta G^{\ddagger}_{cat}$). In the case of active catalysis there is a difference in binding between the ground state and transition state binding ($\Delta G^{\ddagger}_{uncat} > \Delta G^{\ddagger}_{cat}$).

The difference between the uncatalysed reactions in solution and the catalysed reactions in the active site of enzymes are the additional interactions provided by the well defined structure of the cavity. For phosphoryl transfer, upon progression from the ground state to the transition state there is a change from tetrahedral to a trigonal bipyramidal configuration which necessitates relocation of the non-bridging oxygens. The electrostatic interactions in the cavity provide efficient stabilisation of the transition state, see Figure 1.29.

The mechanistic path along which the reaction proceeds is determined by studying the structure of the transition state. Since the transition state is intrinsically a very short lived species (life time generally don't exceed 10^{-13} - 10^{-14} s) it is not possible to study directly but it is rather inferred using mechanistic investigation.

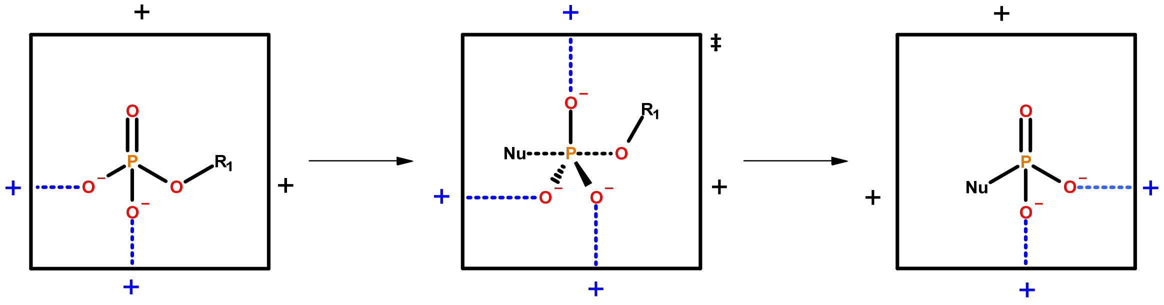

Figure 1.29. A schematic representation of a phosphate monoester binding to an active site in the ground state, transition state and product state. The dotted blue lines represent interactions with positively charged active site residues (or potentially H-bonding).

1.4 - Studying the transition state

The single most important structure in the investigation of mechanisms is that of the rate limiting transition state. The use of stable compounds that mimic the transition state structure should efficiently inhibit a catalysed reaction.[59,60] The problem is that the use of transition state analogues is a limited approach since it is difficult to strictly control the distances between the leaving group and nucleophile relative to the phosphorous center. The differences between a loose and a concerted transition state in terms of bond lengths between the entering and leaving group could be as little as 0.5 Å.[38] It is also worth noting that the transition state analogue would most likely adapt the most energetically favorable binding mode which does not necessarily translate into the same mode as the reacting substrate. Additionally, the use of transition state analogue inhibitors would not be useful for elucidation of the mechanism of the non-catalysed reaction in solution.

It is important to note that the Boltzmann distribution of structures of the transition state varies for different substrates depending on the nature of its intrinsic components and on its environment. A poor leaving group is likely to depart in a transition state that has progressed farther along the reaction coordinate (late transition state) compared to a good leaving group. The extent of bond fission and formation in the transition state will vary depending on whether the reaction is catalysed or not since the catalyst can stabilise structures that would be unfeasible in solution. The different transition states that can form are distinguished by the extent to which a bond is broken or a new bond is formed to the phosphorous center. The transition states are referred to as tight, synchronous or loose depending on the extent of the bond breakage/formation to the phosphorous center.

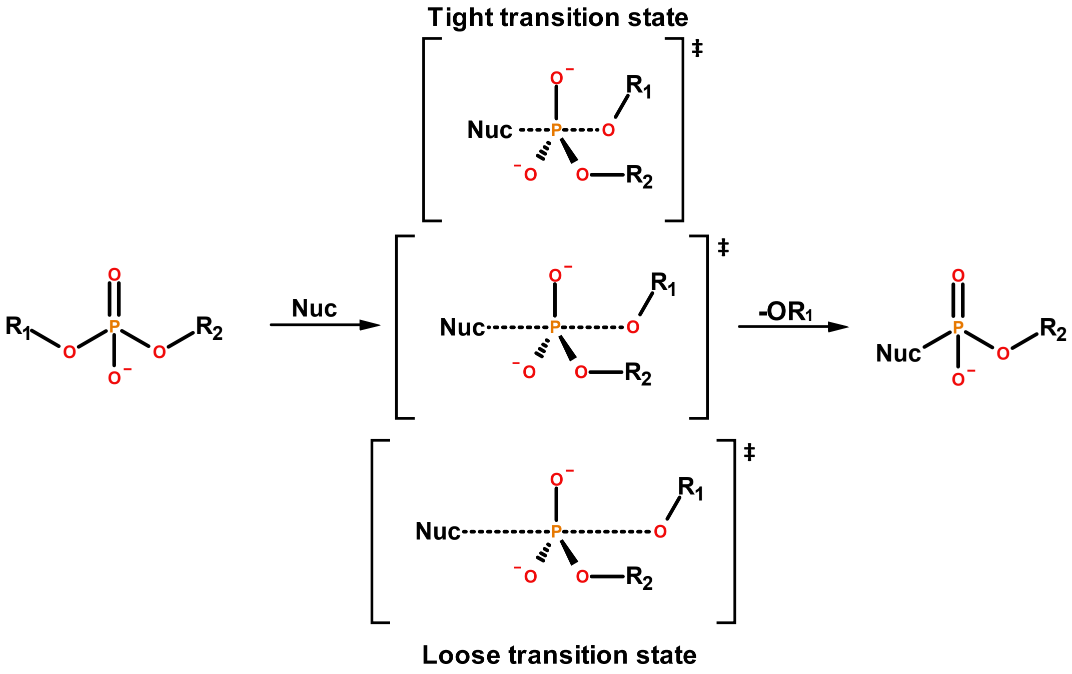

Figure 1.30. The schematic hydrolysis of a phosphate diester using a nucleophile (Nuc) through a tight, synchronous or loose transition state. R_1 and R_2 represent various substituents.

The hydrolysis or transesterification of phosphate diesters proceeds through a pentacoordinate phosphorane that decomposes into the product. The schematic representation in Figure 1.30 illustrates the nucleophilic attack on the phosphorus center of a diester where OR_1 is a better leaving group than OR_2. These potential transition states can be characterised through carefully devised experiments that have been developed for the mechanistic investigation of reactions.

1.4.1 - Linear Free Energy Relationships

A tool commonly used for characterising transition states involves the linear free energy relationships (LFER). The concept of free energy relationships is based on the notion that a bond breakage or formation represents a change in the electron density in the transition state around the bond in question. It can be intuitively deduced that the introduction of an electrondonating or withdrawing group (EDG/EWG) on either of the moieties around the bond will affect the electron density. The charge development in the transition state of a given reaction provides a potential for charge stabilising interactions that can enhance the rate of the reaction. A carefully selected EDG or EWG that is incorporated into the structure of the substrate in order to interact with the developing charge can provide a deeper understanding of the reaction pathway.

A simple and well established example[61] of this stereoelectronic effect is the increased acidity observed for phenol upon the introduction of an electron-withdrawing NO_2-group in the 4-position, see Figure 1.31.

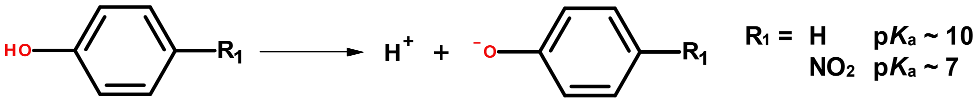

Figure 1.31. The difference in the acidity constant for the phenol and 4-nitrophenol.

The effect of the substituent R_1 in Figure 1.32 on the overall rate constant can be determined by measuring the rate constant of the reaction using different leaving groups with varying pK_a.

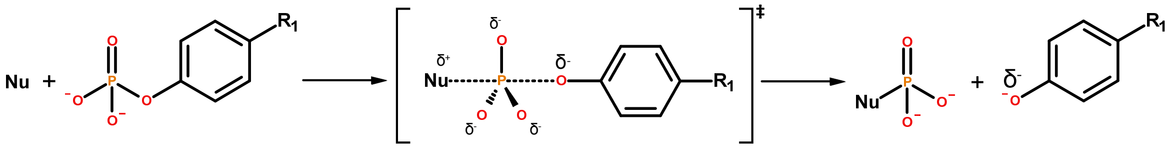

Figure 1.32. The partial negative charge (δ-) on the leaving group develops over the transition state and is fully formed in the product. R_1 represents various substituents.

The logarithm of the rate constant (log k) plotted versus pK_a (for the leaving group or nucleophile) provides a linear fit for which the slope is β_{LG} and β_{NUC}, respectively. The β_{LG}-values are generally negative since reducing the acidity of leaving groups leads to lower reaction rates. The magnitude of β_{LG} indicates the extent of bond breaking to the leaving group in the transition state. The β_{NUC}-values are generally positive and indicate the extent of the bond formation to the starting material since the increase in basicity translates into increase nucleophilicity.

In loose transition states the bond to the leaving group is extensively broken and significant charge has developed. A leaving group with lower pK_a would in this case cause a more dramatic increase in rate than for a tight transition state where not much charge has developed on the leaving group. The β_{LG} is a good indicator for the mechanism of the reaction although some catalysed reactions have displayed large β_{LG}-values despite the presumed associative nature of their mechanism.[38] It is therefore important to evaluate the participation of the nucleophile through the β_{NUC} in order to accurately determine the transition state.

The relationship between the logarithm of the equilibrium constant (log K_{EQ}) and the pK_a gives the gradient β_{EQ} which can be used to normalise the β_{LG} and β_{NUC}-values. The normalisation indicates how similar the charge development in the transition state is to the final reaction product. The ratios $X= |\beta_{LG}/\ \beta_{EQ}|$ and $Y= |\beta_{NUC}/\ \beta_{EQ}|$ can be plotted in a More O'Ferrall-Jencks diagram, see Figure 1.33, which quantitatively presents the experimentally determined nature of the transition state. These ratios correspond to the slope of (log k) versus (log K_{EQ}) which reveals the extent to which the phosphorous-leaving group bond (P-LG) has broken and the extent to which the phosphorous-nucleophile bond (P-NUC) has formed. The scales on the axes in the More O'Ferrall-Jencks diagram range from 0-1 and are sometimes referred to as the bond order. These values correspond to the similitude between the transition state and the product with respect to the P-LG and P-NUC bonds.

Any given reaction can pass through a continuum of different paths from the bottom left corner to the top right corner of the diagram in Figure 1.33. The loose transition state is used to describe any transition state that has a dissociative character (elimination-addition) and passes below the diagonal usually denoted as D_N+A_N. The tight transition state indicating an associative mechanism (addition-elimination) and passing above the diagonal is usually denoted as A_N+D_N. It is important to note that each of these paths can contain more or less of the dissociative or associative characteristics. The synchronous transition state is an S_N2-like (concerted, A_ND_N) mechanism that passes along the diagonal and signifies proportional bond breaking and bond formation.

The nature of a compound determines the structure of the transition state for the uncatalysed reaction. It has been suggested in early studies that the hydrolysis of phosphate monoesters proceeds though a metaphosphate intermediate although a substantial amount of evidence has been suggesting a metaphosphate intermediate it has been challenged by more recent findings.[16] These studies suggest that the mechanism is a concerted process which passes through a metaphosphate-like, loose transition state.

Phosphate diester hydrolysis proceeds through a more concerted mechanism whereas

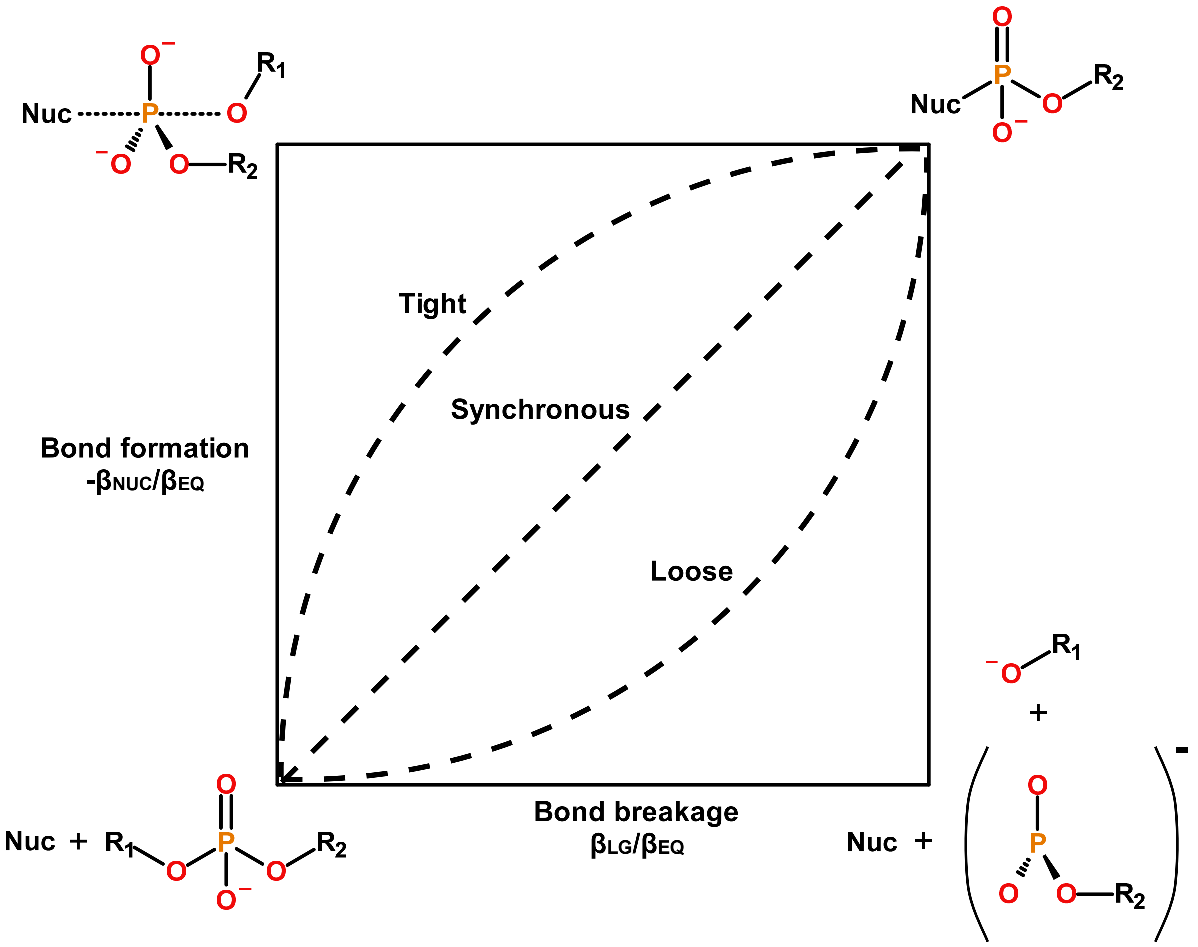

Figure 1.33. The two dimensional More O'Ferrall-Jencks diagram illustrating the mechanistic paths for the respective transition states. R_1 and R_2 represent various substituents.

phosphate triesters proceed through a tighter phosphorane-like transition state. An illustrative example for the use of LFER can be found in literature for the hydrolysis of phosphorylated pyridines, see Figure 1.34, using nucleophiles of substituted pyridines and morpholine.[62,63]

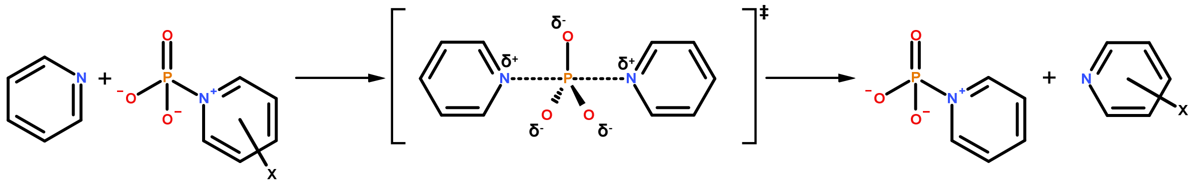

Figure 1.34. The nucleophilic attack of various nitrogen nucleophiles on phosphorylated pyridines as reported in literature.[62,63] The partial charge (δ^- or δ^+) is displayed next to relevant atoms.

The data for the mechanistic analyses provides the parameters β_{LG} (-0.95) and β_{NUC} (0.16) which were obtained using the linear fits to the data shown in Figure 1.35, and β_{EQ} has been reported as 1.05 in literature.[63] The linear relationship plotted between the pK_a for the leaving group (LG) or nucleophile (NUC) with the rate of the reaction is referred to as a

Brønsted plot. The normalisation of the obtained β-values with β_{EQ} yields $X = |\beta_{LG}/\ \beta_{EQ}| = 0.90$ and $Y = |\beta_{NUC}/\ \beta_{EQ}| = 0.15$.These values indicate extensive breaking of the P-LG bond and little bond formation for P-NUC as can be seen in the bottom right corner in the Figure 1.33. This corresponds to a loose transition state where the mechanism is dissociative and the transition state is therefore metaphosphate-like.

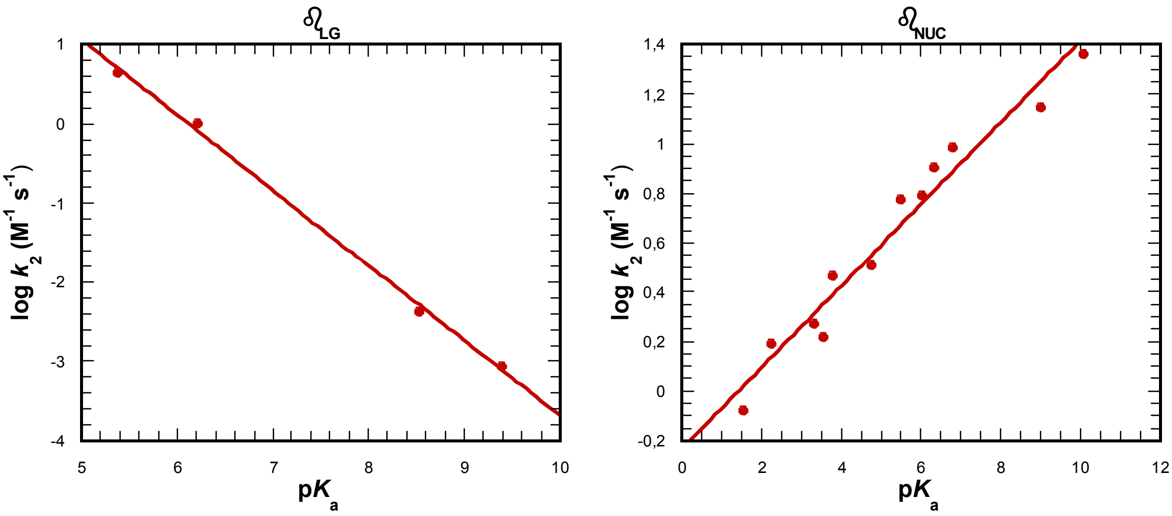

Figure 1.35. The β-values for the leaving group (LG) and nucleophile (NUC) determined from literature data.[62,63]

1.4.2 - Kinetic Isotope Effect

Another widely used tool for investigating the transition state and mechanistic paths is the kinetic isotope effect (KIE). The concept entails the use of an isotope in or near the bond that is broken/formed. The KIE is based on the principle of the zero-point energy of the bonds that are involved in the reaction. Using a heavier isotope reduces the vibrational energy relative to the lighter isotope which results in a larger activation energy (E_a) upon progression to the transition state, see Figure 1.36.

The remote label method involves changing an atom that is not directly involved in the bond formation/fission and which is paired with an isotopic substitution near the site of cleavage. The 4-nitrophenol leaving group can be studied with the primary isotope effect using $^{16}O/^{18}O$ or with the secondary isotope effect where the ^{14}N of the nitro functionality can be replaced by ^{15}N in the phosphorylated substrate.[29]

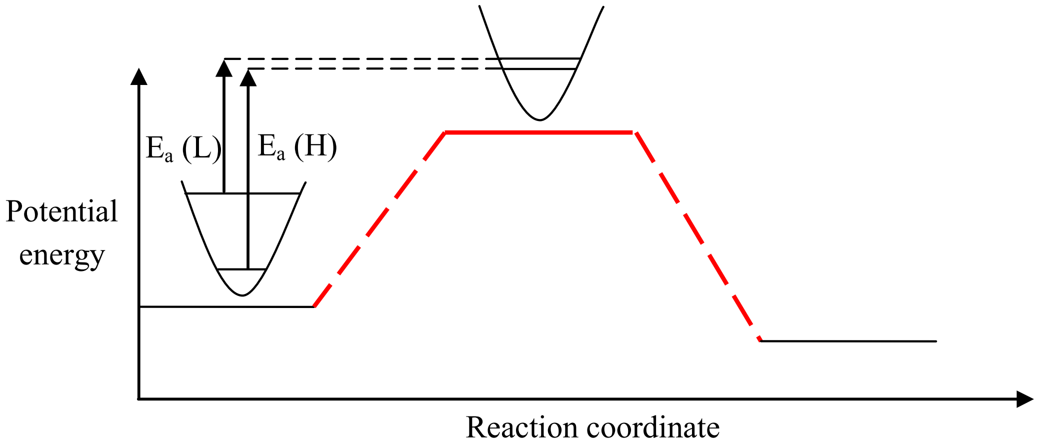

Figure 1.36. The illustration of the KIE where the difference in energy for the light (L) and heavy (H) isotope is exaggerated to indicate the observed ratio of reaction rates. The figure is illustrates the commonly observed $k_{light} > k_{heavy}$ which is associated with the reversed relationship of E_a (L) < E_a (H).

The observed ratio of the rate constants when using the isotopes (k_{light}/k_{heavy}) indicates the extent of the bond fission in the transition state since the difference in vibrational energy becomes less pronounced as the bond length is increased. This method can be used for both catalysed and uncatalysed reactions. When studying the catalysed reaction it is obviously more difficult to vary the nucleophile in enzymes compared to the reaction in solution and normal LFER are therefore abandoned in favor of KIE.

The incorporation of an isotope into the substrate is not very invasive in the sense that the structure of the substrate remains unchanged and it is therefore reasonable to assume that the overall properties of the compound are retained. The main disadvantages of isotope chemistry are the high-precision instrumentation required for the analysis, the limited dynamic range of the potential effects, and the dependence on theory to interpret the data in structural terms. Despite this the KIE still remains a powerful tool for mechanistic investigation.

1.5 - General Aims

The overall aim of this project is to study the behavior of catalytic Zn(II) complexes and develop an understanding of the interactions that are important for catalytic activity. The small molecular complexes serve as simplified models of enzyme active sites and can be synthetically modified to study the effects of specific interactions (hydrogen bonding, nuclear Lewis acidity, internuclear distance etc.).

The initial studies focus on the reactivity of dinuclear Zn(II) complexes. The use of the dinuclear arrangements in small molecular catalysts[64] stems from the extensive precedence of multinuclear configurations in the active site of many enzymes.[36]

Although mononuclear complexes have proven to be reactive towards phosphate diesters[14] it is clear that internuclear association is important for highly reactive systems since the dinuclear arrangement can offer cooperatively interacting nuclei.[51,65–67]The dinuclear complexes presented herein incorporate a bridging functionality that encourages the cooperation of the Zn(II) nuclei. These complexes have been reported to be among the most reactive complexes to date.[51]

A further aim of this project is to study the interactions between mononuclear Zn(II) complexes in different association-promoting environments and its effect on the rate of HPNPP transesterification. The reactivities of these systems are generally less impressive than the covalently linked dinuclear complexes. There have been reports of mononuclear complexes and dinuclear complexes lacking cooperative internuclear bridges that surpass the reactitivity of bridged dinuclear complexes although these activities have been attributed to medium effects.[68,69] The effects of incorporating mononuclear complexes in membranes and peptides will be discussed herein and compared to the dinuclear complexes.

Lastly, the use of nucleophilic species in mononuclear complexes for the hydrolysis of the DNA model compound BNPP will be discussed as well as their potential incorporation into larger peptidic scaffolds.

Chapter 2 - Dinuclear complexes

2.1 - Introduction

The stability to hydrolysis of the phosphate diester bond was described in the previous chapter, along with the fact that this reaction is very efficiently catalysed by enzymes. A major challenge is to achieve similar catalytic efficiency using small molecular catalysts and significant effort has been made over the years to study and develop these catalysts.[22,40,70–72]

It has been described in the previous chapter that metal ions can assist in the deprotonation of the intramolecular 2’-OH nucleophile as well as aid in leaving group departure through general acid-base catalysis. This has also been suggested to be the case for dinuclear metal complexes based on the observations by Morrow *et al.*[66] where the lack of coordinated H_2O/OH in Cu(II), see Figure 2.1, due to the five-coordinate nature of the metal ions has been proposed to be the reason for its lack of reactivity towards HPNPP. The Zn(II) nuclei on the other hand can adapt a 6-coordinate geometry which allows for metal bound nucleophiles to exist simultaneously with a bound substrate.

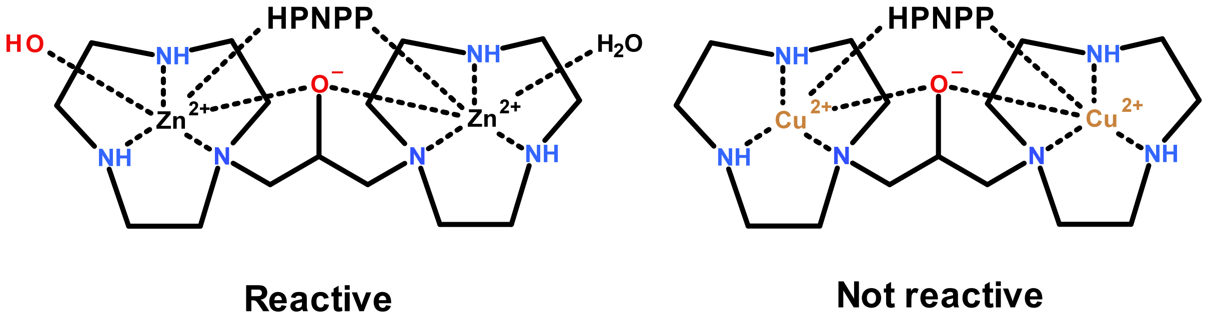

Figure 2.1. The different coordination geometries of Zn(II) and Cu(II) in a dinuclear complex has been proposed to affects their reactivity towards HPNPP.

However, more recently it has been reported that these assumptions are not substantiated by experimental observations. The dinuclear Zn(II) complex indicated no solvent kinetic isotope effect (SKIE) for either mononuclear[73] or dinuclear Zn(II) complexes[30] and normal equilibrium solvent isotope effects were observed for the pK_a of metal-bound water which excludes the involvement of Brønsted acid-base catalysis.[30]

In contrast, a larger SKIE has been observed for guanidinium functionalities that use the general acid catalysis for phosphate hydrolysis.[74] These results suggest that the main contribution of the dinuclear complexes towards the transesterification of HPNPP is the electrostatic stabilisation of the transition state through the dinuclear cationic core.

This chapter focuses on the dinuclear Zn(II) complex catalysed transesterification of HPNPP and builds on previous studies[51] with suggestions for potential future modifications of the catalyst structure.

2.1.1 - Zn(II) ions in complexes

Mononuclear metal complexes are molecular entities in which one metal ion is coordinated to one or more molecular ligands that alter its coordination geometry and/or Lewis acidity. The chemical properties of the metal ion are central to the activity of the complex as a whole and can be tailored by various coordinating functionalities. The Lewis acidity of a metal ion indicates its ability to activate a substrate or nucleophile towards a specific chemical reaction.

Zn(II) has been reported to catalyse the cleavage of RNA[48] in solution but the catalysis is limited by the solubility of the metal ion which decreases with increasing pH due to the formation of poorly soluble zinc hydroxides. Coordinating Zn(II) to a ligand helps avoid precipitation. The pK_a of water bound to the metal ion, which indicates its Lewis acidity, increases with increasing tightness of binding to the ligand (the reported pK_a for $[Zn(H_2O)_6]^{2+}$ is 8.96).[75] It has been reported by Kimura *et al.*[76] in their study of carbonic anhydrase mimics that a small structural change in the ligand results in tighter metal binding and reduced Lewis acidity of the Zn(II), see Figure 2.2. Thus, complex stability and one of the parameters correlated with activity are in conflict with each other.

The ability of the metal ion to polarise a substrate is an important property as the increased acidity of the metal-bound water will increase the concentration of nucleophile available at low pH. It has generally been considered desirable to obtain highly acidic metal complexes since this is indicative of a highly Lewis acidic Zn(II). Many enzymes contain relatively acidic metal bound species (e.g. bovine carbonic anhydrase pK_a 7.5) which lends further support to this reasoning. However, it is important to remember that enzymes operate under physiological conditions which necessitate this acidity in order for the formation of

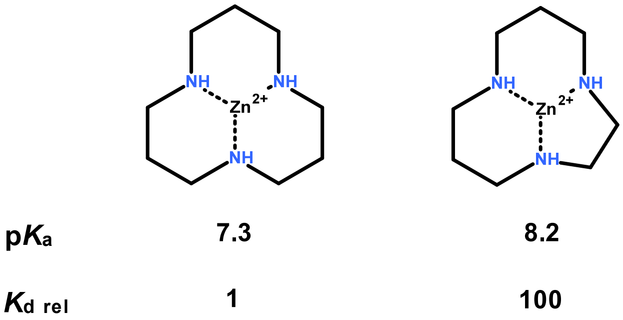

Figure 2.2. The pK_a of the metal bound water increases with increasing tightness of binding between metal and ligand.

sufficient amounts of nucleophile. Reducing the pK_a of the metal bound water leads to larger amounts of the active nucleophile being present at low pH but concomitantly reduces its nucleophilicity.

A series of complexes, see Figure 2.3, were investigated by Bonfá *et al.* and showed that the acidity of the metal-bound water in Zn(II) complexes is highly dependent on the ligand structure and coordination geometry.[73]

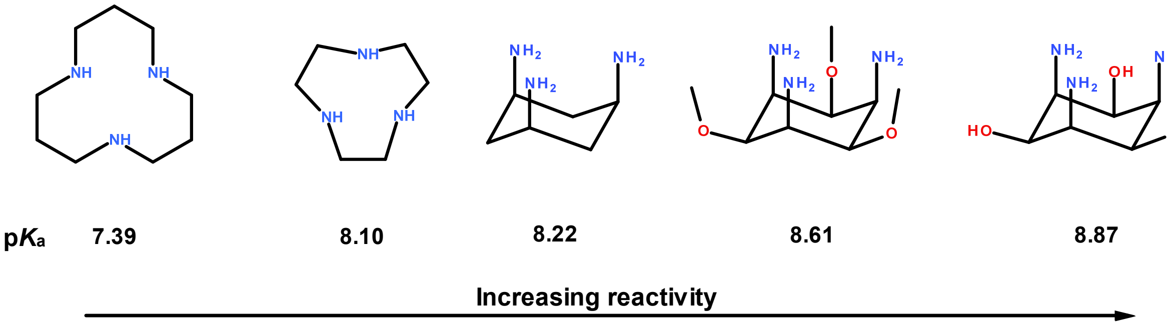

Figure 2.3. The structure of the ligands used in literature with Zn(II) where the reactivity of the complexes increases with basicity. The pK_a reported for the compounds in the figure are for the corresponding Zn(II) complexes.

The HPNPP transesterification was studied with these mononuclear Zn(II) complexes and the Brønsted plot yielded a steep slope (β_{NUC} = 0.75) which displays a strong correlation between basicity of the metal bound hydroxide and the observed activity. The coordination environment was also found to determine the reactivity of the catalyst since the metal ion is required to have free binding sites for the substrate.

The tridentate ligands are more reactive than the tetradentate ones due to the different Lewis acidity of the Zn(II). Interestingly, some tetradentate ligands displayed a difference in reactivity despite having Zn(II) ions of similar Lewis acidity. The reason the discrepancy is that the ligands which can form a facial coordination environment around the metal ions can bind the substrate more efficiently than ligands that are unable to provide such a coordination geometry.[73]

The activity of mononuclear complexes is usually limited to highly reactive substrates. Given that many enzymes utilise two or more nuclei in the active site, it is reasonable to investigate the effects of combining multiple mononuclear complexes to encourage cooperative interaction.[39,71] It is has been shown that ligands containing two metal coordinating sites form dinuclear complexes that are more reactive than their mononuclear equivalents if cooperative interaction is encouraged.[51,65] In small multinuclear complexes the bridging interaction is often achieved using a covalently bound functionality (e.g. alkoxy, phenoxy[40,64,77] etc).

Among the most studied artificial catalysts for phosphate diester hydrolysis are the 1,4,7-triazacyclononane (TACN) based complexes that have been studied both in a mononuclear and dinuclear arrangement.[66,67,78–81] The complexes in Figure 2.4 were used for HPNPP transesterification by Iranzo *et al.* and provide a good benchmark for comparing the effects on reactivity of having two covalently linked mononuclear complexes in close proximity.[66,67]

The dinuclear complexes were all found to form stable complexes with Zn(II) but the large differences in rate constants between the alkoxy-bridged complex and the non-bridged ones is symptomatic of the inability of the non-alkoxy-bridged complexes to form cooperative interactions between the nuclei. A 2-fold rate increase for a dinuclear complex over its mononuclear equivalent is consistent with the additive reactivity of non-interactive subunits whereas a larger increase indicates internuclear cooperativity.

The desired structural feature of a catalyst for the hydrolysis of phosphate diesters is to provide a high local positive charge density that can stabilise the developing negative charge in the transition state. The relative rates presented in Figure 2.4 can be seen in light of the increasing internuclear association. A tether containing a negatively charged bridge will shield the cationic repulsion between the Zn(II) and deliver two mononuclear complexes in relatively close proximity to each other. Likewise, the alkoxy-bridged dinuclear complex provides two closely associated mononuclear complexes resulting in cooperative (120-fold) rate acceleration. Moreover, the tightness of binding is increased 6-fold for the dinuclear

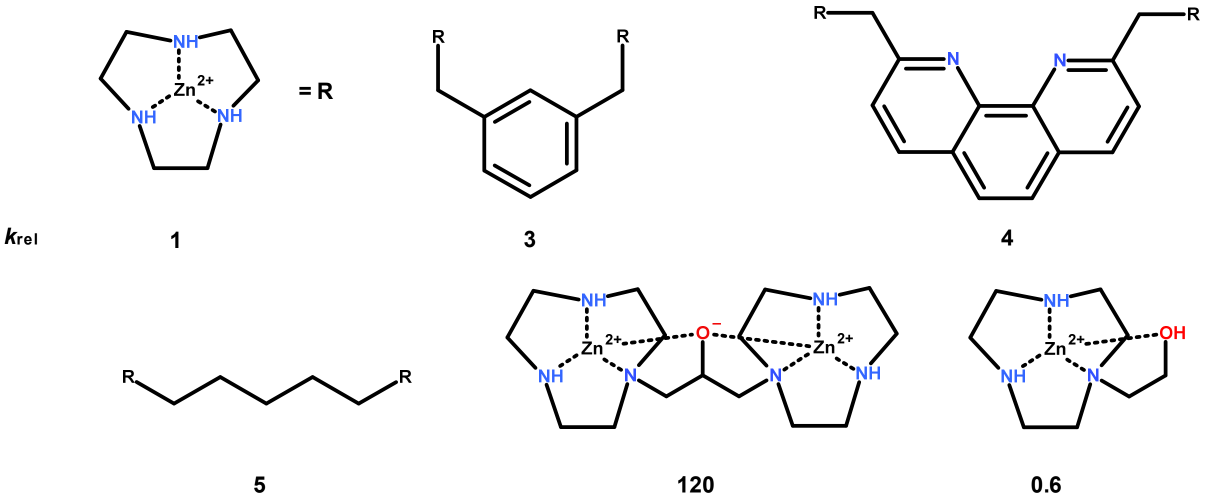

Figure 2.4. The relative rates for HPNPP transesterification at pH 7.6 for the TACN based complexes indicate cooperative interactions between the Zn(II) nuclei.

complex which only accounts for one twentieth of the observed rate increase. The introduction of an alkoxide appendage into the mononuclear complex led to a reduction of reactivity at pH 7.6[67] and an increase of the pK_a to 9.5 (8.1 for TACN)[73] which indicates that the alkoxide reduced the Lewis acidity of the Zn(II). It appears that the internuclear bridge is important for efficient cooperativity in dinuclear complexes but it raises questions about the potential interference of the oxyanion due to electrostatic effects.

The logical arguments against the anionic bridging are based on the potential electrostatic repulsion with the anionic substrate and the reduction of the Lewis acidity of the metal nuclei. Despite this apparent loss of favorable charge interactions with the substrate, there is an overall beneficial cationic charge density from the Zn(II) ions that stabilises the developing net negative charge in the transition state.The effect of the alkoxy-bridge has been studied in non-aqueous media (MeOH) following the enormous rate acceleration[69] seen for the dinuclear complex in Figure 2.5.

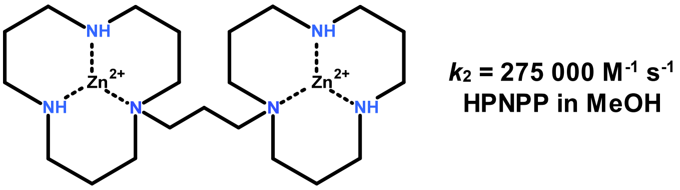

Figure 2.5. The dinuclear complex studied by Brown *et al.* for the transesterification of HPNPP in MeOH.[69]

Although the rates observed in methanol cannot be directly compared to the aqueous system the results were compared to methanol experiments internally between relevant complexes, see Figure 2.6. The conclusion is that the permanent anionic bridge is not required to achieve strong cooperativity between the nuclei in methanol but rather it seems to have a detrimental effect on the activity. This effect is consistent with the proposed reduction of Lewis acidity and change in the coordination geometry upon binding the alkoxide. Despite these results in methanol it is clear that the reactivity in aqueous media is dependent on a bridging functionality in order to achieve internuclear cooperativity. It would be interesting to compare the effects of the alkoxy-bridge with less nucleophilic bridging functionalities in the dinucleating environment and this will be discussed in later sections.

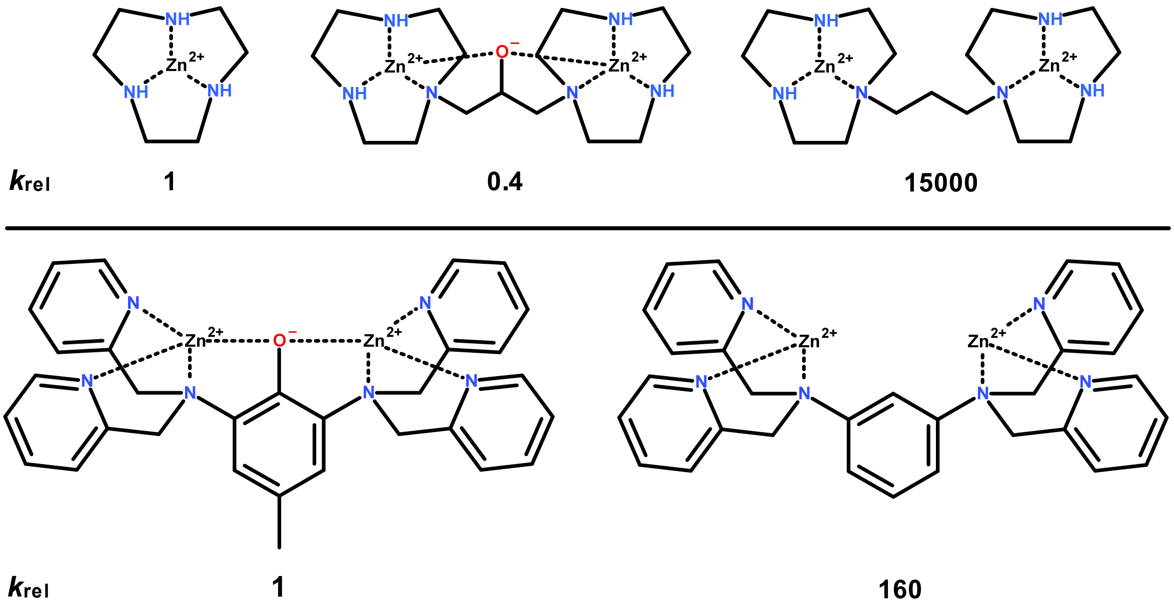

Figure 2.6. The relative rates for the transesterification of HPNPP in MeOH using bridged and non-bridged complexes.

2.1.2 - Internuclear association

The distance between the nuclei in dinuclear complexes is likely to be important for the activity of the complex given the expected bidentate interaction with the substrate. The importance of the internuclear distance has been highlighted in the literature and further encourages the investigation of the impact of flexibility between the Zn(II) centers. The effect of the internuclear distance on reactivity has been reported by Kawahara *et al.*[82] for the transesterification of UpU with complexes having different spacing between di-2-pyridylmethylamino ligands. The dinuclear arrangement can be found in the active sites of many enzymes with either a homonuclear or a heteronuclear pair of metal ions. In the alkaline phosphatase superfamily the internuclear distance varies from one enzyme to another.[37] The effect of internuclear distance has also been indicated by the study of 2,6-diaminomethylpyridine Zn(II)/Cu(II) complexes functionalised on the upper rim of calix[4]arenes, see Figure 2.7.[83,84] The flexibility of the structure due to the low conformational energy barriers which permits close association of the nuclei is proposed to promote enzyme-like dynamic binding. This assumption has been further supported by comparing the flexible structures with structurally rigid equivalents where the lower rim of the calix[4]arenes is covalently bridged. The rates for HPNPP transesterification is 60-fold faster for the flexible structure compared to the rigid linker which points to the importance of having a suitable internuclear distance in complexes.

Multinuclear arrangements have also been reported using allosterically controlled structures to encourage association of the mononuclear subunits and the formation of active complexes.[85–87]

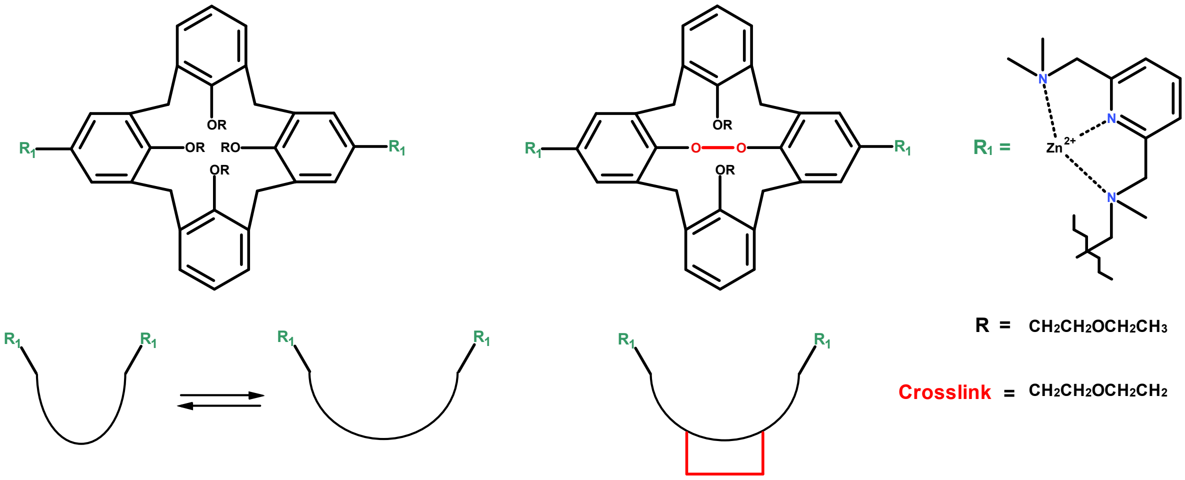

Figure 2.7. The structural difference between the flexible and rigid calix[4]arenes.

2.1.3 - Interactions in the nuclear microenvironment

The binding of phosphates to enzymes is usually attributed to the interactions between the metal ion nuclei and the non-bridging oxygens of the phosphate although there are other interactions that also contribute to strong binding. The substrate selectivity of an enzyme is determined by the hydrogen bonding and lipophilic interaction in the active site pocket. Given these interactions it is sensible to alter the microenvironment of artificial catalysts to achieve similar interactions.[88] Charge stabilisation is very important in the transition state and interactions with charged moieties of the catalyst therefore make more of an impact on the activity compared to lipophilic interaction.

There have been many attempts made to synthesise mimics of enzyme active sites by including the functionalities that are present in the enzyme's coordination sphere around the metal nuclei. The resulting complexes have not been nearly as efficient as the native enzyme which indicates that either additional interactions are present in the active site, or the utilisation of these components are difficult to optimise using small complexes.[64]

The ammonium functionality in the second coordination sphere in enzymes (provided by the amino acid lysine) is usually involved in hydrogen bonding in the active site. Artificial analogues can be found in the form of methylated amines used in conjunction with bipyridyl Zn(II)[89] and Cu(II)[90] complexes. Crystallographic studies show that the Zn nucleus adapts a more tetrahedral-like geometry whereas the Cu adapts a square planar (2,2'-bipyridine) or a square pyramidal (with either of the ammonium ligands) geometry, see Figure 2.8.[91] The expected geometries for Zn(II), i.e. trigonal-bipyramid and octahedral, are disfavored due to steric interactions with the alkyne moieties. The square pyramidal Cu(II) geometry would allow for an in-plane interaction with the metal-bound hydroxide and ammonium functionality.

The proposed mechanism of hydrolysis indicates the role of the hydrogen bonding interaction with the substrate. The addition of the ammonium functionality leads to an increase of more than 3 orders of magnitude in the rate constant for BNPP hydrolysis compared to the rate constant observed for 2,2'-bipyridine Cu(II) complex. The pK_a for the di- and trimethylated ammonium ligands were estimated to be approximately 6.8 which indicates that the difference in reactivity is not due to the acidity of the metal bound hydroxide. The reactivity of the dimethylated ligand decreases by an order of magnitude when the water content is increased to 15% which indicates that the low polarity of the medium plays a role in promoting the interaction between substrate and complex. This is not unexpected given that water can disrupt the hydrogen bond and electrostatic interaction between the phosphate and the $NHMe_2^+$ as seen in Figure 2.8. These electrostatic interactions with methylated amines have been highlighted in the descriptions of phosphate hydrolysis in the literature.[92]

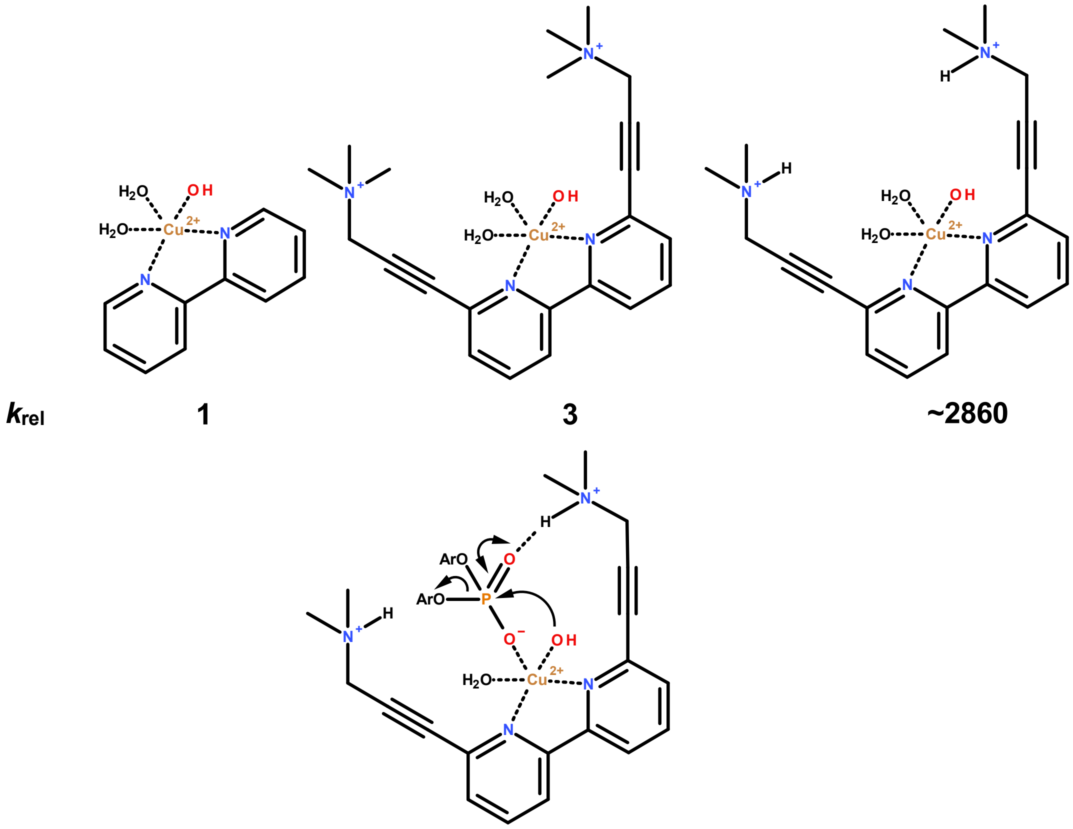

Figure 2.8. The structures of the Cu(II) complexes used by Krämer *et al.* to evaluate the effects of hydrogen bonding interactions on reactivity.[91]

The reactivity of the complexes, both relative and absolute, can seem somewhat capricious in light of the discussed observations in the experiments. The problems encountered range from Cu(II)-Cu(I) reduction, precipitation and some cases of poor reproducibility. Despite this there is no denying that substantial rate increase was achieved for the hydrolysis of BNPP of 4×10^7 fold.

With regard to Zn(II) complexes studied for the transesterification of HPNPP, Brown *et al*. reported the effect of various functionalities in the vicinity of the metal ions in methanol.[93] The greatest effects were observed with amine or amide functionalities.

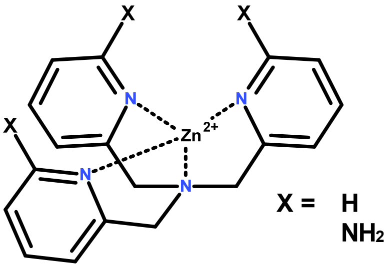

Figure 2.9. The structure of the mononuclear ligand studied by Feng *et al.*[58]

It has also been shown by Feng *et al*. that the introduction of a hydrogen bonding amino functionality in the 2-pyridine position of a mononuclear complex, see Figure 2.9, resulted in a 750-fold rate increase relative to the unsubstituted ligand.[58] The effect of hydrogen bonding of the amino functionality in the 2-pyridine position was also compared to a dinuclear complex, see Figure 2.10, for which the reactivities were virtually identical. This demonstrated that the effect of the amino functionality in the mononuclear complex can have the same effect as an additional metal nucleus.[65]

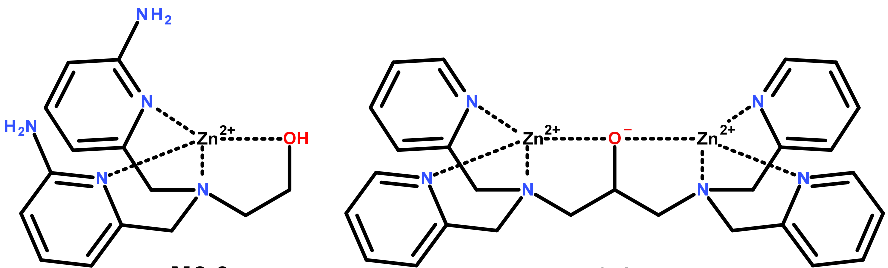

M2-3 **2-1**

Figure 2.10. Complex M2-3 is the mononuclear equivalent of complex 2-3. The mononuclear (M2-3) and dinuclear complex (2-1) are equally reactive although the substrate binding is tighter in the latter.[65]

Cooperativity between metal ions in the dinuclear complex is suggested to be additive with respect to the amino functionality in the 2-pyridine position. These results have been combined in the development of the most reactive dinuclear Zn(II) complex to date, see Figure 2.11, which has been reported to have a second-order rate constant of 53 M^{-1} s^{-1} for the transesterification of HPNPP.[51]

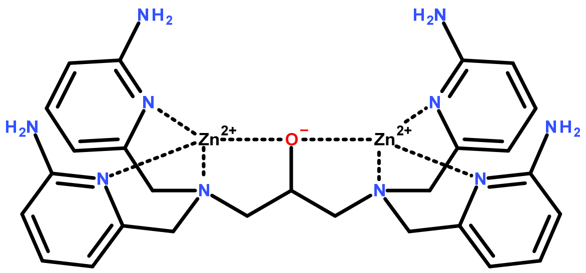

Figure 2.11. The most reactive dinuclear Zn(II) complex to date for the transesterification of HPNPP.

The work presented herein is based on this complex (Figure 2.11) and addresses the effects of changing the functionality in the 2-pyridine position as well as the bridging functionality.

2.2 - Aims

The aim of this study of dinuclear Zn(II) complexes is to evaluate the effect of incorporating two Lewis acidic centers in close proximity to provide double Lewis activation of the RNA-like substrate HPNPP. Additionally, the nuclear microenvironment is studied by altering the functional groups around the metal ions in an attempt to simulate and understand the interactions, for example hydrogen bonding, in the secondary coordination sphere of the active site in enzymes. Finally, the possibility to circumvent the use of a structurally important but electrostatically problematic bridging functionality is evaluated.

2.3 - Synthetic procedure

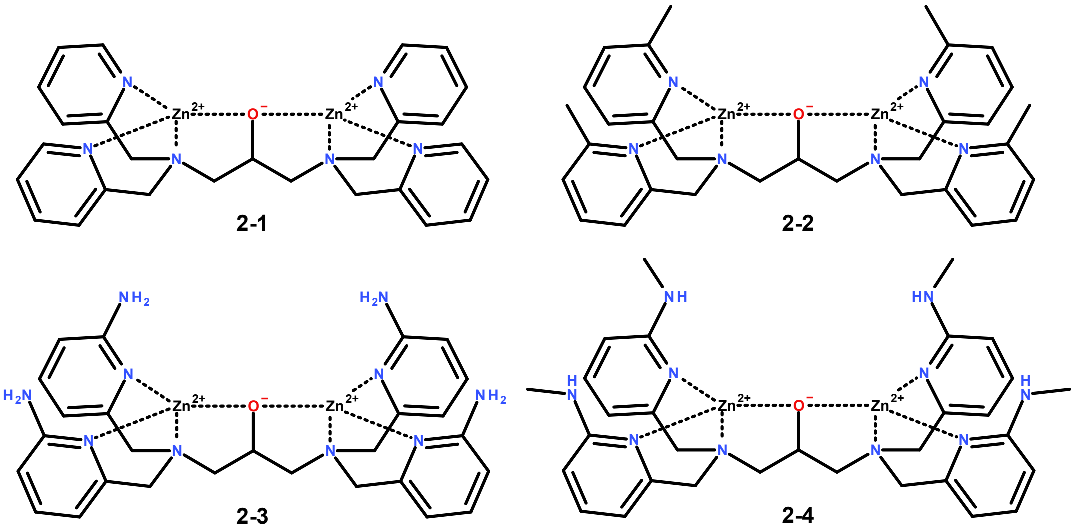

Figure 2.12. The dinuclear alkoxy-bridged complexes used for the binding and hydrolysis of phosphate diesters.

The dinuclear complexes studied in this section are illustrated in Figure 2.12 and have been synthesised with different substituents on the 2-pyridine position which should offer a variation in microenvironment around the Zn(II) nuclei. Complex **2-1** is based on the parent pyridine ligand and serves as a benchmark for the effect of substitution at the 2-position. There will be a steric effect around the metal ions regardless of the functional group being introduced into the 2-pyridyl position and complex **2-2** serves as a gauge for the steric effects and potentially lipophilic interactions. Complex **2-3** provides a hydrogen bond donor in the form of an amino functionality in the 2-pyridyl position that could mimic a primitive version of the hydrogen bond network found in many enzyme active sites. The final complex **2-4** was synthesised using a methylated amine in the 2-position which eliminated the byproduct formation that was encountered in the synthesis of **2-3**, see Scheme 2.9.

2.3.1 - Synthesis of the dinuclear complexes

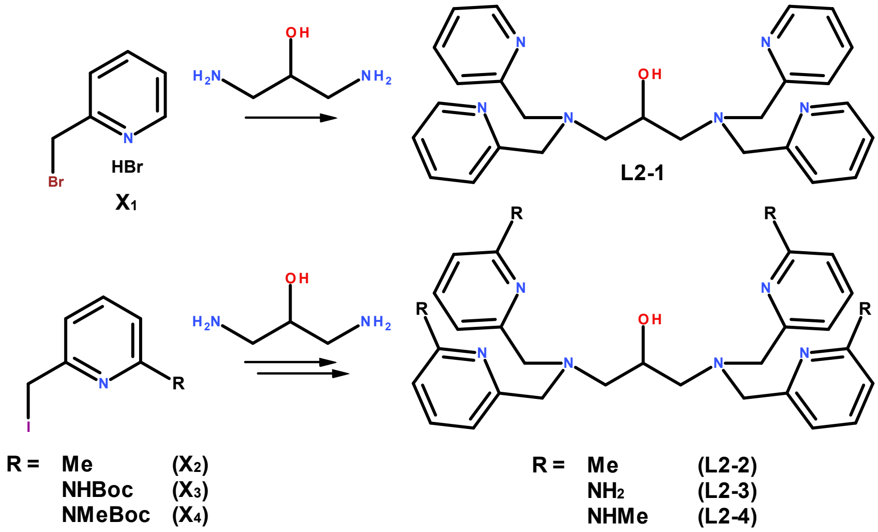

Scheme 2.1. The general procedure for the synthesis of the dinuclear ligands.

The syntheses of the dinuclear ligands are virtually identical once the pyridyl precursors **X_1**, **X_2**, **X_3** and **X_4** have been obtained Scheme 2.1. The metal-free ligands are assigned the same designation as the corresponding complex with the addition of the prefix "**L**", for example **L2-1**. The synthesis of **L2-1** was repeatedly attempted starting from 2-pyridinemethanol. The formation of the mesyl ester followed by substitution with iodine has successfully been used for similar compounds, see precursors **X_2**, **X_3** and **X_4** in Scheme 2.4, Scheme 2.6 and Scheme 2.13, but unfortunately did not yield the desired product in the case of 2-pyridinemethanol. The reaction with methanesulfonyl chloride, see step (i) in Scheme 2.2, produced an intensely red compound that was not identified as the desired product. Although, it is interesting to note that the red compound was also seen when using another starting material, see Scheme 2.3

An alternative synthetic route was devised using the commercially available precursor 2-(bromomethyl)pyridine hydrobromide (**X_1**). The ligand **L2-1** was successfully synthesised in 25 % yield. Interestingly the precursor **X_1** turns a intense red color upon deprotonation

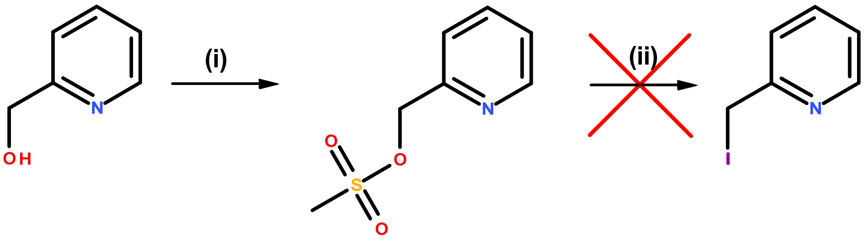

Scheme 2.2. The unsuccessful synthesis of precursor for L2-1. (i) MsCl, Et_3N, THF; (ii) LiI, THF.

(after addition of DIPEA), see Scheme 2.3. It appears as if the compound **X_1** is stabilised in its acidic form but long-lived enough in its deprotonated form, in the presence of a primary amine, to allow for S_N2 displacement of the bromide.

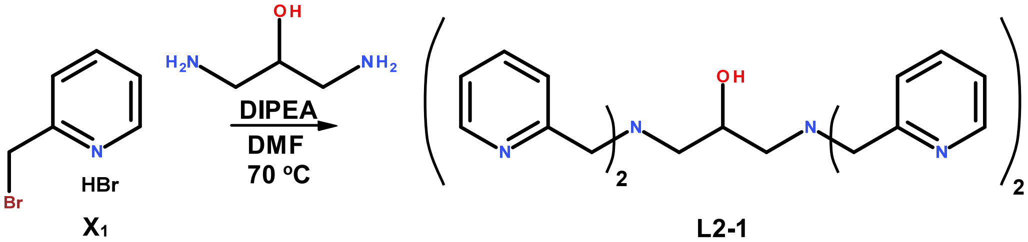

X_1 **L2-1**

Scheme 2.3. The synthetic procedure in which L2-1 was obtained in 25 % yield.

Similarly the synthetic procedure for **L2-2** was performed using the precursor 2-(iodomethyl)-6-methyl-pyridine (**X_2**) synthesised from (6-methylpyridin-2-yl)methanol, see Scheme 2.4. It is unclear why this reaction appears to work whereas the analogous reaction in Scheme 2.2 does not.

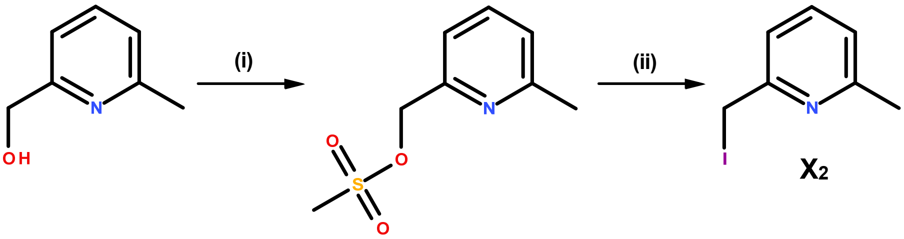

X_2

Scheme 2.4. The synthesis of the precursor X_2. (i) MsCl, Et_3N, THF, 99 %; (ii) LiI, THF, 97 %.

There are commercial equivalents of **X_2** available, although not at a convenient scale. The synthesis in Scheme 2.4 utilised the relatively inexpensive (6-methylpyridin-2-yl)methanol and proceeded with approximately 96 % overall yield. The synthesis of **L2-2**, see Scheme 2.5, was performed using the standard procedure employed for S_N2 reactions in this work which consists of the reactants and DIPEA dissolved in dry DMF and heated to 70 °C for 12 hours to afford **L2-2** in 23 % yield.

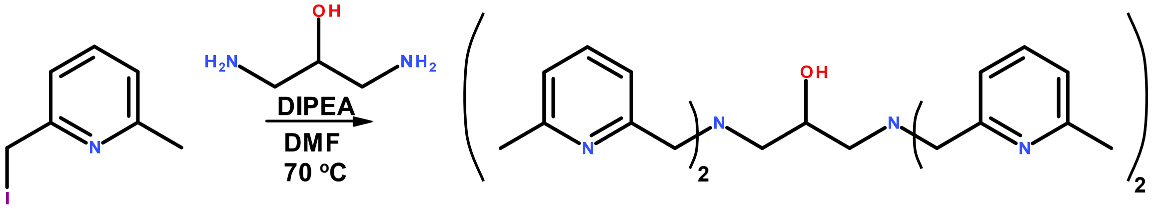

X2 **L2-2**

Scheme 2.5. The synthesis of L2-2. The reaction was performed at 70 °C for 12 h.

The synthesis of the precursor *tert*-butyl N-[6-(iodomethyl)-2-pyridyl]carbamate (**X$_3$**) for the ligand **L2-3** was more laborious, see Scheme 2.6. The compound **X$_3$** required larger scale synthesis in order to produce feasible amounts since the overall yield was around 10 - 20 %.

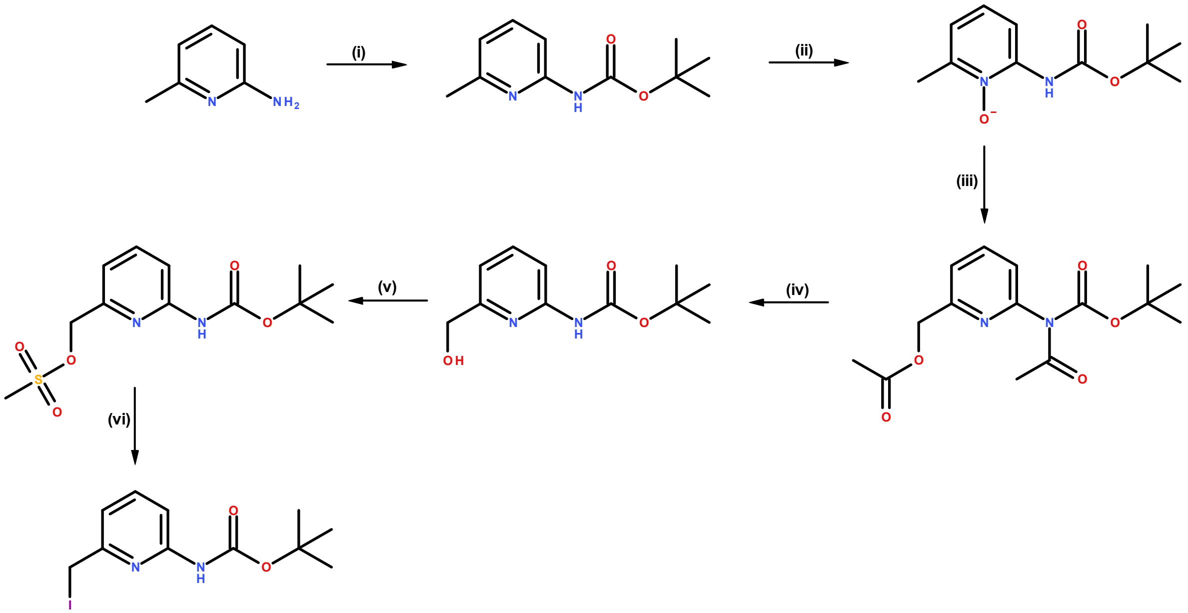

X$_3$

Scheme 2.6. The synthetic route for the precursor X$_3$. **(i) Boc$_2$O, Et$_3$N, DMAP, DCM, 80 %; (ii) mCPBA, DCM, 97 %; (iii) Ac$_2$O, 70 °C, 22%; (iv) NaOH, MeOH, 86 %; (v) MsCl, Et$_3$N, THF, 94 %; (vi) LiI, THF, 95 %.**

The synthetic procedure for coupling the precursor **X$_3$** to the 1,3-diamino-2-propanol was analogous to the previous methods used for **L2-1** and **L2-2**. The final TFA treatment deprotects the amino functionality at the 2-pyridine position, see Scheme 2.7.

The synthesis of **L2-3** required relatively large amounts (10 - 50 g) of the starting material 2-amino-6-methylpyridine in order to yield sufficient amounts of the desired product. The single largest loss of material was observed at step (iii), see Scheme 2.6, where the yield rarely exceeded 20 - 30 % and it was observed that large amounts of byproduct were formed which precipitated during the work up procedure.

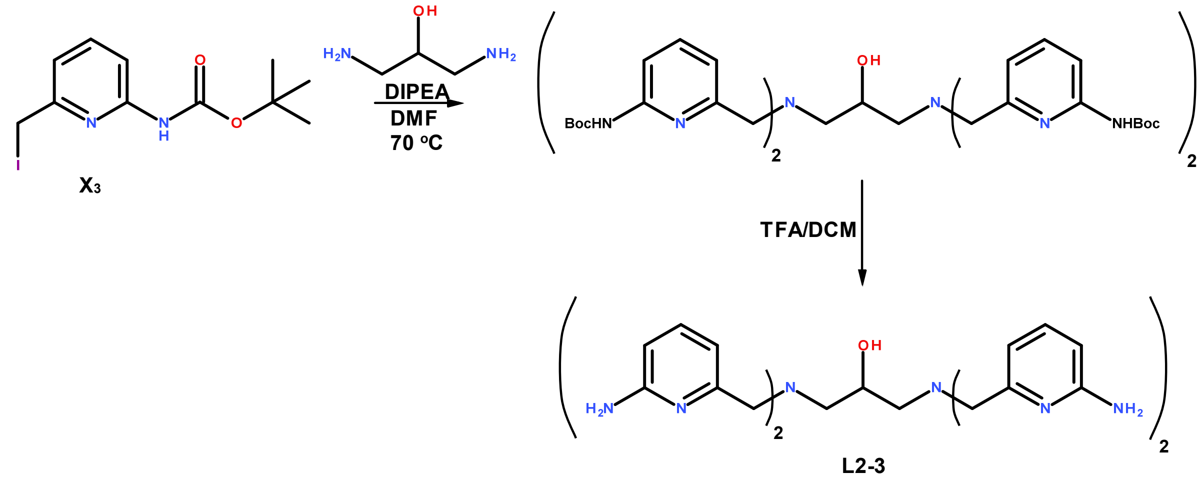

Scheme 2.7. The procedure used for the synthesis of L2-3. The yields were 31 % and 100 %, respectively.

The synthetic route to **X₃**, see Scheme 2.6, involved the introduction of an acetate functionality on the 6-methylpyridine position but acetylation was also observed at the 2-aminopyridine position. This hints at the mechanism of the reaction that forms the byproduct in such substantial amounts (40 - 50%). The byproduct that was formed in step (iii) was characterised, see Scheme 2.8, and indicated a mechanism that involved the partitioning of an intermediate that was essential to the formation of the desired product.

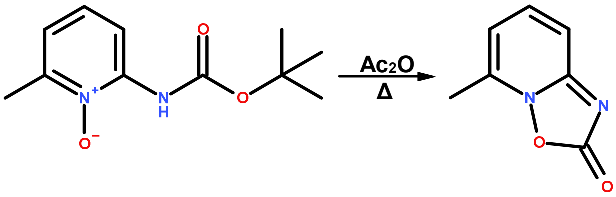

Scheme 2.8. The formation of byproduct from the N-oxide and acetic anhydride.

The byproduct was isolated with relative ease since it was the only component that did not dissolve in EtOAc. The quantity of byproduct (40 - 50%) relative to the product posed a problem that needed to be addressed. First the starting material was refluxed in chloroform to rule out heat induced degradation. The proposed mechanism for the formation of the byproduct, see Scheme 2.9, is very similar to the mechanism for the formation of the desired product. The acetylation reaction yielded both a mono-, see Scheme 2.10, and diacetylated product, see Scheme 2.11, although the latter was obtained in larger amounts.

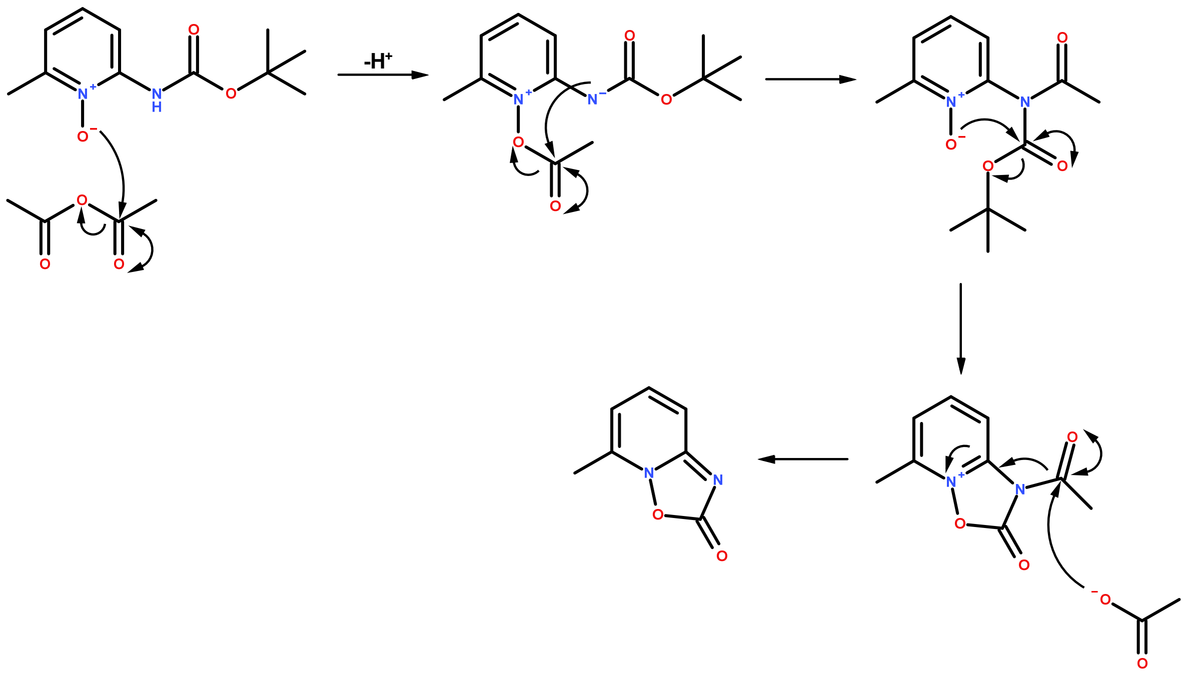

Scheme 2.9. The proposed mechanism for the formation of the byproduct in the acetylation reaction.

The acetylation reaction will proceed as long as the N-oxide functionality is present and the intermediate (**I1**, Scheme 2.11) in the diacetylated product reaction is identical to the precursor for the undesired byproduct, see Scheme 2.9.

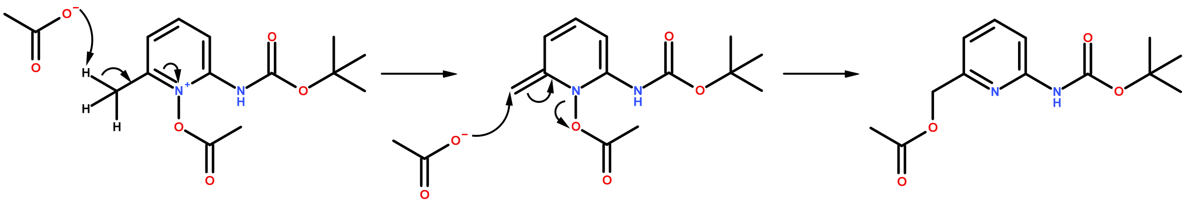

Scheme 2.10. The mechanism for the formation of the monoacetylated product.

Alternative synthetic routes that were designed using different activating agents to eliminate the formation of byproduct, see Scheme 2.12.

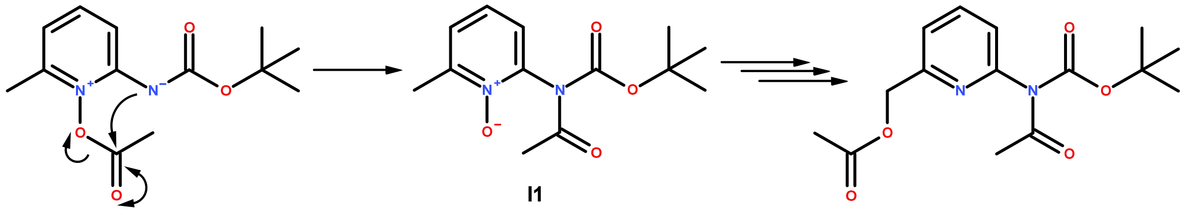

Scheme 2.11. The proposed mechanism for the formation of the diacetylated product (main product of the reaction). The reaction proceeds with the acetylation of the carbamate followed by acetylation of the 6-pyridine position through the mechanism proposed in Scheme 2.10.

These reactions were unsuccessful and instead a different protecting group strategy (phthalimide) was considered, see Figure 2.13, but the acetylation of the N-oxide was difficult and the compound displayed low solubility and reactivity in acetic anhydride.

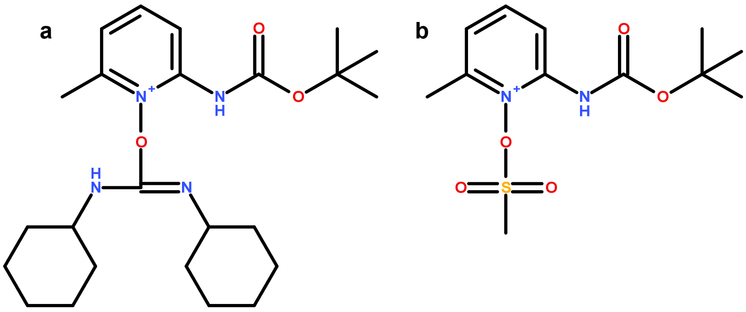

Scheme 2.12. The proposed compounds that could minimise the formation of byproduct. The compounds were synthesis using *tert*-butyl N-(6-methyl-1-oxido-pyridin-1-ium-2-yl)carbamate under the following conditions (a) DCC, DMF; (b) MsCl, DMF. The acetylation was attempted through the subsequent addition of AcOH/Et_3N to the same reaction vessel as the respective activations.

After multiple attempts to circumvent the formation of the undesired byproduct it was found that methylation of the 2-aminopyridine position completely inhibited the formation of the byproduct (corroborating the involvement of the carbamate as a nucleophile in the proposed mechanism). This led to the synthesis of the precursor *tert*-butyl N-[6-(iodomethyl)-2-pyridyl]-N-methyl-carbamate (**X_4**), see Scheme 2.13.

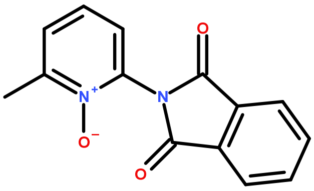

Figure 2.13. The phthalimide protected compound used for the acetylation reaction.

The overall yield for **X_4** was estimated to be at least twice that for **X_3**, despite the additional synthetic step, simply due to the introduction of a methyl group in the 2-aminopyridine position. The synthesis of **L2-4** starting from **X_4** was identical to that of **L2-3** apart from the differing starting material, see Scheme 2.14.

Complex **2-3** was synthesised first, since it had been reported as the most reactive covalently bound dinuclear complex to date[51,71,84]for the transesterification of HPNPP. This was followed by the synthesis of **2-1** and **2-2** which served as controls. Complex **2-4** was the result of altering the synthetic strategy for **L2-3** and was initially not an intend as a target

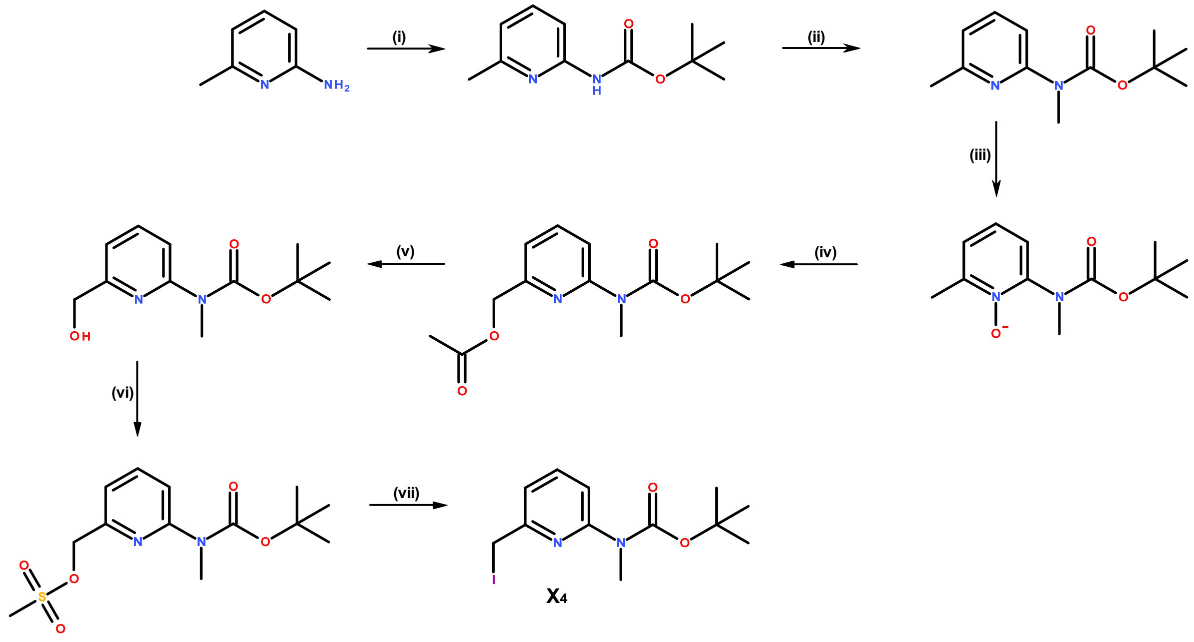

Scheme 2.13. The synthetic route used to obtain the precursor precursor X_4. (i) Boc_2O, Et_3N, DMAP, DCM, 80 %; (ii) NaH, MeI, DMF, 100 %; (iii) mCPBA, DCM, 100 %; (iv) Ac_2O, 70 °C, 93 %; (v) NaOH, MeOH, 80 %; (vi) MsCl, Et_3N, THF, 91 %; (vii) LiI, THF, 90 %.

compound but does provide some insight into the potential effects of methylation on reactivity. Despite the different synthetic problems related to each of the dinuclear ligands (**L2-1**, **L2-2**, **L2-3** and **L2-4**) the difference in the final yields was not compelling.

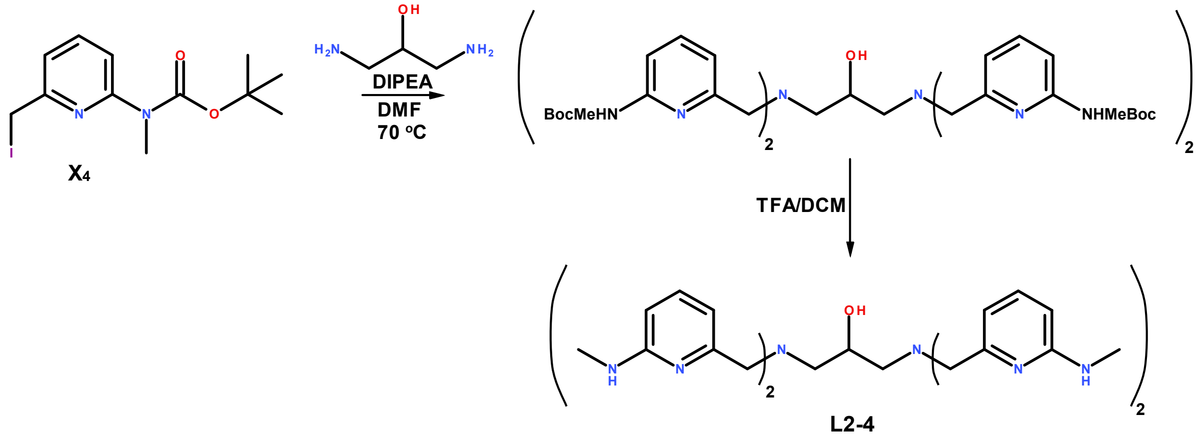

Scheme 2.14. The synthesis of L2-4 from precursor X_4. The yields were 41 % and 50 %, respectively.

2.3.2 - Synthesis of HPNPP

The synthesis of 2-hydroxypropyl-(4-nitrophenyl) phosphate (HPNPP) was initially attempted using a modified literature procedure[29] using the *tert*-butyldimethylsilyl (tBDMS) instead of the *tert*-butyldiphenylsilyl (tBDPS) protecting group. The protected alcohol was synthesised, see Scheme 2.15, although very little product was obtained after the final purification step using fractional distillation. The compound could not be purified using flash chromatography due to the overlap of polarity of the components in the reaction mixture.

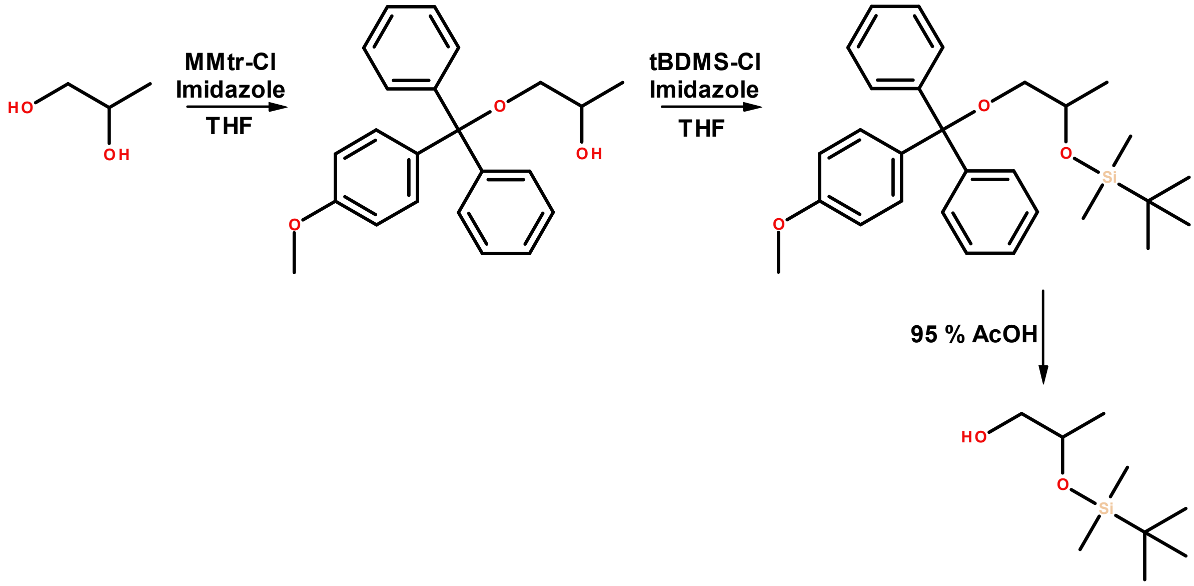

Scheme 2.15. The synthesis of the protected alcohol used in the synthesis of HPNPP. The yields were 72 %, 100% and 18%, respectively.

A different procedure had been proposed in the same literature reference that reduced the number of synthetic steps and improved the overall yield, see Scheme 2.16. The reaction produced near quantitative yields in each step. The subsequent reaction steps were

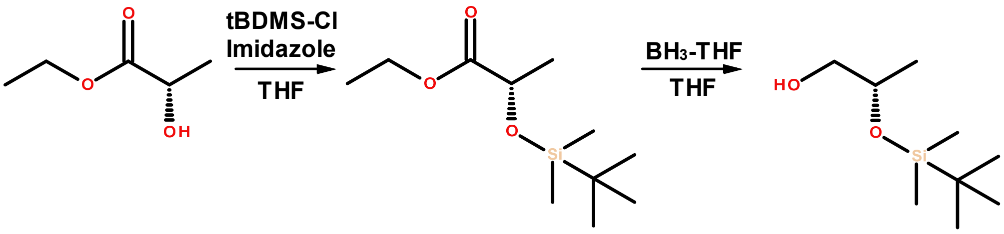

Scheme 2.16. The alternative synthesis of the nucleophilic appendage. The yields were 99 % and 90 %, respectively.

straightforward, see Scheme 2.17, and sufficient amounts of HPNPP were obtained although the yields were not optimal.Interestingly, this reaction revealed some inherent stability issues with the tBDMS protecting group that did not cause any synthetic problems here but is nevertheless important to bear in mind, see Chapter 8.6.

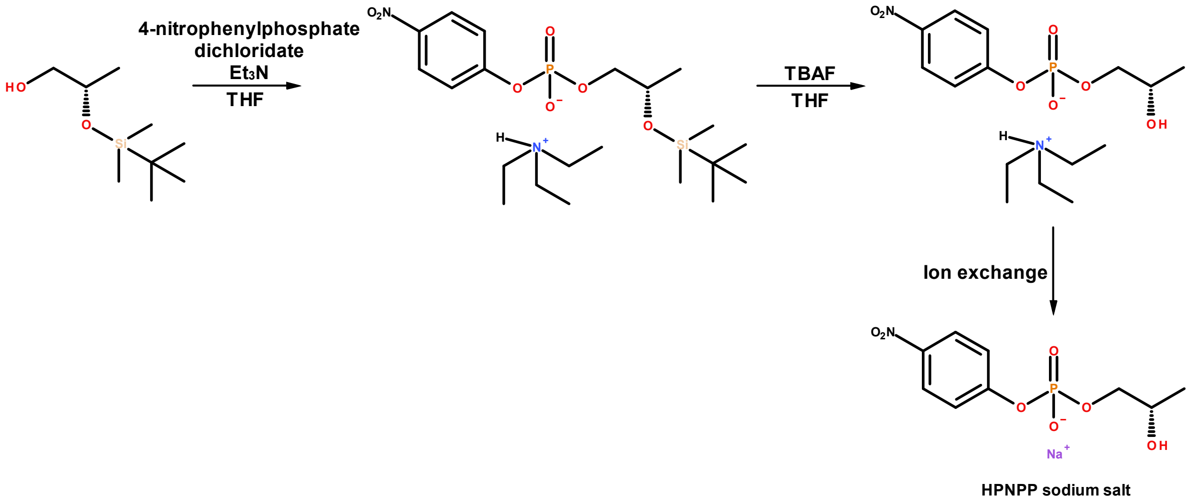

Scheme 2.17. The synthesis of HPNPP. The yield was 4 % over 3 steps.

2.4 - Results and discussion

2.4.1 - Kinetic results

The initial kinetic examination of the complexes was performed at varying complex concentrations depending on the observed reactivity for the transesterification of HPNPP. Complexes **2-1** and **2-2** were both used at 2 mM concentration but the highly reactive **2-3** and **2-4** only required a concentration of 0.2 mM to completely transesterify the substrate in less than 20 min. The pH-rate profile in Figure 2.14 shows the dependence of the observed rate constants on pH for the complexes, see Chapter 8.3, and a single ionisation model, **Equation 2.1**, was fitted to the data.

$$k_{obs} = k_{obs}^{max} \times \frac{K_a}{K_a + [H^+]} \qquad \text{(Equation 2.1)}$$

The initial results from the kinetic experiments clearly demonstrate a higher reactivity for **2-3** but also brought to light the instability of the complex in solution. It quickly became clear that **2-3** was more sensitive to the conditions in solution such as pH and apparently even gaseous exchange, as will be discussed later in this chapter.

The reactivity of **2-4** was even higher than **2-3** but the solution stability of **2-4** also appeared to span an even smaller pH-range than **2-3**. The complexes **2-1** and **2-2** proved to be less reactive but more stable over a wider pH range compared to **2-3** and **2-4.** The lack of data points for **2-3** and **2-4** at higher pH as can be seen in Figure 2.14 is due to precipitation.

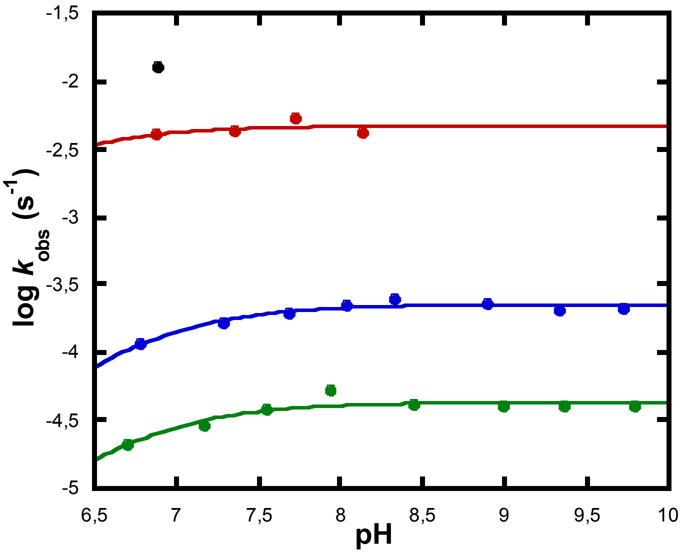

Figure 2.14. The observed rate constant versus pH for 2 mM 2-1 (blue), 2 mM 2-2 (green), 0.2 mM 2-3 (red) and 0.2 mM 2-4 (black) with 50 µM HPNPP and 50 mM HEPES or CHES with 0.1 M ionic strength ($NaNO_3$).

The concentration dependence of the reactivity of complexes **2-1** and **2-2** was studied using a 96 well plate reader and were carried out in triplicate at each pH. The rate constants were determined by the initial rate method, see Chapter 8.2, which only follows the initial 10 % of the reaction progress and assumes a linear relationship for the appearance of product over time. The initial rate provides the second-order rate constant which is plotted versus pH, see Figure 2.15.

A single ionisation model, **Equation 2.2** which in essence is identical to **Equation 2.1**, was fitted to the data points. These equations only account for one deprotonation of the complex and the corresponding observed activity is obtained by multiplying the maximum rate with the percentage of available active complex. The equations take into account the percentage of complex that is available in the active form at any given pH, based on the pK_a

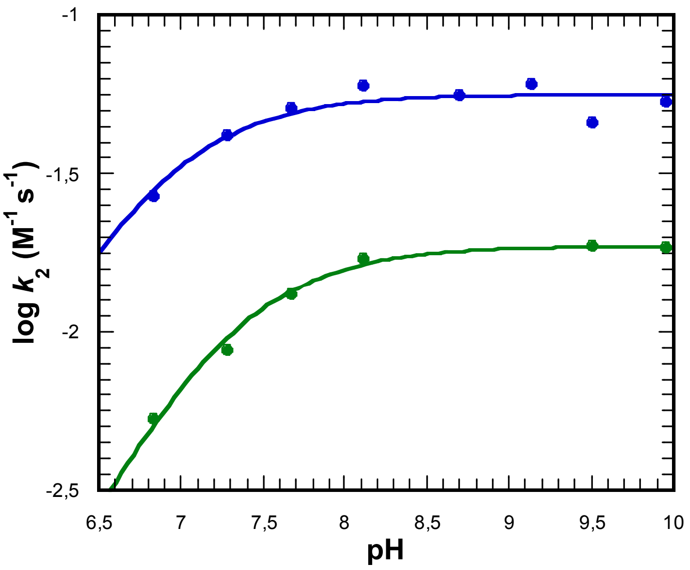

Figure 2.15. The second-order rate constants for 2-1 (blue) and 2-2 (green) versus pH. The data collected around pH 8 were intermittently unreliable due to occasional precipitation which is why some data points were omitted. The experiments performed in 50 mM HEPES or CHES at 0.1 M ionic strength ($NaNO_3$).

$$k_2 = k_2^{max} \times \frac{K_a}{K_a + [H^+]} \qquad \text{(Equation 2.2)}$$

of the complex. The second-order rate constants, k_2^{max}, and pK_a were determined by the least square fits to be 5.6 (± 0.25) × 10^{-2} M^{-1} s^{-1} (pK_a 6.83 ± 0.09) and 1.9 (± 0.06) × 10^{-2} M^{-1} s^{-1} (pK_a 7.26 ± 0.04) and for **2-1** and **2-2**, respectively. The data for **2-1** is in good agreement with the existing literature 7.3 × 10^{-2} M^{-1} s^{-1} (pK_a 6.4).[51,65]

It should also be noted that the estimated limiting second-order rate constant for **2-1** is 3 orders of magnitude lower than that for **2-3**.[51] The increased rate for **2-3** can therefore be attributed to the amino functionality in the 2-pyridine position.

The experimental rate constants indicate that complex **2-1** is 3-fold more reactive than complex **2-2** and that the methyl group in the 2-pyridine position has a detrimental effect on the apparent reactivity. Care needs to be taken when interpreting the second-order rate constants of the complexes since the observed increase in activity could be due to either tighter binding of the substrate or higher rates of reaction of the bound substrate. This will be addressed in the binding studies in the subsequent section, see Chapter 2.4.2.

In the case of **2-3** and **2-4** the experimental setup used in the previous experiments proved problematic. The first indication of the ambiguous behavior of the complexes was the apparent influence of $NaNO_3$ on the solubility of the complexes. The ionic strength of the solution was kept at 0.1 M using $NaNO_3$ and this seemed to cause precipitation of the complex. This setback only manifested itself when the concentration of the complex was increased, since previous experiments at 0.2 mM were not affected by this problem, see Figure 2.14.

Experiment	HEPES pH 6.9	$NaNO_3$ 80 mM	NaCl 80 mM	$NaClO_4$ 80 mM	NaOTf 80 mM	Result
1	*					Clear
2	*	*				Precipitate
3	*		*			Clear
4	*			*		Precipitate
5	*				*	Precipitate

Table 2.1. The solubility of 1 mM 2-3 at pH 6.9 in the presence of sodium nitrate, sodium chloride, sodium perchlorate and sodium triflate.

A series of experiments, see Table 2.1, with various salts revealed that the only salt that did not cause precipitation was NaCl. This could possibly be explained by the oxygen atoms of the anionic counter ions of the salt binding to the Zn(II) nuclei in a bridging fashion. The fact that this was not observed in the case of complexes **2-1** and **2-2** indicates the possible influence of the 2-pyridine substituent on binding. The influence of the 2-pyridine substituent on binding will be presented in the following section: quantitatively by inhibition studies and qualitatively by indicator displacement assays.

2.4.2 - Binding and reactivity

The reactivity of the complexes towards phosphates in general and RNA analogues in particular can be dissected into two main components. These components are related to the binding of the substrate and the rate of conversion (turnover) into product. The overall reactivity represents the combined effect of both these factors. Two different catalysts may appear to be equivalent in overall reactivity but it might very well be so that one is more efficient at turning over the substrate and the other provides more efficient binding.

A relevant example in literature is the kinetic comparison between the mononuclear and dinuclear Zn(II) complexes, see Figure 2.10. The two complexes cover a range of parameters that can be investigated with carefully designed experiments. The complex **M2-3** is the mononuclear equivalent of the dinuclear complex **2-3**. Complex **2-1** illustrates the effect of having double Lewis activation and the mononuclear complex **M2-3** can only offer single Lewis activation. The additional parameter that can affect the reactivity of **M2-3** is the possible hydrogen bond donors in the vicinity of the metal ions. Interestingly the observed maximum second-order rate constants for these two complexes are virtually identical but the tightness of binding is stronger for complex **2-1**. The tighter binding of the dinuclear complex (166-fold) compared to **M2-3** is expected. The tight binding of the substrate simply translates into a greater portion of the substrate being bound to the complex and ready to react. This make product inhibition a problem that needs to be taken into account since both substrate and product are phosphate diesters. The reaction rates indicate that the hydrogen bond interaction in **M2-3** provides a rate acceleration equivalent to having an additional Zn(II) nucleus. The high reactivity of **M2-3** coupled with low substrate binding are highly desirable properties since they indicate that the complex provides very useful rate acceleration despite having less substrate bound.

In light of the similar rates yet tighter substrate binding for **2-1** it can be concluded that the saturating rate for **M2-3** will be higher. If interactions separate to the intrinsic binding properties of the catalytic centre (e.g. additional recognition factors) are introduced, **M2-3** has the potential to generate a higher turnover rate.

When studying possible ways to improve the reactivity of catalytic complexes in a particular reaction it is important to understand the contribution of each factor in order to tailor the interactions. When a catalyst binds a substrate the rate of the reaction increases due to the higher concentration of the catalyst-substrate species referred to as a Michaelis-Menten complex. The Michaelis-Menten equation, **Equation 2.3**, can be used to fit experimental data that measure the reactivity of catalysts versus the concentration of substrate.

$$\mathrm{C} + \mathrm{S} \underset{k_{-1}}{\overset{k_1}{\rightleftharpoons}} [\mathrm{CS}] \xrightarrow{k_{\mathrm{cat}}} \mathrm{C} + \mathrm{P}$$

Scheme 2.18. The schematic representation of the catalytic reaction progression from substrate to product. The catalyst (C) and substrate (S) forms the reversible Michaelis-Menten complex [CS] with the rate constant k_1. The complex breaks down into either the reactants with the rate k_{-1} or the product (P) and catalyst with the rate k_{cat}.

The parameters that can be obtained from the equation are k_{cat} (s^{-1}) and K_M (M) that represent the catalytic turnover and tightness of binding to the substrate, respectively, see Scheme 2.18. In **Equation 2.3** the rate of product [P] formation is related to the total concentration of catalyst $[C]_0$ and substrate concentration [S] through k_{cat} and K_M.

$$\frac{\partial[P]}{\partial t} = \frac{k_{cat}[C]_0[S]}{K_M + [S]} \qquad \text{(Equation 2.3)}$$

For the experiments presented here the substrate has been used at sub-saturating concentrations meaning that **Equation 2.3** can be reduced to **Equation 2.4** since $K_M >> [S]$.

$$\frac{\partial[P]}{\partial t} = \frac{k_{cat}[C]_0[S]}{K_M} = k_2[C]_0[S] \qquad \text{(Equation 2.4)}$$

The **Equation 2.4** is a second-order rate equation and the k_2 is the second-order rate constant (M^{-1} s^{-1}) corresponding to K_M / k_{cat}.

$$K_M = \frac{k_{-1} + k_{\mathrm{cat}}}{k_1} \qquad \text{(Equation 2.5)}$$

The K_M is referred to as the Michaelis constant and is defined as the two-directional decay of the catalyst-substrate complex as illustrated in Scheme 2.18, see **Equation 2.5**. In the case of most artificial catalysts $k_{-1} >> k_{\mathrm{cat}}$ since their reactivity and binding of substrate are relatively limited which lead to **Equation 2.6** where $K_M \approx K_d$.

$$K_M \approx \frac{k_{-1}}{k_1} = \frac{[C][S]}{[CS]} = K_d \qquad \text{(Equation 2.6)}$$

Many highly efficient enzymes have high rates of turnover but relatively moderate substrate binding to allow for easy product release and limit the effect of product inhibition. Examples of this can be found in nature (e.g. carbonic anhydrase, chymotrypsin) where the K_M is in the range of 10^{-3} M whereas the k_{cat} ranges from 10^{-1} to 10^{5} s^{-1} which equates to high second-order rate constants k_2. These values are in good agreement with the expected values for the “average” enzyme.[57]

For artificial catalyst the more challenging parameter to improve is k_{cat} since the processes involved in rate acceleration are not as well understood as the interactions that improve binding.

The overall rate for the transesterification of HPNPP was measure in the presence of the competitive inhibitor dimethyl phosphate (DMP).[51] DMP was used since it can be expected to bind to the complex in the same fashion as any other phosphate diesters but without being hydrolysed. Since the compound lacks both an internal nucleophile and an acidic leaving group the rate of spontaneous hydrolysis will be negligible (half-time 1.3 × 10^5 years)[56] and the compound does not interfere with UV measurements.

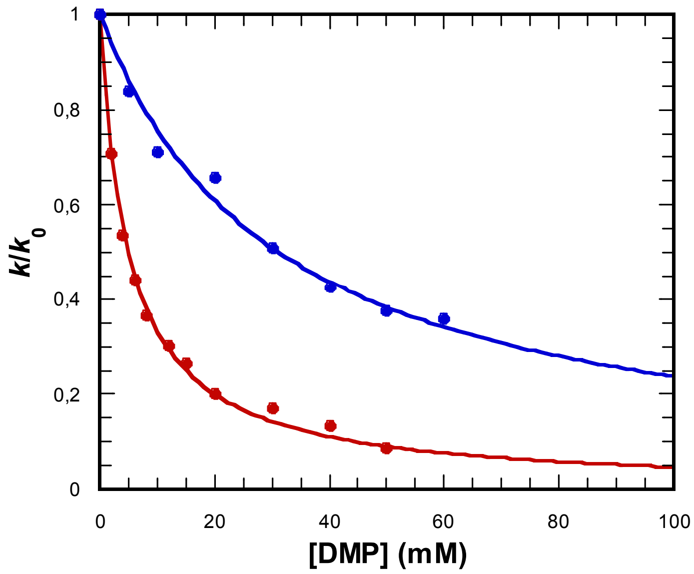

Figure 2.16. The inhibition experiment illustrated by normalised rate k/k_0 versus the concentration of DMP in mM at pH 6.9. The complex 2-1 (red) and 2-2 (blue), both used at 1 mM with 0.5 mM HPNPP at pH 6.9 in 50 mM HEPES and 0.1 M ionic strength ($NaNO_3$).

The kinetic analysis was performed using **2-1** and **2-2** at several DMP concentrations and monitoring the reduction in reactivity. The conclusions that can be drawn from these experiments rely on the premise that DMP binds to the complex in a similar fashion to the hydrolysable substrate. The graph in Figure 2.16 shows the normalised rate k/k_0 where k_0 represents the rate constant with no inhibitor present.

Equation 2.7 was used to fit the inhibition data for competitive inhibition[51] and yielded K_i 5.0 (± 0.13) × 10^{-3} M and 3.1 (± 0.15) × 10^{-2} M for **2-1** and **2-2**, respectively.

$$\frac{k}{k_0} = \frac{K_i}{K_i + [DMP]} \qquad \text{(Equation 2.7)}$$

The difference in K_i can be seen in light of the previous data, see Figure 2.15, where the difference in rate constants was first observed. The difference in tightness of binding is roughly a factor of 6 which can be compared to the 3-fold difference in the limiting second-order rate constant in favor of **2-1**. This translates into more substrate being bound to **2-1** compared to **2-2**.

The decaying rate signifies the tightness of binding for the complex with respect to phosphate diesters and can be related to the observed overall activity to dissect it into its components. The DMP is similar to the substrate HPNPP in the sense that both are phosphate diesters and the binding of DMP simulates the binding of the substrate in the ground state. Other inhibitors (phenyl phosphate) that are dianionic have been used to estimate the transition state binding.[58] The Michaelis-Menten parameter K_M is the substrate concentration at which the catalyst reaches half its maximum rate. The decaying curves for the DMP inhibition can be viewed as inverted Michaelis-Menten curves which means that the concentration at which the reactivity is halved, K_i, is equal to K_M. The inhibition was also studied at pH 7.4, see Figure 2.17, which indicated a difference in observed inhibition, K_i.

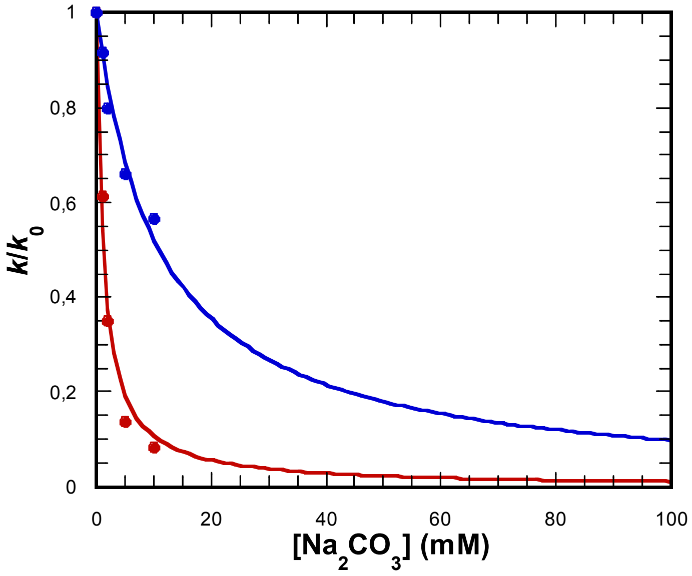

Figure 2.17. The inhibition experiment illustrated by normalised rate k/k_0 versus the concentration of DMP in mM at pH 7.4. The complex 2-1 (red) and 2-2 (blue), both used at 1 mM with 0.5 mM HPNPP at pH 7.4 in 50 mM HEPES and 0.1 M ionic strength ($NaNO_3$).

At higher pH it is evident that the binding is reduced for both complexes since K_i equals 1.0 (± 0.01) × 10^{-2} M and 6.2 (± 0.43) × 10^{-2} M for **2-1** and **2-2**, respectively, although the ratio of K_i between the complexes remains 6-fold.

As previously mentioned, the use of $NaNO_3$ to adjust the ionic strength of the reaction solutions proved to be problematic for **2-3** and **2-4**. In order to obtain a valid comparison between all the complexes the inhibition studies for **2-1** and **2-2** were repeated using NaCl, see Figure 2.18.

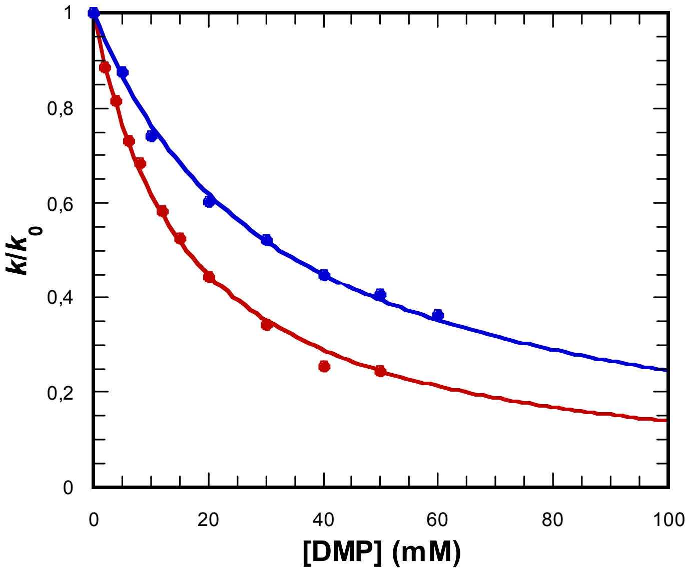

Figure 2.18. The DMP inhibition using 1 mM 2-1 (red) and 2-2 (blue) with 0.5 mM HPNPP in 50 mM HEPES at pH 6.9 and 0.1 M ionic strength (NaCl).

Complex **2-2** displays similar binding (K_i = 3.2 (± 0.07) × 10^{-2} M) to previous measurements in $NaNO_3$ containing solutions but binding for complex **2-1** differs by a factor of 3 (K_i = 1.6 (± 0.33) × 10^{-2} M). Although a difference might be expected, it is unusual that the binding remains virtually unaffected for one complex but changes for the other.

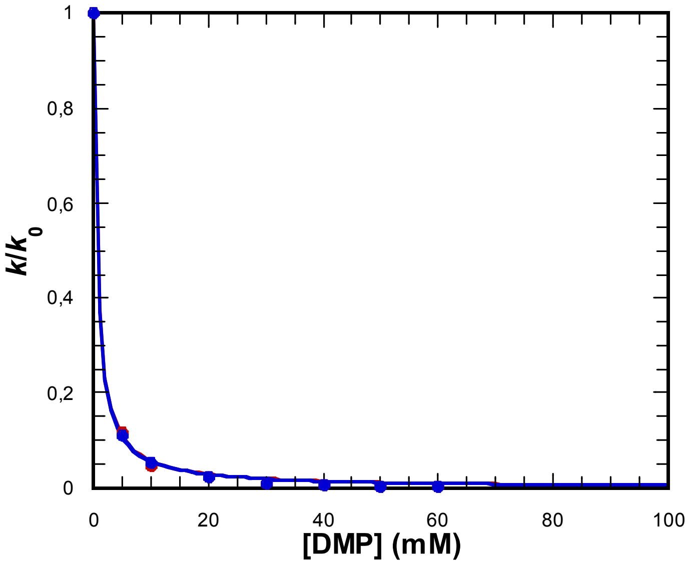

Figure 2.19. The inhibition experiment illustrated by normalised rate *k/k*₀ versus the concentration of DMP using 0.2 mM 2-3 (red) and 2-4 (blue) with 50 µM HPNPP in 50 mM HEPES at pH 6.9 and 0.1 M ionic strength (NaCl).

The binding properties of **2-3** and **2-4** were kinetically analysed with DMP, see Figure 2.19, in the same fashion as **2-1** and **2-2** except that the concentration of the complexes was reduced to 0.2 mM. The binding of DMP (K_i) at pH 6.9 is virtually identical for the two at 6.0 (± 0.44) × 10^{-4} M (**2-3**) and 5.9 (± 0.33) × 10^{-4} M (**2-4)** which is around 25-fold less than **2-1** and 50-fold less than **2-2**.

Based on the data obtained for **2-3** at 0.2 mM, see Figure 2.14, the limiting second-order rate constant can be estimated using k_{obs} at pH 7.4 divided by the concentration of complex **2-3** (0.2 mM) to ≈ 23 M^{-1} s^{-1}. With a K_M of 6.0 (± 0.44) × 10^{-4} M, k_{cat} can be estimated to be 0.014 s^{-1}. These kinetic parameters for **2-3** are in reasonable agreement with literature values[51] although the reported limiting second-order rate constant and K_i are 53 M^{-1} s^{-1} and 3.7 × 10^{-4} M, respectively, at pH 7.4.

An experiment with **2-3**, see Figure 2.20, had been performed at the highest pH at which the complex was stable in solution. This data serves as a crude indicator that the tightness of binding seems to decrease for **2-3** (K_i = 1.9 (± 0.08) × 10^{-3} M at pH 8.1) with increasing pH, as seen for **2-1** and **2-2**, although some reservations are required as the influence of the $NaNO_3$ is not fully understood.

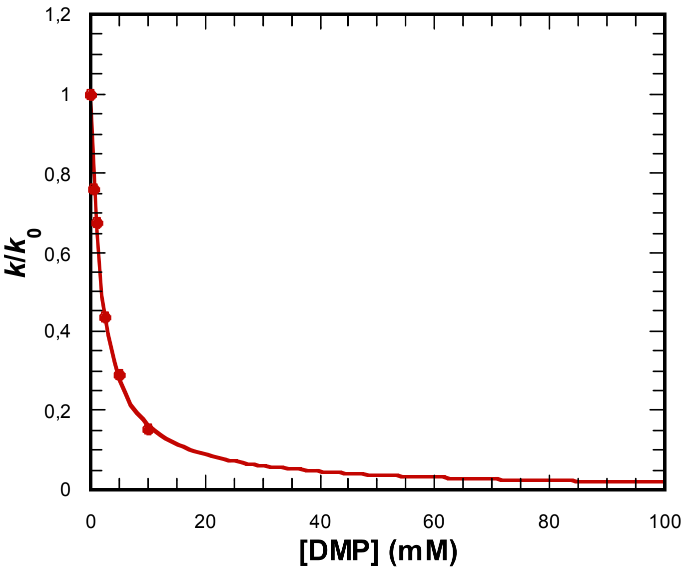

Figure 2.20. The inhibition experiment illustrated by normalised rate k/k_0 versus the concentration of DMP using 0.2 mM 2-3 in 50 mM HEPES at pH 8.1 and 50 µM HPNPP and 0.1 M ionic strength ($NaNO_3$). In this case $NaNO_3$ had been used before the salt induced precipitation was discovered.

A summary of the K_i-values is listed in Table 2.2 showing the results at various pH using either $NaNO_3$ or NaCl.

	pH 6.9	pH 6.9	pH 7.4	pH 8.1
Complex	K_i (mM) $NaNO_3$	K_i (mM) NaCl	K_i (mM) $NaNO_3$	K_i (mM) $NaNO_3$
2-1	4.98 (± 0.13)	16.23 (± 3.30)	9.76 (± 0.10)	-
2-2	31.09 (± 1.50)	32.54(± 0.70)	62.54 (± 4.30)	-
2-3	-	0.60 (± 0.044)	-	1.94 (± 0.08)
2-4	-	0.59 (± 0.033)	-	-

Table 2.2. K_i for the dinuclear complexes at various pH. The experiments were all performed in 50 mM HEPES using either $NaNO_3$ (red) or NaCl (green) to adjust the ionic strength to 0.1 M. Additionally, 0.5 mM HPNPP with 1 mM complex was used for 2-1 and 2-2 and 0.2 mM complex with 50 µM HPNPP for 2-3 and 2-4.

The apparent second-order rates for the complexes at pH 6.9, measured at zero concentration DMP in the inhibition experiments, are listed in Table 2.3 and the difference in binding can be used to evaluate the contribution of binding to the overall reactivity. The apparent second-order rates were estimated from the initial rate or first-order fit of the data at pH 6.9 and normalised to the least reactive complex. The listed rates appear lower than the observed rates in $NaNO_3$.

Complex	Apparent k_2 (M^{-1} s^{-1})	k_2 ratio	K_i (mM)	K_i ratio	k_{uncat} (s^{-1})
2-1	0.013 ($\pm 4.17 \times 10^{-5}$)	1.5	16.23	28	-
2-2	0.0086 ($\pm 2.40 \times 10^{-5}$)	1	32.54	55	-
2-3	15.03 (± 0.10)	1750	0.60	1	-
2-4	47.79 (± 1.05)	5570	0.59	1	-
HPNPP	-	-	-	-	5.16×10^{-9}

Table 2.3. The apparent second-order rate constant and the observed K_i at pH 6.9 for the dinuclear complexes. The data was collected at pH 6.9 in 50 mM HEPES at 0.1 M ionic strength (NaCl). The k_{uncat} for HPNPP is given at pH 6.9 (k_2 = 0.065 M^{-1} s^{-1}).[65]

The relative binding constants for **2-3** and **2-4** compared to **2-1** and **2-2** differ by an order of magnitude whereas the relative rates differ by over 3 orders of magnitude. This implies that the binding is stronger for the complexes a containing hydrogen bond donor in the 2-pyridine position. The main conclusion is that the improved reactivity is mainly due to higher catalytic turnover rather than tighter binding of the substrate.

These effects can be determined quantitatively using the transition state theory where the contributions of binding and reactivity of a complex can be related to the free energy of activation (ΔG^θ) for the transition state. The interactions involved in the stabilisation of the transition state for the transesterification of HPNPP can be determined using the Eyring-Polanyi equation, **Equation 2.8**, where the parameters k, k_B, h, R and T are the rate constant, Boltzmann constant, Planck's constant, gas constant and absolute temperature, respectively. The free energy of activation can estimated, **Equation 2.9**, using the obtained parameters (reaction rates or binding constants) of the reaction.

$$k = \kappa \left(\frac{k_B T}{h}\right) e^{\left(-\Delta G^{\ddagger}/_{RT}\right)} \qquad \text{(Equation 2.8)}$$

$$\Delta G^{\ddagger} = 4.576 \times T[10.319 + \log\left(^{T}/_{k}\right)] \qquad \text{(Equation 2.9)}$$

The slowest rate of hydrolysis is expected to be the uncatalysed reaction which is reflected by the highest energy of activation, see Figure 2.21. The catalysed reaction, for any given complex, should display a lower energy of activation and represents the combination of the ground state and transition state stabilisation.

The Gibbs free energy of activation ($\Delta G^{\ddagger}$) for the complex catalysed transesterification reaction of HPNPP can be calculated and compared to the uncatalysed reaction under similar conditions.

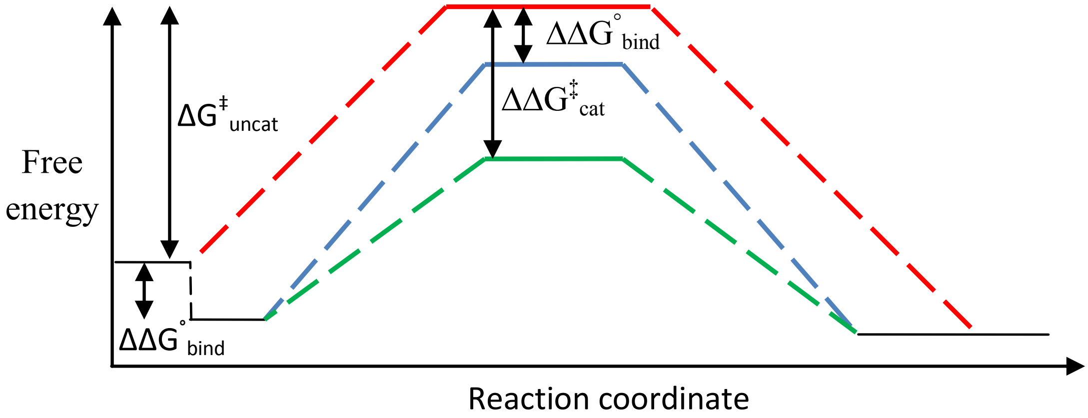

Figure 2.21. A schematic energy diagram, where ΔG° represent the free energy for the ground state and $\Delta G^{\ddagger}$ represents the free energy for the transition state, showing the difference in free energy between catalysed (green) and uncatalysed (red) reactions. A complex that displays similar binding to the ground state and transition state (blue) will not change the rate of the reaction relative to the uncatalysed reaction.

The transition state stabilisation, $\Delta\Delta G^{\ddagger}_{cat}$, represents the difference between the energy of activation of the uncatalysed transesterification and the complex catalysed equivalent ($\Delta G^{\ddagger}$ (**HPNPP$_{uncat}$**) - $\Delta G^{\ddagger}$ (**2-X**)).

The stabilising effect attributed to ground state binding $\Delta\Delta G^{\circ}_{bind}$ is estimated based on DMP inhibition experiments at pH 6.9 where the inhibitor is assumed to bind to the complexes similarly to the substrate. This indicates that the remainder of the $\Delta\Delta G^{\ddagger}_{cat}$ is due to the interactions preceding the transition state. The $\Delta G^{\ddagger}_{stab}$ and ΔG°_{stab}, see Figure 2.22, represents the percentage of $\Delta\Delta G^{\ddagger}_{cat}$ that can be attributed to the transition state and ground state interactions, respectively.

The contribution of the ground state interaction increases with increasing reactivity with **2-2** < **2-1** < **2-3** < **2-4**. The overall increasing reactivity **2-2** < **2-1** < **2-3** < **2-4** and the contribution of k_{cat} and K_M is illustrated in Figure 2.22 and quantitatively summarised in Table 2.4.

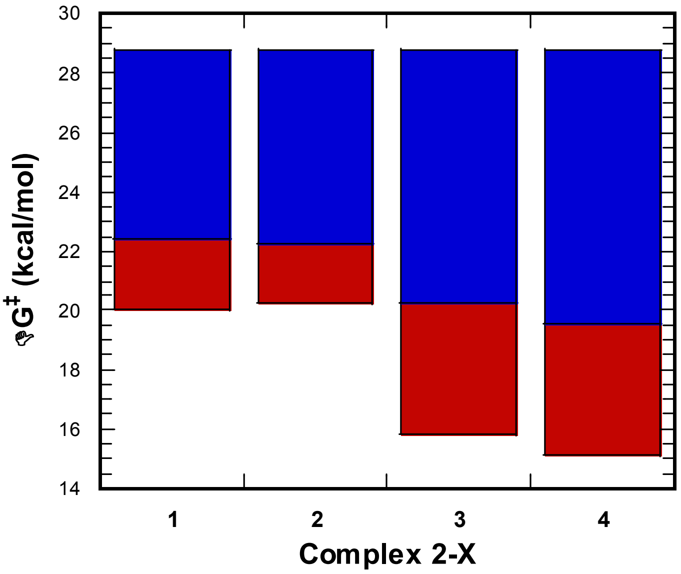

Figure 2.22. The free energy of activation illustrated as transition state interaction, $\Delta G^{\ddagger}_{stab}$ (blue). and ground state interaction, ΔG°_{stab} (red), for each complex. The upper limit of the combined (red and blue) bars corresponds to the free energy of activation for the uncatalysed transesterification of HPNPP and the lower limit corresponds to that of the catalysed reaction.

The reactivities of the complexes increase in the order **2-2** < **2-1** < **2-3** < **2-4** which translates to the effects of the functionality in the 2-pyridine position **Me** < **H** < **NH$_2$** < **NHMe**.

The decrease in reactivity upon changing to a Me-functionality indicates a reduction in ground state binding but an increase in transition state stabilisation, i.e. less substrate is bound in the ground state but the reactivity is higher for **2-2** compared to **2-1**.

Complex	k_2 ratio (**2-X/2-1**)	K_M ratio (**2-1/2-X**)	k_{cat} ratio (**2-1/2-X**)
2-1	1	1	1
2-2	0.7	0.5	1.4
2-3	1200	30	43
2-4	3700	30	130

Table 2.4. The K_M and k_{cat} ratios for the complexes indicate the contribution to the observed reactivity for each complex relative to 2-1.

The effect of the NH_2-functionality is an increased ground state binding (30-fold) as well as an increased transition state stabilisation (43-fold). The NHMe-functionality of complex **2-4** indicates similar ground state binding to the complex **2-3** but a greater transition state stabilisation (130-fold).

2.4.3 - Indicator displacement assay

The indicator displacement assays of the dinuclear complexes were motivated by reports in the literature.[94] Morgan *et al.* used various indicators with a phenoxy-bridged equivalent of complex **2-1**, see Figure 2.23. The use of indicator displacement assay is a well established method for the detection of the binding of anions to metal complexes.[95]

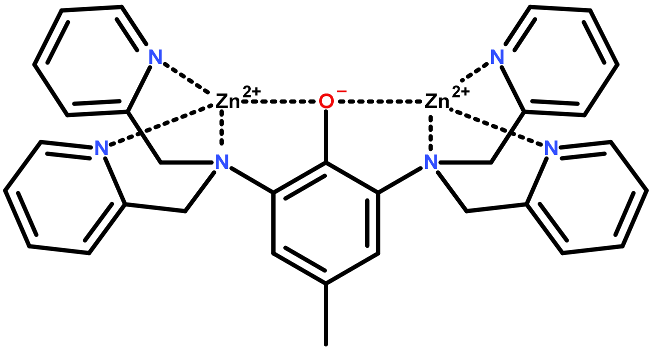

Figure 2.23. The dinuclear complex used in the literature to study the displacement of indicators.

The indicator pyrocatechol violet (PV), see Figure 2.24, was selected due to its large difference in absorbance maximum wavelength between free and bound indicator. This allows for both qualitative colorimetric and quantitative spectrophotometric determination of binding.

The indicator PV is expected to bind to the complex though the catechol moiety which would have to compete with the negatively charged oxygens of the dianionic phosphate. The fact that dianionic substrates bind tighter to the electrophilic metal ions of dinuclear zinc complexes than their monoanionic analogues has been used to estimate the transition state binding of substrates.[58] The expected tight binding of complexes **2-3** and **2-4** should result in a much more obvious displacement of the indicator than for **2-1** and **2-2**.

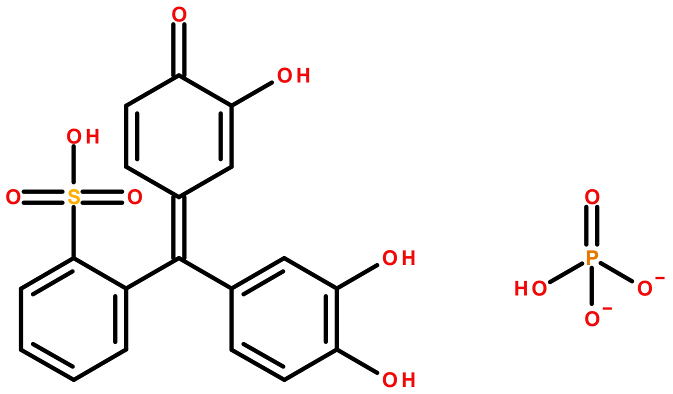

PV **HPO_4^{2-}**

Figure 2.24. Pyrocatechol violet (PV) indicator and the phosphate HPO_4^{2-} used to displace the indicator.

It is evident from the indicator displacement experiments, see Figure 2.25, that the two most reactive complexes (**2-3** and **2-4**) are displaying lower sensitivity towards the dianionic phosphate compared to the two least reactive ones (**2-1** and **2-2**). It is unexpected that this is the case given that the dianionic phosphate is supposedly more nucleophilic compared to the PV and should be expected to bind more tightly to the electrophilic dinuclear Zn(II) complex. The binding and displacement of PV was supposed to be used as an indicator for the behavior of the complexes towards phosphate but raised more questions than it answered.

Since the interaction between the indicator and the complexes was not fully investigated there is little to justify any conclusion. The main observation from this is that the profiles of the indicator displacements show strong resemblance between **2-1** and **2-2** as well as between **2-3** and **2-4**, respectively. This seems to indicate that the less reactive complexes, **2-1** and **2-2**, bind phosphates tighter than the more reactive complexes, **2-3** and **2-4**.

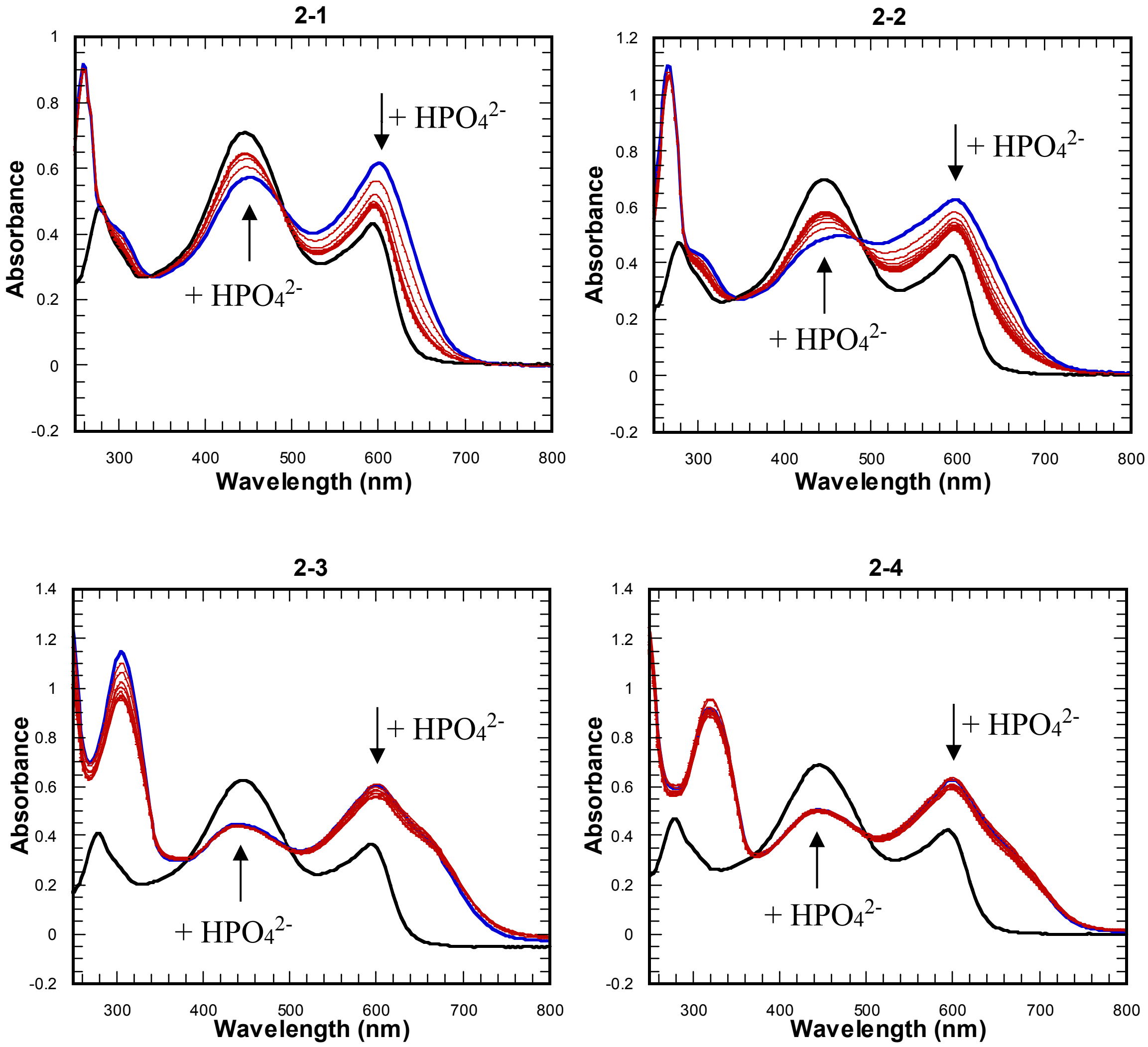

Figure 2.25. The UV-vis profiles of the titrations of HPO$_4^{2-}$ into a 1:1 complex:PV (50 µM of each) in 50 mM HEPES at pH 7.4 and 0.1 M ionic strength (NaNO$_3$). Each complex was titrated up to 2 equivalents of HPO$_4^{2-}$ with 10 additions at 0.2 equivalents of PV each. The complex bound PV (blue trace), the titration curves representing the consecutive additions of phosphate (red trace) and the unbound PV (black trace)

2.4.4 - Carbon dioxide effect on reactivity

An issue that prompted an investigation was the apparent deterioration in reactivity for the dinuclear complex **2-3** over time. The first observations of this nature were made using complex **2-3** buffered at pH 7.4.

The stock solutions of buffer were freshly prepared prior to the kinetic experiments and stored in capped vials. Upon repeated use of these stock solutions under identical condition at pH 7.4, a clear reduction of reactivity was observed over time (approximately one third decrease over 12 hours). The reactivity was regained upon use of freshly prepared buffer solution. This seems to indicate that complex itself was not inherently unstable but rather some external factors that were being introduced over time affected the reactivity. The progression of this effect seemed to be inversely proportional to the volume of the buffer stock since buffer stored in smaller volumes lead to a reduction of activity at a faster rate. The size of the vials in which the buffer was being stored also seemed to affect the outcome since buffers stored in narrow vials maintained the activity for longer than wider ones. After repeated experiments in which the buffers were stored in different sized vials (glass or plastic) it was determined that the only thing that could come in contact with the buffer solutions was the ambient atmosphere and from the atmosphere only CO_2 seemed to be the plausible culprit.

In order to confirm this theory CO_2 was passed through the buffer stock solution for 10 seconds, where the pH was maintained at ≈ 7.4, which was subsequently used. A slight drop in pH (0.07 units) was observed after treatment with CO_2 gas. Air was then passed through the same buffer stock solution for 20 min and the buffer was then used for an identical experiment. The results from the CO_2 experiments are presented in Figure 2.26.

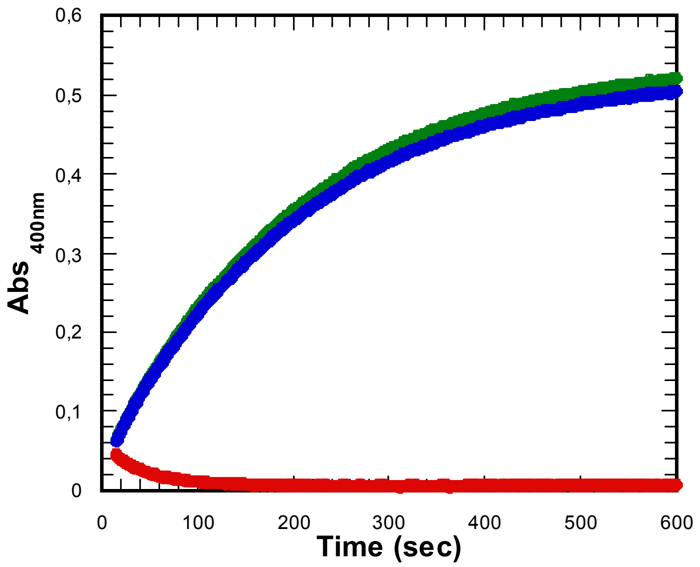

Figure 2.26. The transesterification of 50 µM HPNPP catalysed by 0.2 mM 2-3 (green) and the effect of passing CO_2 through the buffer for 10 seconds (red). The activity was regained after passing air through the CO_2 treated buffer 20 minutes (blue). The experiments were performed in 50 mM HEPES at pH 7.4 with 0.1 M ionic strength ($NaNO_3$).

CO_2 seems to completely deprive the complex of activity although interestingly passing air through the solution seems to reverse the effect. One possible explanation is that the physical bubbling of gas disfavors the retention of CO_2 in solution and in effect becomes sparging.The spontaneous hydration of CO_2 has a half-time of a few seconds[54] at neutral pH. It is likely that the carbonate that forms in aqueous solution from CO_2 binds the dinuclear complex although the equilibrium lies towards CO_2, see Figure 2.27, rather than carbonate.[96]

There are data suggesting that some buffers may affect the activity of carbonic anhydrase from plants[97] under certain conditions (high concentrations of CO_2) but despite the use of the same buffer (HEPES) it is unclear whether this can be related to the inhibition presented here. The binding mode for the mononuclear active site in carbonic anhydrase differs from that of the dinuclear complex. Once the carbonate is formed it is expected to bind to the metal ions in a bridging fashion[98] and act as an inhibitor at sufficiently high concentrations.

$$CO_2 + H_2O \overset{K_{eq}}{\rightleftharpoons} H_2CO_3$$

Figure 2.27. The spontaneous hydration of CO_2 at 25 °C ($K_{eq} = 2.6 \times 10^{-3}$).[96]

The inhibitory effect of CO_2 was investigated using sodium carbonate in order to accurately estimate the concentration of carbonate in solution, see Figure 2.28.

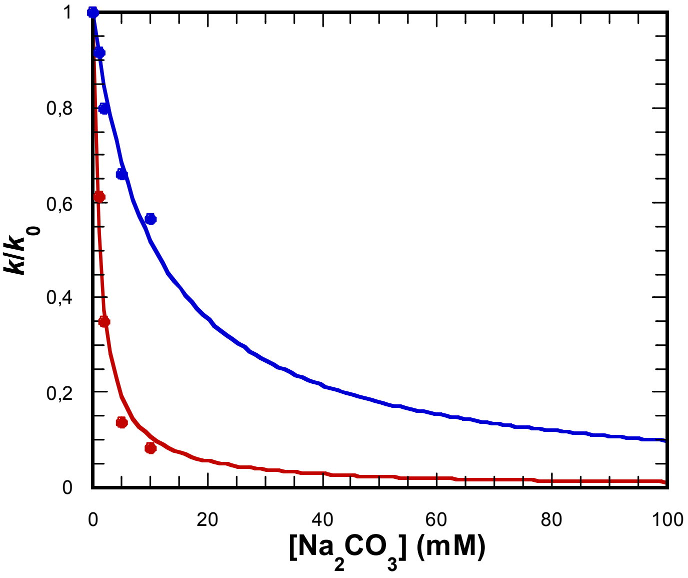

Figure 2.28. The Na_2CO_3 inhibition of 1 mM 2-1 (red) and 2-2 (blue) in 50 mM HEPES at pH 6.9 with 0.5 mM HPNPP and 0.1 M ionic strength ($NaNO_3$).

The carbonate clearly inhibits the activity of the complex **2-1** and **2-2** more efficiently than DMP with K_i-values of 1.2 (± 0.15) × 10^{-3} M and 1.1 (± 0.10) × 10^{-2} M, respectively. Given the dianionic nature of carbonate it is not unexpected that the compound binds to the complexes tightly. Although the carbonate is not the targeted compound it is likely bridgingthe Zn(II) nuclei, given its charge, similarly to a transition state analogue (phosphate monoester) as has been reported for **2-1**.[98]

Comparing the estimated K_i for the carbonate with the catalytic proficiency $(k_{cat}/K_M)/k_{uncat}$ where the k_{cat}/K_M (i.e. k_2) was determined at pH 6.9 from the data in Figure 2.15 and k_{uncat} at pH 6.9 (5.16×10^{-9} s^{-1})[65] yielding (0.39 μM and 0.58 μM, respectively) reveals a discrepancy of 6300-fold and 11200-fold for **2-1** and **2-2**, respectively. These differences can be indicative of additional stabilising interactions in the transition state that are not fully accounted for by the Lewis acidic interactions with the Zn(II).[58] These conclusions are based on the assumption that the dianionic carbonate behaves similarly to the dianionic transition state in the phosphate diester hydrolysis which might not be entirely accurate.

Carbonate inhibition was not studied with **2-3** and **2-4** but in light of the data obtained from the DMP inhibition it is reasonable to expect the binding to be even tighter and inhibition to be more effective.

The observation that CO_2 affects the Zn(II) metal complexes in such a manner was serendipitous and initially unexpected, although not surprising in light structure of the enzyme carbonic anhydrase[99] and research around artificial complexes for carbon capture in the literature.[100]

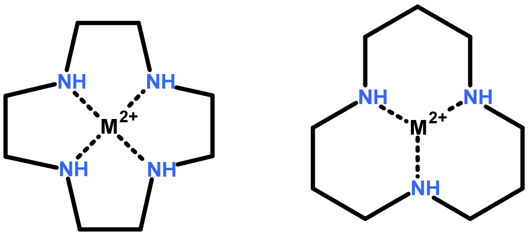

Figure 2.29. The Zn(II) 1,4,7,10- tetraazacyclododecane and 1,5,9-triazacyclododecane that have been reported to display the highest rate of CO_2 hydration for small metal complexes.

Many carbonic anhydrase mimics have been studied[101–103] that bear strong structural resemblance to the hydrolytic catalysts studied here and some have displayed reactivity towards phosphate diesters. The most reactive small metal complexes, see Figure 2.29, for the hydration of CO_2[104] have also been used to study the hydrolysis of phosphate diesters which further consolidate the premise of this discussion.

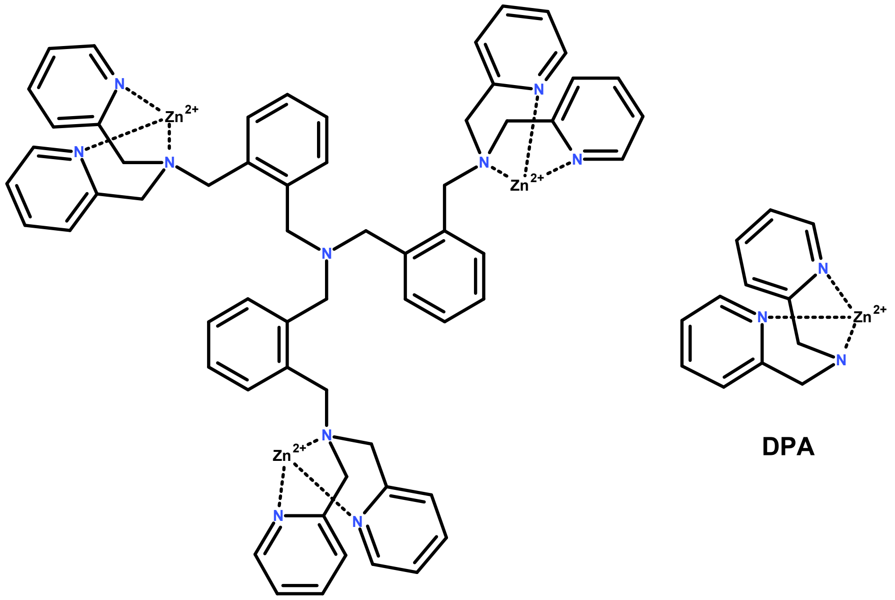

Figure 2.30. The trinuclear complex (left) based on $[Zn(DPA)]^{2+}$ (right) used by Cao *et al.*[105]

Most molecular mimics of CO_2 binding enzymes use similar mononuclear arrangements although multinuclear Zn(II) structures have also been studied, see Figure 2.30.[81,105] DPA (di-(2-picolyl)amine) has commonly been used as a ligand in conjunction with Zn(II) for binding or catalytic purposes. The trinuclear complex has been found to bind both CO_2 and phosphates. The monomeric $[Zn(DPA)]^{2+}$ has an association constant of 1.43×10^{7} M^{-1} at neutral pH[106] which indicates that it will be unstable in the presence of CO_3^{2-} ($ZnCO_3$ has a solubility product of 1.46×10^{-10}).[105] Despite this apparent limitation of the DPA ligand the multinuclear complex seems to resist demetallation by carbonate.[105]

This result can be extended for the dinuclear complexes **2-1**, **2-2**, **2-3** and **2-4** since they either remain relatively active in presence of carbonate or regain activity after treatment with CO_2. The apparent reversible binding of CO_2 poses an inconvenience that is readily solved by using freshly prepared buffers.

2.4.5 - Oxazole-bridged dinuclear complexes

The structural change that is of interest to study would be the removal of the bridging hydroxyl group. The role of the bridging hydroxyl group is to promote the association of the two mononuclear moieties through binding of the two Zn ions to the central alkoxy. The potential drawbacks of having an anionic oxygen between two electrophilic metal ions become apparent when the function of the complex is taken into account. The incoming substrate that the complex is meant to target is a negatively charged phosphate diester that will experience electrostatic repulsion from the alkoxy-bridge. The activation and interaction that is central in the catalytic role of the complex is dependent on the Lewis acidity of the metal nuclei which depends on the binding geometry and character of the metal coordinating ligands. It is therefore reasonable to assume that the electron-rich negatively charged alkoxy-bridge reduces the Lewis acidity of the positively charged Zn(II).

The reactivity of bridged dinuclear complexes is significantly higher than their mononuclear equivalents. The effects are cooperative rather than additive since the difference can be several orders of magnitude.[14,51,65]

A potential neutral alternative to the polar alkoxy group is required to encourage association of the nuclei and a viable option is pyrazole, which has been reported in literature.[75]

A series of compounds linked by an oxazole group, see Figure 2.31, was kindly supplied by Dr. Guoqiang Feng at Wuhan University. These ligands were complexed with Zn(II) and screened for activity under similar conditions to the alkoxy-bridged complexes

Equation 2.1 was fitted to the observed rate constants measured at various concentrations, see Figure 2.32, although a successful fit was not possible for **2-6** due to insufficient data points.

The observed rates indicated that the amino functionality in the 2-pyridine position gave the most reactive complex as had previously been established for **2-3** and that the complexes **2-5** and **2-7** were equally reactive. Complex **2-6** appeared even less stable in solution than **2-3** and the data point pH 7.4 is unreliable due to the appearance of precipitate during the reaction. The activity of **L2-6** was studied using Co(II) to determine whether changing metal ions could be of benefit to the reactivity or stability in solution, see Figure 2.33.

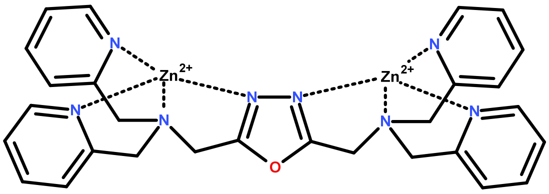

2-5

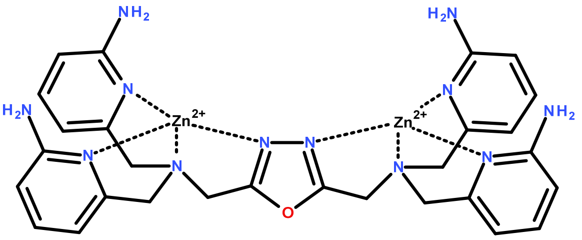

2-6

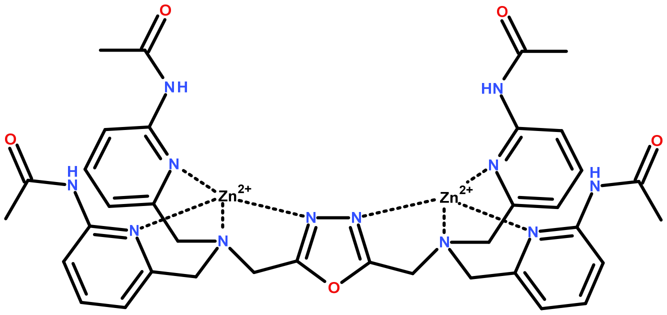

2-7

Figure 2.31. The oxazole-bridged dinuclear complexes.

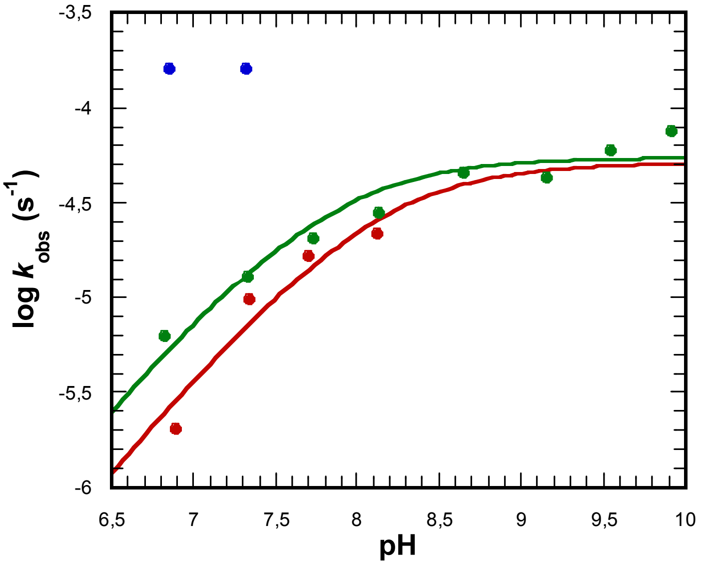

Figure 2.32. The observed rate versus pH for complexes 2-5 (red), 2-6 (blue) and 2-7 (green) at 0.4 mM complex concentration and 50 µM HPNPP. The solutions were buffered using 50 mM HEPES or CHES with 0.1 M ionic strength ($NaNO_3$).

There are numerous examples of Co(III) being used in the context of hydrolytic catalysis[13,107] although there have not been as many examples in literature of small metal complexes using Co(II) compared to Co(III) despite the fact that the former can replace Zn(II) in many enzyme active sites. The investigation of Co(II) for both catalytic and binding applications in catalytic biopolymers has been reported[36,50,108,109] as well as small di- and trinucleating complexes.[81,110]

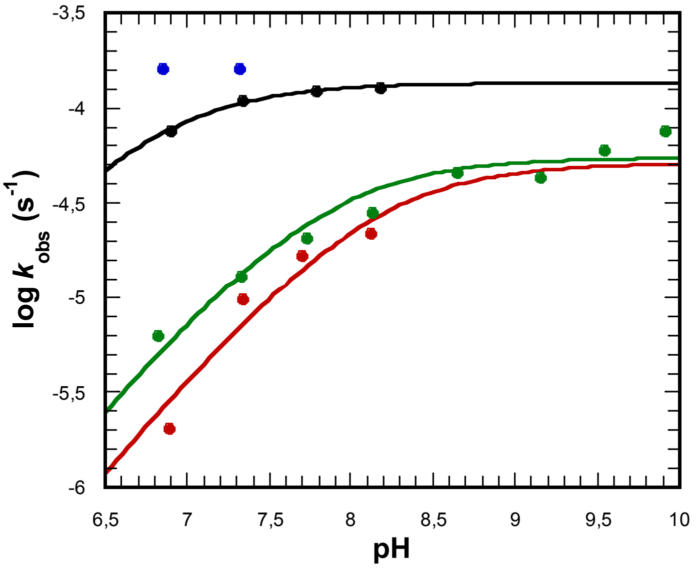

Figure 2.33. The use of equimolar amounts of Co(II) with 0.4 mM L2-6 (black) proved more fruitful and lead to the a more reasonable solution stability of the complex. The red (2-5) and green (2-7) plots are the same as in the previous figure. The solutions were buffered using 50 mM HEPES or CHES with 0.1 M ionic strength ($NaNO_3$).

The reactivity of **2-3** has been reported to quadruple upon changing the metal ions from Zn(II) to Co(II) for the transesterification of UpU.[111] The reactivity of **L2-6-Co(II)** does not seem to surpass that observed for **2-6** (data point at pH 6.9) but did yield an improved solution stability. These results allowed direct comparison between **2-1** and **2-5** as well as between **2-3** and **2-6** (compared at pH 6.9). The apparent second-order rates for the alkoxy and oxazole-bridged complexes are listed in Table 2.5.

Complex	Apparent k_2 ($M^{-1}s^{-1}$)
2-1	0.056 (± 0.003)
2-3	23.33 (± 2.23)
2-5	0.13 (± 0.11)
2-6	0.40 (± 0.001)
L2-6-Co(II)	0.34 (± 0.007)

Table 2.5. The apparent second-order rate constant k_2 determined for 2-1 (Figure 2.15) and 2-3 (Figure 2.14) compared to the relevant oxazole complexes.

Despite the apparent 2-fold rate increase the conclusion is that the reactivity of the complex **2-5** is approximately the same as for **2-1**. A more significant difference is observed between **2-3** and **2-6** amounting to more than a 50-fold increase in favor of the former.

The overall result seems to be that the oxazole-bridged complexes are not more reactive than their alkoxy-bridged equivalents.

The effect of CO_2 on reactivity was qualitatively investigated for complex **2-6** which is the oxazole-bridged equivalent of complex **2-3**. The reactivity of **2-6** before and after CO_2 treatment, see Figure 2.34, displayed similar behavior as seen for **2-3**. The reactivity of **2-6** was completely lost due to the exposure to CO_2 although passing N_2 through the solution did not restore activity in this case.

Complex **L2-6-Co(II)** was also studied with CO_2 at pH 7.32 (pH 7.08 after CO_2) and yielded similar results to **2-6**. This apparent difference in reactivity and irreversible CO_2 interaction for the oxazole complexes could possibly be explained by the less tightly coordinated metal ions and larger internuclear distance. The reduced tightness of binding to the metal by the neutral bridging group should yield more Lewis acidic metal nuclei that bind the CO_2 tighter. The CO_2 could possibly displace the oxazole and bind to the resulting tricoordinated metal ion in a facial bidentate way.[101]

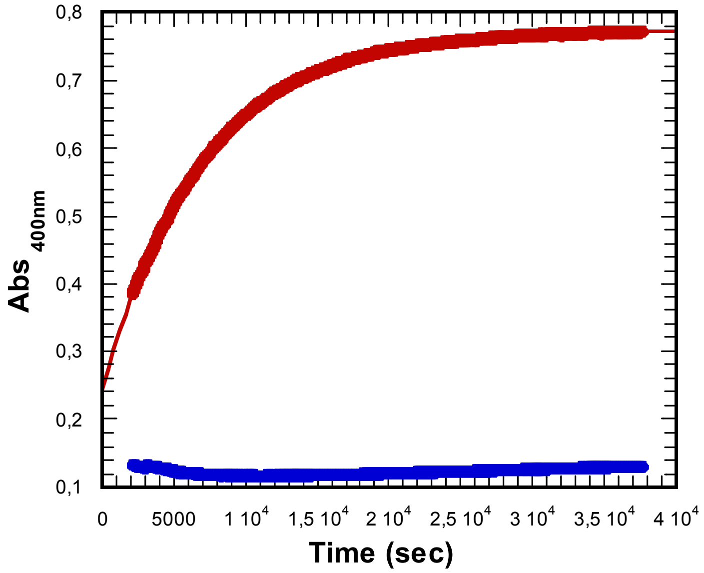

Figure 2.34. The activity of 0.4 mM 2-6 with 50 µM HPNPP before (red) and after treatment with CO_2 (blue) displayed similar behavior to 2-3 but the complex was not reactivated upon bubbling N_2 gas through the solution. The solution conditions were 50 mM HEPES with 0.1 M ionic strength ($NaNO_3$) at pH 7.4 before and pH 6.9 after CO_2 treatment.

Pyrazole complexes with Zn(II) have been reported in literature as β–lactamase models[75,112] and form different structures depending on length of the linker unit, see Figure 2.35.

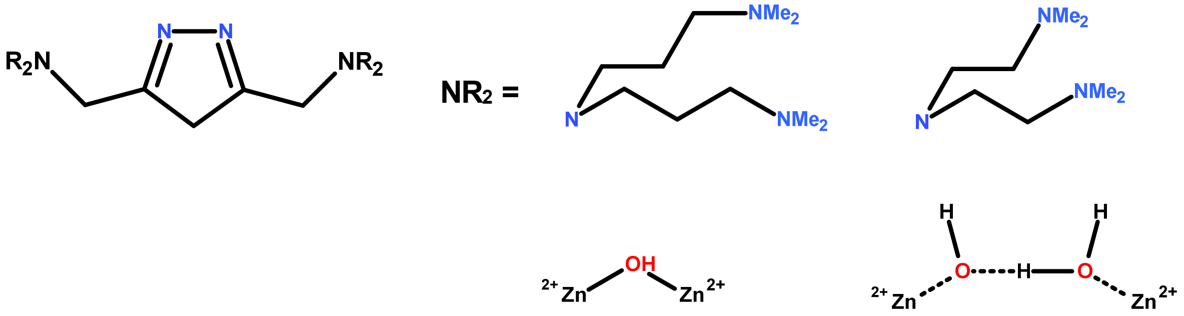

Figure 2.35. The structure of the pyrazole-bridged ligand affect the interaction between the Zn(II) nuclei.

The linkers lead to the formation of the structure due to the Zn(II) being forced apart. The Zn_2OH (μ-hydroxo) structure has been reported to be less reactive than the $Zn_2.H_2O.HO$ structure. Given the length of the linkers in the complexes studied herein it is likely that $Zn_2.H_2O.HO$ structure is more relevant. This would further validate the assumption that the greater internuclear distance reduces the possibility for double Lewis activation of the phosphate.

2.5 - Conclusion

The dinuclear complexes presented here have successfully been used for the transesterification of HPNPP and have highlighted the effects of different substituents in the 2-pyridine position. The native dinuclear complex **2-1** containing no functionality in the 2-pyridine position (2-H) was more reactive than the complex **2-2** containing a methyl functionality (2-Me). This seems to be mainly due to tighter ground state binding for **2-1**. The amino functionalised complexes **2-3** and **2-4** display improved ground state binding over **2-1** but also significant additional transition state stabilisation. The amino functionalities could potentially provide hydrogen bonding to the substrate which leads to the higher rates of transesterification. The increased reactivity of **2-3** and **2-4** comes at the cost of their stability in solution since both complexes are sensitive to pH changes. Additionally, the complexes were discovered to be sensitive to carbonate after the observation that exposure to ambient atmosphere reduced their reactivity.

The kinetic study of complexes containing a neutral bridging group (oxazole) revealed that the complexes were not more reactive than their alkoxy-bridged counterparts. This could potentially be attributed to the larger internuclear distance in the oxazole complexes that leads to poorer interaction with substrate. These results confirm what has previously been reported for dinuclear complexes in aqueous media, i.e. that the presence of an appropriate bridging group is important for the catalytic activity.

Subsequent chapters will introduce the concept of the association of mononuclear complexes without a covalent bridging unit to produce similar reactivities to those observed for dinuclear complexes.

2.6 - Future work

The concept of removing the bridging group will be the basis of subsequent chapters but the changing of the bridging group is a potential future study of covalently bound dinuclear complexes. The effects in the case involving the oxazole bridging unit were modest from a reactivity perspective but there are other neutral moieties that can serve as potential bridging groups. Triazole based bridging groups have been considered in the course of this work and although it was not used here the starting materials, see Figure 2.36, for this were synthesised for other applications, see Chapter 4.

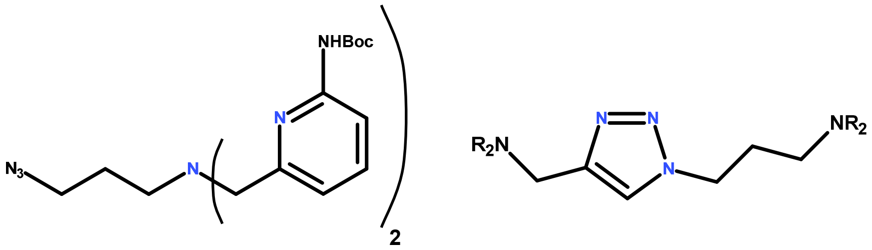

Figure 2.36. The azide compound used for peptide coupling and triazole synthesis (left) and the triazole linker in a potential dinuclear ligand (right).

Another compound that was considered due to the simplicity of the suggested synthesis was the keto-bridged equivalent of **2-2**, see Scheme 2.19. The attempted synthesis yielded a mixture of products that were difficult to separate. The resulting reaction mixture was similar to that of other attempts to oxidise alcohols with potentially acidic α-protons (see Chapter 5, **L5-8**). The reaction mixture turned increasingly green with time and was dark green in the work up. This unidentified green colour was not observed for other (successful) oxidations using Dess-Martin periodinane and became indicative of formation of undesired byproducts.

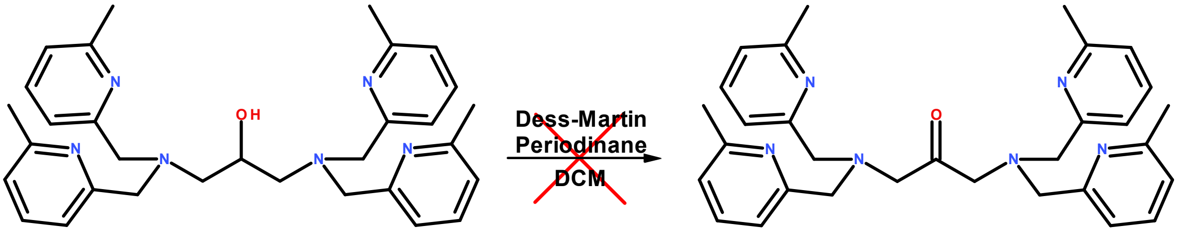

Scheme 2.19. The attempted oxidation of 2-2 using Dess-Martin Periodinane.

Despite not being as easy to synthesise as initially envisioned the keto-bridged complex would still be interesting to study due to the less anionic nature of the carbonyl oxygen compared to the alkoxy oxygen.

An alternative synthetic route lies in the preparation of the starting material, in this case the 1,3-diamino-2-propanol. The oxidised analogue of the starting material 1,3-diaminoacetone dihydrochloride is commercially available although it quickly became evident that upon deprotonation of the amines the formation of imine polymers would strongly interfere with the S_N2 displacement of iodine.

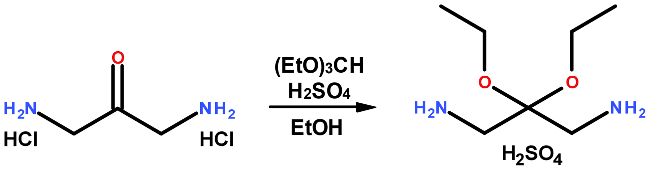

Scheme 2.20. The formation of the protected starting material using triethyl orthoformate and concentrated H_2SO_4 in EtOH.

The other option was to convert 1,3-diaminoacetone dihydrochloride into a protected ketone in the form of a ketal. This was attempted using an acidic procedure, see Scheme 2.20, in order to avoid deprotonation of the amines.

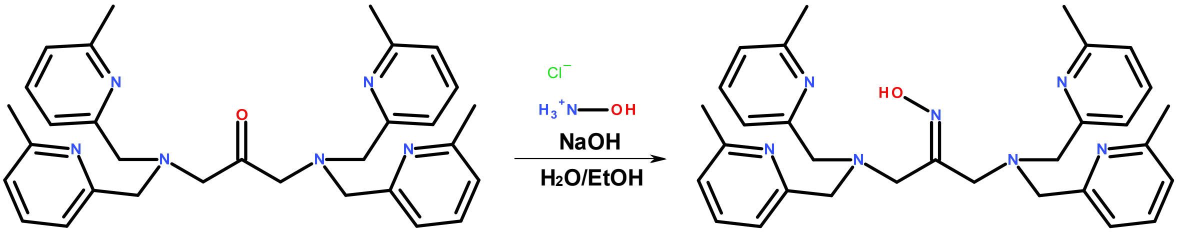

Scheme 2.21. Suggested synthesis of an oxime-bridged dinuclear complex.

The procedure was successful and the starting material was obtained. The amino ketal was used in the synthesis with precursor $\mathbf{X_2}$ although the reaction was unsuccessful.

It might be questionable as to whether the target compound itself will resist the eliminations that has plagued its predecessors but it is still an alluring molecule to study which leads the quest on. If the keto-bridged complex can be synthesised it would be interesting to investigate the possibility to convert the ketone into an oxime, see Scheme 2.21.

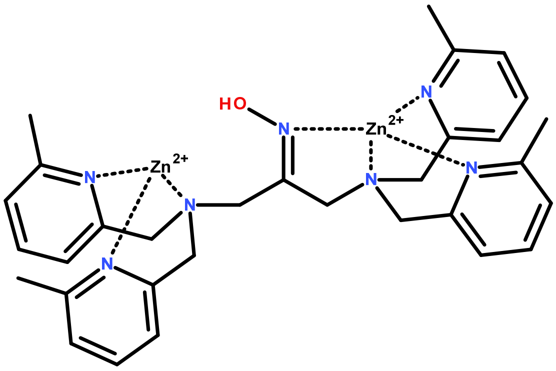

Figure 2.37. The proposed structure of a dinuclear oxime complex.

Since the oxime functionality will most likely only bind to one Zn(II) it will not bridge the two nuclei but rather have a non-coordinated nucleus as an appendage, see Figure 2.37. Similar oxime containing mononuclear complexes will be presented in Chapter 5.

Chapter 3 - Membrane based complexes

3.1 - Introduction

The concept of organisation at the interface of membranes can be traced back to features derived from nature. The cell membrane is a prime example of an organised structure that is of utmost importance for the compartmentalisation of cellular components as well as intercellular communication. The formation of the membrane structure in solution is driven by the disfavored interaction between the lipophilic structure of the surfactant tail and the solvent.

On a cellular level there are a multitude of different molecules of varying sizes that are encouraged to associate by the macromolecular structure that is the membrane of the cell.[113] Mimicking these features is a valid approach to investigating the structural interactions that are of relevance for reactivity given that many binding processes are known to occur on membrane surfaces. Biological membranes consist of various surfactants that are of the general phospholipid structures seen in Figure 3.1. The self-assembled structures that are spontaneously formed by these phospholipids in aqueous solution are similar to cell membranes and serve as appropriate models for it.[114]

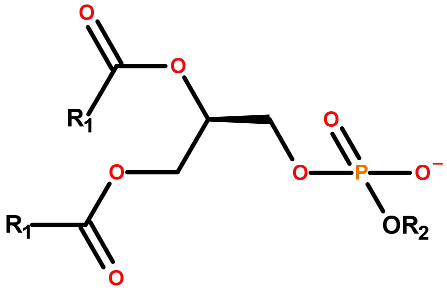

Figure 3.1. The general structure of the phospholipid membrane component where R_1=aliphatic chain and R_2 = charged species.

The interactions at the membrane interface has been studied using Cu(II) binding receptors.[115] The binding interactions displayed cooperativity and were substantially enhanced in the interface compared to the solution which has been suggested to be due to the lower polarity of the environment as well as a local concentration effect when the receptors are localised to the surface.

An example of the local concentration effect is the hydrolysis of lipophilic esters and amides in the membrane interface by carboxyl functionalised lipids.[116] The experiments consisted of simply mixing various long alkyl chains with polar head groups that are known to form micelles in solution with an alkyl ester (**S1**) and amide (**S2**), see Figure 3.2. Of these surfactants the carboxyl functionalised hexadecanoate (**Cat 1**) was found to efficiently hydrolyse ester and amide substrates.

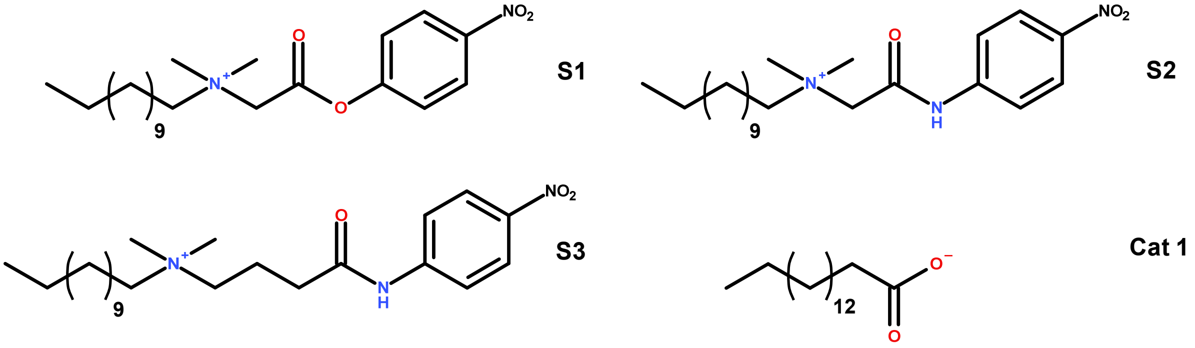

Figure 3.2. The structures of various substrates used to study the reactivity of Cat 1 at the membrane interface.

The rate of reaction was measured under different conditions and the estimated half-lives of the uncatalysed, acetate-catalysed and **Cat 1** catalysed hydrolysis of **S2** were 1 year, 2.5 weeks and 3 min, respectively. The **Cat 1** accelerated hydrolysis is approximately 8 orders of magnitude faster than the acetate-catalysed reaction assuming a linear dependence on the concentrations of the catalysts (which were 20 μM and 200 mM, respectively). The reaction is stochiometric which indicates that the hydrolysis of the mixed anhydride that is formed is rate determining for the turn-over, see Figure 3.3. The interesting point to note is the structural constraints for the hydrolysis achieved. The presence of three methylene groups (**S3**) is enough to cause a complete loss of activity which indicates the importance of proximal interaction (carboxylate-ammonium) to the targeted functionality.

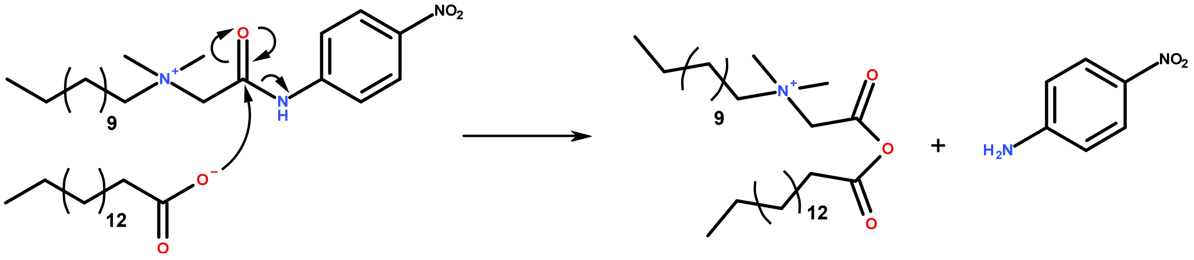

Figure 3.3. The proposed mechanism for the hydrolysis of the amide bond resulting in a mixed anhydride.

The mechanism of action is arguably similar to that of Carboxypeptidase A (CPA) where the glutamic acid anion functions as a nucleophile[91] and it has tentatively been proposed that the random search through lipophilic aggregates could prove surprisingly rewarding in terms of catalytic activity.

In light of these membrane induced effects it is chemically sound to study the effects of introducing metal complexes into these environments.[117–120] The effect of introducing a 1,4,7,10-tetraazacyclododecane derivative, see Figure 3.4, was reported[121] for the hydrolysis of fluorescein diacetate (FDA) which revealed a 25-fold rate increase when embedded in a membrane structure compared to solution. The rate increase was found to depend on the fluidity of the membrane structures where a more flexible membrane allowed for more pronounced cooperativity.

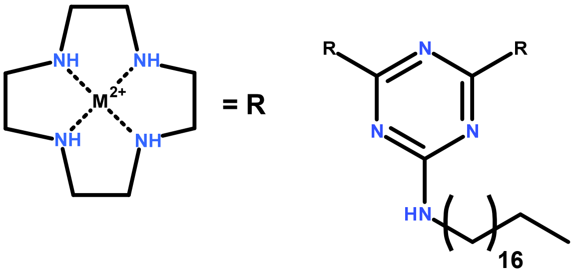

Figure 3.4. The structure of the lipophilic metal complex using a dinuclear arrangement of 1,4,7,10-tetraazacyclododecane monomers.

Similar complexes have been used to study vesicle-based phosphate diester hydrolysis[122] and have been reported to result in substantial rate accelerations compared to the equivalent solution-based structures, see Figure 3.5. The mononuclear solution-based catalyst was reported to provide 3 orders of magnitude rate acceleration when covalently bound in a dinuclear fashion as can be seen illustrated by the middle structure in Figure 3.5. When the mononuclear complex was embedded into a vesicle the acceleration over the solution-based system was up to 7 orders of magnitude. These experiments were carried out at pH 8 but they are still remarkable since the relative rates for the vesicle based hydrolysis of BNPP at pH ≈ 7 is 5 orders of magnitude faster than the background reaction. The reactivity of flexible structures containing mononuclear complexes that are held in close proximity to each other through non-covalent interactions has been reported using gold nanoparticles.[123–125] The nanoparticle bound complexes could be referred to as semi-covalent systems given the solid core to which the complexes are anchored (thiol-Au) through a flexible linker, see

Figure 3.6. Although these structures are relatively rigid, they arguably become more similar to membranes when used in conjunction with long flexible complexes.

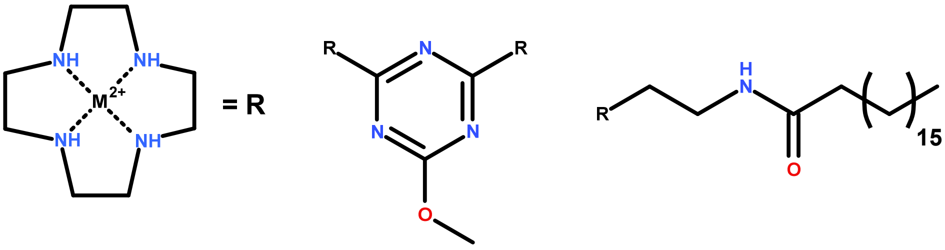

Mononuclear **Dinuclear** **Vesicle**

Figure 3.5. The Zn(II) catalysts used in the highly reactive vesicle system reported by König *et al.*[122]

The investigation of HPNPP transesterification promoted by the complexes in Figure 3.6 shows that the incorporation of the 1,4,7-triazacyclononane (TACN) complex into a nanoparticle system significantly increases the rate of the reaction.[123]

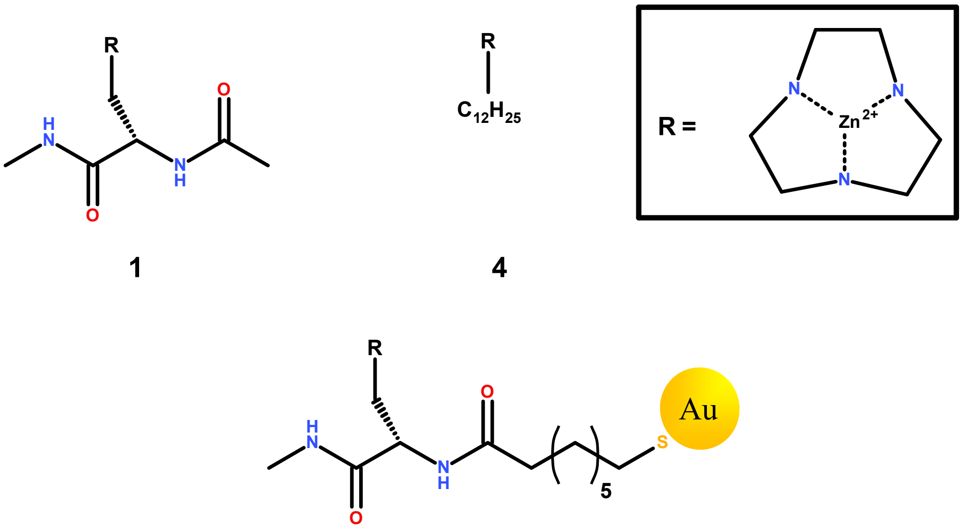

k_{rel} **1** **4**

629

Figure 3.6. The relative rates for transesterification of HPNPP were normalised to the mononuclear complex and revealed a 4-fold and 629-fold rate acceleration for the micellar complex and the functionalised nanoparticle, respectively.

Despite the fact that the micellar complex is more reactive than the mononuclear equivalent it is still 2 orders of magnitude slower than the nanoparticle system.Bonomi *et al.*[126] reported the activity of a similar system for the hydrolysis of the DNA model compound bis-(4-nitrophenol) phosphate (BNPP), see Figure 3.7. The mononuclear control

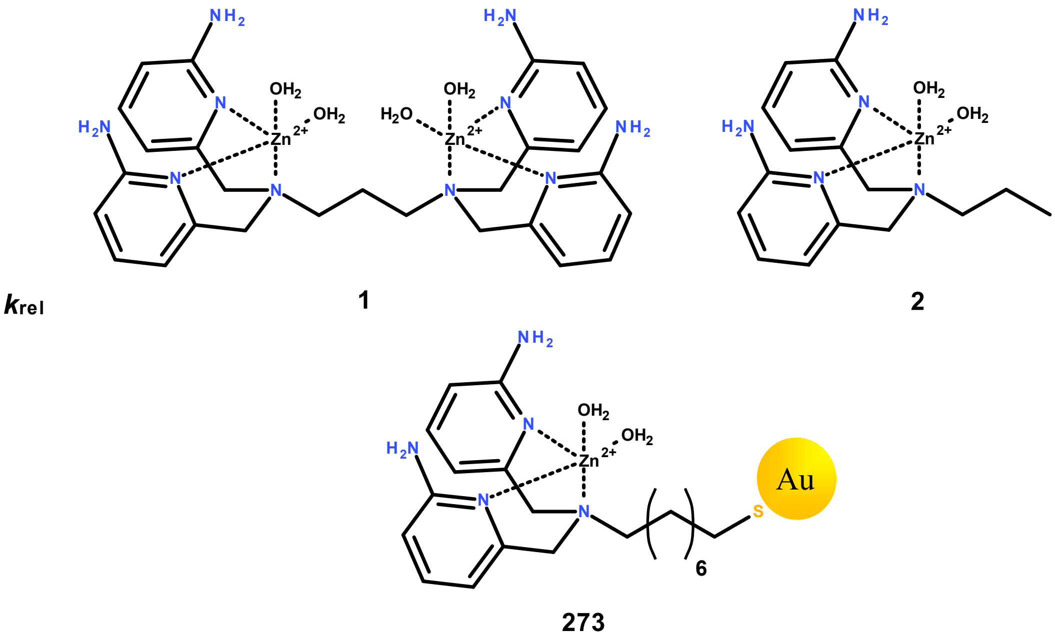

Figure 3.7. The relative rate constants observed for the hydrolysis of BNPP for the covalently linked dinuclear Zn(II) complex (left), the mononuclear complex (middle) and the nanoparticle based complex (right).

was compared to the nanoparticle system which revealed over 2 orders of magnitude higher reactivity in favor of the latter. Interestingly the reactivity of the flexible nanoparticle system is significantly higher than the covalently linked dinuclear equivalent. Even the mononuclear complex appears more reactive than the dinuclear complex despite the fact that the binding constant for dimethylphosphate (measured by its inhibition effect) is 3-fold greater for the latter.

Recently a gold nanoparticle system was reported to cleave HPNPP with a second-order rate constant of 250 M^{-1} s^{-1}, see Figure 3.8, representing the most reactive Zn(II) based system in aqueous media to date.[68] The structure is very similar to the previously reported TACN nanoparticle system. The two most reactive systems studied indicate a substantial effect of the linker length on the reactivity. The observed reactivity appears to be highly dependent on the environment around the catalytic units since the introduction of a more polar polyethylene glycol linker reduces the activity of the system.

Remarkably the increased rates seem to be mainly due to an increase in k_{cat} since the K_M is very similar between the structures. An orthogonal measure for the lipophilicity of the nanoconstruct was obtained using the compound 6-nitrobenzisoxazole-3-carboxylate (NBIC) that decarboxylates at faster rates with decreasing polarity of the medium. The rate of reaction for NBIC correlates well with the difference in reactivity of the nanoparticle system observed for HPNPP transesterification which led to the conclusion that the reduced polarity of the environment around the nanoparticles is the largest contributor to the observed reactivity.

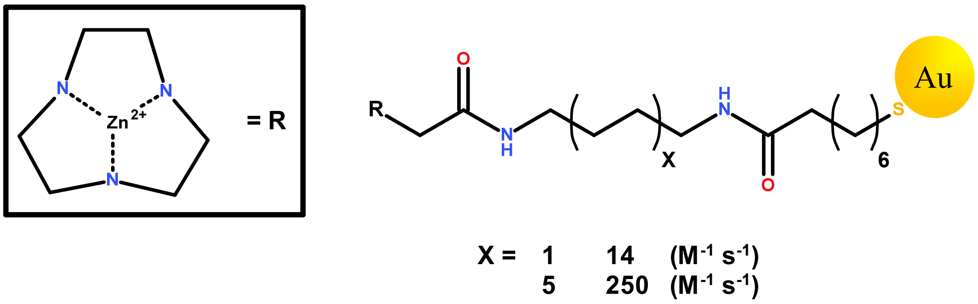

Figure 3.8. The structure of the linker between the gold nanoparticle and the catalytic head group appears to significant affect the activity of the system.

The reactivity of the hydrolytic systems presented above is cooperative and thus the association enhances the reactivity non-linearly with respect to the complex concentration. The embedding of structures into membranes has proven this to be the case for many complexes and is therefore a tantalisingly simple method of achieving cooperative reactivity.

3.2 - Aims

The aim of the membrane based complexes is to examine the potential for association of mononuclear complexes on the surface of vesicles to yield more reactive systems. The non-covalent association on the surface of vesicles permits the formation of more flexible catalytic systems and may therefore provide better accommodation of the substrate.

3.3 - Synthesis of the membrane ligands

Ligands **L3-1** and **L3-2** were synthesised using the same procedure used for the synthesis of **L2-3**, see Chapter 2, using the precursor *tert*-butyl N-[6-(iodomethyl)-2-pyridyl]carbamate (**X_3**). The precursor (**X_3**) was reacted with either hexadecylamine or butylamine in dry DMF with DIPEA at 70 °C for 12 hours, see Scheme 3.1.

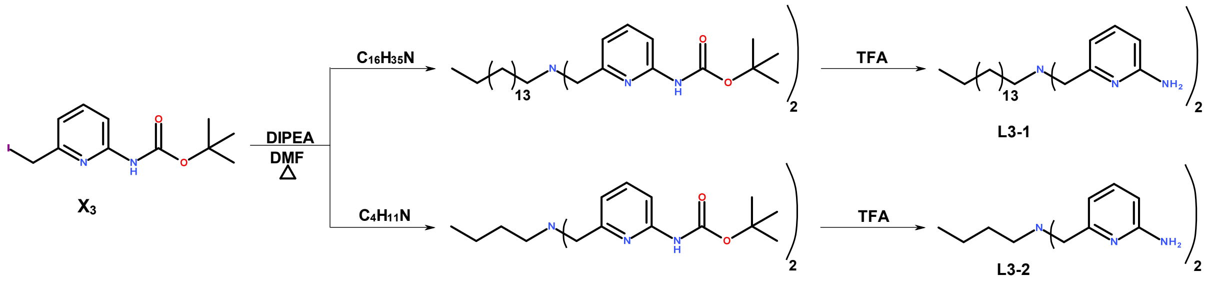

Scheme 3.1. The synthesis of L3-1 (top) and L3-2 (bottom) from the same precursor X_3. The yields were 55 % and 100 % for L3-1 and 60 % and 100 % for L3-2 for the respective synthetic steps.

3.4 - Results and discussion

The membrane-like structures used in this study are vesicles based on a phospholipid 1,2-dimyristoyl-*sn*-glycero-3-phosphocholine (DMPC) or a quarternary alkyl amine dimethyldioctadecylammonium chloride (DMDODA). The structure consist two layers of surfactant molecules arranged with their lipophilic appendages facing each other and the hydrophilic head groups facing the solution. This structure is usually referred to as a membrane bilayer or vesicle, see Figure 3.9.

The methods by which the vesicles were produced are discussed below but the main feature of interest is the lipophilic inner layer that allows hydrophobic alkyl anchoring. A concern in terms of size is the potential issue of light scattering affecting the UV measurements thus initially 50 nm vesicles were made.

Among the first compounds to be considered in this project for studies of membrane based interaction was the 2-aminopyridyl ligand, see Figure 3.10. The Zn(II) coordinating head group was chosen due to the reactivity displayed by complex **2-3**, see Chapter 2.

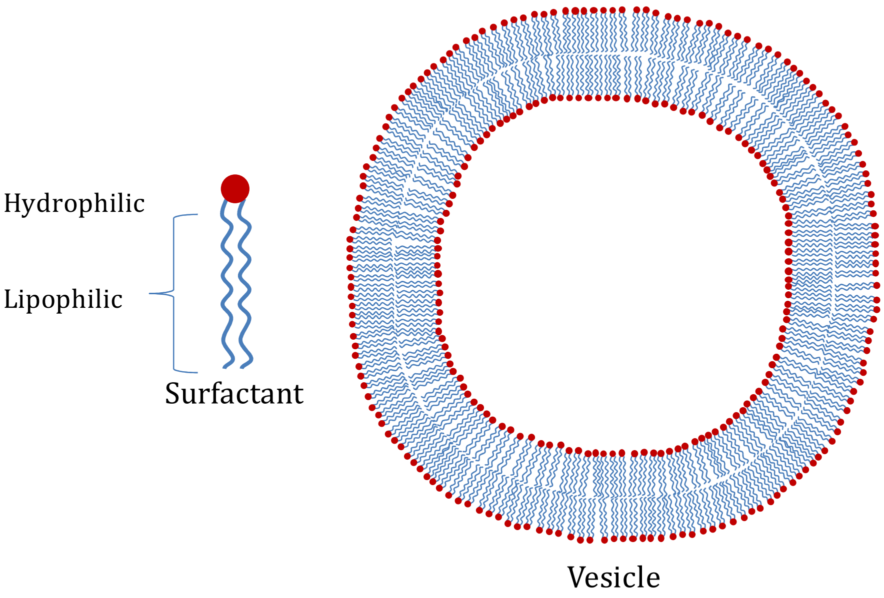

Figure 3.9 The schematic structure of the surfactant and the vesicle.

Although complex **2-4** was more reactive it was also less stable in solution. The aim was to study if it was possible to achieve similar activity as seen for **2-3** simply by encouraging non-covalent interaction in solution.

Cholesterol is a component of natural cell membranes and had successfully been used to embed cholesterol-dansylamide probes into membrane surfaces.[115] Although initial attempts were made to synthesise the compound it was abandoned in favor of the simpler alkyl ligands that could be synthesised in two steps starting from the intermediate (**X$_3$**), see Scheme 3.1.

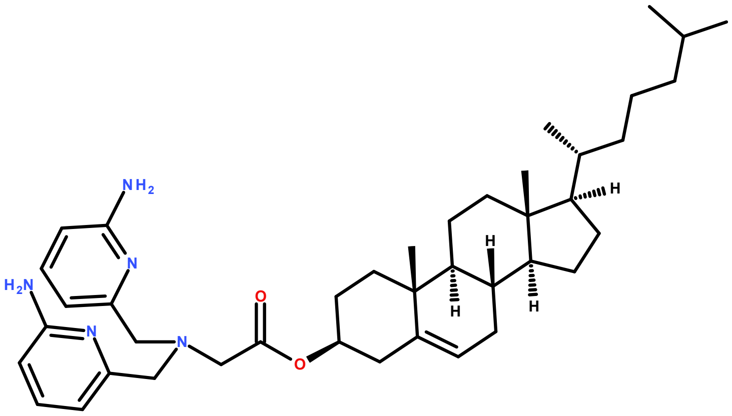

Figure 3.10. The proposed structure for the potential cholesterol ligand.

The use of a long aliphatic tail allows the complex to embed itself into the membrane and freely associate with other monomeric units thus avoiding the use of the alkoxy-bridging group used for highly reactive dinuclear complexes.

The structural requirements for the membrane complex **3-1**, see Figure 3.11, are simple and include a lipophilic tail and the catalytic head group comprised of the monomeric Zn(II) binding 2-aminopyridyl moiety. Due to the polar Zn(II) complex component, the structure of the complex is very similar to a surfactant. The monomeric complex **3-2** serves as a control compound that mimics the catalytic head group of **3-1** but lacks the means for a strong lipophilic interaction with membranes.

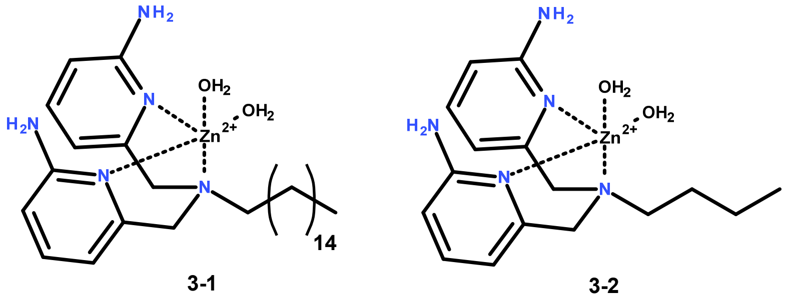

Figure 3.11. The structure of the membrane embedding complex 3-1 and the water soluble control 3-2.

Complex **3-2** is not only a control compound for **3-1** but can arguably also be used as a comparison to **2-3** despite the lack of the coordinated alkoxy group. The simple mononuclear **3-2** was initially envisioned to reach the reactivity of the complex **2-3** if it could be held in close proximity to another unit of **3-2**. The potential added advantage of **3-2**, apart from flexibility, is avoiding the reduction in Lewis acidity of the Zn(II) and electrostatic repulsion of the anionic substrate due to the alkoxy-bridging unit.

The complexation of ligand **L3-1** with $Zn(OTf)_2$ was analysed using NMR spectroscopy, see Figure 3.12, in MeOD-d_4 due to the poor solubility of the compound in D_2O. The concentration of ligand is significantly higher than for the kinetic experiment but was necessary due to the set parameters of the NMR spectrometer. The NMR spectrum of **3-1** is consistent with a 1:1 complex and shows that a complex is formed.

The membrane interaction is based on the idea of introducing a catalyst containing a long alkyl tail into the lipophilic layer of a membrane. The structure itself is made up of a surfactant, in this case DMPC, which is from the phophatidylcholine family of lipids, see Figure 3.13, and is one of the major components in biological cell membranes.

DMPC vesicles were made by dissolving the surfactant in the desired buffer and using a bespoke syringe as an extrusion device. The liquid was passed through a silicone membrane with a pore size of 50 nm, see Figure 3.14. The pore size was selected in order to form smaller

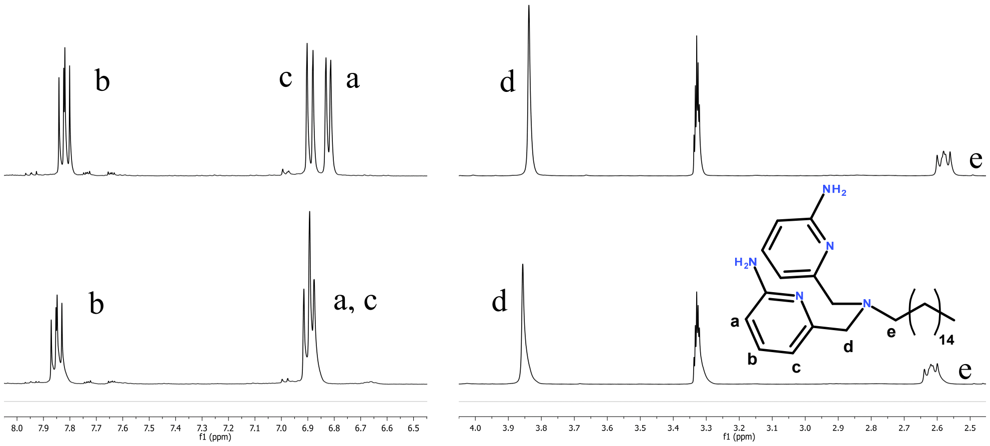

Figure 3.12. The partial ^{1}H-NMR spectrum in MeOD-$d_4$for L3-1 60 mM (top) and after addition of 60 mM $Zn(OTf)_2$ complex 3-1 (bottom).

vesicles which reduce the effects of light scattering (increases with size) that would interfere with the measurements if larger structures were made.

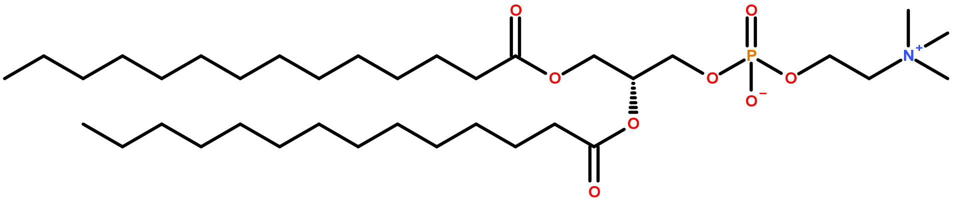

Figure 3.13. The structure of the phospholipid 1,2-Dimyristoyl-*sn*-glycero-3-phosphocholine (DMPC)

The liquid was passed through the membrane 21 times ending on the opposite side to the initial state (i.e. an odd number of extrusions) to eliminate any risk of retaining structures in the initial solution that were larger than specified.

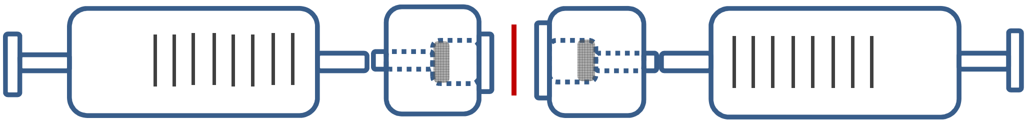

Figure 3.14. An illustrative drawing of the membrane extrusion device with the 50 nm pore membrane (red) in the middle.

The size of the vesicles are only stable for a few days (3-4 days) if the solution was kept at 4 °C and thus the time window for reproducible experiments is limited. Another issue that needs to be considered is the "flip-flop" mechanism, see Figure 3.15, which allows the movement of the membrane components between the inner and outer leaflets. This is not an issue when the structure is entirely homogeneous since the movement occurs in both directions and they would in effect cancel out. In nature the membrane interactions are based on multi-component systems working in conjunction with each other and are therefore not homogeneous. The introduction of an alien component into one leaflet of a preformed membrane leads to a concentration gradient between the outer and inner leaflet and since the membrane structure is fluid a dynamic equilibrium will be established over time.

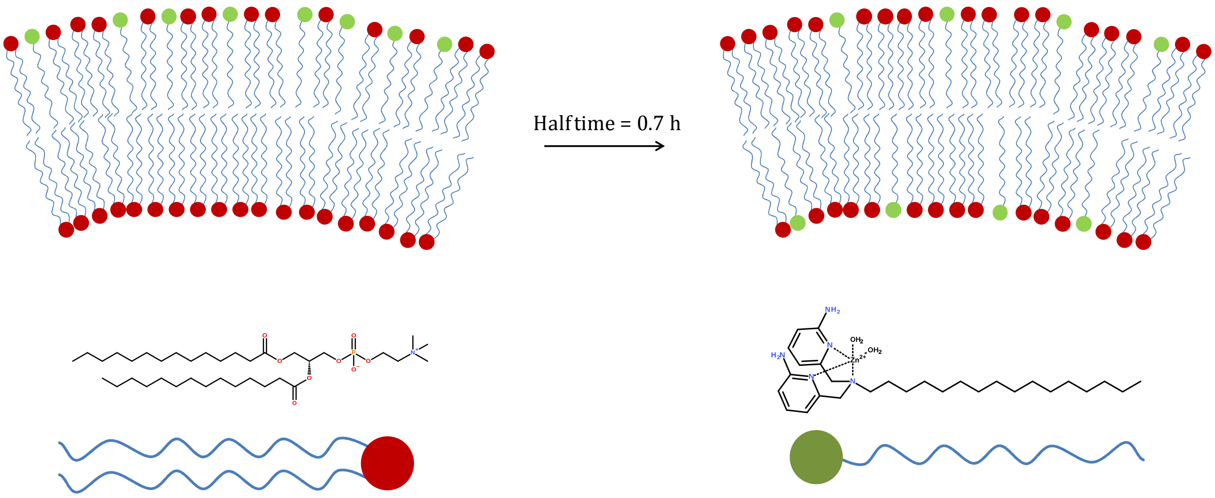

Figure 3.15. An illustrative example of flip flop between the outer and inner leaflet of a membrane bilayer (top). The representation of the DMPC (red) and 3-1 (green) as presented in the membrane (bottom).

In the case of DMPC the half-time for the flip-flop has been determined using exchange experiments at 50 °C and estimates the upper limit to be around 40 minutes.[127,128] The flip-flop rate will not translate directly to the case of **3-1** but since we are not investigating that particular mechanism the estimation for DMPC serves as a useful approximation for the longest time that the system requires to reach equilibrium. It has previously been suggested that cationic species might actually have a shorter half-time for the flip-flop mechanism.[115] The practical implications of this is that if the progression of the reaction is monitored on a time scale similar to that of the intramembrane flip-flop the effective concentration of catalyst exposed to the solution will be varying. This was not taken into consideration for the initial experiments since the aim was to qualitatively verify the existence of reactivity.

The initial experiments were performed using vesicles made from 200 μM DMPC with a 10 % loading of the catalytic complex **3-1** at pH 7.4 and 50 μM HPNPP with 0.1 M ionic strength ($NaNO_3$). The vesicle solution was incubated with the complex for approximately 10 minutes prior to the addition of the substrate. No reaction was seen over 2 hours which led to the conclusion that the complex was either too dilute or being inhibited by the DMPC.

DMPC contains a phosphate diester with aliphatic ester groups that is very unlikely to hydrolyse by action of the catalyst but is nevertheless a potential candidate for binding to the complex, inhibiting potential action on the substrate. Given the position of the phosphate group at the vesicle interface it is very likely that the high local concentration of the DMPC competes with the relatively low solution concentration of HPNPP. Similar Zn(II) complexes, see Figure 3.16, have been used as fluorescent probes for phosphatidylserine in biological systems which further supports these concerns.[129,130] The dinuclear complex **2-3**, see Chapter 2, has been reported to bind tightly ($K_{\mathrm{d}} \approx 80$ nM) to lipopolysaccharide (LPS) attached to gold surfaces.[131]

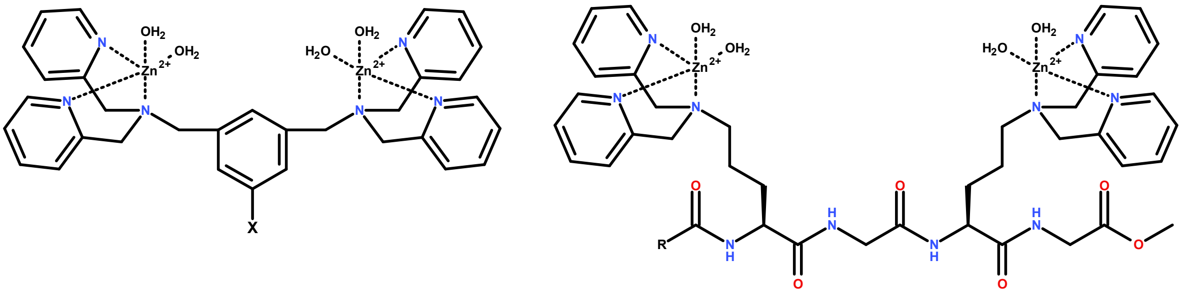

Figure 3.16. The structure of the Zn(II) complexes used in literature for phosphatidylserine detection.[129,130]

The likelihood of inhibition of the complex by DMPC was addressed by simply introducing the surfactant as an “observer” in a reaction involving the substrate and a catalytic complex of known activity. Complex **2-3** is the dinuclear equivalent of **3-1** and was expected to provide a reasonable benchmark for the potential inhibitory effect of DMPC. The experiments were performed using 100 µM **2-3** and 20 µM HPNPPi and then repeated to include 10 µM DMPC vesicles, see Figure 3.17. There was no difference in the rate of reaction between the two experiments and the conclusion is that the DMPC does not inhibit the reaction.

There have been similar phospholipids used in conjunction with metal complexes that catalyse phosphate diester hydrolysis and no inhibition has been reported by the surfactant.[122]

The concern regarding the concentration of the complex was tested using **2-3** at varying concentrations and monitoring the reactivity. The concentration of 20 µM **3-1** at which activity was not seen would create 10 µM of dimer, and so this is the key concentration for the comparison using **2-3**.

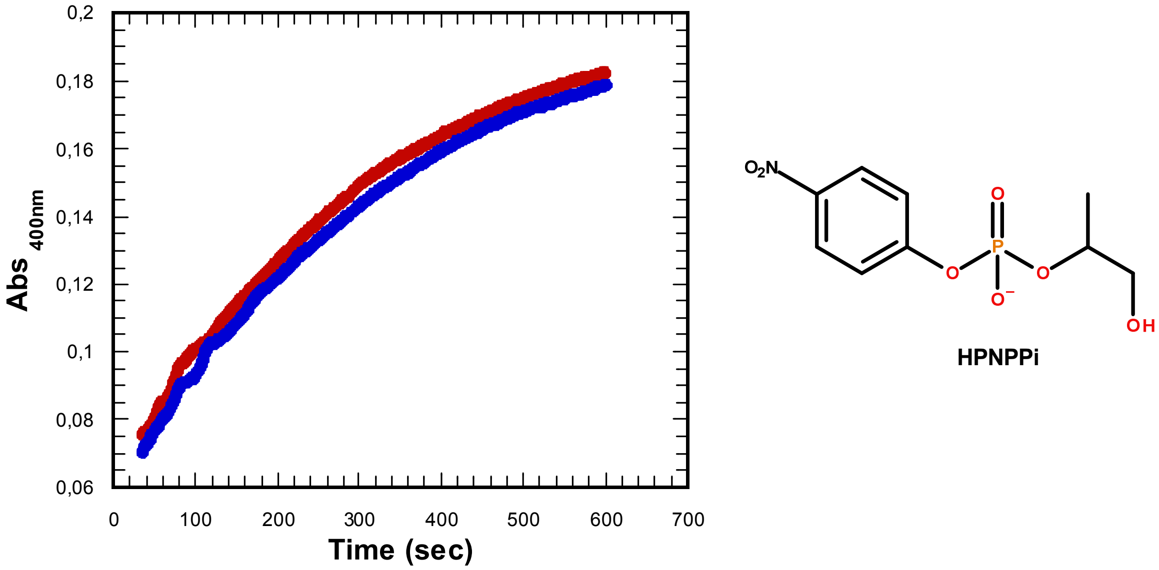

Figure 3.17. The observed effect of DMPC on reactivity of 100 µM 2-3 studied using 20 µM HPNPPi (red) and after the addition of 10 µM DMPC (blue). The activity was monitored at pH 7.33 in 50 mM HEPES and 0.1 M ionic strength ($NaNO_3$).

This experiment was also performed for **3-2** which yielded the same result i.e. a complex concentration of 20 µM is too dilute to observe activity as can be seen in Figure 3.18.

Since it is clear that a higher effective (i.e. locally within the supramolecular structure) concentration of **3-1** is likely required to observe activity, the formation of micelles using complex **3-1** alone was investigated. Given the structure of **3-1** it could potentially behave like a surfactant and therefore it is worth trying to form micelles at similar concentration (20 µM) as previously investigated with DMPC. This experiment would prove whether it was possible to form stable/reactive micelles in solution using only **3-1** and achieve the maximum surface concentration of the complex.

Reaction progress was monitored at 400 nm after the addition of **3-1** to a buffered solution containing HPNPP. An increase in absorbance was observed over 10 minutes which would suggest significant activity although not as reactive as **2-3**. Upon closer inspection of the reaction mixture it was apparent that the increase in absorbance was not due solely to a specific band at 400 nm that corresponds to product formation, and so this change could not be clearly assigned to the transesterification reaction. A UV-scan from 200-600 nm confirmed that the increased absorbance was actually caused by light scattering of the complex, presumably as it forms larger aggregates, since the absorbance increased over the entire

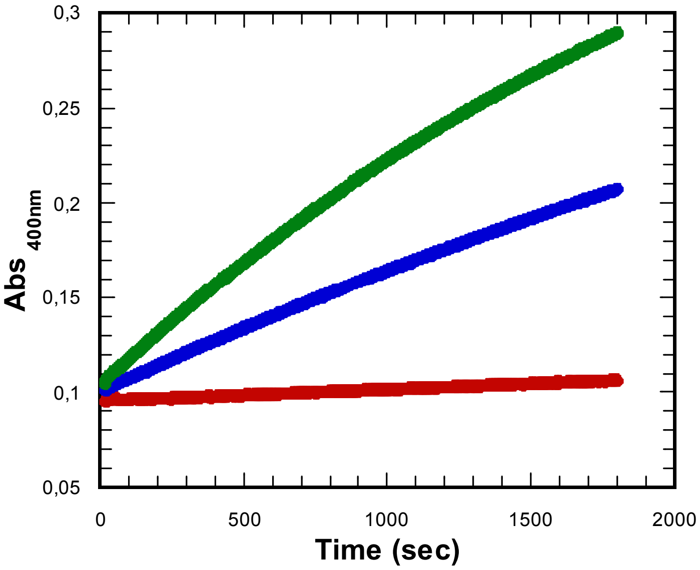

Figure 3.18. The activity of 3-2 at 20 µM (red), 200 µM (blue) and 400 µM (green) with 50 µM HPNPPi in 50 mM HEPES at pH 7.32 and 0.1 M ionic strength ($NaNO_3$).

wavelength spectrum. The same changes were observed even in the absence of substrate and so any potential reaction can only be a small fraction of the observed changes in absorbance.

A more thorough attempt to form soluble structures using only **3-1** was made were 1 mM **3-1** was added to a solution containing 50 mM buffer and sonicated, see Figure 3.19. Sonicating the solution reduced the size of the light-scattering structures but the solution was not stable and a few minutes after sonication the absorbance increased. It was concluded that the complex does not form stable structures in aqueous solutions without the aid of other surfactants at these concentrations.

Since the DMPC vesicles had a limited lifetime and with limited access to the membrane extrusion device, the procedure for the micelle/vesicle manufacture was changed to sonication using Sanyo Soniprep 150 with a titanium probe (10 µm amplitude for 2 min).

The vesicles were studied in solution using dynamic light scattering (DLS) and the structures were found to be relatively uniform in size (50 ± 3 nm). The surfactant was also changed to a simpler tetraalkyl amine, dimethyldioctadecylammonium chloride (DMDODA), see Figure 3.20.

The long alkyl tails forms a lipophilic layer that could potentially accommodate the aliphatic anchor of **3-1** and the cationic head group eliminates the risk of an inhibitory binding interaction with the Zn(II) ion of the complex.

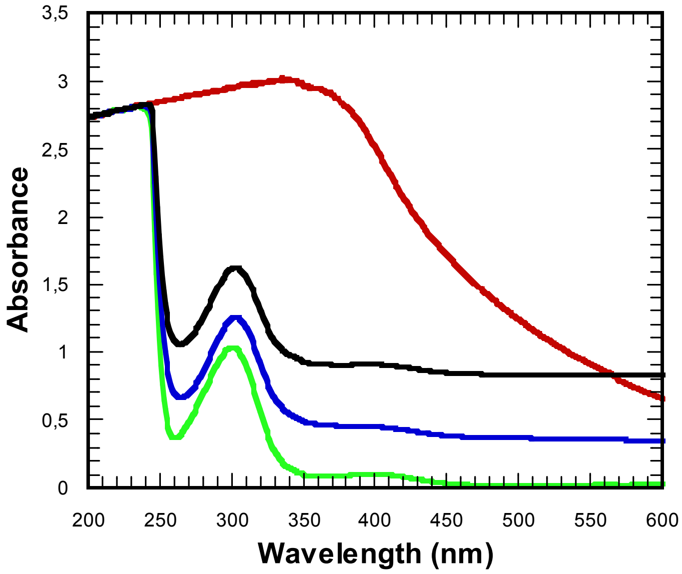

Figure 3.19. The attempted formation of stable micelles using 1 mM 3-1. The initial conditions were 50 mM HEPES buffer at pH 6.9, 0.1 M ionic strength ($NaNO_3$) and 50 µM HPNPPi (green) after which 3-1 was added (red) and sonicated (blue) but a few minutes later the absorbance was increasing (black).

The surfactant stock solution was made by dissolving solid DMDODA in water to approximately 10 mM and sonicating the mixture until a homogeneous cloudy solution was obtained.

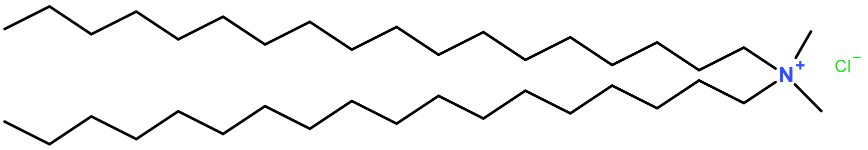

Figure 3.20. The structure of the surfactant dimethyldioctadecylammonium chloride (DMDODA).

The catalyst was added to water together with surfactant prior to sonication. The complex **3-1** (2 mM) was sonicated together with DMDODA (2 mM) for approximately 5 minutes using a titanium probe sonicator until the solution turned clear. The solution was allowed to cool down to ambient temperature and the subsequent experiments were performed using 50 mM HEPES buffer at pH 6.9 and 50 µM HPNPP with 0.1 M ionic strength ($NaNO_3$).

Under these conditions, there was obvious precipitation in the reaction solution. This seems to indicate that the complex was not stabilised enough by the DMDODA to remain in solution. Additional experiments revealed that the source of the precipitation was mainly DMDODA that interacts with the salt ($NaNO_3$). The influence of the salt on precipitation differs from the effects seen in Chapter 2 due to the obvious role of DMDODA in this case.

The same result was obtained with NaCl and the decision was made to omit the salt altogether from subsequent experiments since the surfactant itself was found to precipitate.

This method of formation of the vesicles with the complex **3-1** leads to a homogeneity between the inner and outer leaflet of the structure and it is therefore not necessary to account for the flip flop mechanism (see Figure 3.15). If this assumption is correct the effective concentration of **3-1** exposed to the bulk solution on the exterior of the vesicle would be half the total concentration of **3-1**. The experiments presented here have not been corrected for the effective concentration and simply use the bulk complex concentration.

Initial experiments with **3-1** were performed at pH 6.9 and a complex concentration of 1 mM with 100 μM HPNPP and no salt to control the ionic strength, see Figure 3.21. The reaction was confirmed by UV-vis analysis that showed an increasing absorbance band at 400 nm that was consistent with the release of 4-nitrophenolate.

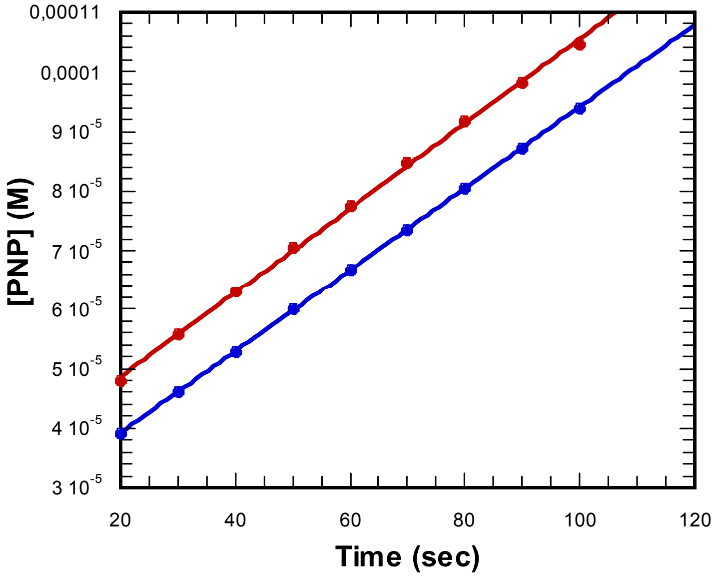

Figure 3.21. The initial rate of reaction of 1 mM HPNPP in the presence 1 mM 3-1 in 1 mM DMDODA at pH 6.9 in 50 mM HEPES.

Observed rate constants were determined from the initial rate of the reaction and the apparent second-order rate constant from this initial test was estimated to be 0.7 M^{-1} s^{-1} at pH 6.9, see Table 3.1.

Further experiments with the HPNPP were performed using complex **3-1** and complex**3-2** as a control in a solution with DMDODA at various pH. The less lipophilic equivalent **3-2** provides the control for the activity of the system in absence of the anticipated

Experiment	Initial rate (× 10^{-7}) (M s^{-1})	k_2 (M^{-1} s^{-1})	log k_2
1	6.86 (± 0.02)	0.69 (± 0.002)	-0.16
2	7.10 (± 0.07)	0.71 (± 0.007)	-0.15

Table 3.1. The apparent second-order rate constants for the transesterification of HPNPP catalysed by complex 3-1 performed in duplicate at in 50 mM HEPES at pH 6.9. The second-order rate constants were calculated from the initial rate divided by the concentration of the complex and substrate.

localisation of the complex at the aggregate interface.The experiments were performed using 1 mM complex in 1 mM DMDODA and 100 µM HPNPP at pH 7 – 10 with no salt to adjust ionic strength. The solution stability of the aggregates seemed to deteriorate with increasing pH and this was particularly evident for complex **3-1** above pH 8. It is not clear why this is the case but it does indicate a difference in behavior compared to **3-2**. A single ionisation model was fitted to the data obtained for **3-2** plotted versus pH, see Figure 3.22, using **Equation 3.1**, see Chapter 8.3. Although the complex **3-2** has two ionisable species (metal bound water molecules) only one deprotonation can be assigned with certainty since the second deprotonation occurs at a pH outside the monitored interval.

$$k_2 = k_2^{max} \times \frac{K_a}{K_a + [H^+]} \qquad \text{(Equation 3.1)}$$

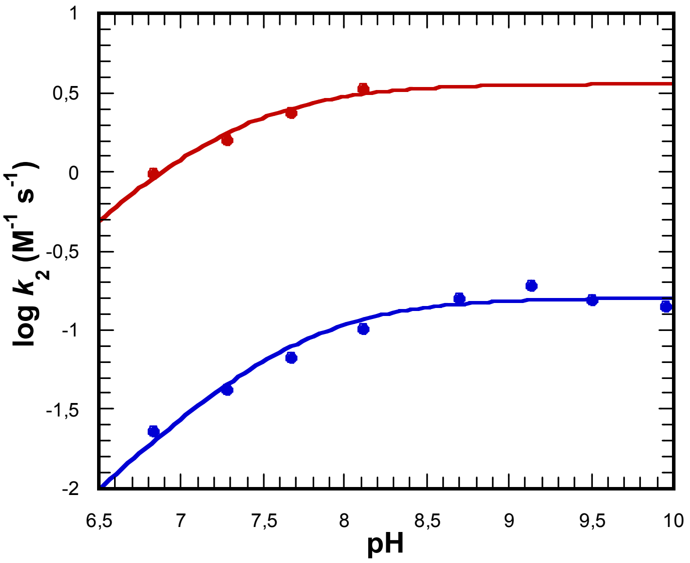

Figure 3.22. The apparent second-order rate constant at varying pH for the transesterification of HPNPP (1×10^{-4} M) using 3-1 (red) and 3-2 (blue) both at 1×10^{-3} M with DMDODA 1×10^{-3} M in HEPES/CHES 50×10^{-3} M (no additional salt for ionic strength was used).

The kinetic complex pK_a and k_2^{max} were determined for **3-1** and **3-2**. The rate constant for the transesterification of HPNPP by **3-1** measured at pH 8.7 was excluded from the fit since the stability of the complex in solution deteriorates at high pH. The first pK_a (pK_{a1}) for complex **3-1** (7.30 ± 0.11) and **3-2** (7.68 ± 0.07) are relatively similar although the limiting second-order rate constants differ by more than one order of magnitude, 0.16 (± 0.01) M^{-1} s^{-1} and 3.59 (± 0.43) M^{-1} s^{-1}, respectively. The first deprotonation (pK_{a1}) leads to the active complex being formed and the second deprotonation (pK_{a2}), which was not accurately determined here, leads to reduced activity due to formation of the inactive complex, see Scheme 3.2.

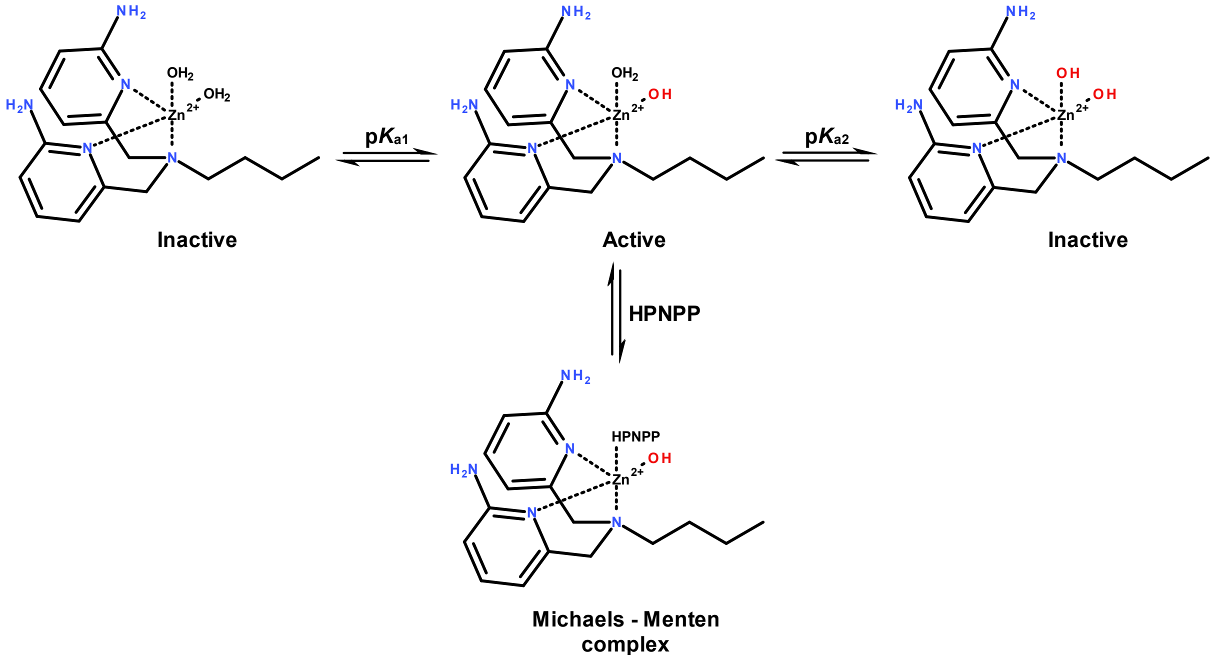

Scheme 3.2. The proposed protonation states for the complex 3-2.

The obtained rate constant and kinetic pK_a-value were in good agreement with literature data for the complex **3-3** which differs from **3-2** by one methyl group, see Figure 3.23.

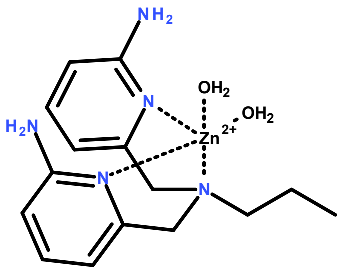

3-3

Figure 3.23. The complex 3-3 that has been studied by Mancin *et al.*[14]

Complex **3-3** had been analysed with HPNPP (and BNPP) from which the kinetic pK_a were obtained. The complex has also been potentiometrically titrated and the results are presented in Table 3.2.

Complex	Kinetic pK_{a1}	Kinetic pK_{a2}	Potentiometric pK_{a1}	Potentiometric pK_{a2}	k_2^{max} ($M^{-1}s^{-1}$)
3-2	7.68 (± 0.07)	-	-	-	0.16 (± 0.01)
3-3	7.7	10.7	8.01	10.18	0.28

Table 3.2. The rate constants with HPNPP pK_a for 3-2 compared to 3-3 from literature.[14]

Given the remarkable effects of CO_2 on **2-3,** the effects on **3-2** were explored. The treatment of **3-2** with CO_2 led to a significant reduction in observed activity although the effect was not as dramatic as for **2-3**, see Figure 3.24.

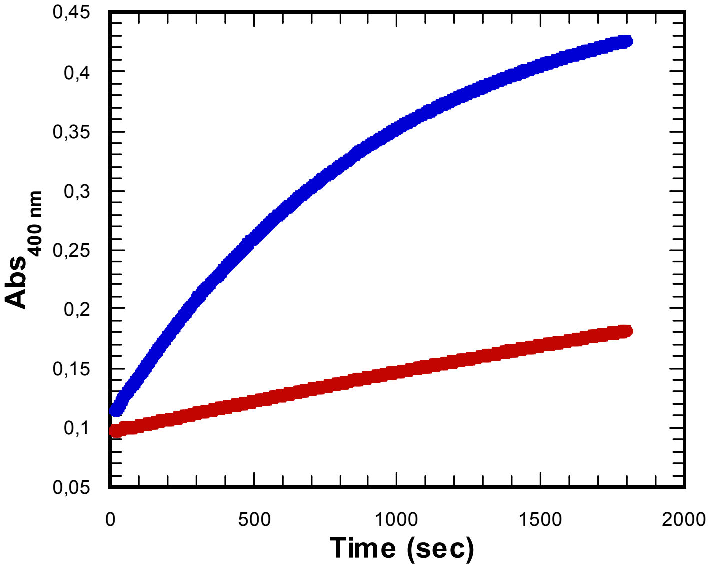

Figure 3.24. The effects of CO_2 on the reactivity of 1 mM 3-2 with 50 µM HPNPPi in 50 mM HEPES at pH 7.4 and 0.1 M ionic strength ($NaNO_3$). The unaltered reaction (blue) and the CO_2 treated (red).

A more detailed investigation of the inhibition by carbonate is seen in Figure 3.25 for the assumed competitive inhibition[51] by Na_2CO_3. **Equation 3.2** yielded a good fit to the plot where k equals the observed rate constant, k_0 the observed rate constant in the absence of inhibitor, $[I]$ the concentration of inhibitor and K_i the inhibition constant.

$$\frac{k}{k_0} = \frac{K_i}{K_i+[I]} \qquad \text{(Equation 3.2)}$$

The K_i is estimated to be approximately 0.79 (± 0.04) × 10^{-3} mM, see Figure 3.25, which is relatively close to the estimated K_i of 1.20 mM for complex **2-1**. The only available experimental data for inhibition obtained for **2-3** to compare with these data are for dimethylphosphate (DMP) which was estimated to be 0.60 mM at pH 6.9 (0.37 mM in previous report[51]). Since there is no experimental data for Na_2CO_3 inhibition for the complex **2-3** the comparison can only be qualitative.

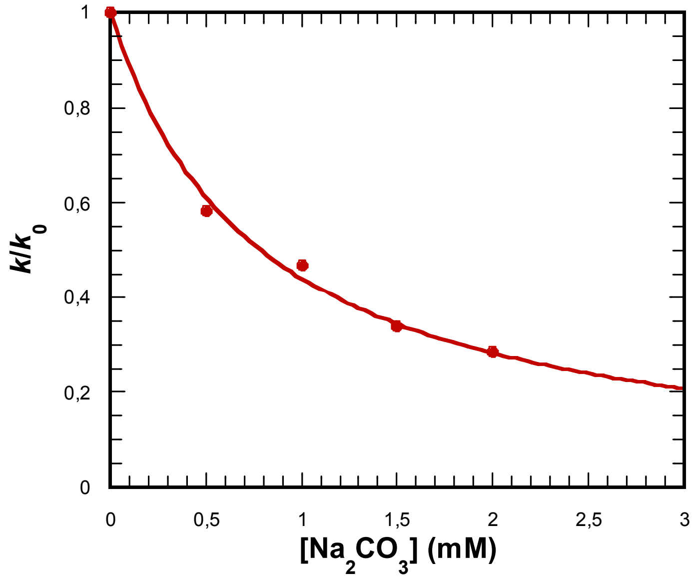

Figure 3.25. Inhibition by Na_2CO_3 of the action of 1 mM 3-2 and on 50 µM HPNPPi in 50 mM HEPES at pH 7.4 in 0.1 M ionic strength ($NaNO_3$).

It is clear that complex **3-2** is not as strongly inhibited by the carbonate as the dinuclear complexes. This is not surprising given the bridging bidentate fashion with which the carbonate is likely to bind to the dinuclear complexes, see Figure 3.26.

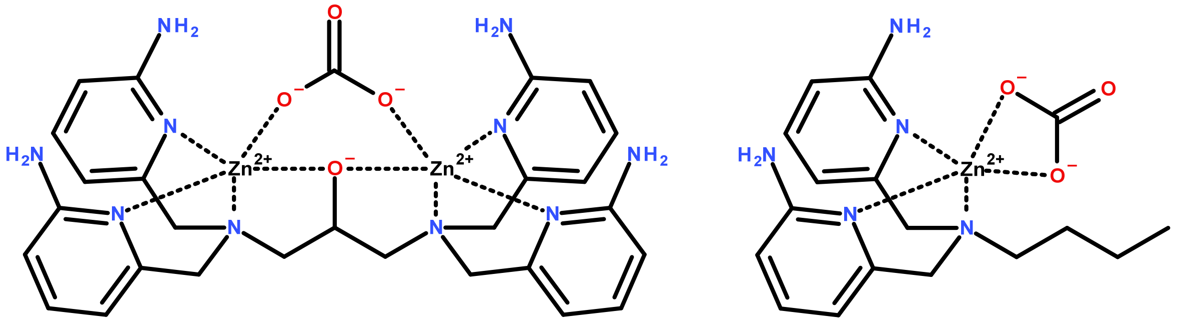

Figure 3.26. The proposed binding mode of carbonate to the dinuclear complex 2-3 and the mononuclear complex 3-2.

The fact that the K_i for the inhibition by DMP of **2-3** is so low would indicate the K_i of the dianionic carbonate would be significantly lower.

In keeping with the previous comparison between the mono- and dinuclear complexes, **2-3** and **3-2**, a mononuclear equivalent of **2-4** was synthesised. Ligand **L3-4** was synthesised using the same procedure as for **3-2** but using the precursor *tert*-butyl N-[6-(iodomethyl)-2-pyridyl]-N-methyl-carbamate (**X$_4$**), see Scheme 3.3.

The highly reactive complex **2-4** suffered significant drawbacks in terms of pH instability and therefore could not be fully investigated. The mononuclear analogue could possibly display a more stable behavior over a wider pH range and indicate the true role of the methylamino group in the 2-pyridyl position.

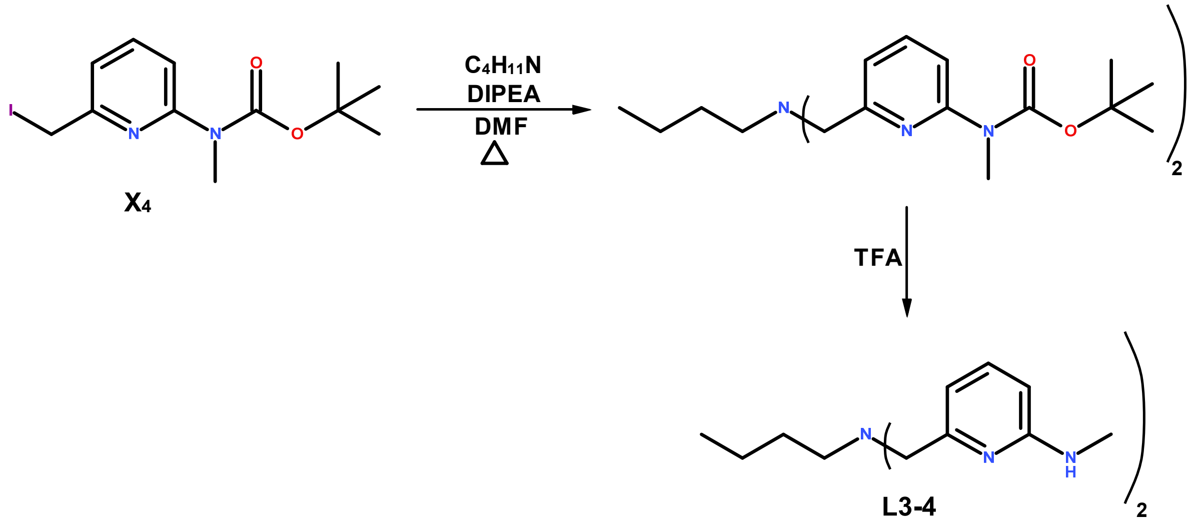

Scheme 3.3. The synthesis of ligand L3-4 from the precursor X$_4$. The yields were 51 % and 90 %, respectively.

Unfortunately **L3-4** was not analysed kinetically partly due to problems related to solubility and precipitation under the experimental conditions. The high activity observed for **2-4** could be due to the methylated amino functionality in the 2-pyridine position forming a less polar environment around the catalysts which has been reported to increase reaction rates.[69,122]

For many reactions performed in MeOH the observed rate constants have been reported to increase compared to water.[69,132] The effects on the reaction rate that have been observed in the membrane interface compared to free solution reactions can indicate the level of MeOH “likeness” at the interface.

The improved rates for the membrane bound complex could be due to either the reduced polarity at the membrane-solution interface or due to the formation of a dinuclear-like structure through complex-complex association. Saturation experiments in the presence of surfactant would indicate if the observed rate increase is due to tighter binding or higher reactivity of the bound substrate. Varying the ratio between surfactant and complex would reveal whether it is the environment or the association of the complexes that causes the observed effect.

It is not entirely clear whether it is the formation of dinuclear-like structures or medium effects that causes the observed rate increase although it has previously been suggested that the main contribution is due to the latter for nanoparticle based systems. Additionally, the effect of the less polar medium on reactivity appears to be greater for k_{cat} than K_{M} which does not change as much.[68]

It has been reported by Scrimin *et al.* that substrates that decrease the polarity of the nanoparticle monolayer affect the reaction pathway.[133] This suggests that embedding the catalytic head group further down in the lipophilic membrane might affect the reactivity since the environment becomes less polar than at the interface.

3.5 - Conclusion

The observed difference in rate of phosphate diester hydrolysis for the vesicle based system **3-1** compared to the solution based system **3-2** was determined to be more than 1 order of magnitude in favor of the former at pH 6.9.

Without further experiments detailing the effect of changing the local environment around the complex versus the association of complexes in supramolecular structures it is difficult to confidently assign the reactivity to a certain property or behavior of the complex.

It is clear that there is a significant change upon addition of the complex to the membrane structure and it would therefore be interesting to study the behavior of the preformed dinuclear complex **2-3** in this environment since that would reveal the contribution of the low polarity since the dimerisation has already been achieved.

3.6 - Future work

Given the observed effect of the vesicle structure presented herein and the reported gold nanoparticle systems in literature, the use of reactive membrane-like environments appears to be a viable alternative to reactions in solution. There has been a lot of research related to reactive nanosystems which implies its potential.[134]

The introduction of a dinuclear complex **2-3** into a membrane would indicate the effect of the environment compared to **3-1**. In order to efficiently embed the dinuclear complex **2-3** it would be necessary to modify its structure to include a membrane embedding structure, see Figure 3.27.

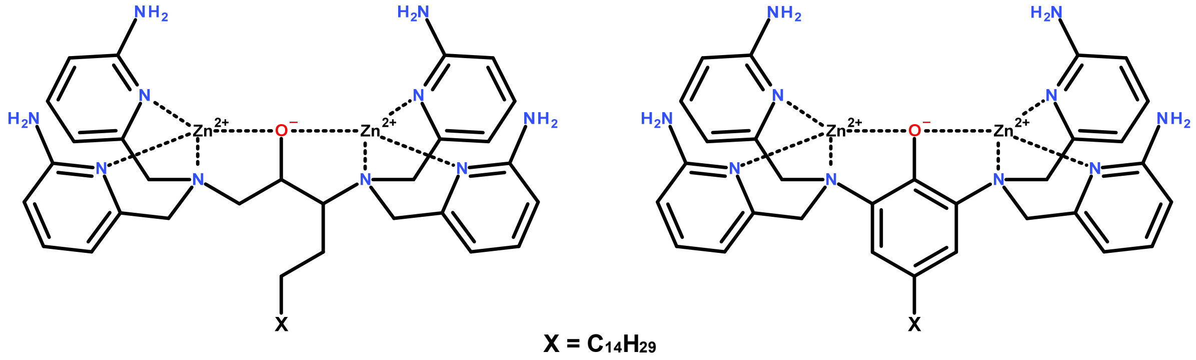

Figure 3.27. The suggested structure of potential membrane embedding dinuclear complexes.

Another interesting system that could be used to study the membrane-like structure that share similarities with both the surfactant based vesicles and the nanoparticles is the use of core-polymerisable micelles, see Figure 3.28. These systems could be designed to form micelles in solution of a certain size and composition followed by polymerisation to stabilise the structure formed. This structure would also make adjustments of embedding depth possible by copolymerisation with polymerisable lipophilic molecules of various lengths.

It is also possible to pre-associate the complexes in the desired catalytic arrangement using substrate analogues. The best explanation to date for the catalytic activity of the membrane-based complexes is the reduced polarity of the environment although the exact interactions are not well understood. If the medium effect is the main contributor to the reactivity it is possible to imagine that the design of a solvent excluding environment could lead to a highly reactive system.

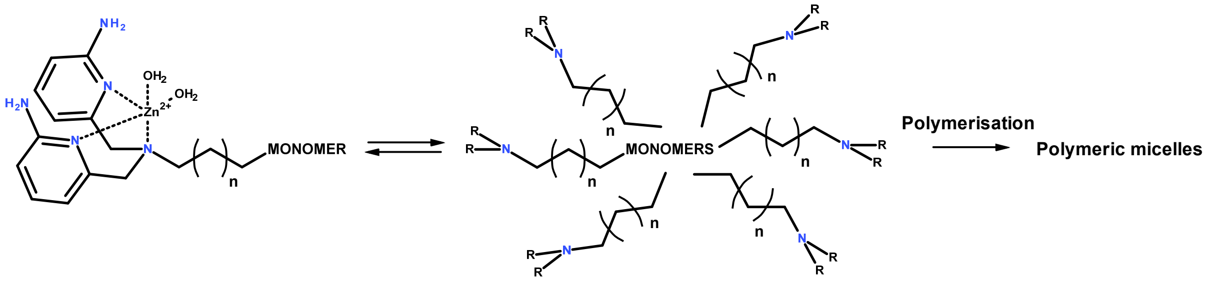

Figure 3.28. The proposed structural analogue of membranes using polymerisable complexes.

The use of templating in polymerisation could also be applied to more complex structures where the catalytic structure internalised in a less hydrophilic environment than the membrane-solvent interface. Although these structures would be more rigid than in the membrane structure the use of substrate templating should provide the complexes in the most appropriate configuration.

An example of this can be found in the work by Zhao *et al.* where the lipophilic environment is suggested to accelerate the nucleophilic reactions by several orders of magnitude. [135] They used simple surfactant place holders in the micelles that did not contain a polymerisable functionality. The non-covalently bound surfactants can diffuse out of the structure post polymerisation which leaves channels into the lipophilic core that can accommodate the substrates.

A similar structure is not farfetched from a synthetic view point in the case of phosphate diester hydrolytic complexes since there are a multitude of commercially available polymerisable units that could be incorporated in the structure of a metal complex. These approaches provide a variety of possible environments that could be used to explore the effects of a low polarity environment.

Chapter 4 - Peptide based complexes

4.1 - Introduction

The use of peptidic scaffolds for catalytic purposes is the quintessential design of enzymes in nature and it is therefore logical to extend this concept to artificial catalysts that aim to mimic enzymatic activity. This research field began with the studies of the structures of natural enzymes but has boldly evolved into *de novo* design of artificial peptidic scaffolds.[108,136–138]

The disadvantages of enzymes and large proteins in terms of the bulkiness of their structure and their inherent structural vulnerabilities (temperature, pH, degradation etc.) can be at least partially circumvented if smaller peptidic analogues are used.

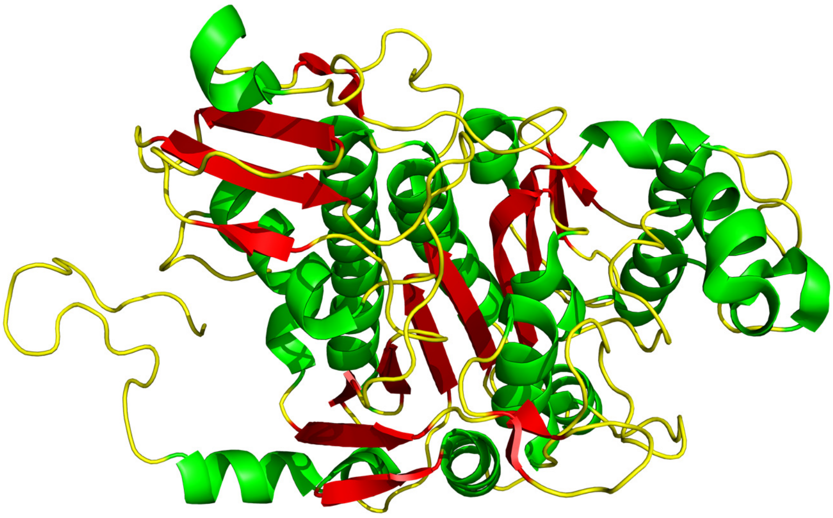

Figure 4.1. The structure (monomer) of the E-coli alkaline phosphatase enzyme. The structure contains α-helices (green), β-sheets (red) and random coils (yellow) (PDB code: 3TG0).[45]

The central structural features of the active sites of enzymes can be simulated using the structural units that are available in peptide chemistry (α-helix, β-sheet or random coil), see Figure 4.1. These structures provide a scaffold that is better defined than membranes but still allows for flexibility. The final structure depends on the linear peptide sequence which can be altered to include residues with varying structural propensity.

It is worth noting that linear peptide sequences have been used to promote internuclear association, see Figure 4.2. These compounds use the linear distance between the residues in the structure of the peptide.[130,139] The interactions cannot be said to employ supramolecular non-covalent interactions but rather uses spatially controlled intramolecular association due to the intrinsic spacing in the sequence.

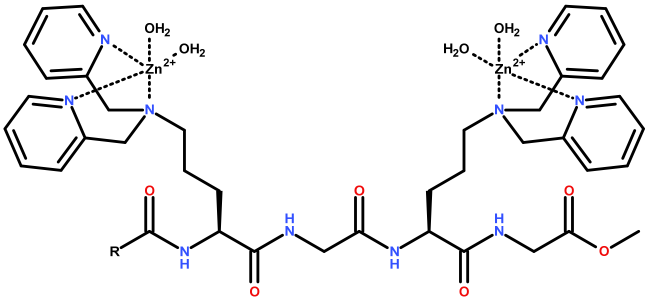

Figure 4.2. The polyglycine is used as a linear spacer between the Zn(II) nuclei.

The role of the well defined protein structure is to arrange the relevant residues that are involved in catalysis to interact in the enzyme's active site. This can be translated into structural requirements for artificial peptide-based scaffolds. It is clear that the random coil structure is of little help in organising a well defined structure but the α-helix and β-sheet are viable candidates.

The β-sheet structure is well known for its ability to form stable structures, in some cases with disastrous consequences like for example Amyloid beta fibrils in Alzheimer's disease.[140,141] In a less sombre context the β-sheets form extensive interactions in enzymes and provide essential active site residues in the desired arrangement, see Figure 4.3. The proximity of the β-sheet is the desired feature for simple artificial catalyst[34,142] since this could potentially allow for proximal incorporation of mononuclear complexes.

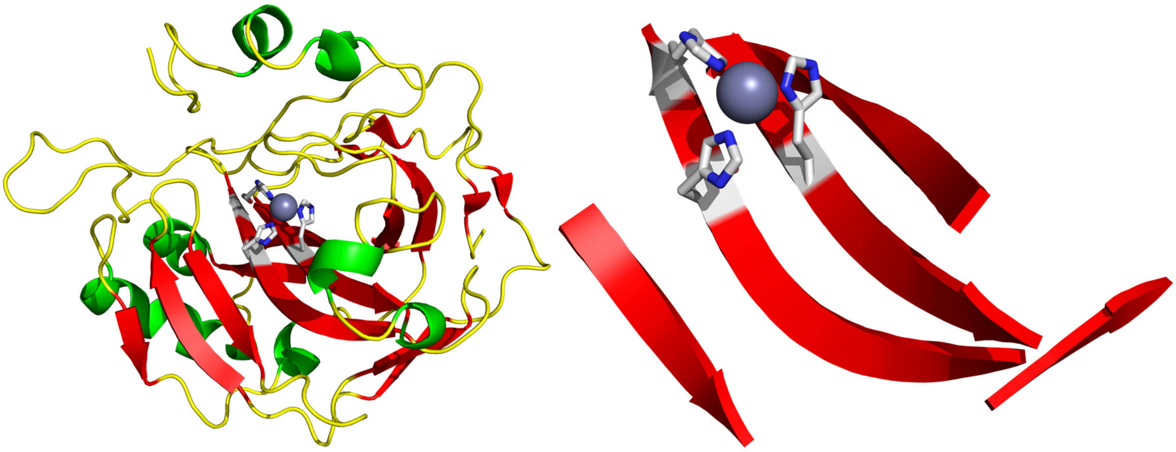

Figure 4.3. The structure of carbonic anhydrase II (left) with the three active site histidine residues, His_{94}, His_{96} and His_{119}, of the β-sheet (right) visualised (PDB code: 2CBA).[45]

The β-sheet structure has been utilised by Yamada *et al.* in a cyclic peptide, see Figure 4.4, which incorporates two mononuclear Zn(II) complexes for HPNPP transesterification.

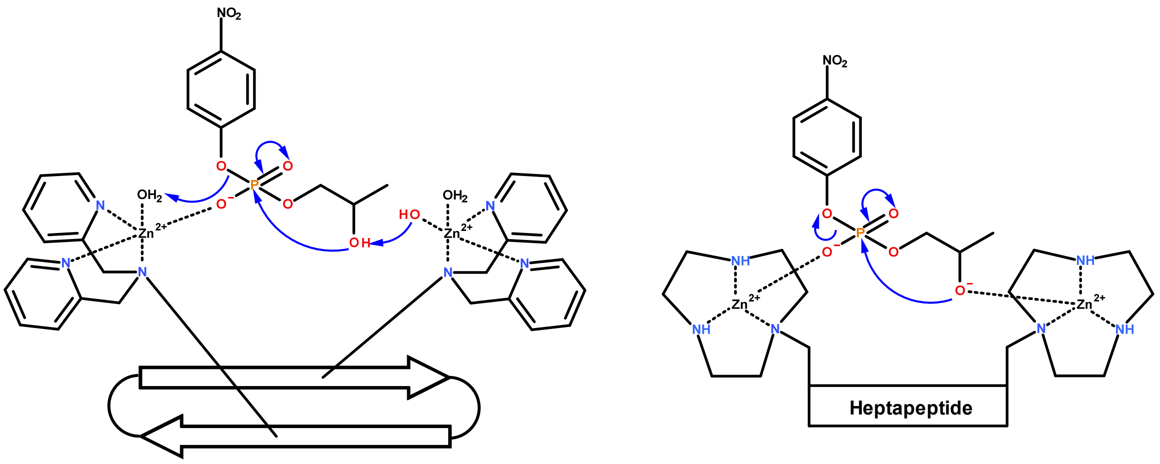

Figure 4.4. The two kinetically equivalent mechanisms that have been proposed for the transesterification of HPNPP using the cyclic β-sheet structure (left)[143] and the helical heptapeptide (right)[144].

The use of helical peptide structures as general scaffolds for catalytic units has been reported in the literature.[145,146] The peptidic structures have been reported to catalyse the transesterification of HPNPP using Zn(II) in short heptapeptides that form relatively stable α-helix structures[144,147] supporting the design concept. The heptapeptide complex, see Figure 4.4, caused a 5-fold rate acceleration compared to the mononuclear complex. HPNPP is proposed to coordinate to one metal ion through the non-bridging oxygen of the phosphate while the other metal nucleus activates the nucleophile though direct coordination. The mechanism differs from the proposed double-Lewis activation of the non-bridging oxygens for the more closely associated nuclei of dinuclear complexes.[51]

Helix-loop-helix structures have been extensively reviewed and studied by Baltzer *et al.* as scaffold for catalytically active residues[145,148–157] which in most cases include histidines. Other examples include the use of metal complexes in helix-loop-helix structures for phosphate binding[146] and hydrolysis[158]. The mechanism for the transesterification of HPNPP in the helix-loop-helix complex has been proposed to be similar to the mechanism in Figure 4.4.

Another interesting example has been reported by Copeland *et al.* where a helical peptide containing a His_2 coordinated Zn(II) or a β-sheet structure containing a $AspGlu_2$ coordinated Zn(II) was covalently linked to a DNA intercalator.[159] The incorporation of a

DNA binding intercalator and a catalytic unit in one supramolecular structure is arguably a more accurate representation of the two processes that occur in enzymes (recognition and catalysis). These structures have been proven to cleave both supercoiled plasmid and linear DNA and are enticing given their nuclease-like two-pronged approach to binding and catalysis.

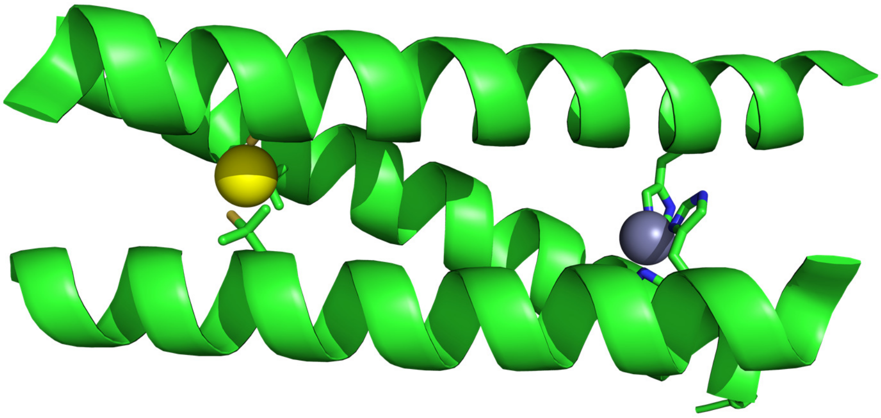

Figure 4.5. The trihelix structure studied by Pecoraro *et al.* for catalytic activity. The metal binding sites include Hg(II) (yellow) and Zn(II) (grey) (PDB code: 3PBJ).[45]

Pecoraro *et al.* demonstrated the potential to design an active site analogue of the enzyme carbonic anhydrase using a trimeric coiled-coil structure containing His_3 coordinated Zn(II). Additionally, the trimer contained a thio-coordinated Hg(II) structural unit to further stabilise the interhelical interaction, see Figure 4.5.[160,161]

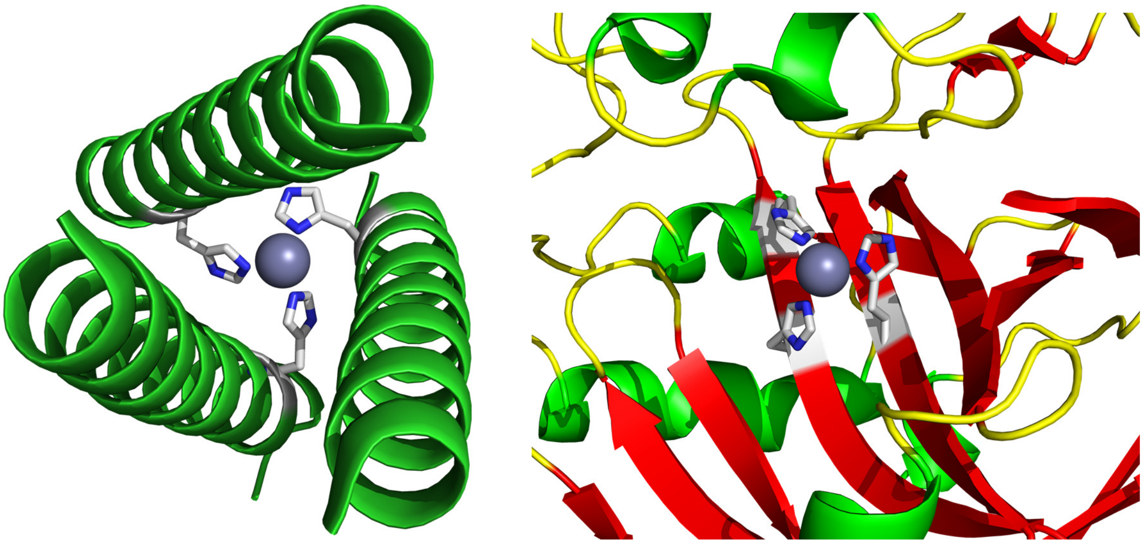

Figure 4.6. The Zn(II) coordination sites in the trihelix (left) with the Hg(II) site removed for clarity and CAII (right). In both structure the Zn(II) is coordinated to 3 histidine residues (PDB code: 3PBJ and 2CBA).[45]

The helices form a central cavity around the active site which could be modified to mimic the interactions in the secondary coordination sphere.

The catalytically active site containing Zn(II) is very similar to the coordination sphere around Zn(II) in the enzyme carbonic anhydrase II (CAII).[99] The trihelical system has the highest reactivity towards CO_2 hydration reported for any synthetic catalyst. The reported rate constant for hydration for the helical system (1.8 × 105 M^{-1} s^{-1}) is approximately 500-fold lower than for CAII (9.7 × 107 M^{-1} s^{-1}).[162] The similarities in Zn(II) coordination between the trimeric coiled-coil structure and the CAII active site is illustrated in Figure 4.6.

Given the apparent success of using helices and coiled-coil structures in the literature, as presented above, it would conceivably be possible to employ the well-defined structure in our investigation.

Coiled-coils have been extensively studied in the past and are used in several *in vivo* processes.[163,164] One particular coiled-coil structure that has got the desirable properties of having a well defined structure and the ability to bind the phosphate diester biopolymer DNA is the basic leucine zipper domain which is sometimes referred to as GCN4-bZIP, see Figure 4.7.

GCN4-p1 is a 33 amino acid sequence, Ac-*RMKQ LEDKVEE LLSKNYH LENEVAR LKKLVGE R*, found in the yeast transcriptional activator GCN4-bZIP and consists of the leucine zipper sequence. The peptide forms a parallel two-stranded coiled-coil structure that has been studied extensively for its folding properties due to its relative simplicity.

The 33 amino acid sequence is the C-terminal segment of the GCN4-bZIP protein, see Figure 4.7, where the N-terminal is rich in basic residues that interact with the cationic DNA. The helices part at the N-terminal of the GCN4-p1 where the peptide helices become rich in basic residues and bind on either side of the DNA helix.[165]

There have been numerous studies conducted on the stability of the GCN4-p1 employing N- and C-terminal truncation of the sequence. The folding properties of the GCN4-p1 and its truncated equivalents have been extensively studied and will be discussed in subsequent sections.

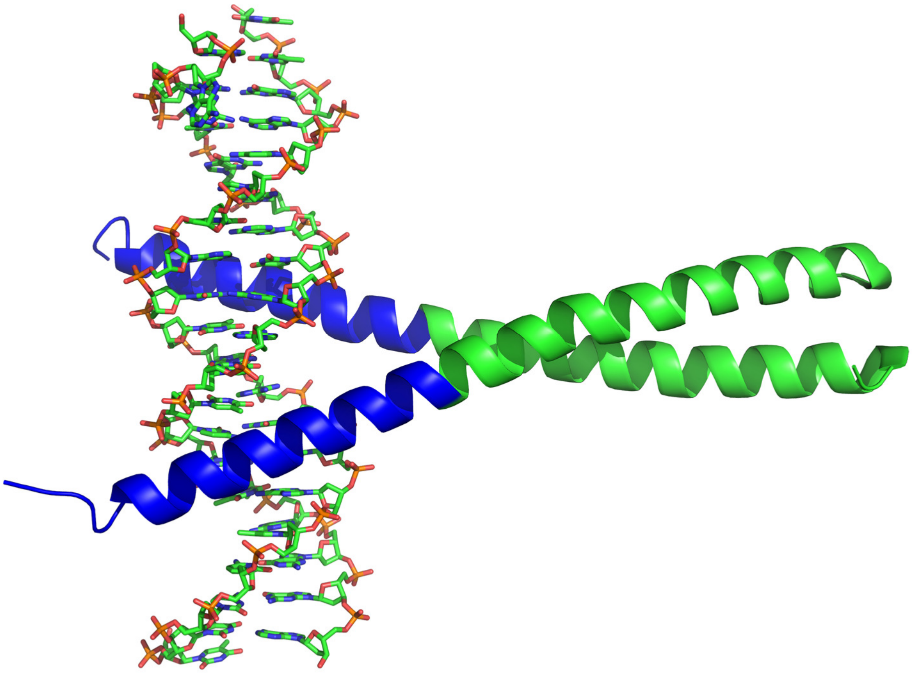

Figure 4.7 The structure of GCN4-bZIP bound to a DNA double helix. The blue segment of the coiled-coil structure represents the basic residue rich sequence responsible for peptide-DNA interaction and the green segment represents the GCN4-p1 leucine zipper. The structure was obtained from RCSB Protein Data Bank (PDB code: 1YSA).[45]

4.1.1 - Solid Phase Peptide Synthesis (SPPS)

The first paper on solid phase peptide synthesis was published in 1963 by R. B. Merrifield where he described the synthesis of a tetrapeptide covalently linked to a polymer support.[166] The principles of SPPS are ingenious yet simple. The idea is to perform reactions with one reactant attached to an insoluble macroscopic solid support making purification a simple matter. The solid support is a cross-linked polymer with linkers to which an amino acid can be attached. The first amino acid forms an ester or amide bond to the solid support and subsequent amino acids attach to the first amino acid by formation of an amide bond in a condensation reaction. The reaction is usually carried out in a container with a filter on one end which is impermeable for the macroscopic polymer particles but allows the reaction solution through. This is a very simple way to separate the product from the unreacted starting material and reaction byproducts. The synthetic procedure is of such simplicity and so repetitive, see Chapter 8.9.2, that an automated synthesis machine is usually employed for this purpose. The chemical principles of SPPS are highly dependent on the protecting groups on the amino acids. There are many different types of protecting groups that the peptide chemist can employ but the general idea is to have so called temporary and permanent protecting groups, see Figure 4.8. The temporary protecting groups are as the name implies designed to provide protection only for a limited period of time and are located on the growing end of the peptide. The permanent protecting groups on the other hand are attached to the amino acid side chains and are designed to resist the reaction condition during chain elongation.

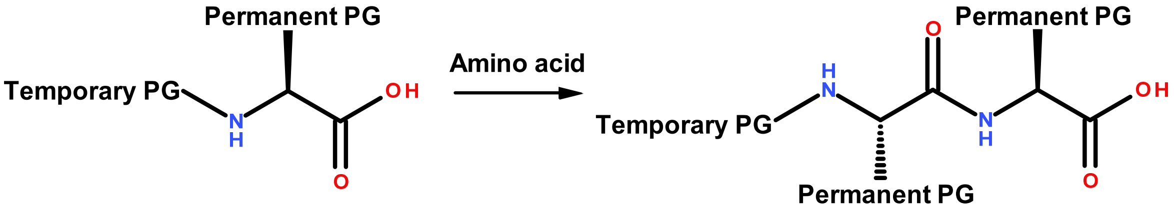

Figure 4.8. The schematic representation of the protecting group (PG) strategy used for Fmoc solid phase peptide synthesis.

These permanent protecting groups are usually removed by the same conditions that cleave the peptide of the solid support. The actual cleaving of the peptide from the resin is usually complete within minutes or seconds, depending on the sensitivity of the linker but the reaction is usually allowed to proceed for up to an hour or two. This is because the permanent protecting groups that are supposed to be cleaved off under these conditions require longer exposure.

It is worth noting that the most prevalent SPPS methodology today uses fluorenylmethyloxycarbonyl (Fmoc)[167–169] as the temporary protecting group, see Figure 4.9. Fmoc is removed in the presence of a non-sterically hindered base (usually 20 % piperidine in DMF) which allows the use of acid-labile protecting groups elsewhere on the peptide (including the linker to the solid support). This is a much safer synthesis protocol compared to the original synthesis proposed by Merrifield that utilised hydrofluoric acid.

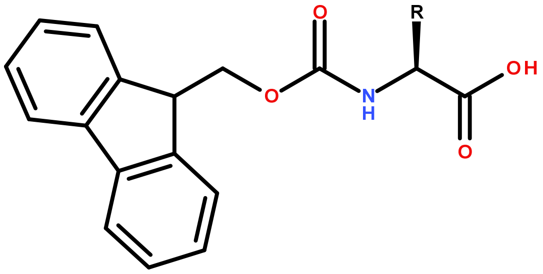

Figure 4.9. The generic structure of Fmoc amino acids (R = side chain functionality).

The couplings of amino acids in the SPPS require the use of activating agents. The coupling reagents promote the formation of the peptide bond by forming an activated ester, see Chapter 8.9.1, with the carboxyl moiety. The coupling reagents that have been used in this synthesis are HBTU and HATU, represented as their guanidinium salts[170] with hexafluorophosphate counterions in Figure 4.10.

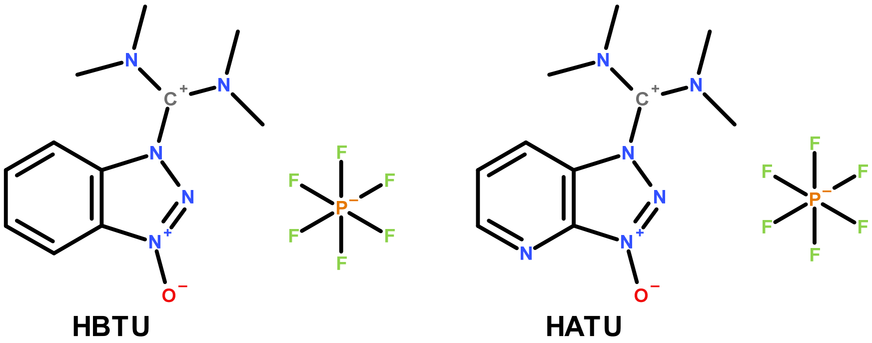

Figure 4.10. The coupling reagents used in the amide bond formation.

Additional factors affecting the synthetic outcome of the SPPS are solvent, linker functionality and polymeric support. The standard solvent used for most SPPS procedures is dimethylformamide (DMF) unless solubility limitations prompt the use of a different solvent.

The linkers that allow the amino acid to attach to the otherwise inert polymer can have a wide range of functions and degree of lability toward acids/bases. The linker functionality that has been used herein is the 2-chlorotrityl chloride linker, see Figure 4.11, which is arguable the most popular linker for SPPS. Cleavage is achieved upon treatment with mildly acidic conditions and yields the free peptide acid.

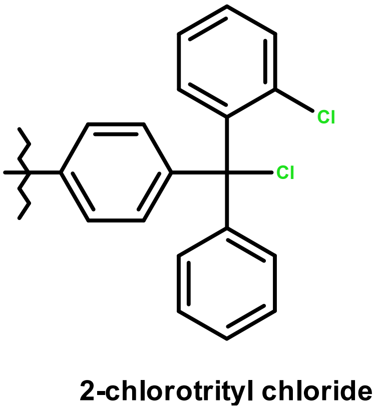

Figure 4.11. The structure of the commonly used 2-chlorotrityl linker.

The polymeric support that is most commonly used alongside the trityl linker is polystyrene. The accessibility of the internalised linker functionalities in the polymer support (only 1% of the linkers are on the surface) depends on the degree of crosslinking in the polymer (usually 1-2 %). For some purposes there might be a need to change the swelling properties of the polymer which can be achieved using commercial equivalents (polyamide or polyethylene glycols).

The alternative approach for obtaining the peptide is enzymatic expression of proteins. There has been substantial development in the area of enzymatic expression of proteins using unnatural amino acids and post-synthesis chemical modifications of proteins.[171,172] The main argument against the use of enzymatic expression and in favor of SPPS is the orthogonality of the protecting groups in standard Fmoc-chemistry. The lack of protecting groups limits the possible chemical functionalisations that can be selectively preformed. Additionally, the enzymatic expression is usually performed on smaller scales than SPPS which limits the amount of product that can be obtained.

4.1.2 - Circular dichroism spectroscopy

Circular dichroism spectroscopy (CD) is a widely used method for analysing the secondary structure of proteins.[173,174] The technique is based on the circularly polarised light interacting with molecules of chiral character that are either chiral in nature or become chiral due to asymmetric binding or other interactions in their environment. Short peptide sequences usually adapt α-helical, β-sheet or random coil structures that each produces different CD profiles. Larger proteins can contain multiple segments which can each be any of the mentioned secondary structures.

The CD spectra for proteins are therefore less characteristic of each individual structure and display weighted average spectra compared to short peptides. The protein CD usually presents a combined profile averaging the contribution from each structure. Although short peptides usually appear to adapt only one of the secondary structures it is can contain the characteristics of the other two.

Alternative methods used to study peptide or protein structures include x-ray crystallography and NMR-spectroscopy. X-ray structures very accurately represent the atomic arrangement in a protein but the disadvantage is that the crystallisation only displays one rigid conformation of the protein rather than the dynamic structure in solution. NMR analysis provides a way to analyse the protein structure in solution although the concentrations required for observing the NMR signals can cause precipitation of some proteins. Additionally, there might be a need for isotopic labeling of proteins which can be a significant investment of effort.

Circular dichorism provides an easy, fast and non-destructive method for structural characterisation of peptides and proteins.

4.2 - Aims

The aim of the peptide based approach is similar to that of the membrane based complexes, see Chapter 3. The non-covalent association between the mononuclear peptide based complexes provides a more flexible system but additionally offers better control of the internuclear distance compared to vesicles. The peptide structure provides a more flexible system than the covalently bound dinuclear complexes but a more rigid system than the vesicles.

4.3 - Results and discussion

4.3.1 - The truncated GCN4 sequence

The GCN4 leucine zipper was selected for the association of the mononuclear complexes mainly for its well-defined structure. The coiled-coil configuration provides structural rigidity compared to solution or membrane based interactions yet still allows for flexibility. The GCN4 transcriptional activator is a DNA binding protein, thus the incorporation of the complex into the peptide also provides a proof of concept for the future integration of catalyst with synthetic peptides that bind phosphate diester biomolecules. An example of a leucine zipper containing a DNA binding motif is the GCN4-bZIP transcription factor.[165]

The peptide is based on the coiled-coil sequence *VEELLSKNWH LENEVARLKK LVKQGGC*[175] which itself is a N-terminally truncated version of GCN4-p1, Ac-*RMKQ LEDKVEELLSKNYHLENEVARLKKLVGER*, that had previously been studied.[176] The truncated sequence consists of 27 amino acids forming the characteristic coiled-coil sequence found in leucine zipper peptides exemplified by GCN4-p1 in Figure 4.12.

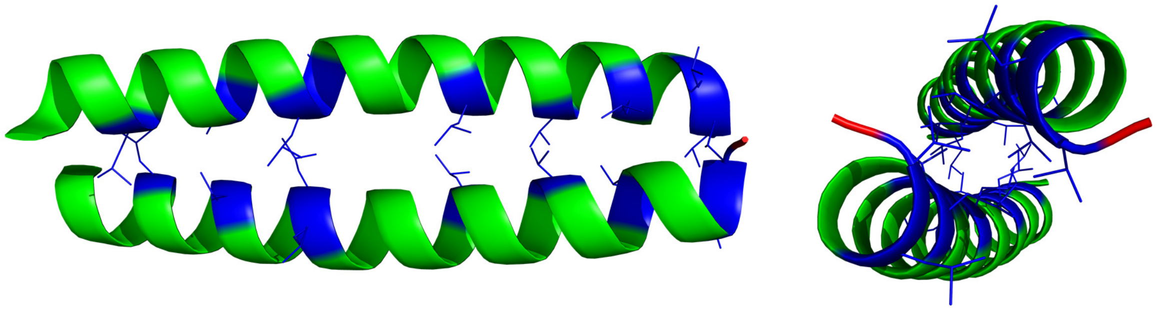

Figure 4.12 The homodimeric structure of the peptide GCN4-p1 as determined by O'Shea *et al.*[176] The characteristic coiled-coil intertwining of GCN4-p1 (left) and the view from the C-terminus along axis of the coiled coil (right) with the internal hydrophobic residues leucine/valine (blue) visible. The structure was obtained from Protein Data Bank (PDB code: 2ZTA).[45]

The selected sequence that was decided upon was a short (16 amino acids) sequence located at the C-terminus of the GCN4-p1$_{9\text{-}35}$ -c" reported by Bunagan *et al.*[175] without the C-terminal GC (the glycine-cysteine disulfide linker). This sequence is similar to native GCN4-p1 in which the first two C-terminal heptad repeats have been suggested to be the likely sources of interhelical association.[177]

It is worth noting that the selected peptide contains a so called "trigger" sequence[163,178,179] that has been found to be essential for initiation of the coiled-coil formation. The coiled-coil promoting subdomain has been found in many proteins to consist of a sequence of 13 amino acids with limited sequence variation.

The peptide GCN4-p1$_{9\text{-}35}$ -c" was truncated from the N-terminus after His$_{10}$ in order to avoid the potential interference by the amino acid as a potential allosteric coordination site for the Zinc (II). Since the truncated peptide lacks a chromophore, tyrosine was added to the N-termius in order to enable UV-detection. Tryptophan was the chromophore in GCN4-p1$_{9\text{-}35}$ -c" but tyrosine is present in the native GCN4-p1. Additionally, the sensitivity of tryptophan to chemical modification further favors the more robust tyrosine.

The fully protected peptide sequence was purchase from Severn biotech on a polystyrene solid support as Fmoc-*LENEVARLKKLVKQG*-2-Cl trt resin (i.e. Fmoc-GCN4-

p1$_{(18-33)}$-c”- 2-chlorotrityl resin) which is C-terminal end of GCN4-p1$_{9-35}$ -c” from the work by Bunagan *et al.*[175]

The resin supported peptide can be used to obtain a longer peptide sequence growing from the N-terminal to mimic the GCN4-p1$_{9-35}$ -c”, apart from the C-terminal GC. The synthesis could be either step-wise using standard Fmoc chemistry or a fragment condensation with the truncated N-terminal sequence.

In order to confirm the potential of the coiled-coil approach to support association of mononuclear complexes the distances between the Zn(II) nuclei in dinuclear complexes of known activity needs to be determined. The concept of introducing mononuclear complexes into molecular peptidic scaffolds is highly dependent on the distances in the final structures. If the distance between the helices is too large the mononuclear complexes will not be able to form dinuclear structures. The structures will therefore not be expected to provide double Lewis activation to the substrate and the observed reactivity will likely be that of the mononuclear unit.

The most reactive Zn(II) complex towards HPNPP transesterification to date in literature is the dinuclear complex **2-3** studied in Chapter 2. The crystal structure published by Williams *et al.*[51] provides a good starting point from which to estimate the internuclear distances, see Figure 4.13. The distance between the Zn(II) nuclei can be estimated to be 3.7 Å which is too short to allow for interactions between the coiled-coil helices since the interhelical distance is estimated to be approximately 6 Å.

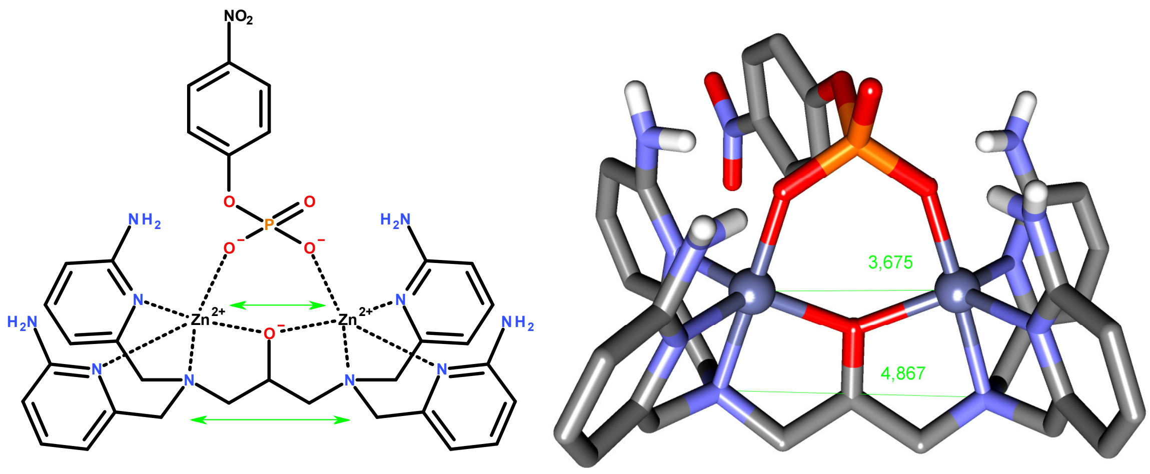

Figure 4.13. The graphical representation of the x-ray structure of complex 2-3 coordinated to 4-nitrophenyl phosphate (PNPP).[51] The calculated internuclear distances for Zn$_1$-Zn$_2$ (≈ 3.7 Å) and the distance between the tertiary amines of the backbone (≈ 4.9 Å) are highlighted.[45]

The interhelical distance was estimated using the crystal structure for the native coiled-coil peptide (PDB code: 1YSA), see Figure 4.25. The distance between the tertiary nitrogens of the ligand is slightly larger (4.9 Å) but still falls short of bridging the interhelical gap.

These measurements of the complex **2-3** are not true representations of the length of the mononuclear analogue. The actual distances in these complexes needs to include the length of the flexible linker, see Figure 4.14, which is estimated to be 6.3 Å using molecular modelling of the three dimensional structure. Combining the distances relevant to these structures gives a total reach of two mononuclear complexes of around 12 Å in addition the distance between the central nitrogen of each ligand (4.9 Å). This indicates that the interhelical gap can be bridged with relative ease given the flexibility of the ligands.

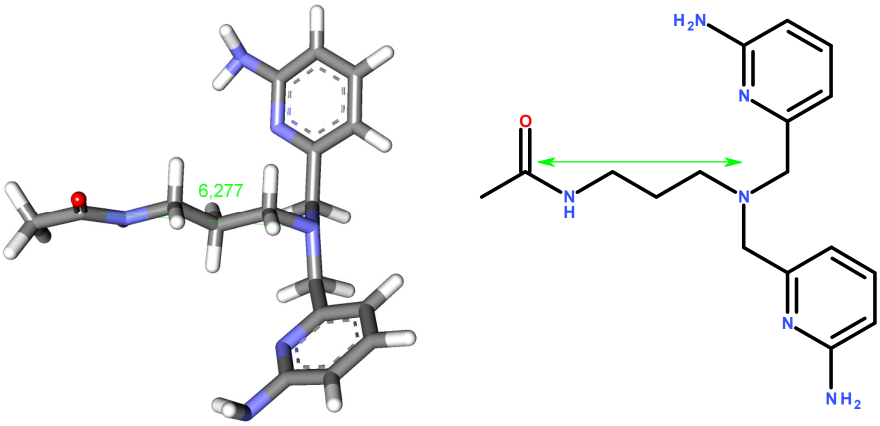

Figure 4.14. The structure of the acetylated control ligand L4-2 for the C-terminal peptide ligand L4-1 is presented for illustration (not from crystal structure) and the geometry was optimised using the MMFF94 computational force field with 5 × 10^4 iterations.[180] The distance between the carbon of the amide functionality (representing the peptide backbone) and the tertiary amine (representing the central nitrogen in the mononuclear catalyst) is approximately 6.3 Å.[181]

4.3.2 - The C-terminal functionalisation

The peptide ligand was synthesised using the *tert*-butyl N-[6-(iodomethyl)-2-pyridyl]carbamate precursor ($\mathbf{X_3}$) from Chapter 2. The propyl linker was synthesised from 1,3-dibromopropane and attached to the Boc-protected amino pyridyl through S$_N$2 displacement of the iodine by the amine. The resulting intermediates **L4-1'** and **L4-1''**, see Scheme 4.1, will be used in subsequent synthetic procedures.

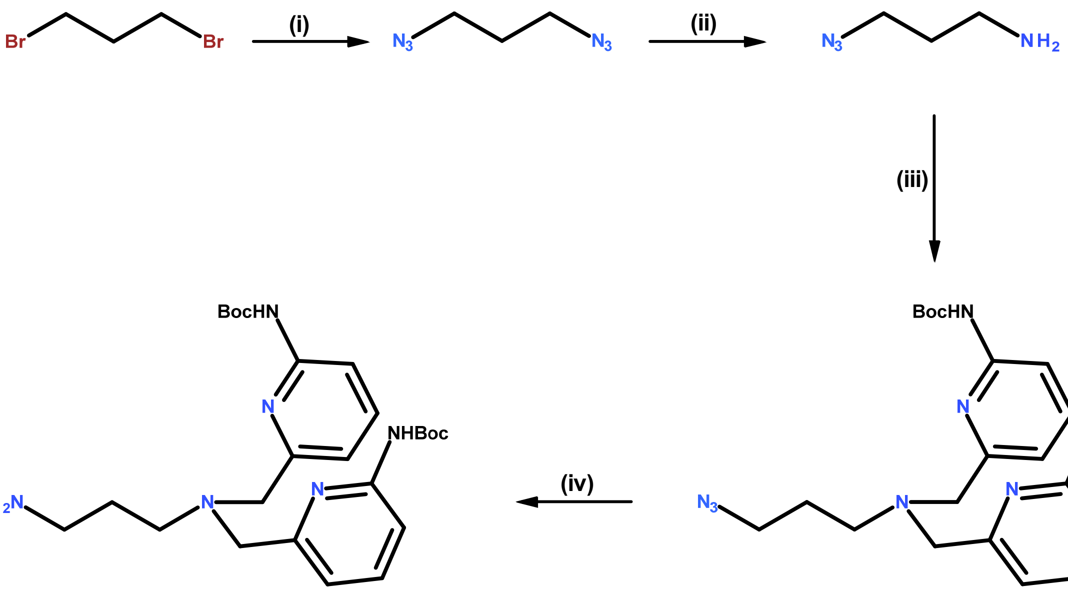

L4-1''

L4-1'

Scheme 4.1. The synthesis of the precursor for peptide complex 4-1. (i) NaN_3, DMF, 70 °C, 89 %; (ii) Triphenylphosphine, Et_2O/Hexane, 1 M HCl, 41 %; (iii) *tert*-butyl N-[6-(iodomethyl)-2-pyridyl]carbamate, DIPEA, DMF, 70 °C, 37 %; (iv) H-Cube (40 bar H_2 at 40 °C), Pd/C, EtOAc, 100 %.

The peptide was purchased as Fmoc-*LENEVARLKKLVKQG*-OH attached to a 2-chlorotrityl funtionalised polystyrene resin. This allows for modification of the N-terminus though selective coupling of various amino acids.

The desired sequence was synthesised through standard Fmoc protocol synthesis. The selected sequence (Ac-*YLENEVARLKKLVKQG*) was synthesised using the purchased sequence by solid phase peptide synthesis (SPPS) adding Tyrosine (Y) on the N-terminal followed by acetylation. The Tyrosine was initially inserted into the sequence to provide the peptide with a chromophore that would allow for UV determination of the concentration. This became redundant in the final determination of the concentration once the intermediate **L4-1''** was attached as shall be presented below.

Once the sequence was synthesised it was cleaved off the solid support using mildly acidic conditions (1-5% TFA/DCM) that leaves the permanent side chain protecting groups intact, see Figure 4.15.

The attachment of the precursor ligand **L4-1''** to the peptide proceeds through standard amide bond formation using the HBTU or HATU activated C-terminus of the peptide although HBTU yielded more consistent results, see Scheme 4.2.

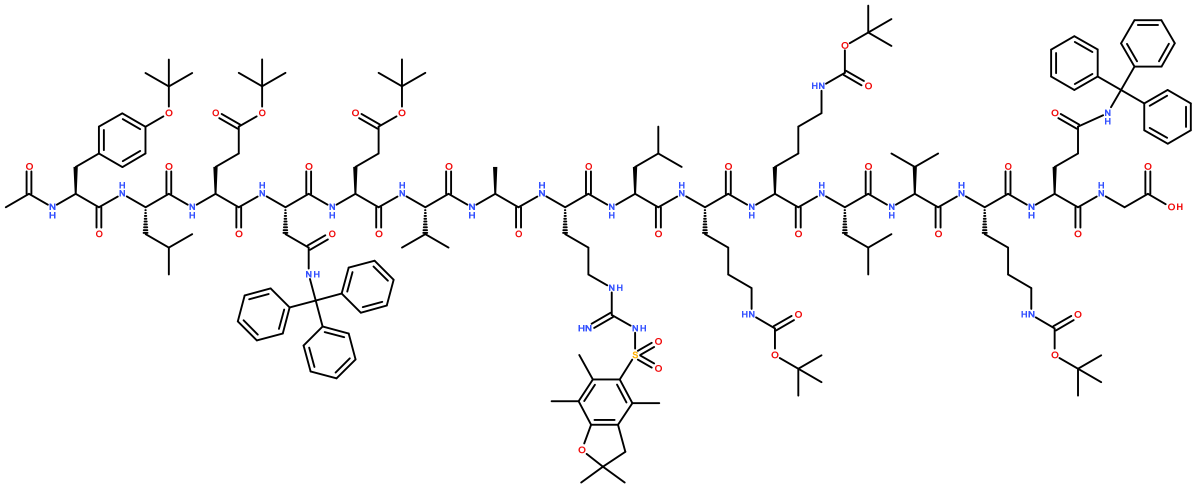

Figure 4.15. The fully protected Ac-*YLENEVARLKKLVKQG*-OH with the carboxyl on the C-terminus unprotected.

The precursor **L4-1''** was attached to the peptide Ac-*YLENEVARLKKLVKQG*-OH and purified by extraction. The fully protected product was deprotected using the cleavage mixture TFA/TIS/H_2O (90/5/5) and subsequently purified using HPLC to afford the product **L4-1.**

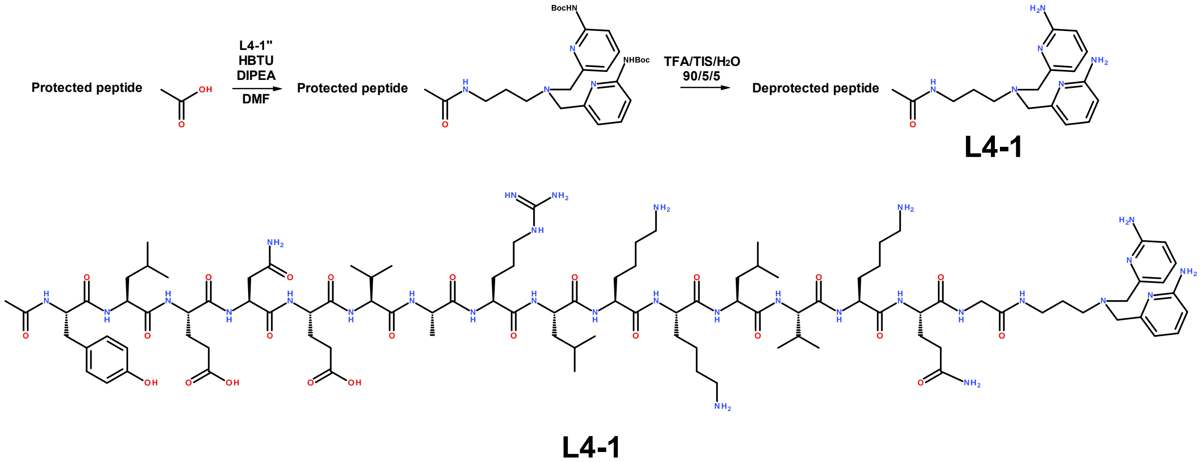

L4-1

L4-1

Scheme 4.2 The coupling of L4-1'' to the peptide yielding L4-1. The yield was 5 % over 2 steps.

Ligand **L4-2** was synthesised as a control compound to determine whether the peptidic scaffold contributes to association and if the concept of association promoted rate acceleration introduced in Chapter 3 holds true.

The ligand was synthesised in the same way as described for the precursor **L4-1''** followed by acetylation of the resulting amine. The intermediate was then treated with

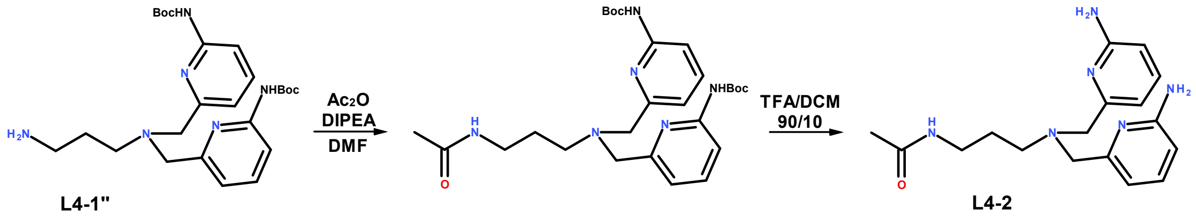

Scheme 4.3. The synthesis of compound L4-2. The yields were 42 % and 39 %, respectively.

TFA/DCM (90/10) in order to remove the protecting group and purified to yield compound **L4-2**, see Scheme 4.3.

In order to obtain accurate data for the structural and kinetic experiments with the peptidic complex **4-1** it is important to determine the concentration as precisely as possible. Given the small scale at which the compound **L4-1** was synthesised and its polar nature, it is highly likely that the peptide retains relatively large amounts of water even after freeze drying. It is therefore reasonable to assume that the gravimetric analysis is not the best way to determine the amount of **L4-1**. UV analysis of **L4-2** should provide an accurate estimation of the amount of **L4-1** obtained.

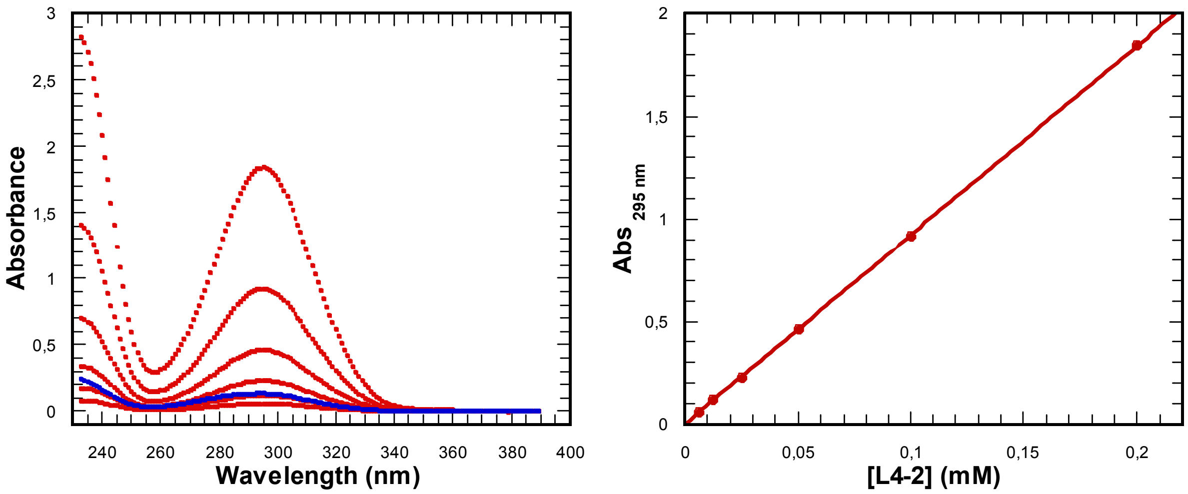

Figure 4.16. The UV absorbance traces (left) for L4-2 (red) and peptide L4-1 (blue) shown and the linear fit of the calibration curve for L4-2 from the absorbance at 295 nm (right).

The concentration of the peptide was determined using a calibration curve obtained from UV measurements at various concentrations of ligand **L4-2**, see Figure 4.16. Compound **L4-1** was diluted and the absorbance reading was intrapolated in calibration curve yielding a total estimated amount of approximately 15 mg **L4-1**.

The stock solution obtained for **L4-1** was used to measure the reactivity of the peptidic

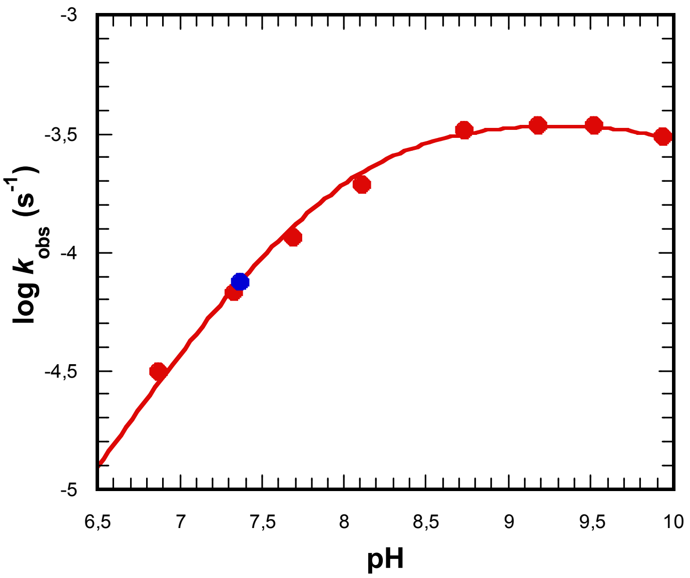

Figure 4.17. The observed rate constant versus pH for 4-1 (blue) and 4-2 (red). The concentrations of the complexes were 0.4 mM and 1 mM, respectively, but the rate constants were normalised at 1 mM complex concentration. The substrate was 50 µM HPNPP and the buffer was 50 mM HEPES or CHES with 0.1 M ionic strength ($NaNO_3$). The complex 4-1 required an excess (6-fold) of $Zn(OTf)_2$ for activity to be observed possibly due to some interfering coordination of the metal ion to other residues in the peptide sequence, see Figure 8.14 in Chapter 8.9.4.

ligand versus the reactivity of the corresponding non-peptidic ligand **L4-2**. The two-fold ionisation model, **Equation 4.1**, see Chapter 8.3, was fitted to the data although the second deprotonation pK_{a2} was not well defined by the data points in Figure 4.17 and was instead fixed to the value obtained from the potentiometric titration, see Table 4.1. The kinetic pK_{a1} for **4-2** was determined to be 7.96 (± 0.03) and the limiting pseudo-first-order rate constant for 1 mM complex was determined to be 3.73 (± 0.15) × 10^{-4} s^{-1}.

$$k_{obs} = k_{obs}^{max} \times \frac{[H^+]K_{a1}}{K_{a1}K_{a2}+K_{a1}[H^+]+[H^+]^2} \qquad \text{(Equation 4.1)}$$

The complex **4-2** was also titrated potentiometrically and the determined parameters are shown in Table 4.1. The potentiometric pK_{a1} is in good agreement with the kinetically determined values.

Complex	$(LH_2)^{2+}$		$(LZn)^{2+}$		
	pK_{a1}	pK_{a2}	log K_f	pK_{a1}	pK_{a2}
4-2	7.51	5.43	6.12	8.03	10.62

Table 4.1. The potentiometrically determined parameters for the complex 4-2.

Complex **4-1** was used at 0.4 mM concentration with 6-fold excess $Zn(OTf)_2$ since activity was not observed at 1 equivalent metal ion. The rate at 0.4 mM was normalised to equal 1 mM which is in excellent agreement with the data obtained for **4-2**, see Figure 4.17.

It is evident that the observed activity for the peptidic complex **4-1** is the same as the non-peptidic complex **4-2** which suggests that the association between the peptide strands is minimal and thus the peptidic complex **4-1** behaves similarly to the non-peptidic **4-2**.

The secondary structure and potential dimerisation of the peptides was studied using circular dichroism (CD) spectroscopy. Compound **L4-1** is clearly forming an α-helical structure as can be seen in Figure 4.18 characterised by a local minimum at 222 nm and a global minimum at 208 where the ellipticity is presented in millidegrees (mdeg).

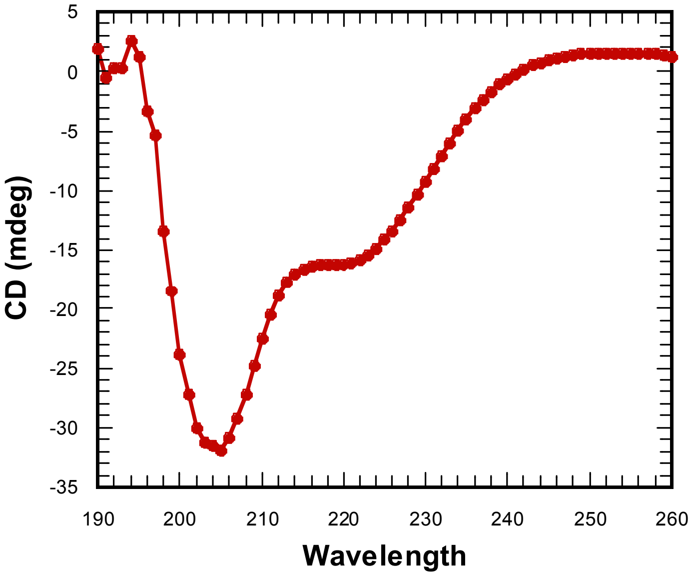

Figure 4.18 . The CD scan of 25 µM L4-1 in 1 mM HEPES (pH 7.4) at 25 °C shows the characteristic α-helical profile. The ellipticity is presented in millidegrees (mdeg).

In order to study the interhelical interactions a temperature scan is required where the change is typically monitored at 222 nm, see Figure 4.19. The sigmoidal character of the plot indicates the loss of coiled-coil interaction with increased temperature and the melting temperature (T_m) of the dimer is determined at the inflection point.

An issue encountered when using 100 µM **4-1** was the high absorbance (particularly at short wavelengths) that caused noisy, unreliable and ultimately faulty readings to be obtained below 205 nm at higher concentrations of **L4-1**. The measurements seemed to be affected by the buffer and salts used which prompted the use of significantly lower concentrations (1 mM

Figure 4.19. The α-helical profile (a) and sigmoidal temperature melting curve indicating coiled-coil dissociation(b, bottom) and the melting profile after guanidinium hydrochloride treatment (b, top) for the truncated GCN4 peptide (GCN4-p1$_{9\text{-}35}$ -c") as reported by Bunagan *et al.*[175] Reprinted (adapted) with permission from Bunagan, M. R., Cristian, L., DeGrado, W. F. & Gai, F. Truncation of a cross-linked GCN4-p1 coiled coil leads to ultrafast folding. *Biochemistry* 45, **10981–6 (2006). Copyright 2006 American Chemical Society.**

HEPES, no $NaNO_3$) than in the kinetic experiments. The Zn counter ion had to be replaced with OTf since the nitrate, and possibly residual TFA, seemed to be at least partly responsible for the high absorbance at shorter wavelengths.

The CD profiles of 100 μM **L4-1** in 1 mM HEPES (pH 7.4) at 5 °C and 95 °C, see Figure 4.20, show the decreased signal at 222 nm which is expected at higher temperatures. The CD temperature profile for **L4-1** is not sigmoidal but rather seems to indicate a $T_m < 5$ °C which is not very useful for most practical applications.

The CD profile for complex **4-1** (100 μM **L4-1** and 1 mM $Zn(OTf)_2$) and after the addition of 80 μM HPO_4^{2-} to encourage potential association yielded similar melting curves. The change in ellipticity indicates a loss of secondary structure with increasing temperature, which can be expected, but the transition from coiled-coil structure to free monomers is not well defined (sigmoidal profile Figure 4.19). This lack of dimerisation strongly suggests that the results obtained for the catalytic activity of **4-1** behaving similarly to the **4-2**, see Figure 4.17, are because both complexes are monomeric.

It is likely that the short peptide sequence in **L4-1** does not have sufficient non-covalent interactions to form stable dimers and it is therefore suggested that terminal covalent interactions could provide further stabilisation without significantly extending the sequence.

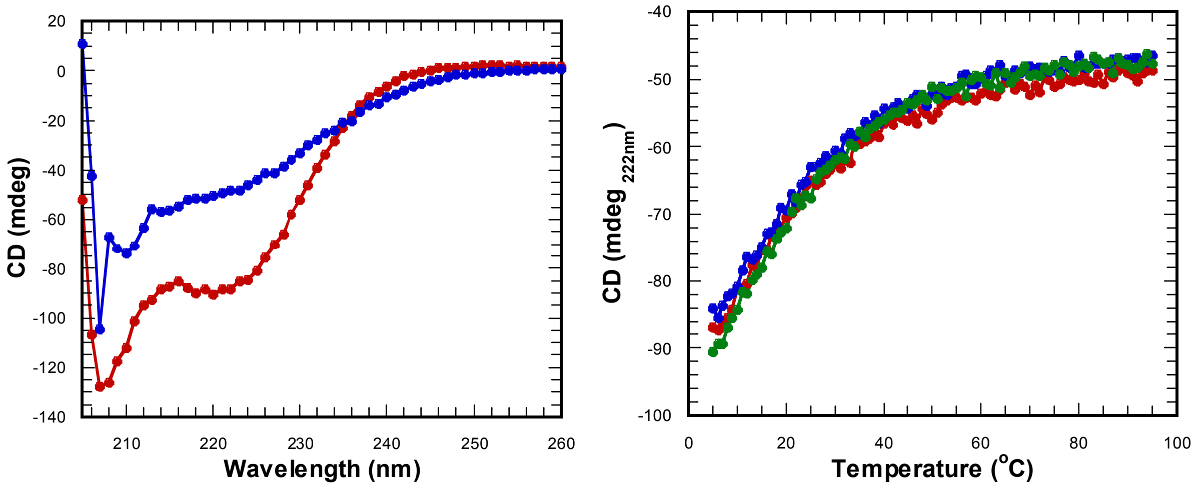

Figure 4.20. The difference of the CD profiles (left) at 5 °C (red) and 95 °C (blue). The temperature scan profile (right) at 222nm from 5 °C to 95 °C for 100 µM 4-1 (red) with 1 mM Zn(OTf)$_2$ (blue) and with 1 mM Zn(OTf)$_2$ and 80 µM HPO$_4^{2-}$(green). The ellipticity is presented in millidegrees (mdeg).

The covalent bond would technically render the claim of non-covalent association invalid. However, the attachment at opposite ends of the peptide sequence of the two complexes will arguably have to involve non-covalent interactions to form the desired dimeric structure locally.

4.3.3 - The disulfide-bridged peptide

The covalent interaction that seems most appropriate to encourage association of the helical peptide sequences is the formation of disulfide bridges since this has already successfully been used by Bunagan *et al.*[175] The peptide GCN4-p1$_{9-35}$ -c” uses a C-terminal disulfide bridge and a similar bridge should be readily obtainable through the introduction of cysteine into the peptide sequence.

Although the literature procedure uses C-terminal cysteines the purchased sequence would not allow for easy incorporation of standard Fmoc amino acids at the C-terminus without significantly altering the synthetic strategy.

Since the procedure for introducing the ligand at the C-terminus has already been established it was decided that the most convenient approach would be to introduce the interhelical disulfide bond at the N-terminus. The final ligand **L4-3**, see Figure 4.21, would be identical to **L4-1** apart from the two additional amino acids.

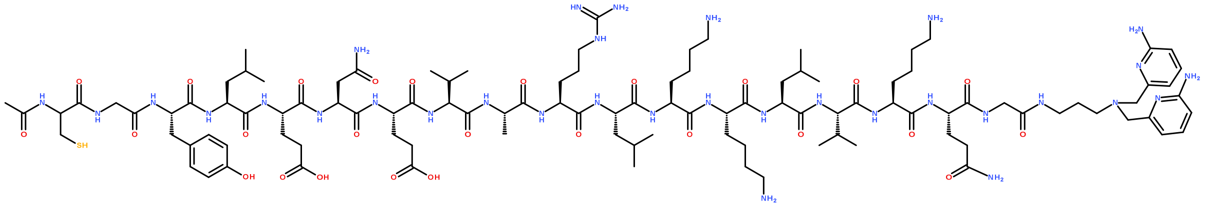

L4-3

Figure 4.21. The structure of L4-3 is identical to L4-1 except for the additional N-terminal cysteine and Glycine.

Building on the previously used sequence, glycine and cysteine were coupled to the N-terminus to give, Ac-*CGYLENEVARLKKLVKQG*-OH. The sequence was decided upon using single residue mutations with crystallographic software on the structure of the native GCN4-p1 (PDB code: 2ZTA). The selected residues ensured the closest interaction between the cysteine side chains (2.2 Å), see Figure 4.22.

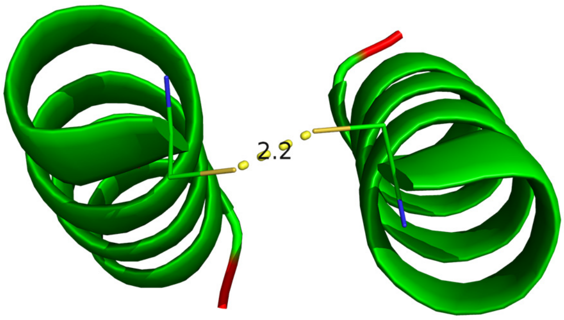

Figure 4.22. The graphical representation of the sequence *CGYLENEVARLKKLVKQG* with the N-terminal cysteines visualised. The cys-cys distance was measured to be 2.2 Å.[45]

The synthesis was performed using standard a SPPS Fmoc-protocol, see Chapter 8.9.2. The ligand **L4-1''** was coupled to the C-terminus as previously described.

An indication that this approach had not proceeded smoothly was the distinct smell of thiol emanating from the reaction vessel after treatment with the cleavage mixture to obtain the ligand **L4-3**. Purification of the cleavage mixture was attempted by HPLC and the crude mixture was analysed by mass spectrometry but the efforts were fruitless. The peptide sequence Ac-*CGYLENEVARLKKLVKQG* itself, without the ligand **L4-1''**, was analysed and found by mass spectroscopy but the modified analogue **L4-3** was not identified even after repeated attempts.

The disulfide-bridged approach was envisioned to be an easy way to encourage association of the peptide helices but the problems encountered indicated a more substantial synthetic obstacle.

It is important to keep in mind that despite the structural role of the disulfide bridge in many enzymes and proteins[182–186] the issue that could arise in the context of Zn(II) complexes is the accessibility of the thiol side chains. The cysteines might interfere with metal ion binding since thiols are known to coordinate to Zn(II)[40,187,188] as well as other metal ions like Au(I)[189] and Hg(II).[161]

4.3.4 - The mid-sequence functionalisation

The incorporation of a ligand is not limited to either terminus of a peptide sequence but in this particular case these conditions had to be adhered to. Since the peptide sequence was purchased fully synthesised it was not possible to selectively introduce a ligand at a specified position.

If the sequence was to be synthesised from start the ligand could be incorporated as a Fmoc-protected unnatural amino acid. The easiest starting point is to look at commercially available Fmoc protected amino acids that could be functionalised on the side chain residue.

In the context of the GCN4 peptide structure there are a number of interactions that need to be taken into consideration when selecting residues to replace. Certain residues play an important role in the dimerisation process and should therefore not be altered, see Figure 4.23. The helical wheel representation indicates the position of the residues that are involved in intra- and interhelical interactions where the heptad repeat is indicated by the letter *abcdefg*, see Figure 4.23. The core lipophilic residues are indicated by the letter *a* and *d* whereas the other residues interplay through electrostatic interactions (dashed lines).

In order to achieve mid-sequence interhelical interaction between potential ligands one would have to try to avoid disrupting the salt bridges. The importance of salt bridges has been highlighted by Meier *et al.* for a coiled-coil peptide containing two heptad repeats. The targeted mutations of residues involved in an essential interhelical salt bridge lead to loss of coiled-coil structure although the individual peptide monomers remained highly α-helical.[190]

Figure 4.23. A helical wheel representation of GCN4-p1 viewed from the N-terminal down the axis of the helices with the heptad repeat represented as (*abcdefg*). The dashed lines represent intra- and interhelical salt bridges seen in the x-ray crystal structure.[176] From O'Shea, E. K., Klemm, J. D., Kim, P. S. & Alber, T. x-ray structure of the GCN4 leucine zipper, a two-stranded, parallel coiled coil. *Science* 254, 539–44 (1991). Reprinted with permission from AAAS.

It appears more difficult than expected to functionalise the peptide with unnatural amino acids in a, at least in theory, non-offensive way. The solution would have to include plain trial and error in the replacement of appropriately distanced residues. It is not an entirely random process and there is some room for rationale. The Zn(II) complex would most probably be cationic and it would seem reasonable to target cationic residues for replacement.

With all these possible ways to destabilise the coiled-coil structure it might seem like the mid-sequence modification of the leucine zipper peptide can be turned into a research field in itself. The fact that interhelical interaction are of essence to the structure clashes with the concept of introducing interhelical ligand interactions. This leaves the intrahelical interactions as a potential scaffold for the ligands since the secondary structure is more robust than the tertiary coiled-coil structure.

For intrahelical interactions the most innocuous residues would appear to be the "f" positioned DSKN but changing these amino acids has also been reported to destabilise the structure.[177]

In this particular case we will not dwell on the potential detrimental effect of residue replacement but rather focus on the possibility to synthesise and incorporate a catalytically active Zn(II) complex.

The initial amino acids that would be directly compatible with ligand **L4-1''** were the Fmoc protected Aspartic and Glutamic acids due to their carboxyl functionalities on the side chain. These would allow for standard amide bond formation with the amine of the ligand. It quickly became apparent that the stability of the Fmoc group under these conditions would be a problem since the free primary amine of ligand **L4-1''** could lead to deprotection.

In the case of Fmoc synthesis there was no room for unprotected primary amines to participate. This also means that the reverse case is not a possibility where amino acids with amine functionalities on the side chains couple to carboxy-functionalised ligands.

It is clear that an orthogonal process is needed and the most suitable approach that was reasonably accessible utilised the azide-alkyne cycloaddition also known as a "click reaction", see Scheme 4.4.

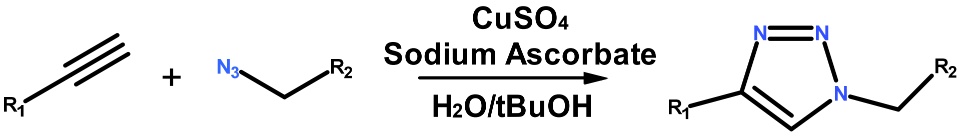

Scheme 4.4. The Cu catalysed "click" cycloaddition.

The first ligand to be synthesised was **L4-4**, see Scheme 4.5, to prove the potential of the reaction and to study the effects of having the triazole functionality in close proximity to the Zn(II). The synthesis was not as effortless as the trivial name "click reaction" would suggest since the solubility of the starting materials in the solvent system was not very high (reaction in MeOH was also attempted[191]). A new solvent system (CH_2Cl_2/MeOH), see Scheme 4.5, that had been suggested in literature[192] which claimed to significantly improve reaction rates and yields was used instead. Despite this new solvent system being employed it still required multiple attempts to yield sufficient amounts of product. The removal of the residual Cu(I) was somewhat problematic given the chelating nature of the compound and adding excess EDTA was of little help in this case. Only after flash chromatography was the undesired metal ion removed.

Ligand **L4-4** was successfully synthesised and the reactivity of its Zn(II) equivalent **4-4** towards phosphate diester hydrolysis was studied using HPNPPi, see Figure 4.24, a substrate which was first used in Chapter 3. The HPNPPi is the more reactive isomer (10-fold more reactive than HPNPP) due to it having a primary rather than a secondary alcohol as a nucleophile.

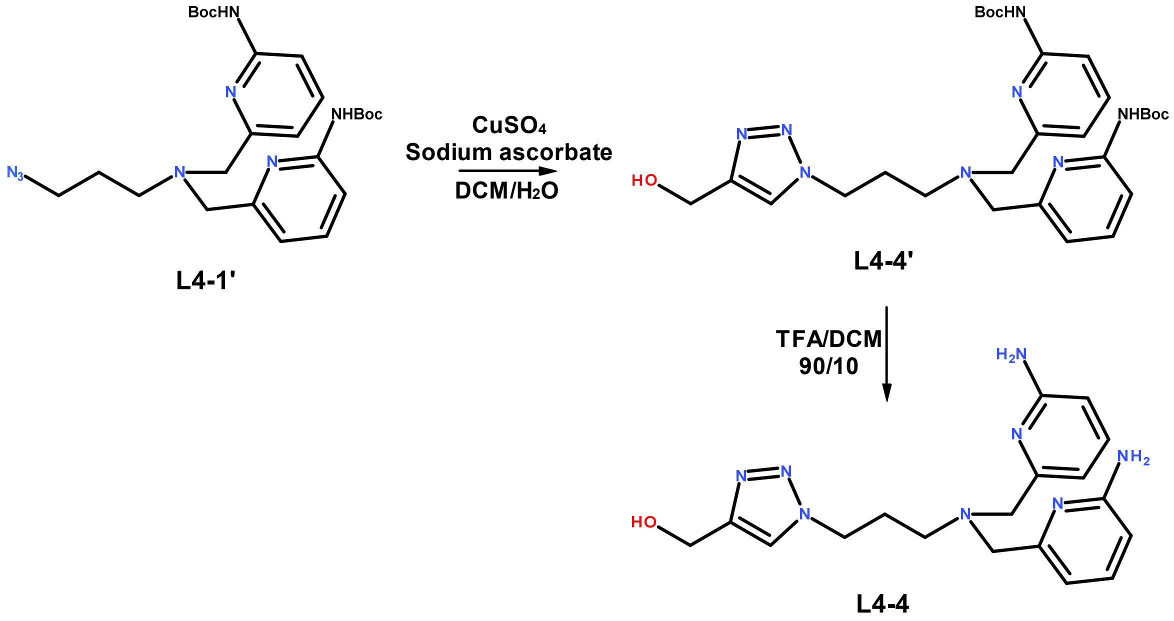

Scheme 4.5. The synthesis of L4-4 that was used as a control for the reactivity of future triazole ligands. The yields were 47 % and 32 %, respectively.

Complex **4-4** was used in 0.4 mM concentration with 50 µM HPNPPi at various pH. The complex **3-2** was used at the same concentration but only at pH 7.3 as a control to verify that the triazole had marginal effect on the reactivity.

The single ionisation model in **Equation 4.2**, see Chapter 8.3, was fitted to the data in Figure 4.24 since the second deprotonation that is expected for the tridentate mononuclear complexes (see Chapter 3) was not well defined within the pH-range studied here.

$$k_{obs} = k_{obs}^{max} \times \frac{K_a}{K_a+[H^+]} \qquad \text{(Equation 4.2)}$$

The kinetic pK_{a1} corresponding to the first deprotonation was determined to be 8.02 (± 0.04) and the limiting pseudo-first-order rate constant was determined to be 3.70 (± 0.17) × 10^{-3} s^{-1} for **4-4**. This is in good agreement with the reported acidity of **3-2**, **3-3** and **4-2** which indicates similarity in the microenvironment of the Zn(II). Additionally, the pseudo-first-order rate constant for the **4-4** is almost identical to **4-2** if the 10-fold increased reactivity of HPNPPi is taken into account.

These data show that the triazole-based ligand is a viable option for introducing ligands into molecular scaffolds, and behaves like an inert linker. The coupling method is completely orthogonal to the Fmoc procedure and it even offers the possibility to incorporate the ligand

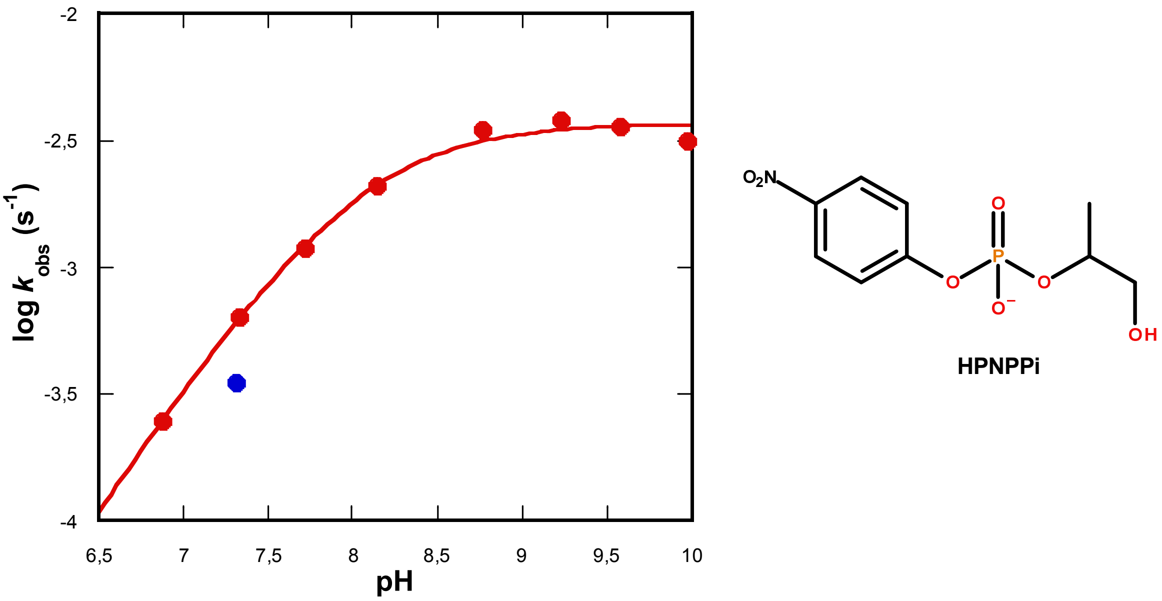

Figure 4.24. The reactivity of 0.4 mM 4-4 (red) and for comparison 0.4 mM 3-2 (blue) towards the transesterification of 50 µM HPNPPi in 50 mM HEPES/CHES at various pH with 0.1 M ionic strength ($NaNO_3$).

post synthesis of the full peptide. The only requirement is that one of the two functionalities, azide or alkyne, is integrated into the sequence.

It was decided that the best course of action is to synthesise an unnatural amino acid containing the ligand prior to the synthesis of the peptide. This would allow direct incorporation of the amino acid into the sequence without further modifications. Synthesis of the envisioned compound **L4-5'** was attempted, see Scheme 4.6, under various conditions but only yielded a mixture of compounds that appeared similar to the starting materials. Thus, the mid-sequence incorporation strategy could not be tested.

Despite suffering a setback in the synthetic procedure the possibility of introducing functionalised amino acids in a controlled fashion at any desired position along the sequence is still tantalising. The cycloadditon reaction has been used to incorporate metal binding cyclams[193] into amino acids in literature which begs the question as to why the reaction failed in this case. The potential causes for this is that the procedure that was used in attempted synthesis for **L4-5'** was different from the procedure reported by Todd *et al.*[193] and that the behavior of the Fmoc protecting group under the reaction conditions is unknown.

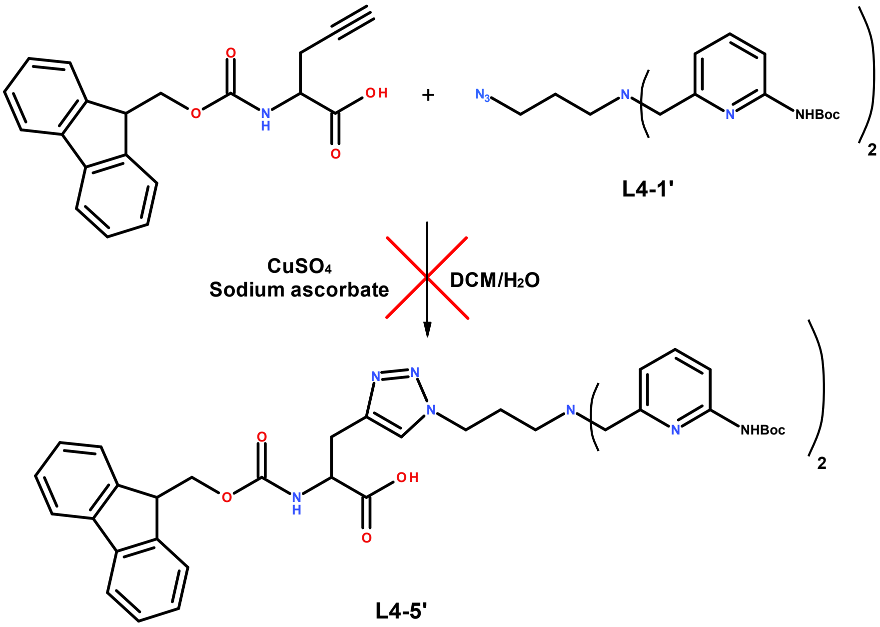

Scheme 4.6. The attempted synthesis of L4-5'.

4.3.5 - The N-terminal functionalisation

The interhelical distance for the GCN4-p1 peptide dimer is very similar at either end of the coiled-coil structure. The measurements between the carbonyl in the amide bonds near the N- and C-terminus (*RMKQ**L**EDKVELLSKNYHLENEVAR**L**KKLVGER*) were calculated using the crystal structure obtained by Ellenberger *et al.*[165] and determined to be 6.5 Å and 6.0 Å, respectively, see Figure 4.25.

It is possible that the fraying might cause the distance to increase between the helices but that would require the sequence to be elongated towards the N-terminal to become more like the bZIP binding region, see Figure 4.7, or modified to remove arginine (R) and not acetylated to allow local unfolding.[194]

The possible functionalisation of the N-terminal is an alternative to the C-terminal functionalisation since the interhelical distances will most likely be very similar. The ligand would be introduced at the N-terminus of the peptide sequence using the standard coupling procedure for amide bond formation. Ligand **L4-6'** was successfully synthesised according to Scheme 4.7.

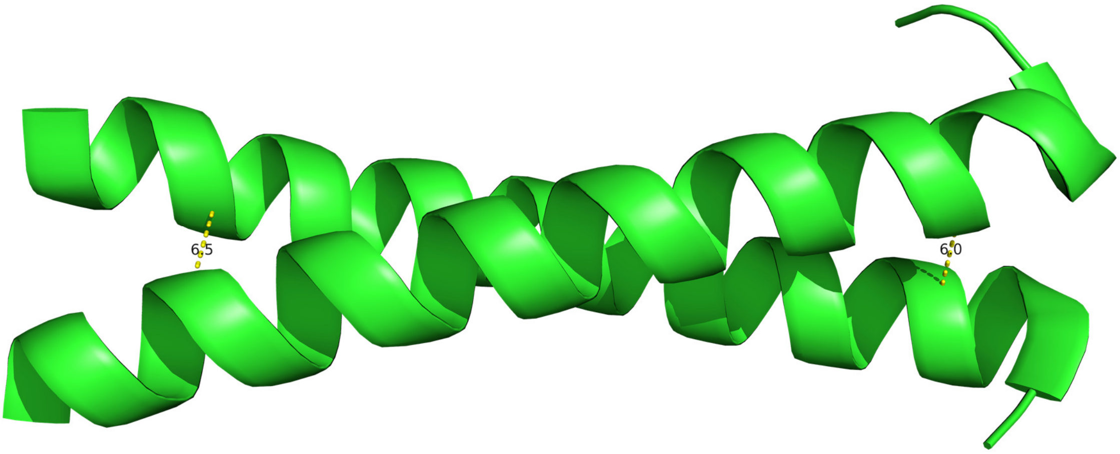

Figure 4.25. The interhelical distance near the N- and C-termius of the GCN4 leucine zipper. This is the same segment shown in Figure 4.7 with the N-terminus to the left and C-terminus to the right. The selected residues were closest to a true representation of the most proximal distance between the helices while still being at opposite ends of the sequence. The structure was obtained from RCSB Protein Data Bank (PDB code: 1YSA). [45]

Although the disulfide-linked C-terminus approach has successfully been used in literature[175] this approach allows for the introduction of a covalent linker between the C-terminus of two helices without the need for cysteine, see the section Future work.

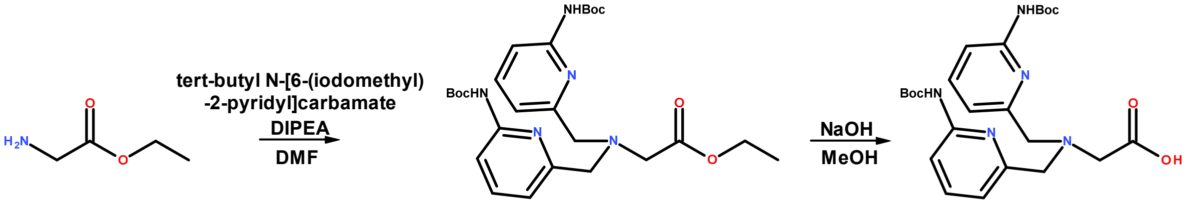

L4-6'

Scheme 4.7. The synthesis of L4-6'. The yields were 45 % and 100 %, respectively.

4.4 - Conclusion

The C-terminally functionalised peptide, **L4-1** is in essence the GCN4-p1$_{18\text{-}33}$-c'' with an acetylated N-terminal tyrosine and a deleted C-terminal GC (the glycine-cysteine disulfide linker). The acetylation of the N-terminus mimics the continuation of the amide sequence i.e. the free amino functionality is neutralised. The lack of capping has been proven to cause structural instability especially at lower pH for parallel coiled-coils due to unfavorable inter- and intramolecular electrostatic interactions involving the protonated N-terminal amine.[194]

The apparent lack of coiled-coil formation for the sequence studied here can be interpreted in light of the sequence truncation study by Lump *et al.*[194] where the N-terminal truncation beyond the 11th amino acid in the sequence leads to mainly unfolded peptide sequences. The lack of a melting temperature for the peptide structure which is evident from the $T_m < 0$ °C, despite the existence of secondary structure (ellipticity, $\text{mdeg}_{222\text{nm}}$, see Figure 4.20), is consistent with results obtained for the peptide **L4-1**.

Both N- and C-terminal truncations seem to reduce the coiled-coil folding of the GCN4-p1 which might indicate that the tertiary interactions between multiple shorter subdomains of the peptide is of greater importance for the folding than the helical propensity of the overall sequence. This concept of secondary structure domains playing an important role in driving the association of coiled-coil helices has also been studied by Matthews *et al.*[177]

As previously mentioned one possibility to increase the interaction is making the peptide sequences longer to increase interaction between α-helices, although this would be going against the aim of making small molecular catalysts. One can argue that the peptide sequence will still be relatively small compared to the large protein structures of enzyme that we are aiming to mimic.

4.5 - Future work

It is worth investigating the potential of the covalent linkage between the truncated GCN4 sequences presented in this chapter despite the apparent lack of dimerisation between the helices. A potential future modification of the GCN4 sequence would be the introduction of an alkyl diamine that forms amide bonds at the C-terminus.

Although the synthesis of the alkyl-linked dimer in Scheme 4.8 was not attempted the synthesis of the control compound **L4-8** yielded a crude mixture that was analysed, see Scheme 4.9.

The crude reaction mixture from the synthesis of **L4-6** was analysed using LC-MS which appeared to contain mainly product (found *m/z* 543.3 [MH^+]) although no further analysis/purification was carried out. If the association is not achieved after covalently linking the N-terminal the only remaining option is to elongate the sequence.

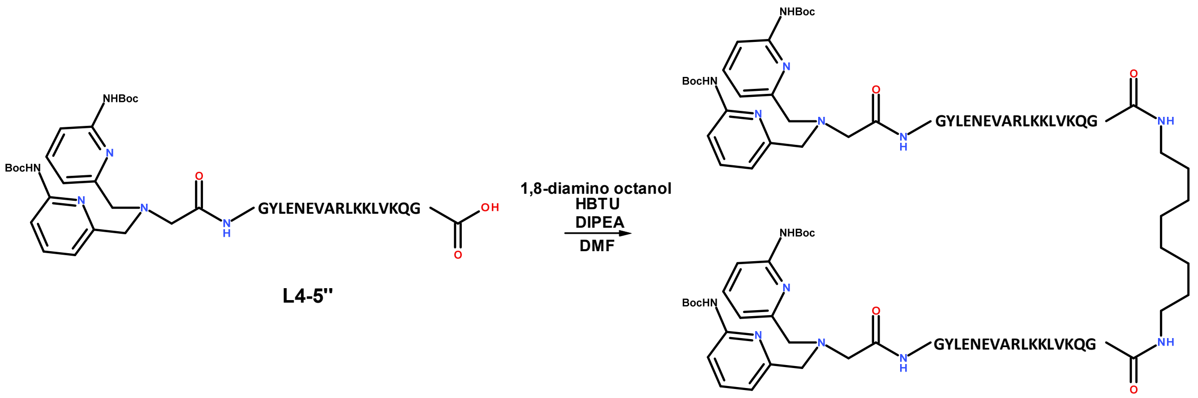

Scheme 4.8. The proposed synthesis of the covalently linked dimer.

The lack of dimerisation observed for the peptide sequence used here could be resolved by extending the sequence. The truncation of the GCN4-p1 has previously been studied, as mentioned above, but when the sequence is shortened the destabilising effects have been offset by cross-linking as in the work of Bunagan *et al.*[175]

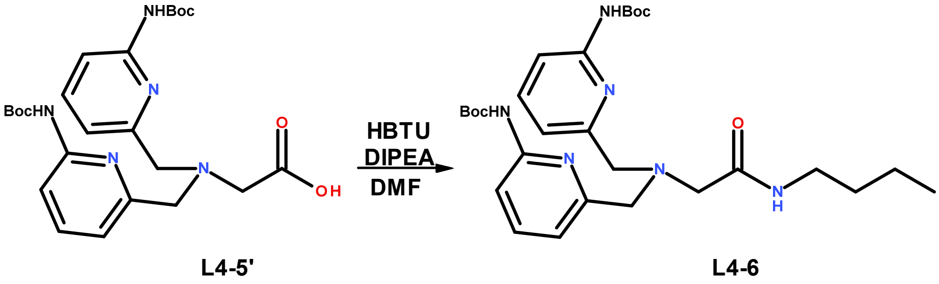

Scheme 4.9. The synthesis of the control ligand for the N-terminal functionalisation.

Despite the possible introduction of a cross-linking moiety, the sequence is still significantly shorter than the cross-linked sequence from literature, i.e. GCN4-p1$_{9\text{-}35}$ -c”, which leaves a variable pertaining to the length unresolved. The solution is to either study the folding properties of the short cross-linked peptides or lengthening and cross-linking the sequence to resemble GCN4-p1$_{9\text{-}35}$ -c”.

It is worth considering the intrahelical functionalisation of the GCN4-bZIP at the N-terminal where the complexes are interacting with the DNA structure, see Figure 4.7, since this could provide a model for future DNA cleaving artificial nucleases which will be discussed in the next chapter.

Chapter 5 - Nucleophilic complexes

5.1 - Introduction

A key structural difference between RNA and DNA is the lack of a 2'-OH in the latter. The difference in reactivity between RNA and DNA is approximately 5 orders of magnitude for the base-catalysed cleavage and is due to the presence of this intramolecular nucleophile. This means that the reactivity observed for some complexes towards HPNPP does not necessarily translate to the DNA analogue bis-(4-nitrophenol) phosphate (BNPP).[14] The answer to this is to incorporate a nucleophile into the structure of the metal complex that would in effect become an intramolecular nucleophile when the substrate binds, see Figure 5.1.

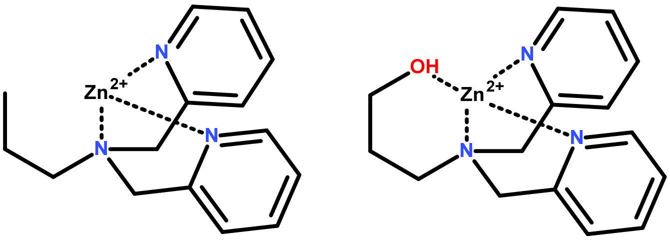

$k_{2(\mathrm{BNPP})}$	**no reactivity**	**4.2×10^{-4} ($M^{-1}\ s^{-1}$)**
$k_{2(\mathrm{HPNPP})}$	**3.9×10^{-2} ($M^{-1}\ s^{-1}$)**	**2.1×10^{-2} ($M^{-1}\ s^{-1}$)**

Figure 5.1. Introducing a nucleophilic appendage leads to substantial rate increase for BNPP cleavage.[14]

A widely used nucleophile is the alkoxide moiety that is incorporated into the metal complex and coordinates to the metal ion. The coordinated nucleophile provides a better nucleophile than metal-bound water in small mononuclear Zn(II) complexes[14,195] for the hydrolysis of BNPP. However, the main disadvantage with this approach is that the reaction principally becomes a transesterification rather than a hydrolysis. The resulting phosphorylated nucleophile is stable and does not dephosphorylate readily thus rendering the entire complex a stochiometric reagent rather than a catalyst.

It has been reported by our lab that the use of a hydrated aldehyde nucleophile[132] overcomes this issue since the phosphorylated hydrate can decompose back into the aldehyde, releasing the phosphate. The aldehyde complex required some structural modification for synthetic reasons. The oxidation of the alcohol to the aldehyde led to loss of product most likely due to an elimination process, see Scheme 5.12. The methylation of the β-position of the alcohol resolved this issue and additionally increased the activity 6-fold compared to the native non-methylated complex, Figure 5.2. The reactivity of the aldehyde hydrate is equal to the corresponding alcohol and the reactive nucleophile has been suggested to be the non metal-ion bound oxygen of the hydrate.

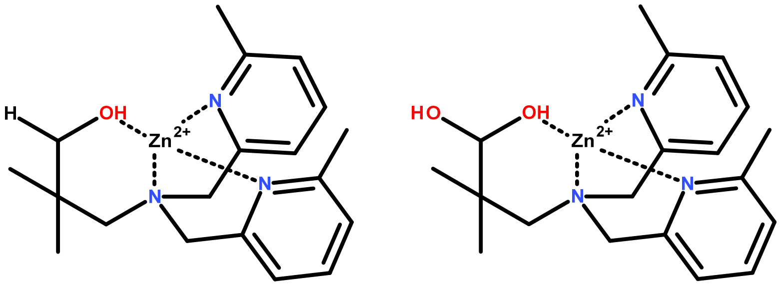

Figure 5.2. The dimethylated complexes that were reported for the hydrolysis of BNPP.[132]

This led to the hypothesis that efficient complexes could be created by using a non-coordinated nucleophile. The use of a non-coordinated approach offers the benefit of proximal localisation of the nucleophile without the deactivating interaction with the metal nucleus.

The requirement of having a coordinating atom next to a highly reactive non-coordinating nucleophile can be satisfied by the use of hydroxylamine derivatives where the nitrogen coordinates and the oxygen is the active nucleophile. The hydroxyl amine (NH_2OH) is a particularly effective nucleophile due to the α-effect (an electronegative atom with an unshared lone pair is directly attached "α-position" to the nucleophilic species). The influence of the α-effect on rate of hydrolysis of the DNA analogue 2,4-dinitrophenylethyl phosphate was compared to the most common nucleophile OH^-. The difference in reactivity between the OH^- and NH_2O^- was 735-fold in favor of the latter, despite its lower pK_a.[196]

The oxime functionality has been used successfully for the hydrolysis of carboxylic esters[197,198] and was initially reported by Breslow *et al.* in 1965.[199] The nucleophilic complex consisted of a pyridine oxime that was intended to serve as a model for the enzyme carboxypeptidase A.

Similar oxime-containing complexes have been reported to efficiently hydrolyse phosphate esters.[200–202] Very recently a complex was studied by our lab using an oxime nucleophile, see Figure 5.3.[203] This resulted in the most reactive complex for the hydrolysis of BNPP reported to date. This complex is the basis on which the nucleophilic complexes presented in this work were designed.

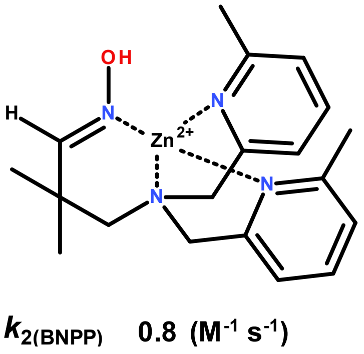

Figure 5.3. The most reactive complex reported to date for the hydrolysis of BNPP.[203]

In the previous chapter the concept of peptide-based artificial complexes was introduced. The complexes were primarily aimed at the transesterification of the RNA analogue HPNPP but this could be extended to include DNA analogues. GCN4-bZIP is a known DNA-binding structure which makes the incorporation of DNA-cleaving complexes a particularly enticing concept.

The incorporation of the complex in Figure 5.3 into a peptide sequence would require some structural modification in order to introduce an anchoring point. The synthetically most accessible attachment points are the gem-dimethyl alkylating site (**b**) or the aldoxime (**a**), see Figure 5.4.

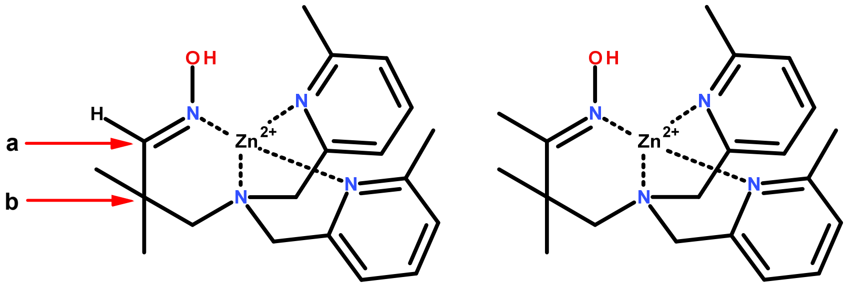

Figure 5.4. The proposed sites for anchoring to the peptidic scaffold of GCN4-bZIP (left) and the ketoxime complex (right).

The functionalisation of position (**b**) in Figure 5.4 would result in a complex that is very similar in structure and most likely also in behavior to the native complex. The functionalisation at position (**a**) would on the other hand yield a chemically different (ketoxime) compound that has not been investigated. Both approaches where considered and their synthetic procedures will be briefly discussed in the Chapter 5.7.

It has been suggest that the difference between the reactivity of aldoxime and ketoxime pyridines towards 4-nitrophenyl acetate (pNPA) is 10-fold in favor of the latter.[204] This led to the synthesis of a ketoxime complex in Figure 5.4.

5.2 - Aims

The aim of the nucleophilic approach to phosphate diester hydrolysis is to broaden the group of potential substrates to include less reactive DNA-like compounds. The structure of the ligand is probed using methylation in order to determine the potential sites for the attachment of supramolecular scaffolds (for example peptides). The incorporation of methyl groups will also be used to study the stability of the complexes towards chemical modification since certain chemical modifications (oxidation) have proven to be problematic in their absence, see Scheme 5.12.

5.3 - Synthetic procedure

The synthesis of the nucleophilic side chain for ligand **L5-1** was achieved by alkylating acetoacetamide with MeI followed by reduction using $LiAlH_4$ according to Scheme 5.1.

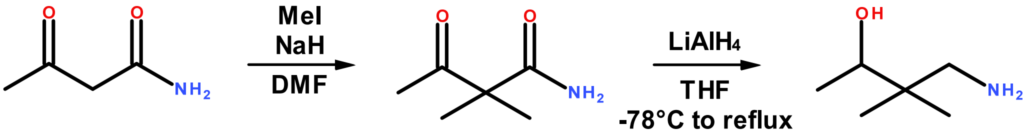

Scheme 5.1. The synthesis of the nucleophilic appendage for the ligand L5-1. The yields were 76 % and 95 %, respectively.

The nucleophilic tail was then coupled to the precursor 2-(iodomethyl)-6-methyl-pyridine (**X$_2$**) to yield ligand **L5-1** using the standard S$_N$2 procedure used for previous reactions, see Scheme 5.2.

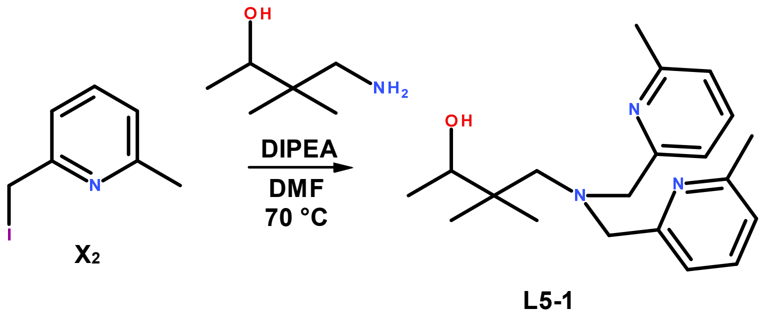

Scheme 5.2. The synthesis of L5-1 using the standard S$_N$2 procedure from Chapter 2. The yield was 82 %.

The ligand **L5-1** was converted to **L5-2** through Dess-Martin oxidation followed by hydroxylamine functionalisation to yield **L5-3**, see Scheme 5.3.

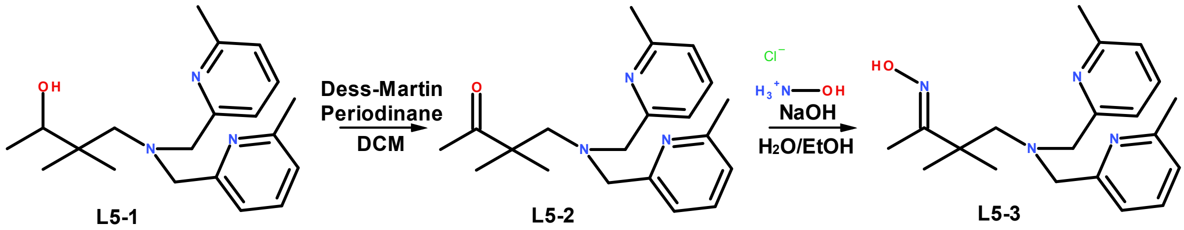

Scheme 5.3. The synthesis of L5-2 and L5-3 from L5-1. The yields were 42 % and 77 %, respectively.

The ligands were incubated with equimolar amounts of $Zn(NO)_3$ and stored as the corresponding complexes, see Figure 5.5, at 4 °C until use in the kinetic experiments.

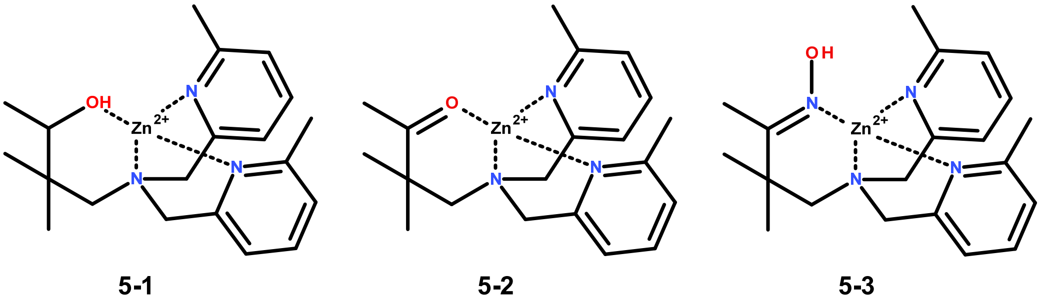

Figure 5.5 The proposed structures of the Zn complexes.

A series of pyridyl oxime compounds were synthesised, see Figure 5.6, and studied to investigate whether the activity of the complex **5-3** is simply due to the oxime nucleophile and metal ion being in close proximity to each other or if the larger structural arrangement and formation of a microenvironment in the catalyst is required.

These oximes were synthesised using their corresponding aldehyde/ketone and hydroxylamine except for bis(2-pyridyl)methanone oxime (**L5-6**) which was purchased from

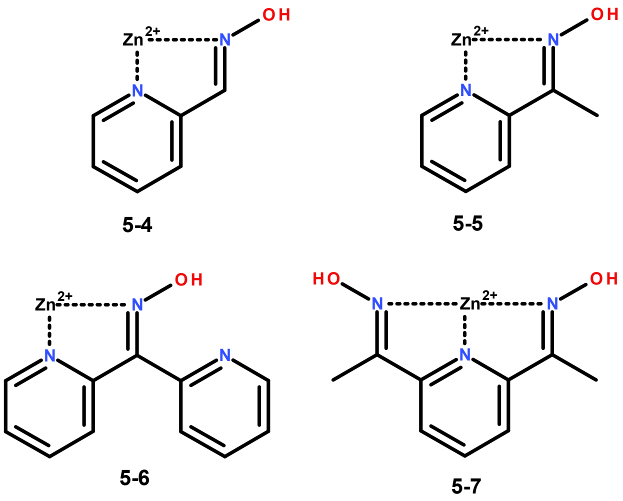

Figure 5.6 The pyridyl oximes synthesised as reference complexes for the nucleophilicity towards pNPA.

Sigma Aldrich and used without further purification. The Zn(II) complexes in Figure 5.6 were kinetically analysed to see if they were as reactive as the larger complex **5-3** which includes a tetracoordinated Zn(II) and a different geometry of the coordinated oxime.

5.4 - Results and discussion

All oxime compounds presented were used with 1 molar equivalent of $Zn(NO_3)_2$ except for **5-6** which was used with 2 equivalents of Zn although it is most likely that only one metal ion coordinates to the ligand. The coordination of the simple pyridyl oxime ligands to the metal ions is bidentate (**5-4**, **5-5** and **5-6**) and tridentate (**5-7**) for which the reported formation constants with Zn(II) are relatively small (log $K_f \approx 2$).

An issue that arises from the low formation constants and lack of coordination to the metal centers is highlighted in studies of the crystal structures formed with these types of compounds. The nature of the coordination has been crystallographically confirmed to occur through the pyridyl and oxime nitrogen atoms. Ligands **L5-4** and **L5-5** along with other oximes have been studied at various ligand (C_L) to metal (C_M) ratios (C_L:C_M, 1:1 to 1:8). The results also indicate that multiple ligands can bind to one metal ion (ML_n, n = 1, 2 or 3). In the case of **L5-4** complexed with Ni(II) the crystal structures have indicated the existence of dimeric complexes. The suggested structures each consist of a nickel center coordinated to three molecules of **L5-4** in an octahedral coordination. The trimeric units are interacting through the oximic oxygens to form a dimer consisting of $(Ni)_2L_6$. These structures are not representative of all metal ions since Cu(II) have been reported to form different complexes with pyridyl oximes[205,206] but they do indicate the tendency of the ligands to form these multicoordinate structures.

In the case of Ni(II) the metal ion titration versus rate of reaction indicates a strong preference for a 1:2 Metal:Ligand complex even at 5-fold excess of metal ion. The reactivity of the Zn(II) complex on the other hand was still increasing even after the addition of up to 5 equivalents of metal ions over ligand which is consistent with the equilibrium being shifted to form more of the active complex, see Scheme 5.4. The complex formation constant for of Cu(II) or Ni(II) complexes were reported to be orders of magnitude larger than for Zn(II).[204]

$$[L] + [M^{2+}] \underset{K_d}{\overset{K_f}{\rightleftharpoons}} [LM]^{2+}$$

Scheme 5.4. The equilibrium is shifted to complex formation. Adding more Zn(II) compensates for the low K_f of oxime complexes.

In light of the data obtained for these types of compounds, the suggestion is to use excess amount of metal ions to encourage the formation of 1:1 complexes when the binding constant is low.

The use of up to 10-fold excess Zn(II) has been recommended for the complexes in Figure 5.6. The results presented herein are largely in accordance with the reported data despite the use of equimolar amounts of $Zn(NO_3)_2$. The use of the metal ion with similar oximic ligands has been reported to increase the rate of nucleophilic attack on pNPA by up to two orders of magnitude compared to the free basic oximate.[198]

Complex **5-3** on the other hand can be assumed to bind the metal ion relatively tightly based on the reported binding constant for its aldoxime analogue ($K_d \approx 12$ mM).[203] For **5-1** and **5-3** the coordination from the ligand can be tetradentate if the nucleophile coordinates to the nuclei which has been proposed for similar nucleophilic complexes.[14,203]

The activity of the respective complexes was studied using bis-(4-nitrophenol) phosphate (BNPP) and 4-nitrophenyl acetate (pNPA) to investigate their ability to activate phosphate diesters and the nucleophilicity of the respective oximes.

Complex **5-2** was not used successfully in the kinetic analysis due to inconsistency and irreproducibility of the results obtained. The complex was intermittently reactive at different pH but not in a reproducible way. This complex would have been interesting to study given its similarity to the aldehyde hydrate in Figure 5.2. All other complexes yielded measureable activity and were compared to literature reports where appropriate.

In order to investigate the nucleophilicity of the oximes the substrate must not bind to the Zn(II) in order to exclude any contribution from Lewis acidic activation. The pNPA is not expected to bind to the metal ion of the complexes and it is significantly more labile. The observed increase in rate for the hydrolysis of pNPA compared to the background reaction under the same conditions corresponds to a nucleophilic attack by the oxime.

The metal ions are thought to aid the activation of the oxime nucleophile (reducing the p*K*a of nucleophile) and to aid in turnover by way of a metal coordinated hydroxide, see Scheme 5.5.[204] The reactivation or turnover has not been demonstrated here since subsaturating concentrations of substrate were used.

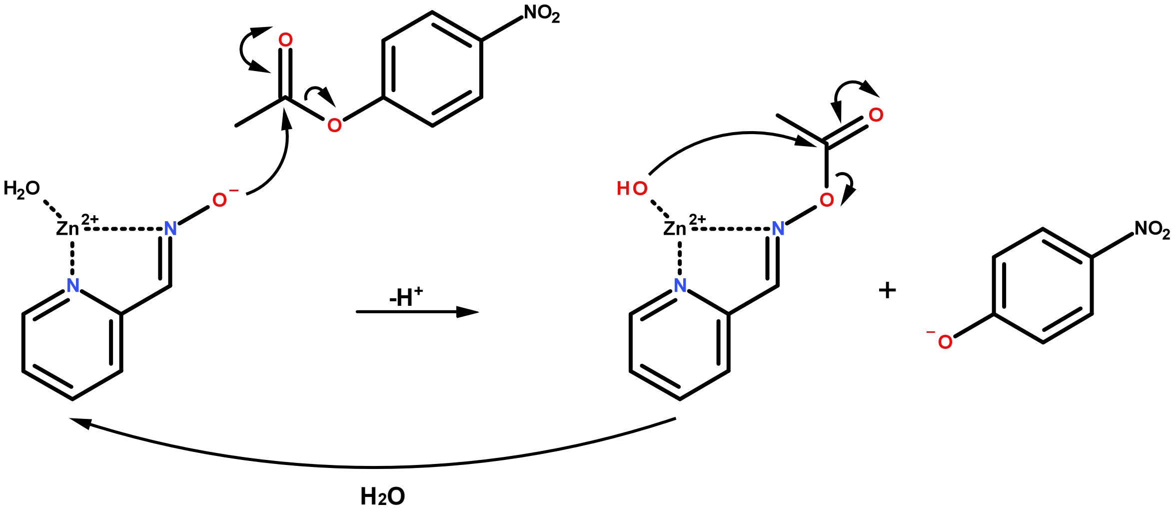

Scheme 5.5. Proposed mechanism for the cleavage of pNPA using oximes illustrated by 5-4.

The reactivity of the complexes towards the hydrolysis of pNPA was monitored at pH 7.4, see Table 5.1. The relative rates for the nucleophilic attack on pNPA revealed that the nucleophilicity of **5-3** and **5-5** are similar. The pNPA is not expected to bind to Zn(II) and this activity is assumed to provide a useful measure of the nucleophilicity of the oximes with minimal or no contribution from Lewis activation of pNPA. The most reactive complex **5-3**, with an oxime nucleophile, was over 10^3-fold more reactive than its alcohol equivalent **5-1**. Although the data set is too small to draw extensive conclusions regarding consistency of activity for different compounds bearing similar nucleophilic moieties, these results do strengthen this notion. Likewise, the structural difference between the oxime moieties in **5-5**

Complex	k_{obs} (× 10^{-5}) (s^{-1})	k_{obs} ratio ($k_{5\text{-}x}/k_{5\text{-}1}$)
5-1	3.92 (± 0.0006)	1.0
5-3	7540 (± 47)	1900
5-4	462 (± 0.81)	120
5-5	6110 (± 22)	1600
5-6	542 (± 0.92)	140
5-7	156 (± 0.10)	40

Table 5.1. k_{obs} for the various complexes (1 mM) in 50 mM HEPES (pH 7.4) and 0.1 M ionic strength ($NaNO_3$) with 50 µM pNPA. Complex 5-6 was used with 2 mM $Zn(NO_3)_2$ and kinetic experiment for 5-7 were performed in 24 % EtOH as reported in literature.[197]

(and **5-3**) compared to **5-4** is one methyl group (aldoxime/ketoxime). This small local structural change leads to an order of magnitude difference in reactivity which is consistent with previously reported data.[204]

Interestingly the metal free equivalents of the oximes (**L5-4** and **L5-5**) were reported to display a reverse relationship[204], where the ketoxime is less reactive than its aldoxime equivalent, see Table 5.2.

Compound	Metal	log K_f (M)	pK_a	k_2 (M^{-1} s^{-1})
L5-4	-	-	10.0	45 (± 1)
L5-4	Cu(II)	4.7	3.2	0.003 (± 0.001)
L5-4	Ni(II)	4.2	6.2	0.46 (± 0.03)
L5-4	Zn(II)	2.2	6.5	9.4 (± 0.1)
L5-5	-	-	10.8	22 (± 1)
L5-5	Cu(II)	5.9	3.5	0.2 (± 0.1)
L5-5	Ni(II)	5.0	6.1	6.5 (± 0.5)
L5-5	Zn(II)	2.6	7.0	200 (± 5)

Table 5.2. The second-order rate constant for the cleavage of pNPA at 25 °C with oximic ligands using metal ions is presented in the table. [ligand] = 0.1 - 1 mM, [metal] = 0.02 M and [buffer] = 0.05 M. Table adapted from Mancin, F., Tecilla, P. & Tonellato, U. Activation of Oximic Nucleophiles by Coordination of Transition Metal Ions. *European J. Org. Chem.* 2000, **1045–1050 (2000).**

The BNPP transesterification was studied using the same nucleophilic complexes as presented in Table 5.1 at 1 mM complex concentration, see Table 5.3. Complex **5-3** is clearly the most reactive, surpassing **5-5** by over 2 orders of magnitude. This stands in stark contrast to the relative rates for pNPA that determine the nucleophilicity of the complexes where these two complexes have practically the same reactivity. This could be due to either more effective Lewis acidic activation and/or a more favorable geometry of the nucleophile in **5-3**.

Complex	Initial rate (× 10^{-12}) (M s^{-1})	k_{obs} ratio (k_{5-x}/k_{5-4})
5-1	97.45 (± 0.02)	50
5-3	12321 (± 188)	6200
5-4	1.99 (± 0.02)	1
5-5	21.71 (± 0.02)	11
5-6	8.79 (± 0.03)	4
5-7	2.38 - 88.04	1.2 - 44

Table 5.3. The transesterification rate for 1 mM complex in 50 mM HEPES (pH 7.4) with 0.1 M ionic strength ($NaNO_3$) and 50 µM BNPP. Complex 5-6 was used with 2 mM $Zn(NO_3)_2$ and kinetic experiment for 5-7 was performed in 24 % EtOH as reported in literature.[197] Complex 5-1 was monitored at pH 7.3 and the UV-profile for complex 5-7 was not linear (see Chapter 8.10.2) and is therefore presented as an interval for the slowest and fastest rates observed.

Further data to support these considerations is the rate constant for the complex **5-1**, which is two to three orders of magnitude slower than the oximes in the hydrolysis of pNPA but is comparable to the oximes for BNPP hydrolysis. The least reactive complex was **5-4** (although the data obtained for **5-7** is unreliable and could not be evaluated). The relative activities observed for **5-4** and **5-5** towards BNPP are consistent with the previously observed (pNPA) ratio for ketoxime/aldoxime (10:1). The second-order rate constant for the BNPP transesterification was studied using complexes **5-1** and **5-3**, see Figure 5.7.

A scheme where the monoanionic ionic form was assumed to be the only active species, see Chapter 8.3, was fitted to the pH-rate profile for **5-3** using **Equation 5.1** yielding two pK_a-values corresponding to the two deprotonations of the complex.

$$k_2^{pH} = k_2^{max} \times \frac{[H^+]K_{a1}}{K_{a1}K_{a2}+K_{a1}[H^+]+[H^+]^2} \qquad \text{(Equation 5.1)}$$

The two-fold deprotonation observed for Zn(II) complexes have usually been considered to signify the release of the acidic protons of metal bound water. This holds true for many tridentate ligands that leave two potential coordination sites that can be occupied by water, see Chapter 3. In the case of the tridentate complexes discussed in Chapter 3, the first deprotonation leads to increased activity and represents the formation of a metal bound aqua-hydroxo complex in which the water molecule can be displaced by a substrate. The second deprotonation leads to the formation of a $M(OH)_2$ species that does not allow for substrate binding and therefore leads to reduced activity. Since the two metal-bound water molecules are kinetically equivalent in the case of tridentate complexes it is not possible (nor necessary)

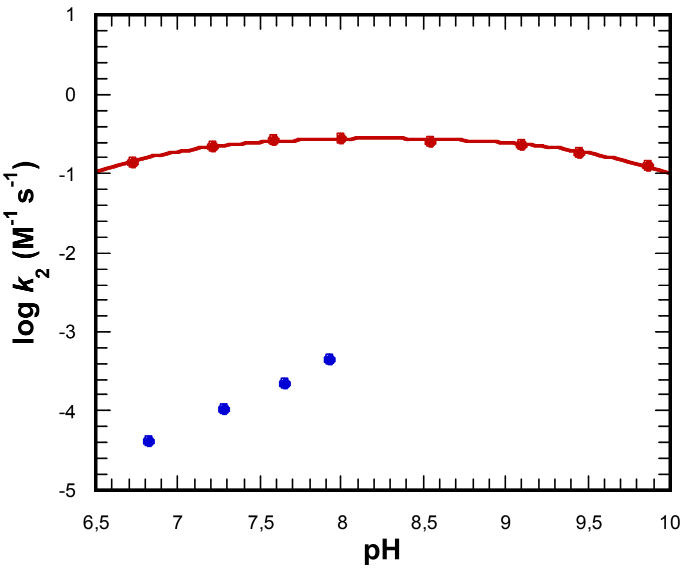

Figure 5.7. The second-order rate constant for 5-1 (blue) and 5-3 (red) in 50 mM HEPES or CHES with 0.1 M ionic strength ($NaNO_3$) at various pH. The data obtained for 5-1 was only reliable up to pH 8 due to precipitation at higher pH.

to determine which of the two is deprotonated first. This becomes more important in the case where there are two non-identical acidic nucleophilic species bound to the metal ion.

In this case **5-1** and **5-3** are both tetradentate with nucleophilic moieties (alkoxy and oxime, respectively) occupying one coordination site of the Zn(II). This indicates that the kinetic pK_a-values represent the deprotonation of the nucleophile (alkoxy or oxime) and a metal bound water molecule, see Scheme 5.6.

The kinetic p$K_{a\text{-value}}$s for **5-3**, 6.74 and 9.72, are difficult to assign to either one of the two potential acidic protons although data in the literature suggest that the coordination of oximes to metal ions reduce their pK_a to between 6.5 and 8.[204] If the metal induced pK_a reduction is taken to be representative of the oxime system, the first pK_a would represent the oxime and the second would represent the water. Regardless of which of the two (aqua or oxime) is deprotonated first, the reactive structure must be the form where the oxime is deprotonated and the other metal bound species is water. Even if the water is the first to be deprotonated the dynamic equilibrium would produce some of the desired deprotonated oxime.

The limiting second-order rate constant for **5-3** was determined from the fit in Figure 5.7 to be 0.29 (± 0.01) M^{-1} s^{-1}. Since it was not possible to fit the equation for two deprotonations to the data for complex **5-1**, it is not possible to carry out a direct comparison

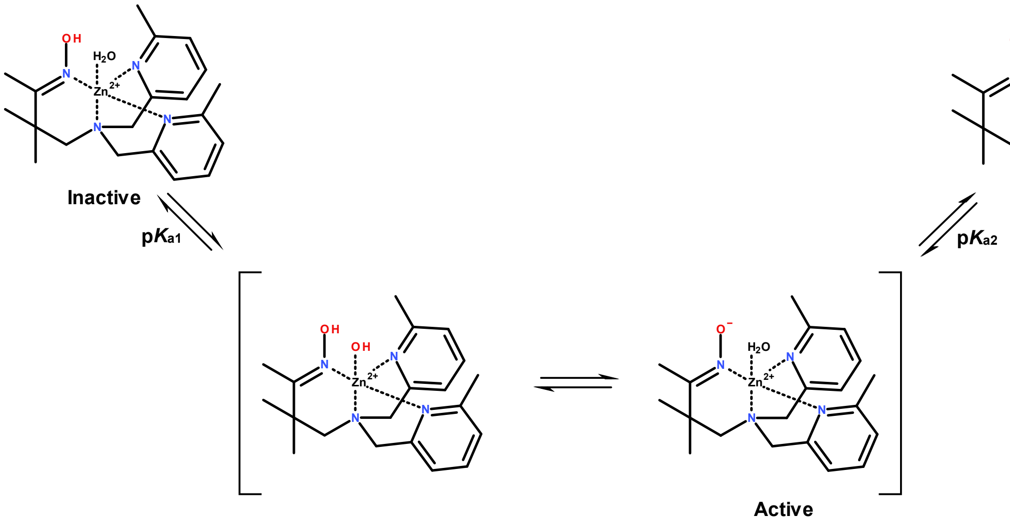

Scheme 5.6. The representation of the protonation states of the complex 5-3.

of the limiting second-order rate constants.The closest comparison that can be made is at pH 8 where the apparent second-order rate constants reveal a 600-fold rate increase for **5-3** over **5-1**. The data indicate that the activity of the complex **5-1** is highly pH dependent since a pH increase of 0.5 translates into one order of magnitude increased reactivity. The steep increase indicates that the measured activity for **5-1** in this particular pH-range is below the pK_a of the nucleophile of the complex, and suggests that more than one deprotonation is required to form the active species.

The mechanism by which the substrate is transesterified needs to be investigated to further understand the interactions involved. The UV profile for the transesterification of BNPP with **5-1**, see Figure 5.8, is a plot of absorbance points (400 nm) measured over time and was carried out in order to follow the single and potentially double displacement of PNP.

Two different concentrations of **5-1** (1 mM and 10 mM) were used to allow slow and fast monitoring of the progression of the reaction. The absorbance for 50 µM BNPP (at 400 nm and pH 8) would be 0.8 respectively 1.6 corresponding to one or both 4-nitrophenolate (50 µM) being displaced.

The pseudo-first-order rate constant *k'* (s^{-1}) was obtained using **Equation 5.2**, where the absorbance at 400 nm, Abs_{400nm}, at any given time, *t*, is proportional to the concentration of 4-nitrophenol released, [PNP].

$$(Abs_{400nm})_t = Abs_{400nm}^{max} + (Abs_{400nm}^{min} - Abs_{400nm}^{max})e^{-k't} \quad \text{(Equation 5.2)}$$

At 1 mM the reaction was monitored for a long time but not long enough to accurately determine the potential two-stage cleavage of BNPP. Therefore the increase in concentration of **5-1** aims to allow for faster monitoring of the reaction. Unfortunately the 10 mM **5-1** reaction produced a cloudy solution and could not be used to draw accurate conclusions regarding the reaction product although the observed pseudo-first-order rate was more than 1 order of magnitude greater than the 1 mM **5-1** experiment.

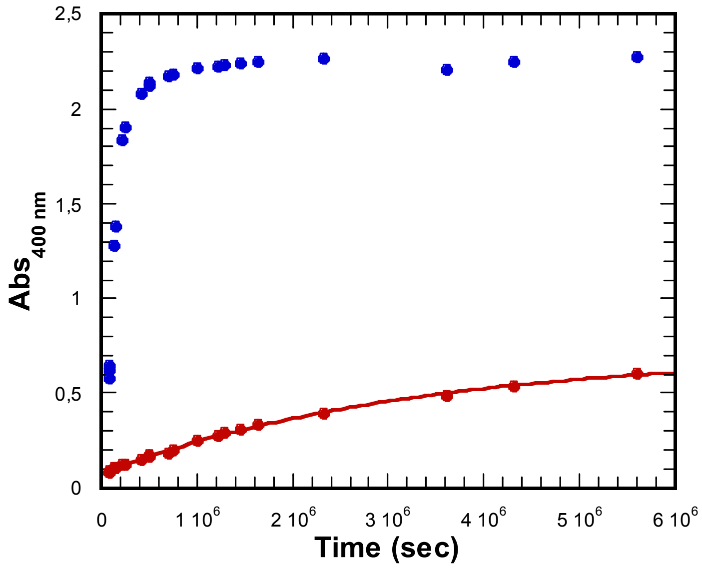

Figure 5.8. The transesterification of 50 μM BNPP using 1 mM (red) and 10 mM (blue) 5-1 in 50 mM HEPES at pH 8 with 0.1 M ionic strength ($NaNO_3$).

Although the experiments have not yielded conclusive results about the mechanism, data from the literature using similar mononuclear nucleophilic complexes suggest that the reaction mainly proceeds by the transesterification involving two units of nucleophilic catalyst.[14] The first nucleophilic attack on BNPP forms the transesterified phosphate with 4-nitrophenol and the ligand, see Scheme 5.7.

The nucleophile is at this stage covalently bound to the phosphate and this likely breaks the coordination to the metal ion since it would otherwise be forced to take the configuration of a distorted eight-membered ring. Once this occurs the metal ion can coordinate another molecule of BNPP if the substrate is in excess compared to the complex, which is not the case here. Therefore the further release of PNP must come from the recruitment of an additional molecule of the complex that transesterifies the phosphate a second time producing the second equivalent of PNP.[14] In the case of BNPP reacting with **5-3** the UV profile indicates full transesterification of BNPP since the amount of 4-nitrophenol released (≈ 100 μM) is

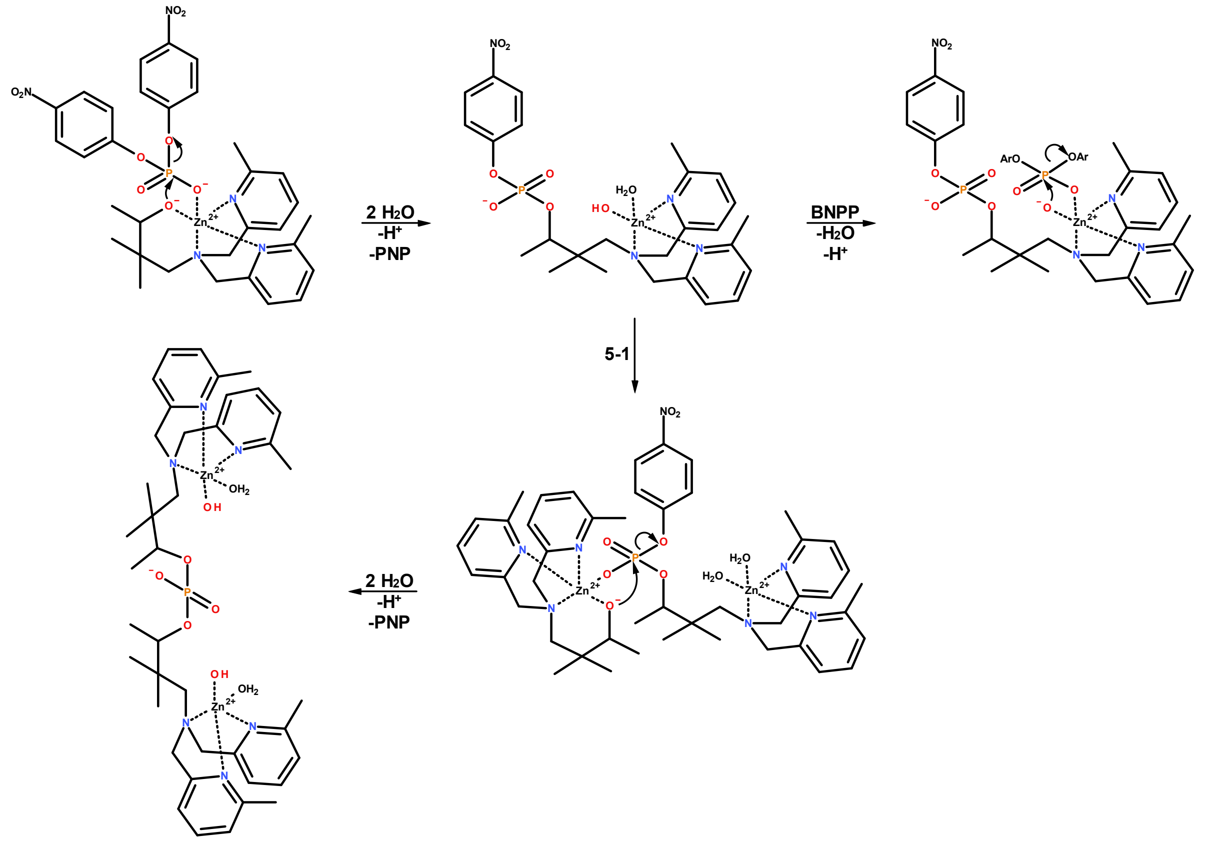

Scheme 5.7. The transesterification mechanism as suggested in literature[14] for BNPP by the nucleophilic complex 5-1 starting with the active hydroxo form of the complex.

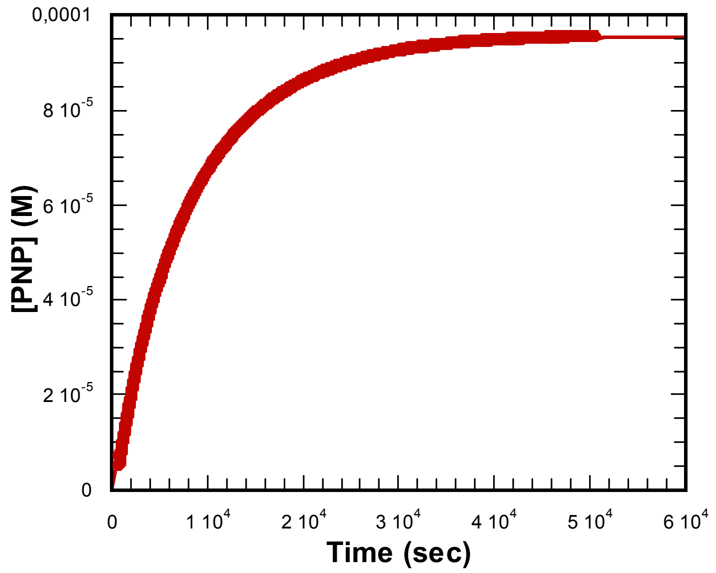

Figure 5.9. The UV profile at 400 nm for 5-3 indicates the (double) displacement of 100 µM 4-nitrophenol at pH 7.4 from 50 µM BNPP. A first-order equation, see Equation 5.2, yielded a smooth fit to the plot.

consistent with the two-fold displacement of PNP from BNPP (50 µM). A first-order equation was accurately fit to the data points, see Figure 5.9, and did not display any deviation over time. This indicates that the second displacement occurs much faster than the first and thus the first displacement is rate limiting.

5.5 - Further investigations

The structures of compounds **L5-1** and **L5-8**, see Figure 5.10, allow comparison of the influence of the dimethyl alkylation on activity in a similar way as has been reported in literature for complexes with nucleophilic primary alcohols.[132]

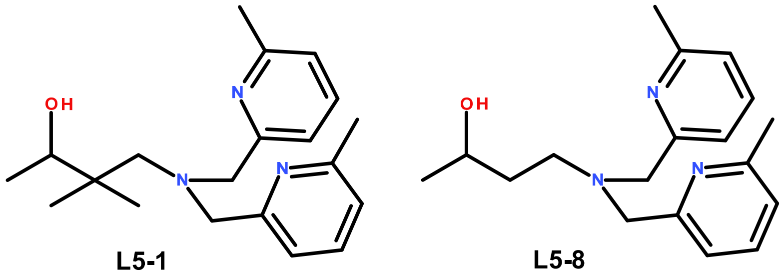

Figure 5.10. The structure of the analogous compounds L5-1 and L5-8.

Having steric interactions that could force the metal nucleus and nucleophile into closer proximity of each other has been reported to form more efficient interactions. The ligand **L5-8** was successfully made after substantial synthetic effort to obtain the commercially unavailable 4-aminobutan-2-ol appendage.

The synthesis of the 4-aminobutan-2-ol starting material was more labor intensive than was initially expected given the simple structure of the compound. An initial attempt involved the reduction of acetoacetamide, see Scheme 5.8.

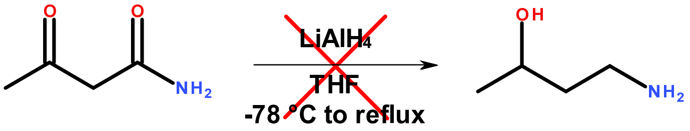

Scheme 5.8. The attempted reduction of acetoacetamide.

This direct route only yielded small amounts of product as assessed by ^{1}H NMR spectroscopy. Attention was then turned to 4-hydroxybutan-2-one that could be used in a

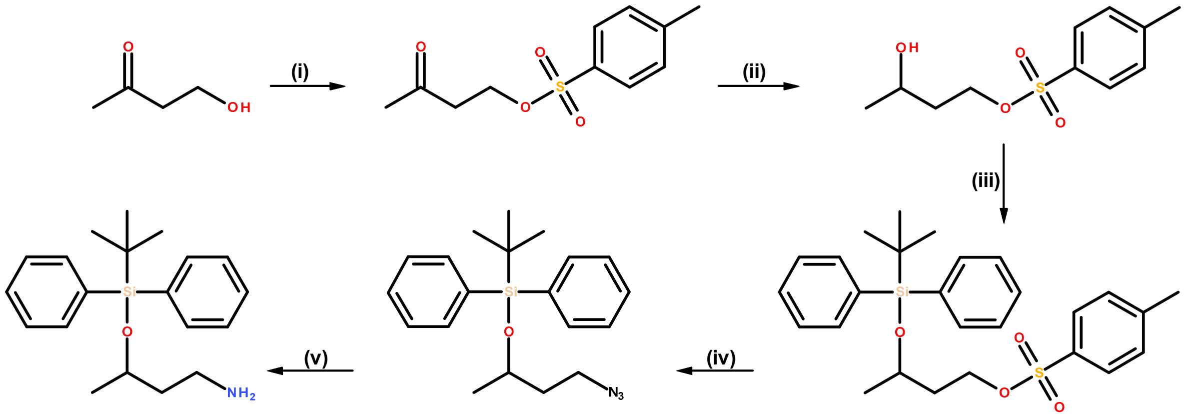

X5

Scheme 5.9. The synthesis of the precursor 3-[*tert*-butyl(diphenyl)silyl]oxybutan-1-amine (X_5) for ligand L5-8. The starting material 4-hydroxybutan-2-one was reacted with (i) TsCl, Pyridine, DCM, 21 %; (ii) $NaBH_4$, EtOH, 81 %; (iii) tBDPS-Cl, imidazole, THF; (iv) NaN_3, DMF, 87 % over 2 steps; (v) H-Cube, H_2, 10 % Pd/C, EtOAc, 100%.

more elaborate synthetic route, see Scheme 5.9. The first reaction in step (i), see Scheme 5.9, was particularly sensitive to heat and multiple batches of the product were lost due to heating during solvent removal until the solvent was changed to DCM and not heated above 30 °C. The tosylated product needed to be purified from the reaction mixture relatively promptly in order to avoid further decomposition.

The reduction in step (ii) using $NaBH_4$ was simple and efficient although a slightly improved yield was achieved using BH_3-THF reduction. The displacement of the tosylate in step (iii) in Scheme 5.9 was initially attempted using NaN_3, step (vi), and phthalimide, step (vii) and (viii), but both approaches failed to yield sufficient amounts of product, see Scheme 5.10. This was most likely due to the small and relatively volatile target compound being lost in the workup.

The target compound was made less volatile and easier to detect by the incorporation of a temporary protecting group *tert*-butyldiphenylsilane (tBDPS). The formation of the azide in step (iv) proceeded without problem as did the final reduction step (v), see Scheme 5.9 to yield the protected target compound **X_5**.

The attachment of the precursor (**X_2**) was achieved using the same procedure as for **L5-1**, see Scheme 5.2. Removal of the tBDPS protecting group was achieved using tetrabutylammonium fluoride (TBAF) in good yield, see Scheme 5.11.

The compound **L5-8** was not kinetically analysed although similar primary alcohols

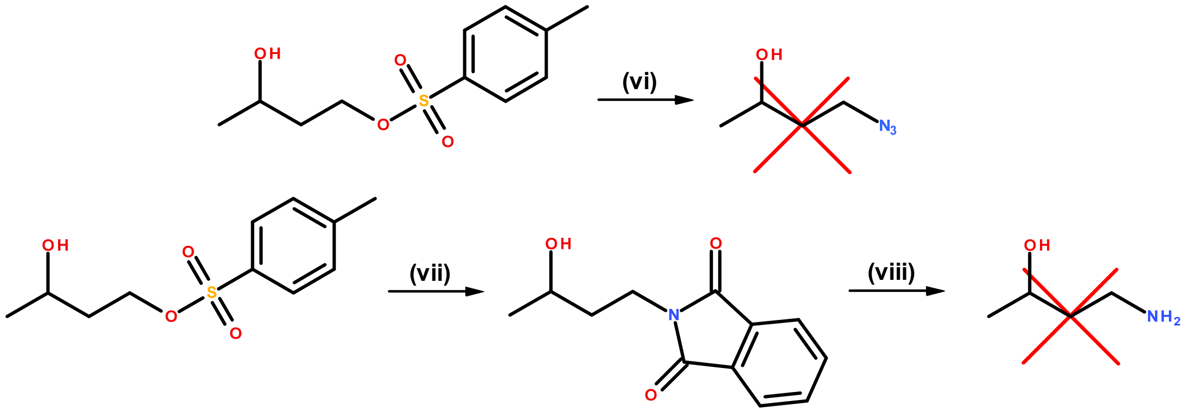

Scheme 5.10. The attempted synthesis of 4-aminobutan-2-ol. The displacement of tosylate using (vi) NaN3, DMF (vii) Potassium phthalimide, DMF (viii) hydrazine hydrate, EtOH, reflux.

have been studied in literature.[132,195] The gem-dimethyl unit was initially incorporated to counter the elimination observed in efforts to synthesise the aldehyde equivalent. The ketone is considered to be less sensitive to this elimination process and thus could possibly yield the

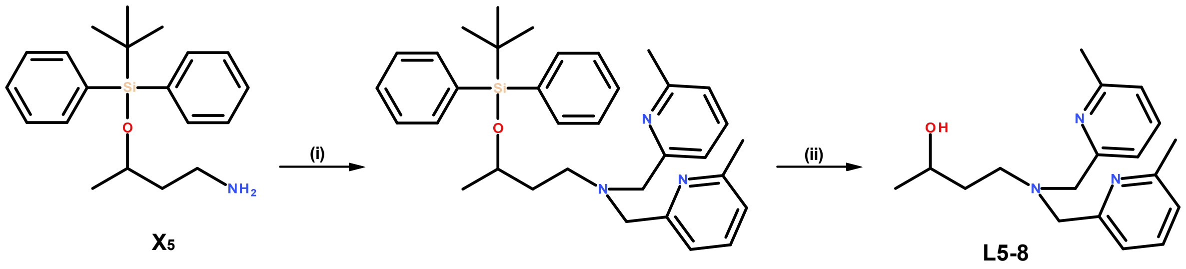

Scheme 5.11. The synthetic route for the synthesis of L5-8 using precursor X_5. The precursor X_5 was reacted with (i) 2-(iodomethyl)-6-methyl-pyridine, 31 %; (X_2), DIPEA, DMF (ii) TBAF, THF, 87 %.

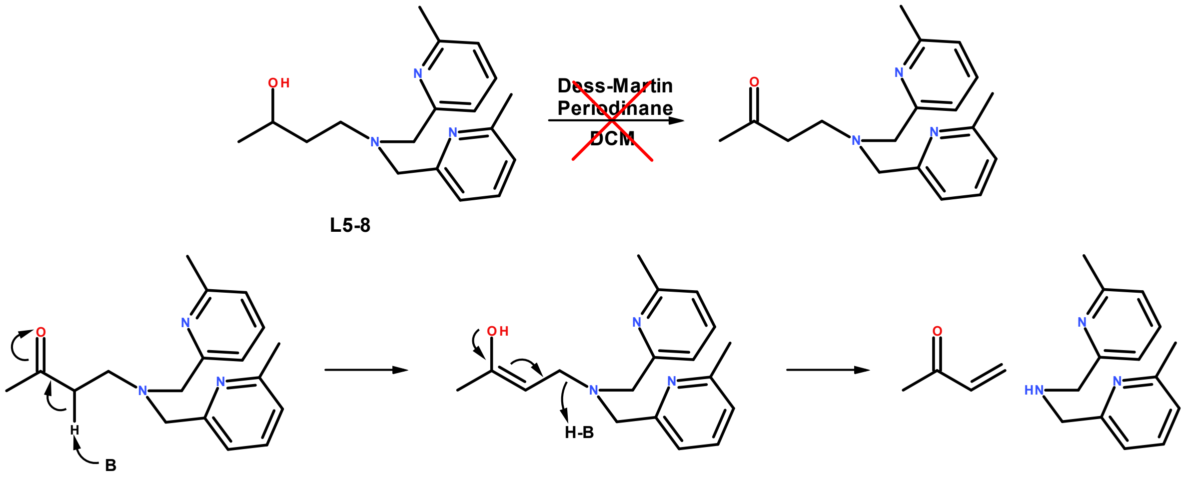

Scheme 5.12. The proposed mechanism for the elimination leading to the loss of product.

desired compound. The attempt to oxidise **L5-8** to the corresponding ketone, see Scheme 5.12, was unsuccessful and the resulting reaction mixture was reminiscent of the attempted oxidation of **L2-1**, see Chapter 2.6.

5.6 - Conclusion

The increased reactivity that was observed for the ketoxime (**5-5**) over the aldoxime (**5-4**) was initially thought to be due to the Thorpe-Ingold effect where the steric compression leads to the nucleophile adapting a more favorable geometry for the nucleophilic attack. This effect can be illustrated by the reported effective molarities (EM)[21] of the intramolecular nucleophilic attack on the mesylates in Figure 5.11.

This would hold true if this difference in reactivity was observed for the Michaelis complex (with a coordinating substrate) where the oxime becomes an intramolecular component for **5-5** (BNPP) and **5-4** (BNPP). It appears that this difference in activity is also observed for the non-coordinating substrate pNPA (not forming a Michaelis complex) which seems to indicate that some other mechanism than simple Thorpe-Ingold compression is involved.

Additionally, it appears that complex **5-3** (0.29 ± 0.01 M^{-1} s^{-1}) is less reactive than its aldoxime equivalent (0.80 ± 0.08 M^{-1} s^{-1}) that had previously been studied[203] which is not consistent with the expected increased reactivity for the ketoxime (10-fold) over the aldoxime.

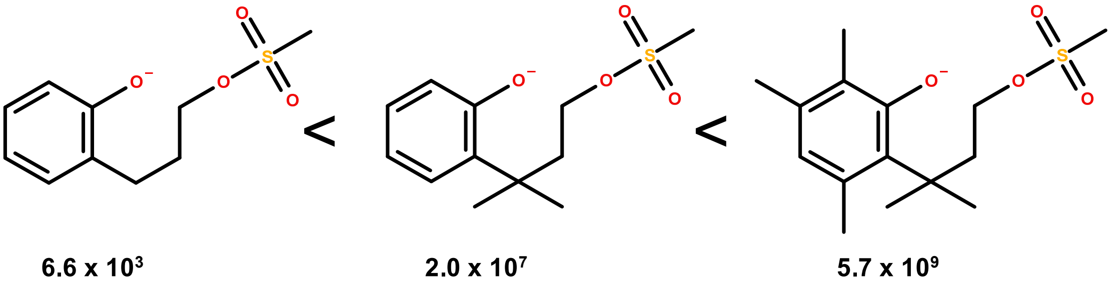

Figure 5.11. The increase in effective molarity with increasing steric interaction.

The 3-fold lower second-order rate constant for **5-3** could therefore represent a 30-fold reduction compared to the expected reactivity. The formation of an inactive dimer, see Figure 5.12, in the context of oximic complexes has been reported in literature[197] and the dimerisation is a potential factor that could cause the observed decrease in activity since it would prevent the substrate from binding to the complex.[207] Although this was not investigated here, similar complexes indicate this behavior.[203]

The dimer has been suggested to cause a reduction in activity since less of the purported active monomeric complex will be available to bind the substrate. This is indicated by a non-linear relationship between the rate and complex concentration which has been reported for the aldoxime complex.

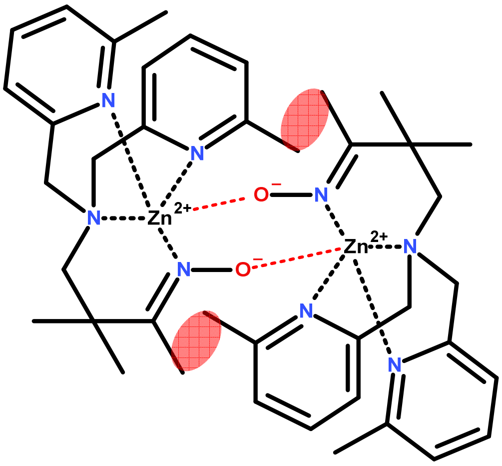

Figure 5.12. The proposed structure of the dimerisation of 5-3 showing the internuclear coordination (red dashed bonds) with potential steric interactions highlighted (red ellipse).

In contrast, complex **5-3** displays a linear relationship in the region of 0.2 mM to 1 mM with no indication of curvature. This does however not exclude the formation of dimeric structures since a linear relationship would also be observed if the dimerisation constant is much higher or lower than concentration range in which the complex is studied.

Interestingly, the linear plots indicate a negative intercept with the Y-axis (initial rate), see Figure 5.13, which in not consistent with the expected positive intercept for the formation of an inactive dimer. This could potentially indicate that the dimer is a reactive species.

The expected rate increase for the ketoxime **5-3** (10-fold) and the observed rate decrease (3-fold) equals an overall discrepancy of 30-fold.

Despite this apparent reduction in reactivity between **5-3** and its aldoxime equivalent, both complexes are sufficiently reactive to justify the incorporation into DNA binding scaffolds.

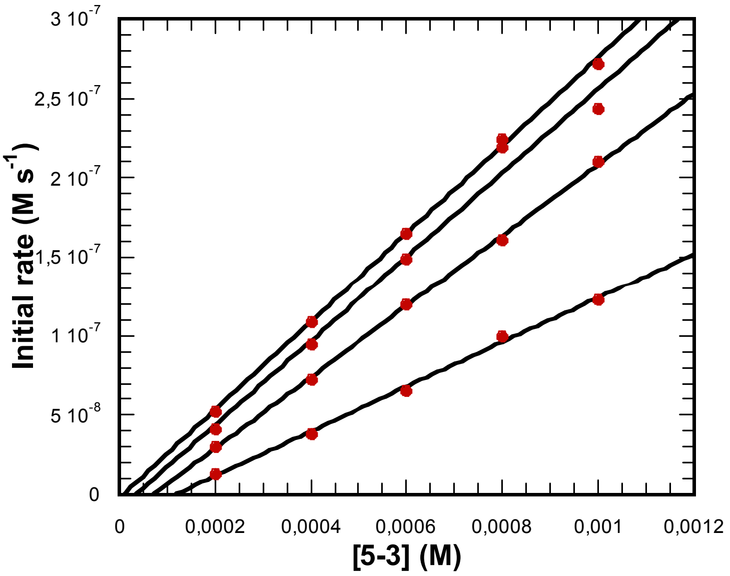

Figure 5.13. The initial rate versus concentration of complex 5-3 at various pH (7-8) displays a linear relationship.

5.7 - Future work

The concept of peptidic complexes discussed in Chapter 4 was based on the peptide coiled-coil structure GCN4-bZIP which is known to bind DNA.[165,208] This inspired the work on nucleophilic complexes that could be incorporated into the peptide backbone.

The non-nucleophilic complexes presented in Chapter 4 have similar structural features to complexes that are known to hydrolyse BNPP but the introduction of a nucleophile has been shown to increase the rate of reaction, depending on the nucleophilic functionality, by orders of magnitude.[14]

The data presented here show the importance of having a structural arrangement that allows for coordination and Lewis activation of the substrate as well as having a highly nucleophilic group in the proximity of the substrate.

The structure of the potential ligands for peptide incorporation could be either an aldoxime or ketoxime, see Figure 5.14. The synthesis of these complexes would require many synthetic steps so it is important to ensure that the end result is worth the effort.

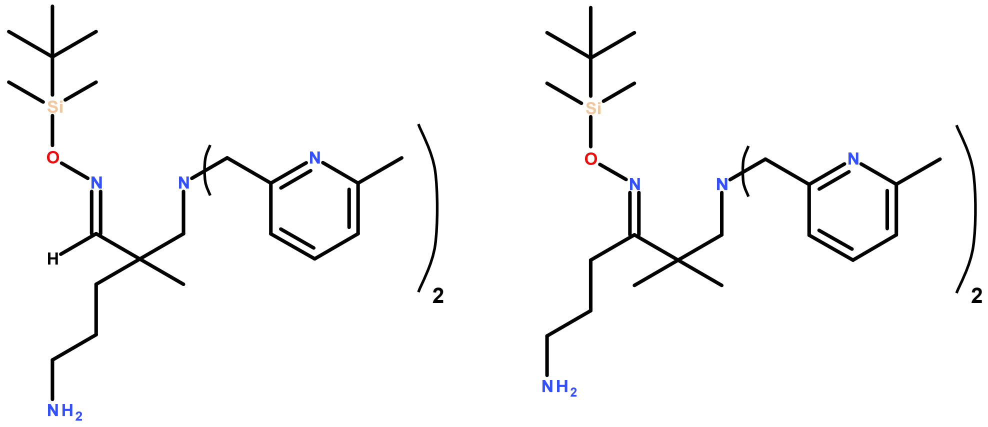

Figure 5.14. The proposed oximic ligand for incorporation into the peptide structure.

Chapter 6 - Final conclusion

This project has involved the study of the effects on reactivity of the microenvironment around dinuclear core in small molecular Zn(II) complexes though the interactions with the 2-pyridine substituents (H, Me, NH_2 and NHMe) of the ligand structure. The investigation into the effects of these functionalities on ground state and transition state binding indicated that the use of potential hydrogen bond donor (NH_2, NHMe) leads to substantial stabilisation of the transition state. The main contribution to activity is electrostatic stabilisation of the transition state structure by the dinuclear cationic core although the hydrogen bonding in the microenvironment is representative of the additional interactions found in secondary coordination sphere around metal ions in enzymes active sites.

Additionally, attention was focused on the effects of the alkoxy-bridging functionality between that is considered undesirable from an electrostatic point of view. The reactivity of the dinuclear complexes containing a neutral oxazole bridging group was only moderate in comparison to the alkoxy-bridged equivalents.

The investigation into the effects of altering the structure of the internuclear bridging functionality (alkoxy) precedes the complete removal of the covalent internuclear linkage in order to study the association of mononuclear complexes in larger structural arrangements.

The non-covalent interactions were studied by incorporating mononuclear Zn(II) complexes into the association-promoting environments of membranes and peptidic coiled-coil structures. The membrane-based approach yielded more than an order of magnitude difference in reactivity between the membrane anchored complex and the solution based equivalent although this result is most likely due to medium effects at the membrane interface. The effect could be further studied for rate enhancement if highly reactive dinuclear complexes could be embedded in the membrane via a lipophilic appendage.

The peptide-based approach was not successful due to the inability of the short sequence to for the coiled-coil structures. This could be solved by extending the peptide sequence or alternatively investigating the possibility of intrahelical association.

The nucleophilic complexes were studied for potential future incorporation in DNA binding peptide sequences. The effects of relatively small structural changes resulted in substantial differences in rate. The dimerisation could potentially be the cause of the reduced activity although this is counter intuitive since a bulkier structure should disfavor close interaction.

These different approaches for the investigation of potential rate-enhancing interactions are small steps on the way to the ultimate goal of artificial catalyst with enzyme-like rate acceleration. The potential future application of the small molecular catalysts has been demonstrated in literature[209,210] in the form of oligonucleotide based artificial nucleases (OBAN). The OBAN's consist of neocuproine functionalized nucleosides in a carefully selected oligonucleotide sequence, see Figure 6.1. The oligonucleotide provides a sequence specific interaction with RNA and the neocuproine complex acts as the cleaving unit.

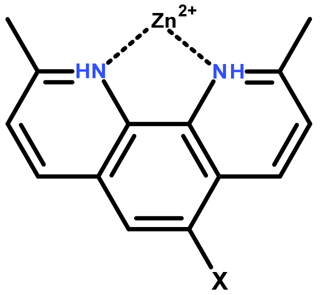

X = Oligonucleotide

Neocuproine-Zn(II)

Figure 6.1. The structure of the neocuproine-Zn(II) complex used in literature to cleave RNA.

The knowledge gained through the research into catalytic phosphate diester hydrolysis is the tantalising prospect of artificial nucleases for therapeutic purposes, although given the obstacles it appears that this is indeed a long term objective.

Chapter 7 - Experimental

7.1 - Instrumentation

All commercially acquired chemicals were used without further purification unless otherwise stated. The TLC analyses were performed using Merck 60 F_{254nm} silica coated aluminium sheets and the flash chromatographic purifications were performed using Fluorochem silica gel 40-60 µ 60Å. All HPLC purifications were performed using a Waters Xbridge OBD 130 Å C-18 19 x 250 mm column or a Phenomenex Kinetex XB-C18 100 Å 5µm 21.2 x 250 mm column in a MeCN/H_2O solvent system with 0.1 % TFA unless otherwise stated.

The ^{1}H NMR, ^{13}C NMR and ^{31}P NMR analyses were performed using Bruker AV1-250, AV1-400, DPX-400 or AV3HD400 corresponding to the frequencies 250MHz and 400 MHz for ^{1}H, 101 MHz and 63 MHz for ^{13}C and 162 MHz for ^{31}P NMR in $CDCl_3$, MeOH-d_4 or D_2O.

The spectra are reported relative to the TMS standard and the multiplicity is reported as: singlet (s), broad singlet (br s), doublet (d), triplet (t), quartet (q) and multiplet (m).

7.2 - Chapter 2 syntheses

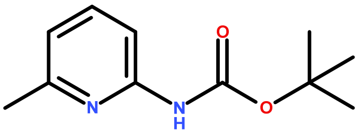

***tert*-butyl N-(6-methyl-2-pyridyl)carbamate**

6-methylpyridin-2-amine (30.00 g, 277.42 mmol) was dissolved in DCM (150 ml). The solution was stirred and di-*tert*-butyl-dicarbonate (60.55 g, 277.42 mmol) was added to the solution along with more DCM (150 ml). Triethylamine (42.30 ml, 305.16 mmol) was added to the stirred solution followed by slow addition of solid DMAP (0.68 g, 5.55 mmol). The reaction was stirred and after a few minutes vigorous. The reaction was left stirring over night after which the solvent was evaporated yielding a yellow/orange viscous liquid. The crude mixture was purified using flash chromatography Et_2O/Hexane (50/50). The product appears as a faint blue spot on fluorescent TLC plates at 254 nm (with a r.f-value of 0.65). The product was obtained in good yield (80 %) as a clear viscous liquid that sometimes crystallises into a white solid (46.00 g, 220.88 mmol).

^{1}H NMR (400 MHz, $CDCl_3$) δ 7.73 (d, *J* = 8.3 Hz, 1H, Py-*H*), 7.56 (t, *J* = 7.9 Hz, 1H, Py-*H*), 7.45 (br s, 1H, N*H*Boc), 6.82 (d, *J* = 7.4 Hz, 1H, Py-*H*), 2.44 (s, 3H, CH_3), 1.52 (s, 9H, $(CH_3)_3$)

^{13}C NMR (101 MHz, $CDCl_3$) δ 156.76(*Py*-CH_3), 152.44 (C=O), 151.20 (*Py*-NHBoc), 138.42 (Py-H), 117.93 (Py-H), 109.03 (Py-H), 80.75 (*C*$(CH_3)_3$), 28.26 $(CH_3)_3$, 24.01 (Py-*C*H_3)

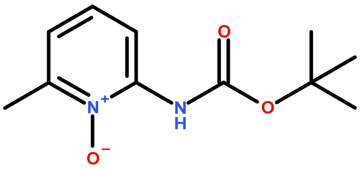

tert-butyl N-(6-methyl-1-oxido-pyridin-1-ium-2-yl)carbamate

tert-butyl N-(6-methyl-2-pyridyl)carbamate (5.56 g, 26.72 mmol) was dissolved in DCM (100 ml) and stirred in an ice bath. After 10 min stirring mCPBA 77% (6.59 g, 38.16 mmol) was added and the reaction mixture was left stirring and allowed to adapt room temperature over night. The reaction mixture went from clear to cloudy to orange during the reaction. The crude mixture was washed with saturated $NaHCO_3$ solution until no more effervescence was observed and the organic phase was dried over Na_2SO_4. The product was concentrated under reduced pressure and was obtained in 97 % yield (5.82 g, 25.95 mmol) as a viscous orange liquid. TLC revealed only one spot with an r.f-value of 0.28 in 75/25 EtOAc/Hexane.

^{1}H NMR (400 MHz, $CDCl_3$) δ 9.43 (s, 1H, N*H*Boc), 8.01 (d, *J* = 8.4 Hz, 1H, Py-H), 7.19 (t, *J* = 8.1 Hz, 1H, Py-H), 6.88 (d, *J* = 7.6 Hz, 1H, Py-H), 2.54 (s, 3H, (CH_3), 1.52 (s, 9H, ((*C*$H_3)_3$)

^{13}C NMR (101 MHz, $CDCl_3$) δ 151.68 (C=O), 147.13 (*Py*-CH_3), 144.61 (*Py*-NHBoc), 126.89 (Py-H), 117.86 (Py-H), 110.46 (Py-H), 81.96 (*C*$(CH_3)_3$), 28.13 ($(CH_3)_3$), 18.20 (Py-*C*H_3)

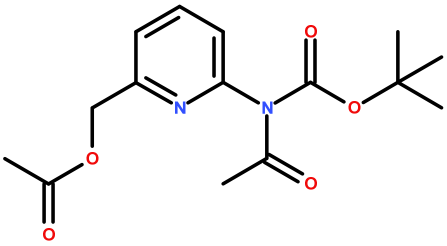

[6-[acetyl(*tert*-butoxycarbonyl)amino]-2-pyridyl]methyl acetate

tert-butyl 1 N-(6-methyl-1-oxido-pyridin-1-ium-2-yl)carbamate (28.38 g, 126.55 mmol) was dissolved in Ac_2O (250 ml, 2644.73 mmol) and stirred at 70 °C over night. The excess Ac_2O was evaporated in vaccuo and the crude mixture was purified by flash chromatography using EtOAc/Hexane (75/25). The title compound (8.74 g, 28.35 mmol) was not the major component of the mixture but it was isolated with a r.f-value of 0.74 in 22 % yield.

^{1}H NMR (400 MHz, $CDCl_3$) δ 7.80 (t, J = 7.8 Hz, 1H, Py-H), 7.35 (d, J = 7.3 Hz, 1H, Py-H), 7.10 (d, J = 7.8 Hz, 1H, Py-H), 5.20 (s, 2H, Py-CH_2), 2.60 (s, 3H, CH_3C=O), 2.14 (s, 3H, CH_3C=O), 1.36 (s, 9H, $(CH_3)_3$)

^{13}C NMR (101 MHz, $CDCl_3$) δ 172.93 (*C*=OCH_3), 170.48 (*C*=OCH_3), 155.69 (*Py*-CH_2), 151.93 (*Py*-N(Ac)Boc), 151.66 N(Ac)*C*=OC$(CH_3)_3$) , 138.85 (*Py*-H), 122.41 (*Py*-H), 121.07 (*Py*-H), 83.61 (*C*$(CH_3)_3$), 66.26 (Py-*C*H_2), 27.76 ($(CH_3)_3$), 26.16 (C=O*C*H_3), 20.85 (C=O*C*H_3)

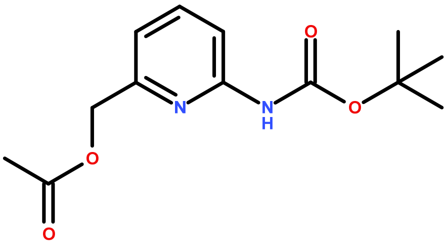

[6-(tert-butoxycarbonylamino)-2-pyridyl]methyl acetate

The purification of [6-[acetyl(*tert*-butoxycarbonyl)amino]-2-pyridyl]methyl acetate using EtOAc/Hexane (75/25) also yielded the title compound in small amounts with a r.f-value of 0.83.

^{1}H NMR (400 MHz, $CDCl_3$) δ 7.88 (d, J = 8.4 Hz, 1H, Py-H), 7.67 (dd, 8.1, 7.8 Hz, 1H, Py-H), 7.01 (d, J = 7.6 Hz, 1H, Py-H), 5.09 (s, 2H, Py-CH_2), 2.16 (s, 3H, CH_3C=O), 1.52 (s, 9H, $(CH_3)_3$).

^{13}C NMR (101 MHz, $CDCl_3$) δ 170.61 (*C*=OCH_3), 153.97 (*Py*-CH_2), 152.31 (NH*C*=$OC(CH_3)_3$), 151.61 (*Py*-NHBoc), 138.88 (*Py*-H), 116.35 (*Py*-H), 111.43 (*Py*-H), 81.03 (*C*$(CH_3)_3$), 66.42 (Py-*C*H_2), 28.23 ($(CH_3)_3$), 20.92 (C=O*C*H_3)

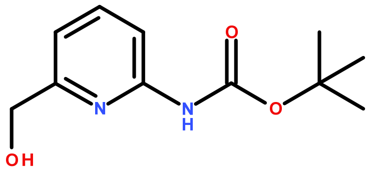

tert-butyl N-[6-(hydroxymethyl)-2-pyridyl]carbamate

[6-[acetyl(*tert*-butoxycarbonyl)amino]-2-pyridyl]methyl acetate (8.74 g, 28.35 mmol) was dissolved in MeOH (30 ml) and stirred while saturated NaOH solution (2 ml) was added dropwise. The solution went from yellow to orange/brown upon addition of NaOH. The reaction mixture was stirred for 1 hour after which the solvent was evaporated. Water was added to the reaction mixture and the compound was extracted with Et_2O and dried over $MgSO_4$. The title compound has a r.f-value of 0.64 in EtOAc/Hexane (75/25). The product did not require any further purification after the extraction and was obtained in 86% yield (5.48 g, 24.44 mmol) as a viscous yellow liquid,

^{1}H NMR (400 MHz, $CDCl_3$) δ 7.85 (d, *J* = 8.3 Hz, 1H, Py-H), 7.68 (dd, *J* = 8.2, 7.5 Hz, 1H, Py-H), 7.43 (s, 1H, N*H*Boc), 6.92 (d, *J* = 7.5 Hz, 1H, Py-H), 4.67 (s, 2H, Py-CH_2), 3.50 (s, 1H, CH_2O*H*), 1.55 (s, 9H, $(CH_3)_3$)

^{13}C NMR (101 MHz, $CDCl_3$) δ 157.36 (*Py*-CH_2), 152.18 (*C*=O), 151.06 (*Py*-NHBoc), 139.04 (*Py*-H), 114.95 (*Py*-H), 110.56 (*Py*-H), 81.24 (*C*$(CH_3)_3$), 63.73 (Py-*C*H_2), 28.25 ($(CH_3)_3$)

HRMS (ESI-TOF) m/z: Calculated for $C_{11}H_{17}N_2O_3$: 225.1234

Found: 225.1231 $[M+H]^+$

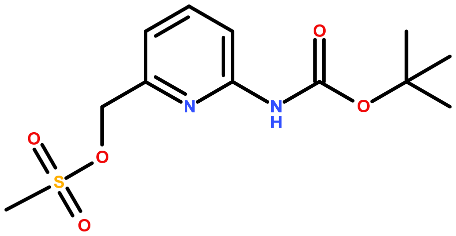

[6-(*tert*-butoxycarbonylamino)-2-pyridyl]methyl methanesulfonate

tert-butyl N-[6-(hydroxymethyl)-2-pyridyl]carbamate (5.48 g, 24.44 mmol) was dissolved in dry THF (100ml) and dry distilled triethylamine (4.40ml, 31.77 mmol) was added under $N_{2(g)}$. The reaction mixture was stirred in an ice bath and after 10 min methanesulfonyl chloride (2.27 ml, 29.32 mmol) was added dropwise. The solution turned cloudy due to formation of triethylammonium chloride salt. The reaction was stirred and allowed to adapt room temperature over night. To the reaction mixture was added saturated NH_4Cl solution and Et_2O (100 ml x 3). The organic layer was dried over $MgSO_4$ and concentrated in vaccuo. The product was obtained as a viscous yellow liquid (6.96 g, 23.02 mmol) in 94 % yield.

^{1}H NMR (400 MHz, $CDCl_3$) δ 7.95 (d, J = 8.4 Hz, 1H, Py-H), 7.73 (dd, J = 8.4, 7.4 Hz, 1H, Py-H), 7.42 (s, 1H, N*H*Boc), 7.12 (d, J = 7.4 Hz, 1H, Py-H), 5.20 (s, 2H, Py-C*H*$_2$), 3.06 (s, 3H, SO_3C*H*$_3$), 1.54 (s, 9H, $(CH_3)_3$)

^{13}C NMR (101 MHz, $CDCl_3$) δ 152.17 (*Py*-CH_2), 151.82 (*C*=O), 151.65 (*Py*-NHBoc), 139.25 (*Py*-H), 117.09 (*Py*-H), 112.28 (*Py*-H), 81.35 (*C*$(CH_3)_3$), 71.15 (Py-*C*H_2), 38.17 (SO_3*C*H_3), 28.23 ((*C*$H_3)_3$)

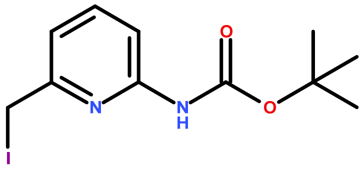

tert-butyl N-[6-(iodomethyl)-2-pyridyl]carbamate

[6-(*tert*-butoxycarbonylamino)-2-pyridyl]methyl methanesulfonate (1.03 g, 3.41 mmol) was dissolved in dry THF (30 ml) and stirred. Lithium iodide (0.91 g, 6.82 mmol) was added and the reaction mixture was heated to 50 °C for 1 hour. The reaction was poured into saturated NH_4Cl solution and extracted with $CHCl_3$ (100 ml x 3). The organic phase was dark purple/red colour and was washed with 10% $Na_2S_2O_3$ which turned the organic phase yellow.

The organic phase was dried over $MgSO_4$ and concentrated in vaccuo to give a yellow/orange viscous liquid (1.08 g, 3.24 mmol) in 95 % yield.

The product tends to turn pink/purple after prolonged periods in organic solution especially when exposed to light.

^{1}H NMR (400 MHz, $CDCl_3$) δ 7.82 (d, *J* = 8.3 Hz, 1H, Py-H), 7.60 (dd, *J* = 8.3, 7.4 Hz, 1H, Py-H), 7.32 (s, 1H, N*H*Boc), 7.04 (d, *J* = 7.4 Hz, 1H, Py-H), 4.39 (s, 2H, Py-CH_2-I), 1.53 (s, 9H, $(CH_3)_3$)

^{13}C NMR (101 MHz, $CDCl_3$) δ 156.38 (*Py*-CH_2), 152.20 (*C*=O), 151.57 (*Py*-NHBoc), 139.09 (*Py*-H), 117.19 (*Py*-H), 111.19 (*Py*-H), 81.09 (*C*$(CH_3)_3$), 28.24 ((CH$_3$)$_3$), 5.93 (Py-*C*H_2-I)

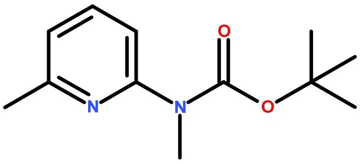

***tert*-butyl N-methyl-N-(6-methyl-2-pyridyl)carbamate**

NaH 60% in mineral oil (5.76 g, 144.05 mmol) was suspended in dry DMF under $N_{2(g)}$. *tert*-butyl N-(6-methyl-2-pyridyl)carbamate (15.00 g, 72.03 mmol) was dissolved in dry DMF and slowly added to the stirring NaH suspension. After 10 min of stirring Methyl iodide (5.38 g, 86.43 mmol) was added to the reaction mixture and stirred over night.

The product was isolated (17.17 g, 77.24 mmol) in quantitative yield with some residual DMF accounting for the slight excess in mass.

^{1}H NMR (400 MHz, $CDCl_3$) δ 7.52 (t, *J* = 7.8 Hz, 1H, Py-H), 7.39 (d, *J* = 8.2 Hz, 1H, Py-H), 6.88 (d, *J* = 7.3 Hz, 1H, Py-H), 3.39 (s, 3H, Py-NCH_3Boc), 2.50 (s, 3H, Py-CH_3), 1.51 (s, 9H, $(CH_3)_3$)

^{13}C NMR (101 MHz, $CDCl_3$) δ 156.50 (*Py*-CH_3), 154.62 (*Py*-NCH_3Boc), 154.50 (*C*=O), 137.13 (*Py*-H), 118.70 (*Py*-H), 116.42 (*Py*-H), 80.83 (*C*$(CH_3)_3$), 34.43 (N*C*H_3Boc), 28.33 ((CH$_3$)$_3$), 24.27 (Py-*C*H_3)

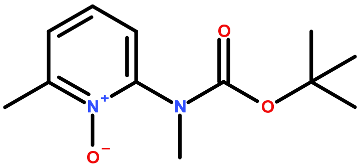

tert-butyl N-methyl-N-(6-methyl-1-oxido-pyridin-1-ium-2-yl)carbamate

tert-butyl N-methyl-N-(6-methyl-2-pyridyl)carbamate (17.17 g, 77.24 mmol) was dissolved in DCM (200 ml) and stirred in an ice bath. After 10 min stirring mCPBA 77% (19.04 g, 110.35 mmol) was added and the reaction mixture was left stirring and allowed to adapt room temperature over night. The reaction mixture went from clear to cloudy to orange during the reaction. The crude mixture was washed with saturated $NaHCO_3$ solution until no more effervescence was observed and the organic phase was dried over $MgSO_4$. The product was concentrated under reduced pressure and was obtained in quantitative yield (18.65 g, 78.27 mmol) as a viscous orange liquid.

^{1}H NMR (400 MHz, $CDCl_3$) δ 7.19 (m, 3H, Py-*H*), 3.20 (s, 3H, Py-NC*H*$_3$Boc), 2.55 (s, 3H, Py-C*H*$_3$), 1.43 (s, 9H, (C*H*$_3$)$_3$)

^{13}C NMR (101 MHz, $CDCl_3$) δ 154.17 (*C*=O), 149.97 (Py-CH$_3$), 148.37 (*Py*-NCH$_3$Boc), 124.88 (Py-H), 124.29 (Py-H), 123.44 (Py-H), 81.29 (*C*(CH$_3$)$_3$), 34.69 (N*C*H$_3$Boc), 28.14 ((*C*H$_3$)$_3$), 18.18 (Py-*C*H$_3$)

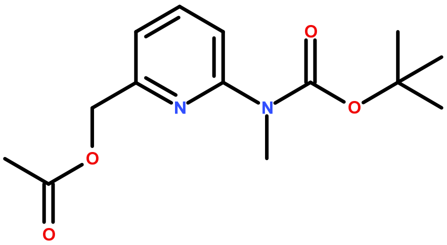

[6-[*tert*-butoxycarbonyl(methyl)amino]-2-pyridyl]methyl acetate

NaH 60% in mineral oil *tert*-butyl N-methyl-N-(6-methyl-1-oxido-pyridin-1-ium-2-yl)carbamate (18.65 g, 78.27 mmol) was dissolved in Ac_2O (100 ml, 1057.89 mmol) and stirred at 70 °C over night. The excess Ac_2O was evaporated in vaccuo and the product was isolated (20.45 g, 72.95 mmol) in 93 % yield. TLC of reaction revealed product at r.f-value 0.44 in Et_2O/Hexane (50/50).

^{1}H NMR (400 MHz, $CDCl_3$) δ 7.62 (m, 2H, Py-H), 7.04 (dd, *J* = 5.3, 2.9 Hz, 1H, Py-H), 5.16 (s, 1H, Py-C*H*$_2$), 3.39 (s, 3H, Py-NC*H*$_3$Boc), 2.17 (s, 3H, Py-CH$_2$-COOC*H*$_3$), 1.52 (s, 9H, (C*H*$_3$)$_3$)

^{13}C NMR (101 MHz, $CDCl_3$) δ 170.68 (CH$_3$*C*=O), 154.75 (*Py*-NCH$_3$Boc), 154.37 (*Py*-CH$_2$), 153.57 (CH$_3$N*C*OOC(CH$_3$)$_3$), 137.49 (Py-H), 118.10 (Py-H), 116.61 (Py-H), 81.18 (*C*(CH$_3$)$_3$), 66.61 (Py-*C*H$_2$), 34.13 (N*C*H$_3$Boc), 28.30 ((*C*H$_3$)$_3$), 20.96 (*C*H$_3$C=O)

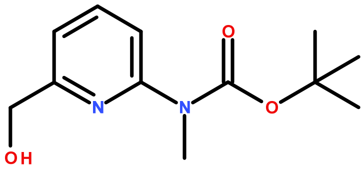

***tert*-butyl-N-[6-(hydroxymethyl)-2-pyridyl]-N-methyl-carbamate**

[6-[*tert*-butoxycarbonyl(methyl)amino]-2-pyridyl]methyl acetate (3.75 g, 13.36 mmol) was dissolved in MeOH (30 ml) and stirred while saturated NaOH solution (2 ml) was added dropwise. The solution went from yellow to orange/brown upon addition of NaOH. The reaction mixture was stirred for 1 hour after which the solvent was evaporated. Water was added to the reaction mixture and the compound was extracted with $CHCl_3$ and dried over $MgSO_4$. The solvent was removed under reduced pressure. The product was obtained in 80 % yield (2.56 g, 10.73 mmol) as a viscous yellow liquid.

^{1}H NMR (400 MHz, $CDCl_3$) δ 7.62 (m, 2H, Py-H), 6.94 (d, *J* = 7.0 Hz, 1H, Py-H), 4.72 (s, 2H, Py-C*H*$_2$), 3.68 (br s, 1H, Py-CH$_2$O*H*), 3.43 (s, 3H, NC*H*$_3$Boc), 1.54 (s, 9H, (C*H*$_3$)$_3$)

^{13}C NMR (101 MHz, $CDCl_3$) δ 156.79 (Py-CH$_2$), 154.30 (CH$_3$N*C*OOC(CH$_3$)$_3$), 137.65 (Py-H), 117.38 (Py-H), 115.34 (Py-H), 81.34 (*C*(CH$_3$)$_3$), 63.79 (*Py*-CH$_2$), 34.16 (N*C*H$_3$Boc), 28.30 ((*C*H$_3$)$_3$)

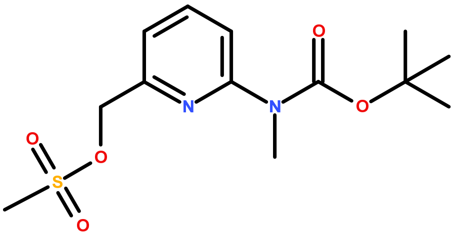

[6-[*tert*-butoxycarbonyl(methyl)amino]-2-pyridyl]methyl methanesulfonate

tert-butyl N-[6-(hydroxymethyl)-2-pyridyl]-N-methyl-carbamate (2.56 g, 10.73 mmol) was dissolved in dry THF (50 ml) and dry distilled triethylamine (2.23 ml, 16.09 mmol) was added under $N_{2(g)}$. The reaction mixture was stirred in an ice bath and after 10 min methanesulfonyl chloride (1.00 ml, 12.88 mmol) was added dropwise. The solution turned cloudy due to formation of triethylammonium chloride salt. The reaction was stirred and allowed to adapt room temperature over night. To the reaction mixture was added saturated NH_4Cl solution and Et_2O (100 ml x 3). The organic layer was dried over $MgSO_4$ and concentrated in vaccuo. The product was obtained as a viscous yellow liquid (3.09 g, 9.78 mmol) in 91 % yield.

^{1}H NMR (400 MHz, $CDCl_3$) δ 7.74 (d, *J* = 8.1 Hz, 1H, Py-H), 7.68 (dd, *J* = 8.3, 7.3 Hz, 1H, Py-H), 7.16 (d, *J* = 7.2 Hz, 1H, Py-H), 5.27 (s, 2H, Py-C*H*$_2$), 3.40 (s, 3H, NC*H*$_3$Boc), 3.09 (s, 3H, SO_3C*H*$_3$), 1.54 (s, 9H, (C*H*$_3$)$_3$)

^{13}C NMR (101 MHz, $CDCl_3$) δ 154.99 (*Py*-NCH$_3$Boc), 154.29 (Py-CH$_2$), 151.19 (CH$_3$N*C*OOC(CH$_3$)$_3$), 137.83 (*Py*-H), 118.83 (*Py*-H), 117.41 (*Py*-H), 81.47 (*C*(CH$_3$)$_3$), 71.57 (*Py*-CH$_2$), 38.08 (SO$_3$*C*H$_3$), 34.07 (N*C*H$_3$Boc), 28.29 ((*C*H$_3$)$_3$)

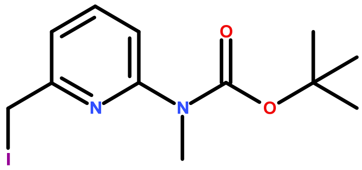

***tert*-butyl-N-[6-(iodomethyl)-2-pyridyl]-N-methyl-carbamate**

[6-[*tert*-butoxycarbonyl(methyl)amino]-2-pyridyl]methyl methanesulfonate (3.09 g, 9.78 mmol) was dissolved in dry THF (50 ml) and stirred. Lithium iodide (2.62 g, 19.56 mmol) was added and the reaction mixture was heated to 50 °C for 1 hour. The reaction was poured into saturated NH_4Cl solution and extracted with $CHCl_3$ (100 ml x 3). The organic phase was dark purple/red colour and was washed with 10% $Na_2S_2O_3$ which turned the organic phase yellow. The organic phase was dried over $MgSO_4$ and concentrated in vaccuo to give a yellow/orange viscous liquid in similar yield to the non-methylated *tert*-butyl N-[6-(iodomethyl)-2-pyridyl]carbamate. The product was obtained in 90% yield (3.06 g, 8.80 mmol).

^{1}H NMR (400 MHz, $CDCl_3$) δ 7.59 (dd, *J* = 8.2, 1.0 Hz, 1H, Py-H), 7.55 (dd, *J* = 8.3, 7.0 Hz, 1H, Py-H), 7.08 (dd, *J* = 6.9, 1.2 Hz, 1H, Py-H), 4.46 (s, 2H, Py-C*H*$_2$), 3.42 (s, 3H, NC*H*$_3$Boc), 1.54 (s, 9H, (C*H*$_3$)$_3$)

^{13}C NMR (101 MHz, $CDCl_3$) δ 155.80 (*Py*-CH$_2$), 154.72 (*Py*-NCH$_3$Boc), 154.36 (CH$_3$N*C*OOC(CH$_3$)$_3$), 137.70 (*Py*-H), 117.74 (*Py*-H), 117.64 (*Py*-H), 81.23 (*C*(CH$_3$)$_3$), 34.15 (N*C*H$_3$Boc), 28.32 ((*C*H$_3$)$_3$), 6.63 (*C*H$_2$-I)

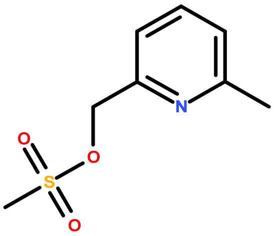

(6-methyl-2-pyridyl)methyl methanesulfonate

(6-methyl-2-pyridyl)methanol (5.82 g, 47.26 mmol) was dissolved in dry THF (100 ml) and dry distilled triethylamine (9.83 ml, 70.89 mmol) was added under $N_{2(g)}$. The reaction mixture was stirred in an ice bath and after 10 min methanesulfonyl chloride (4.39 ml, 56.71 mmol) was added dropwise. The solution turned cloudy due to formation of triethylammonium chloride salt. The reaction was stirred and allowed to adapt room temperature over night. To the reaction mixture was added saturated NH_4Cl solution and Et_2O (100 ml x 3). The organic layer was dried over $MgSO_4$ and concentrated in vaccuo. The product was yellow in solution but turned deep red when solvent was removed. The product was obtained as a viscous red liquid (9.44 g, 46.90 mmol) in 99 % yield. The product did not require any further purification and the r.f-value on the compound is 0.45 (in 100 % Et_2O).

^{1}H NMR (400 MHz, $CDCl_3$) δ 7.63 (t, *J* = 7.7 Hz, 1H, Py-H), 7.26 (d, *J* = 7.7 Hz, 1H, Py-H), 7.14 (d, *J* = 7.8 Hz, 1H, Py-H), 5.27 (s, 2H, Py-CH$_2$), 3.07 (s, 3H, SO$_3$*CH*$_3$), 2.54 (s, 3H, Py-CH$_3$)

^{13}C NMR (101 MHz, $CDCl_3$) δ 158.57 (*Py*-CH_3), 152.84 (*Py*-CH_2), 137.29 (Py-H), 123.30 (Py-H), 119.42 (Py-H), 71.85 (Py-*C*H_2), 38.06 (SO_3*CH*$_3$), 24.31 (Py-*C*H_3)

HRMS (ESI-TOF) m/z: Calculated for $C_8H_{12}NO_3S$: 202.0538

Found: 202.0528 $[M+H]^+$

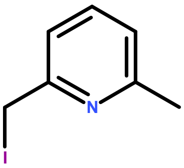

2-(iodomethyl)-6-methyl-pyridine

(6-methyl-2-pyridyl)methyl methanesulfonate (7.21 g, 35.83 mmol) was dissolved in dry THF (50 ml) and stirred. Lithium iodide (5.75 g, 42.99 mmol) was added and the reaction mixture was heated to 50 °C for 1 hour. The reaction was poured into saturated NH_4Cl solution and extracted with $CHCl_3$ (100 ml x 3). The organic phase was dark purple/red colour and was washed with 10% $Na_2S_2O_3$ which turned the organic phase yellow. The organic phase was dried over $MgSO_4$ and concentrated in vaccuo to give a red viscous liquid (8.11 g, 34.82 mmol) in 97 % yield. The product did not require any further purification and the r.f-value on the compound is 0.69 (in 100 % Et_2O).

^{1}H NMR (400 MHz, $CDCl_3$) δ 7.51 (t, J = 7.7 Hz, 1H, Py-H), 7.20 (d, J = 7.7 Hz, 1H, Py-H), 7.00 (d, J = 7.7 Hz, 1H, Py-H), 4.48 (s, 2H, Py-CH_2), 2.53 (s, 3H, Py-CH_3)

^{13}C NMR (101 MHz, $CDCl_3$) δ 158.37 (*Py*-CH_3), 157.59 (*Py*-CH_2), 137.16 (Py-H), 122.15 (Py-H), 119.90 (Py-H), 24.47 (Py-*C*H_2), 6.76 (Py-*C*H_3)

HRMS (ESI-TOF) m/z: Calculated for C_7H_9IN: 233.9774

Found: 233.9769 $[M+H]^+$

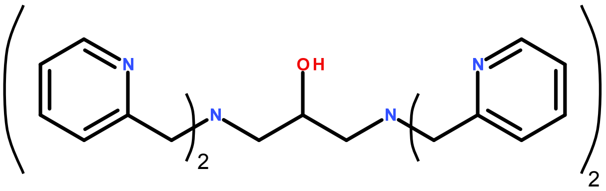

1,3-bis[bis(2-pyridylmethyl)amino]propan-2-ol

2-(bromomethyl)pyridin-1-ium bromide (1.00 g, 3.95 mmol) was dissolved in dry DMF and 1,3-diamino-2-propanol (0.07 g, 0.79 mmol) was added to the solution. DIPEA (2.75 ml, 15.81 mmol) was added and the solution was stirred at 70 °C over night. The solvent was removed under reduced pressure and the dark brown crude oil was purified using flash chromatography in MeOH/EtOAc (50/50) to yield the title compound as a brown liquid (0.09 g, 0.20 mmol) in 25 % yield.

^{1}H NMR (250 MHz, $CDCl_3$) δ 8.50 (ddd, J = 4.9, 1.7, 0.8 Hz, 4H, Py-H), 7.58 (td, J = 7.6, 1.8 Hz, 4H, Py-H), 7.36 (d, J = 7.8 Hz, 4H, Py-H), 7.11 (ddd, J = 7.4, 4.9, 1.1 Hz, 4H, Py-H), 3.99 (m, 1H, $(CH_2)_2C\mathit{H}OH$), 3.87 (d, J = 2.9 Hz, 8H, Py-$C\mathit{H}_2$), 2.65 (dd, J = 11.5, 5.9 Hz, 4H, $(C\mathit{H}_2)_2CHOH$)

^{13}C NMR (63 MHz, $CDCl_3$) δ 159.54 (Py-H), 148.96 (Py-H), 136.33 (Py-H), 123.05 (Py-H), 121.91 (*Py*-CH_2), 67.31 ($(CH_2)_2\mathit{C}HOH$), 60.85 (Py-$\mathit{C}H_2$), 59.09 ($(\mathit{C}H_2)_2CHOH$)

HRMS (ESI-TOF) m/z: Calculated for $C_{27}H_{29}N_6OZn$: 517.1694

Found: 517.1689 $[M^- + Zn^{2+}]^+$

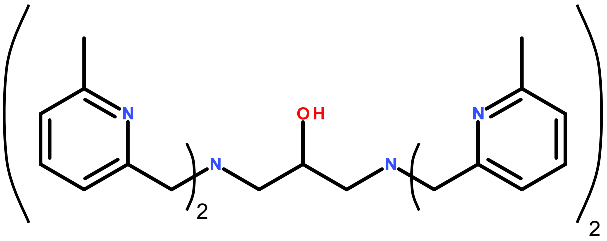

1,3-bis[bis[(6-methyl-2-pyridyl)methyl]amino]propan-2-ol

2-(iodomethyl)-6-methyl-pyridine (2.00 g, 8.58 mmol) was dissolved in dry DMF and 1,3-diamino-2-propanol (0.15 g, 1.72 mmol) was added to the solution. DIPEA (5.98 ml, 34.33 mmol) was added and the solution was stirred at 70 °C over night. The solvent was removed under reduced pressure and the dark brown crude oil was purified using flash chromatography to yield the title compound as a brown liquid (0.20 g, 0.39 mmol) in 23 % yield with a r.f-value of 0.21 in MeOH/EtOAc (20/80).

^{1}H NMR (400 MHz, MeOD) δ 7.62 (t, *J* = 7.7 Hz, 4H, Py-H), 7.30 (d, *J* = 7.7 Hz, 4H, Py-H), 7.11 (d, *J* = 7.7 Hz, 4H, Py-H), 3.97 (ddd, *J* = 11.9, 7.7, 4.4 Hz, 1H, $(CH_2)_2C$*H*OH), 3.79 (d, *J* = 3.2 Hz, 8H, Py-C*H*$_2$), 2.66 (dd, *J* = 13.3, 4.4 Hz, 1H), 2.57 (ddd, *J* = 61.4 Hz, *J* = 13.3, 4.4 Hz, 4H, (C*H*$_2$)$_2$CHOH), 2.48 (s, 12H, Py-C*H*$_3$)

^{13}C NMR (101 MHz, MeOD) δ 158.47 (*Py*-CH_3), 157.27 (*Py*-CH_2), 137.36 (Py-H), 121.81 (Py-H), 120.39 (Py-H), 67.14 $(CH_2)_2$*C*HOH, 60.37 (Py-*C*H_2), 59.14, 22.38 (Py-*C*H_3)

HRMS (ESI-TOF) m/z: Calculated for $C_{31}H_{37}N_6OZn$: 573.2320

Found: 573.2329 $[M^-+Zn^{2+}]^+$

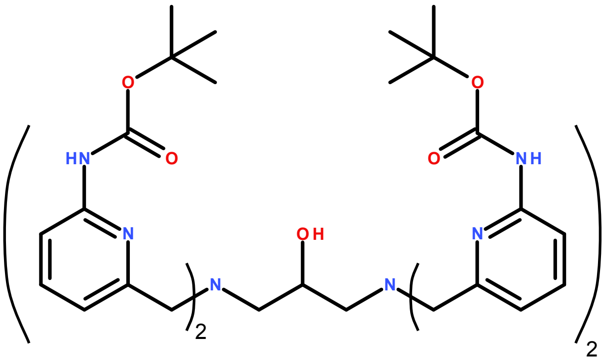

tert-butylN-[6-[[[3-[bis[[6-(tert-butoxycarbonylamino)-2-pyridyl]methyl]amino]-2-hydroxy-propyl]-[[6-(tert-butoxycarbonylamino)-2-pyridyl]methyl]amino]methyl]-2-pyridyl]carbamate

tert-butyl N-[6-(iodomethyl)-2-pyridyl]carbamate (1.38 g, 4.12 mmol) was dissolved in dry DMF (30 ml) and 1,3-diamino-2-propanol (0.07 g, 0.82 mmol) was added to the solution. DIPEA (2.87 ml, 16.48 mmol) was added and the reaction mixture was stirred at 70 °C over night. The solvent was removed under reduced pressure and the dark brown crude oil was purified using flash chromatography to yield the title compound as a clear liquid (0.24 g, 0.26 mmol) in 31 % yield with a r.f-value of 0.22 in MeOH/EtOAc (10/90).

^{1}H NMR (250 MHz, $CDCl_3$) δ 7.78 (d, *J* = 8.2 Hz, 4H, Py-H), 7.63 (s, 4H, N*H*Boc), 7.57 (m, 4H, Py-H), 6.97 (d, *J* = 7.3 Hz, 4H, Py-H), 3.91 (s, 1H, $(CH_2)_2C$*H*OH)), 3.74 (q, *J* = 14.6 Hz, 8H, Py-C*H*$_2$), 2.59 (m, 4H, (C*H*$_2$)$_2$CHOH), 1.51 (s, 36H, (C*H*$_3$)$_3$)

^{13}C NMR (63 MHz, $CDCl_3$) δ 157.48 (*Py*-CH_2), 152.38 (NH*C*OOtBu), 151.36 (*Py*-NHBoc), 138.52(Py-H), 117.70 (Py-H), 110.46 (Py-H), 80.90 (*C*(CH_3)$_3$), 66.97 ((CH_2)$_2$*C*HOH), 60.18 (Py-CH_2), 58.49 ((*C*H_2)$_2$CHOH), 28.27 ((*C*H_3)$_3$)

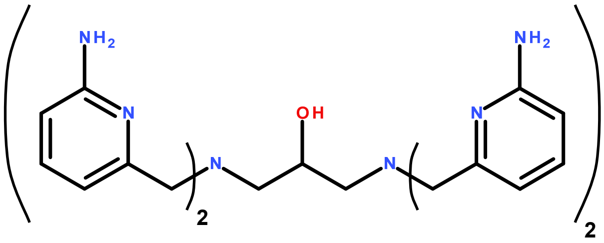

1,3-bis[bis[(6-amino-2-pyridyl)methyl]amino]propan-2-ol

tert-butylN-[6-[[[3-[bis[[6-(*tert*-butoxycarbonylamino)-2-pyridyl]methyl]amino]-2-hydroxy-propyl]-[[6-(*tert*-butoxycarbonylamino)-2-pyridyl]methyl]amino]methyl]-2-pyridyl]carbamate (0.23 g, 0.26 mmol) was dissolved in 10 ml DCM/TFA (50/50) and the reaction was stirred for 1 hour. The solvent was removed under reduced pressure to yield the title compound as a yellow liquid in quantitative yield.

^{1}H NMR (400 MHz, MeOD) δ 7.40 (dd, *J* = 8.0, 7.5 Hz, 4H, Py-H), 6.69 (d, *J* = 7.2 Hz, 4H, Py-H), 6.44 (d, *J* = 8.2 Hz, 4H, Py-H), 3.93 (t, *J* = 7.8, 4.1 Hz, 1H, (CH_2)$_2$C*H*OH)), 3.61 (s, 8H, Py-C*H*$_2$), 2.57 (ddd, *J* = 20.8, 13.3, 6.0 Hz, 4H, (C*H*$_2$)$_2$CHOH))

^{13}C NMR (101 MHz, MeOD) δ 159.10 (*Py*-NH_2), 156.57 (*Py*-CH_2), 138.25 (Py-H), 111.90 (Py-H), 107.15 (Py-H), 66.85 (CH_2)$_2$*C*HOH), 60.20 (Py-*C*H_2), 58.80 (*C*H_2)$_2$CHOH)

HRMS (ESI-TOF) m/z: Calculated for $C_{27}H_{35}N_{10}O$: 515.2995

Found: 515.3007 $[M+H]^+$

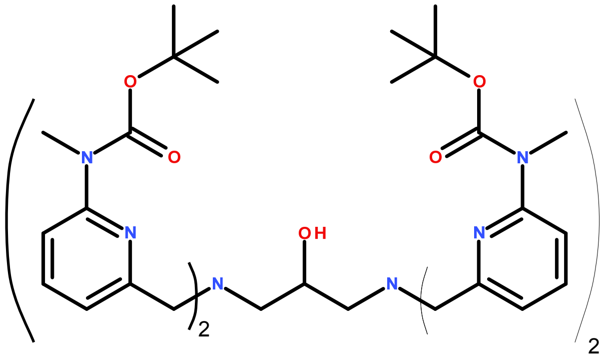

tert-butylN-[6-[[[3-[bis[[6-[*tert*-butoxycarbonyl(methyl)amino]-2-pyridyl]methyl]amino]-2-hydroxy-propyl]-[[6-[*tert*-butoxycarbonyl(methyl)amino]-2-pyridyl]methyl]amino]methyl]-2-pyridyl]-N-methyl-carbamate

tert-butyl N-[6-(iodomethyl)-2-pyridyl]-N-methyl-carbamate (1.50 g, 4.31 mmol) was dissolved in DMF (40 ml) and 1,3-diamino-2-propanol (0.08 g, 0.86 mmol), DIPEA (3.00 ml, 17.23 mmol) were added and the reaction mixture was stirred at 70 °C over night. The solvent was removed under reduced pressure and the dark brown crude oil was purified using flash chromatography in Et$_2$O/Hexane (50/50) to yield the title compound as a clear liquid (0.34 g, 0.35 mmol) in 41 % yield.

^{1}H NMR (400 MHz, CDCl$_3$) δ 7.52 (m, 8H, Py-H), 7.08 (dd, *J* = 6.8 Hz, *J* = 1.2 Hz, 4H, Py-H), 3.98 (m, 1H, (CH$_2$)$_2$C*H*OH), 3.81 (q, *J* = 14.8 Hz, 4H, Py-C*H*$_2$), 3.38 (s, 12H, NC*H*$_3$Boc), 2.68 (ddd, *J* = 21.0, 13.1, 6.0 Hz, 4H, (C*H*$_2$)$_2$CHOH), 1.51 (s, 36H, (CH$_3$)$_3$)

^{13}C NMR (101 MHz, CDCl$_3$) δ 157.35 (*Py*-CH$_2$), 154.54 (NCH$_3$*C*OOtBu), 154.42 (*Py*-NCH$_3$Boc), 137.13 (Py-H), 118.16 (Py-H), 117.22 (Py-H), 80.97 (*C*(CH$_3$)$_3$), 66.77 ((CH$_2$)$_2$*C*HOH), 60.15 (Py-CH$_2$), 58.69 ((*C*H$_2$)$_2$CHOH), 34.24 (N*C*H$_3$Boc), 28.32 ((*C*H$_3$)$_3$)

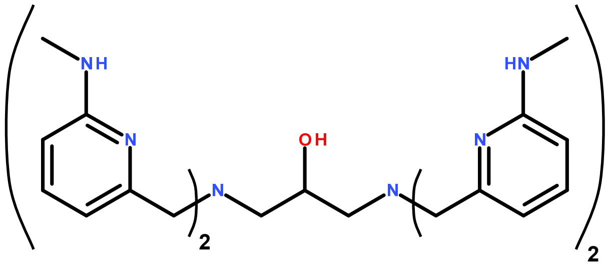

1,3-bis[bis[[6-(methylamino)-2-pyridyl]methyl]amino]propan-2-ol

tert-butyl N-[6-[[[3-[bis[[6-[*tert*-butoxycarbonyl(methyl)amino]-2-pyridyl]methyl]amino]-2-hydroxy-propyl]-[[6-[*tert*-butoxycarbonyl(methyl)amino]-2-pyridyl]methyl]amino]methyl]-2-

pyridyl]-N-methyl-carbamate (0.34 g, 0.35 mmol) was dissolved in 10 ml DCM/TFA (10/90) and the reaction was stirred for 1 hour. The solvent was removed by blowing $N_{2(g)}$ at the solution and $NaOH_{(aq)}$ was added. The product was extracted with $CHCl_3$ and dried over $MgSO_4$. The crude was purified using flash chromatography in EtOAc/MeOH (50/50) followed by 100 % MeOH flush to yield the title compound as a clear liquid (0.10 g, 0.18 mmol) in 50 % yield.

^{1}H NMR (400 MHz, $CDCl_3$) δ 7.36 (t, *J* = 7.8 Hz, 4H, Py-H), 6.69 (d, *J* = 7.2 Hz, 4H, Py-H), 6.21 (d, *J* = 8.2 Hz, 1H, Py-H), 3.95 (s, 1H, $(CH_2)_2C\mathit{H}OH$), 3.69 (m, 8H, Py-$C\mathit{H}_2$), 2.86 (s, 12H, $NC\mathit{H}_3$), 2.65 (ddd, *J* = 20.7, 13.1, 5.8 Hz, 4H, $(C\mathit{H}_2)_2CHOH$)

^{13}C NMR (101 MHz, $CDCl_3$) δ 159.20 (*Py*-NH_2), 158.10 (*Py*-CH_2), 137.92 (Py-H), 111.82 (Py-H), 103.46 (Py-H), 67.19 ($(CH_2)_2\mathit{C}HOH$), 60.57 (Py-$\mathit{C}H_2$), 58.99 ($(\mathit{C}H_2)_2CHOH$), 29.24 ($N\mathit{C}H_3$)

HRMS (ESI-TOF) m/z: Calculated for $C_{31}H_{41}N_{10}OZn$: 633.2756

Found: 633.2741 $[M^-+Zn^{2+}]^+$

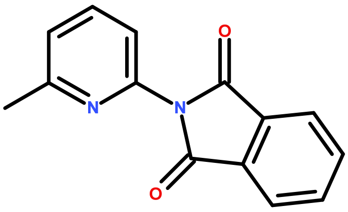

2-(6-methyl-2-pyridyl)isoindoline-1,3-dione

6-methylpyridin-2-amine (20.00 g, 184.95 mmol) and phthalic anhydride (27.39 g, 184.95 mmol) was weighed in a flask, stirred and heated in a heating mantle to 190 °C for 1 hour. The solids melted into a liquid during heating and solidified after cooling down to afford the title compound (43.00 g, 180.49 mmol) in 97 % yield with a r.f-value of 0.64 in 100 % EtOAc.

^{1}H NMR (250 MHz, $CDCl_3$) δ 7.98 (m, 2H, Py-H), 7.80 (m, 3H, Py-H & Ph-H), 7.24 (t, *J* = 7.4 Hz, 2H, Py-H), 2.64 (s, 3H, Py-$C\mathit{H}_3$)

^{13}C NMR (63 MHz, $CDCl_3$) δ 166.83 (Py-$N(\mathit{C}O)_2$), 159.18 (*Py*-CH_3), 145.39 (*Py*-$N(CO)_2$), 138.44 (Py-H), 134.45 (Ph-H), 131.95 (*Ph*-CO), 123.86 (Ph-H), 123.38 (Py-H), 119.41 (Py-H), 24.31 (Py-$\mathit{C}H_3$)

7.2.1 - Synthesis of substrate (HPNPP)

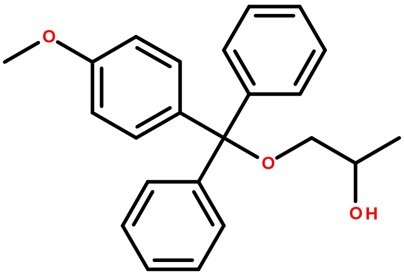

1-[(4-methoxyphenyl)-diphenyl-methoxy]propan-2-ol

1,2-propanediol (4.83 ml, 65.71 mmol) and 4-monomethoxy trityl chloride (16.23 g, 52.57 mmol) were dissolved in dry THF(50 ml). Imidazole (3.58 g, 52.57 mmol) was added and the reaction mixture was stirred over night. The crude reaction mixture was added to H_2O, extracted thrice with EtOAc and the resulting organic phase was dried over Na_2SO_4 and purified using flash chromatography. The title compound was obtained as a viscous clear liquid (13.17 g, 37.80 mmol) in 72 % yield with a r.f-value of 0.31 in Et_2O/Hexane (50/50).

^{1}H NMR (400 MHz, $CDCl_3$) δ 7.47 (m, 4H, Ph-H), 7.30 (m, 8H, Ph-H), 6.87 (m, 2H, Ph-H), 4.01 (m, 1H, $CH_2C\mathit{H}(CH_3)OH$), 3.83 (s, 3H, Ph-$OC\mathit{H}_3$), 3.09 (ddd, J = 17.2, 9.2, 5.6 Hz, 2H, $C\mathit{H}_2CH(CH_3)OH$), 2.44 (br s, 1H, $CH_2CH(CH_3)O\mathit{H}$), 1.13 (d, J = 6.4 Hz, 3H, $CH_2CH(C\mathit{H}_3)OH$)

^{13}C NMR (101 MHz, $CDCl_3$) δ 158.61 (*Ph*-OCH_3), 144.41 (*Ph*-C), 144.37 (*Ph*-C), 135.56 (*Ph*-C), 130.37 (Ph-H), 128.40 (Ph-H), 127.87 (Ph-H), 126.97 (Ph-H), 113.14 (Ph-H), 86.34 ($\mathit{C}(Ph)_3$), 68.91 ($\mathit{C}H_2CH(CH_3)OH$), 67.11 ($CH_2\mathit{C}H(CH_3)OH$), 55.23 (Ph-$O\mathit{C}H_3$), 18.99 ($CH_2CH(\mathit{C}H_3)OH$)

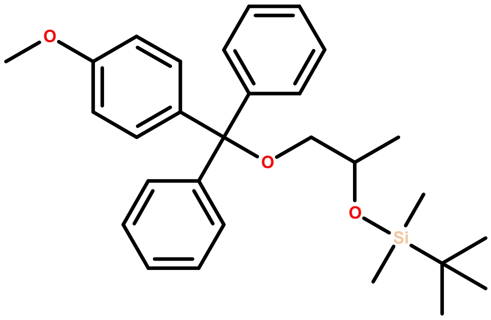

tert-butyl-[2-[(4-methoxyphenyl)-diphenyl-methoxy]-1-methyl-ethoxy]-dimethyl-silane

1-[(4-methoxyphenyl)-diphenyl-methoxy]propan-2-ol (7.00 g, 20.09 mmol) and Imidazole (3.58 g, 52.57 mmol) were dissolved in dry DMF (40 ml). *tert*-Butyldimethylsilyl chloride (9.08 g, 60.27 mmol) was added and the reaction mixture was stirred over night. The crude reaction mixture was added to H_2O, extracted $CHCl_3$ and resulting organic phase was dried over $MgSO_4$ followed by solvent removal under reduced pressure. The resulting crude liquid was purified using flash chromatography. The title compound was obtained as a viscous clear liquid in quantitative yield with a r.f-value of 0.76 in Et_2O/Hexane (50/50).

^{1}H NMR (400 MHz, $CDCl_3$) δ 7.51 (m, 4H, Ph-H), 7.31 (m, 8H, Ph-H), 6.85 (m, 2H, Ph-H), 3.99 (m, 1H, $CH_2C\mathit{H}(CH_3)OH$), 3.82 (s, 3H, Ph-$OC\mathit{H}_3$), 3.00 (ddd, *J* = 103.4, 9.1, 5.7 Hz, 2H, $C\mathit{H}_2CH(CH_3)OH$), 1.17 (d, *J* = 6.2 Hz, 3H, $CH_2CH(C\mathit{H}_3)OH$), 0.92 (s, 9H, $SiC(C\mathit{H}_3)_3$), 0.09 (d, *J* = 3.2 Hz, 6H, $Si(C\mathit{H}_3)_2$)

^{13}C NMR (101 MHz, $CDCl_3$) δ 158.43 (*Ph*-OCH_3), 144.87 (*Ph*-C), 144.73 (*Ph*-C), 136.09 (*Ph*-C), 130.43 (*Ph*-H), 128.58 (Ph-H), 128.54 (Ph-H), 127.68 (Ph-H), 126.72 (Ph-H), 112.97 (Ph-H), 86.01 ($\mathit{C}(Ph)_3$), 69.39 ($\mathit{C}H_2CH(CH_3)OH$), 68.13 ($CH_2\mathit{C}H(CH_3)OH$), 55.21 (Ph-$O\mathit{C}H_3$), 25.91 (Si-$C(\mathit{C}H_3)_3$), 21.27 ($Si\mathit{C}(CH_3)_3$), 18.17 ($CH_2CH(\mathit{C}H_3)OH$), -4.54 ($Si(\mathit{C}H_3)_2$), -4.70 ($Si(\mathit{C}H_3)_2$)

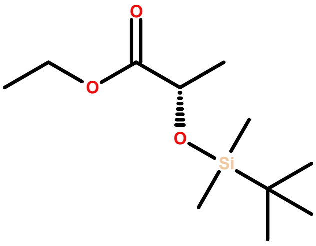

Ethyl (2S)-2-[*tert*-butyl(dimethyl)silyl]oxypropanoate

Imidazole (17.29 g, 253.96 mmol) and *tert*-Butyldimethylsilyl chloride (19.14 g, 126.98 mmol) were dissolved in dry DMF (200 ml) and stirred in an ice bath. Ethyl (2S)-2-hydroxypropanoate (9.65 ml, 84.65 mmol) was added slowly and the reaction was stirred over night at room temperature. H_2O was added to the reaction mixture followed by extraction with Et_2O. The volatile solvent was removed under reduced pressure and the residual DMF was removed with an additional extraction with Et_2O from H_2O. The solvent was removed under reduced pressure to afford the title compound as a clear liquid (19.47 g, 83.80 mmol) in 99 % yield.

^{1}H NMR (400 MHz, $CDCl_3$) δ 4.32 (q, $J = 6.7$ Hz, 1H, $CH_3CH_2OOCC\mathit{H}(CH_3)OSi$), 4.19 (m, 2H, $CH_3C\mathit{H}_2OOCCH(CH_3)OSi$), 1.41 (d, $J = 6.8$ Hz, 3H, $CH_3CH_2OOCCH(C\mathit{H}_3)OSi$), 1.29 (t, $J = 7.1$ Hz, 3H, $C\mathit{H}_3CH_2OOCCH(CH_3)OSi$), 0.92 (s, 9H, $SiC(C\mathit{H}_3)_3$), 0.10 (d, $J = 12.1$ Hz, 6H, $Si(C\mathit{H}_3)_2$)

^{13}C NMR (101 MHz, $CDCl_3$) δ 174.14 ($CH_3CH_2OO\mathit{C}CH(CH_3)OSi$), 68.46 ($CH_3\mathit{C}H_2OOCCH(CH_3)OSi$), 60.74 ($CH_3\mathit{C}H_2OOCCH(CH_3)OSi$), 25.71 ($(\mathit{C}H_3)_3$), 21.31 ($CH_3CH_2OOCCH(\mathit{C}H_3)OSi$), 18.33 ($Si\mathit{C}(CH_3)_3$), 14.19 ($\mathit{C}H_3CH_2OOCCH(CH_3)OSi$), -4.95 ($Si(\mathit{CH}_3)_2$), -5.28 ($Si(\mathit{CH}_3)_2$)

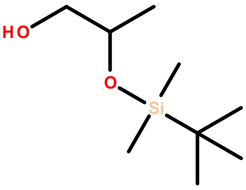

2-[*tert*-butyl(dimethyl)silyl]oxypropan-1-ol

tert-butyl-[2-[(4-methoxyphenyl)-diphenyl-methoxy]-1-methyl-ethoxy]-dimethyl-silane (2.00 g, 4.32 mmol) was dissolved in 95 % AcOH (20 ml) and stirred over night. To the light yellow solution was added H_2O (50 ml) which turned the solution cloudy. The reaction mixture was stirred in an ice bath and Na_2CO_3 was added in small portions until effervescence stopped. The crude mixture was extracted thrice with DCM, dried over $MgSO_4$ and the solvent was removed under reduced pressure. The obtained yellow oil was distilled using a kügelrohr distillator at 150 °C at 2 mbar with a $CO_{2(s)}$/Acetone trap. The title compound was obtained as a clear liquid (0.15 g, 0.79 mmol) in 18 % yield.

Alternative synthesis:

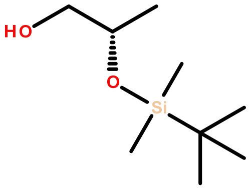

(2S)-2-[*tert*-butyl(dimethyl)silyl]oxypropan-1-ol

ethyl (2S)-2-[*tert*-butyl(dimethyl)silyl]oxypropanoate (15.00 g, 64.55 mmol) was dissolved in dry THF (100 ml) and stirred in an ice bath under $N_{2(g)}$ and 1M BH_3-THF complex (100 ml, 100 mmol) was added over 15 min. The reaction mixture was allowed to reach room temperature and then stirred at reflux for 3 hours. The reaction mixture was allowed to cool to room temperature and H_2O was added slowly followed by three extractions with Et_2O. The organic phase was washed with brine and dried over $MgSO_4$. The solvent was removed under reduced pressure to afford the title compound (11.13 g, 58.47 mmol) in 90 % yield.

^{1}H NMR (400 MHz, $CDCl_3$) δ 3.93 (m, J = 6.3, 3.6 Hz, 1H, $HOCH_2C\mathit{H}(CH_3)OH$), 3.45 (ddd, J = 17.5, 10.9, 5.1 Hz, 2H, $HOC\mathit{H}_2CH(CH_3)OH$), 1.93 (s, 1H, $\mathit{H}OCH_2CH(CH_3)OH$), 1.14 (d, J = 6.2 Hz, 3H, $HOCH_2CH(C\mathit{H}_3)OH$), 0.92 (s, 9H, $SiC(C\mathit{H}_3)_3$), 0.11 (s, 6H, $Si(C\mathit{H}_3)_2$).
^{13}C NMR (101 MHz, $CDCl_3$) δ 69.06 ($CH_2\mathit{C}H(CH_3)OH$), 68.18 ($\mathit{C}H_2CH(CH_3)OH$), 25.82 ($Si\text{-}C(\mathit{C}H_3)_3$), 19.82 ($CH_2CH(\mathit{C}H_3)OH$), 18.06 ($Si\mathit{C}(CH_3)_3$), -4.38 ($Si(\mathit{CH}_3)_2$), -4.80 ($Si(\mathit{CH}_3)_2$)

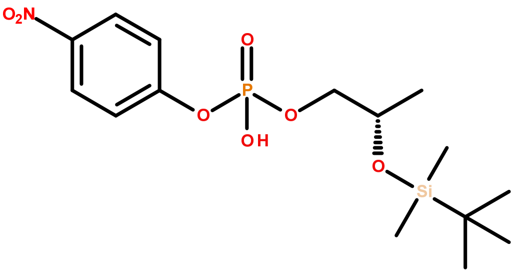

[(2S)-2-[*tert*-butyl(dimethyl)silyl]oxypropyl] (4-nitrophenyl) hydrogen phosphate

4-Nitrophenylphosphodichloridate (4.00 g, 15.63 mmol) was dissolved in dry THF and stirred in an ice bath under N$_{2(g)}$. 2-[*tert*-butyl(dimethyl)silyl]oxypropan-1-ol (2.68 g, 14.06 mmol) and dry Et3N (5.85 ml, 42.19 mmol) were dissolved in dry THF and slowly added to the stirring reaction mixture. The reaction was stirred at room temperature for 4 hours followed by the addition of H2O (0.3 ml). The reaction was stirred for 30 min and then excess H$_2$O was added. The reaction mixture was extracted with DCM and dried over MgSO$_4$. The crude reaction mixture was purified using flash chromatography and the title compound was isolated as a light yellow oil with a r.f-value of 0.63 in MeOH/DCM (25/75).

^{1}H NMR (400 MHz, MeOD) δ 8.20 (d, *J* = 9.1 Hz, 2H, Ph-H), 7.46 (d, *J* = 9.0 Hz, 2H, Ph-H), 3.97 (m, 1H, CH$_2$C*H*(CH$_3$)OSi), 3.83 (dtd, *J* = 15.6, 10.0, 5.6 Hz, 2H, C*H*$_2$CH(CH$_3$)OSi), 1.13 (d, *J* = 6.0 Hz, 3H, CH$_2$CH(C*H*$_3$)OSi), 0.86 (s, 9H, SiC(C*H*$_3$)$_3$), 0.05 (d, *J* = 6.9 Hz, 6H, Si(*C*H$_3$)$_2$)

^{13}C NMR (101 MHz, CDCl$_3$) δ 157.17 (Ph-O), 157.12 (Ph-O), 143.45 (Ph-NO$_2$), 125.29 (Ph-H), 120.45 (Ph-H), 120.40 (Ph-H), 71.44 (*C*H$_2$CH(CH$_3$)OSi), 71.40 (*C*H$_2$CH(CH$_3$)OSi), 67.52 (CH$_2$*C*H(CH$_3$)OSi), 67.42 (CH$_2$*C*H(CH$_3$)OSi), 25.69 (SiC(*C*H$_3$)$_3$), 20.23 (CH$_2$CH(*C*H$_3$)OSi), 18.09 (Si*C*(CH$_3$)$_3$), -4.83 (Si(CH$_3$)$_2$), -4.91 (Si(CH$_3$)$_2$)

^{31}P NMR (162 MHz, CDCl$_3$) δ -10.89

HRMS (ESI-TOF) m/z: Calculated for $C_{15}H_{27}NO_7PSi$: 392.1294

Found: 392.1276 [M]$^-$

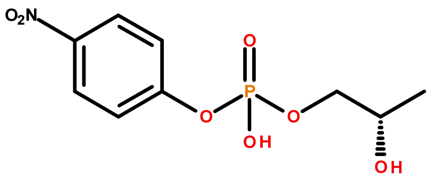

[(2S)-2-hydroxypropyl] (4-nitrophenyl) hydrogen phosphate

[(2S)-2-[*tert*-butyl(dimethyl)silyl]oxypropyl] (4-nitrophenyl) hydrogen phosphate spontaneously lost the *tert*-butyl(dimethyl)silyl protecting group following purification on silica over 2 days. The resulting product was purified using Waters Xbridge C-18 column with a gradient purification 5-41 % MeCN over 8 min and 254 nm UV-detection. The title compound was collected at a retention time of 6.5 min. The product was also analyses by TLC with the same mobile phase used for the purification of the fully protected native compound i.e. MeOH/DCM (25/75) yielding a r.f-value of 0.41.

An alternative deprotection procedure was also utilised involving over night treatment with Triethylamine trihydrofluoride in three fold molar excess followed by flash chromatography to obtain the title compound in a more controlled fashion.

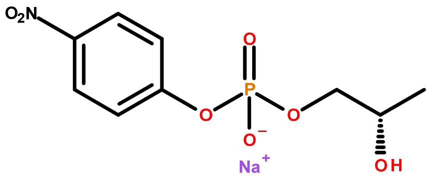

[(2S)-2-hydroxypropyl] (4-nitrophenyl) hydrogen phosphate sodium salt

Amberlite IR-120 H-form was washed with 2 M $NaCl_{(aq)}$ until the eluent from the column was no longer acidic (checked by pH-paper). The resin was washed with 5 column volumes of H_2O in order to eliminate residual salt. [(2S)-2-hydroxypropyl] (4-nitrophenyl) hydrogen phosphate was dissolved in H_2O and a small amount of MeOH and passed through the column. The solvent was removed by freeze drying to afford the title compound (0.16 g, 0.58 mmol) in 4 % yield over 3 steps. Analytical HPLC Phenomenex Kinetex XB-C18 100 Å 5 µm 4.6 x 250 nm, 5-41 % MeCN 8 min gradient, 254 nm detection, retention time 5.3 min.

^{1}H NMR (400 MHz, MeOD) δ 8.22 (d, *J* = 8.9 Hz, 2H, Ph-H), 7.43 (dd, *J* = 9.3, 0.8 Hz, 2H, Ph-H), 3.93 (m, 1H, $CH_2C\mathit{H}(CH_3)OH$), 3.84 (m, 2H, $C\mathit{H}_2CH(CH_3)OH$), 1.16 (d, *J* = 6.3 Hz, 3H, $CH_2CH(C\mathit{H}_3)OH$)

^{13}C NMR (101 MHz, MeOD) δ 158.56 (Ph-O), 158.50 (Ph-O), 143.10 (Ph-NO_2), 124.84 (Ph-H), 120.11 (Ph-H), 120.05 (Ph-H), 71.04 (*C*H_2CH(CH_3)OH), 70.98 (*C*H_2CH(CH_3)OH), 66.35 (CH_2*C*H(CH_3)OH), 66.27 (CH_2*C*H(CH_3)OH), 17.95 (CH_2CH(*C*H_3)OH)

^{31}P NMR (162 MHz, MeOD) δ -5.33.

HRMS (ESI-TOF) m/z: Calculated for $C_9H_{11}NO_7P$: 276.0279

Found: 276.0284 $[M]^-$

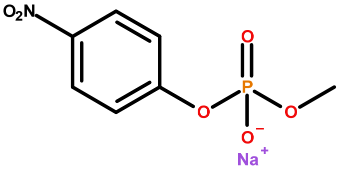

methyl (4-nitrophenyl) hydrogen phosphate sodium salt

The synthesis of [(2S)-2-[*tert*-butyl(dimethyl)silyl]oxypropyl] (4-nitrophenyl) hydrogen phosphate also yielded a small amount of the title compound due to incomplete hydrolysis of the chlorophosphate in the work up step. The subsequent purification using MeOH gave the title compound (10 % relative to target compound). Analytical HPLC Phenomenex Kinetex XB-C18 100 Å 5 µm 4.6 x 250 nm, 5-41 % MeCN 8 min gradient, 254 nm detection, retention time 4.8 min.

^{1}H NMR (400 MHz, MeOD) δ 8.22 (d, J = 8.9 Hz, 2H, Ph-H), 7.43 (dd, J = 9.3, 0.8 Hz, 2H, Ph-H), 3.68 (d, J = 11.2 Hz, 3H, POC*H*$_3$)

^{13}C NMR (101 MHz, MeOD) δ 158.56 (Ph-O), 158.50 (Ph-O), 143.10 (Ph-NO_2), 124.84 (Ph-H), 120.11 (Ph-H), 120.05 (Ph-H), 52.32 (PO*C*H_3), 52.25 (PO*C*H_3)

^{31}P NMR (162 MHz, MeOD) δ -4.21

HRMS (ESI-TOF) m/z: Calculated for $C_7H_7NO_6P$: 232.0016

Found: 232.0019 $[M]^-$

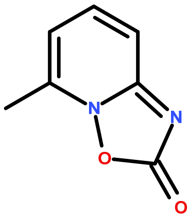

5-methyl-[1,2,4]oxadiazolo[2,3-a]pyridin-2-one

The byproduct formed in the synthesis of [6-(*tert*-butoxycarbonylamino)-2-pyridyl]methyl acetate.

^{1}H NMR (400 MHz, $CDCl_3$) δ 7.63 (dd, *J* = 8.8, 7.5 Hz, 1H, Py-H), 7.17 (dd, *J* = 8.8, 0.6 Hz, 1H, Py-H), 6.76 (d, *J* = 7.5 Hz, 1H, Py-H), 2.66 (s, 3H, Py-CH_3)

^{13}C NMR (101 MHz, $CDCl_3$) δ 160.57 (*C*=O), 156.41 (*Py*-CH_3), 139.12 (*Py*=N), 137.63 (Py-H), 112.37 (Py-H), 111.56 (Py-H), 16.20 (Py-CH_3)

LRMS (ES^+) *m/z* 151 (MH^+) Calculated *m/z* 151.0502 (MH^+)

7.3 - Chapter 3 syntheses

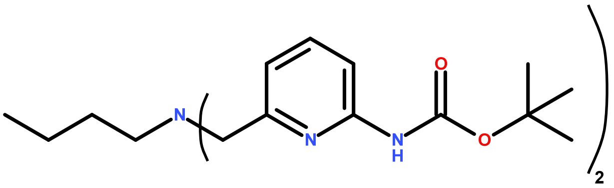

***tert*-butyl N-[6-[[[6-(*tert*-butoxycarbonylamino)-2-pyridyl]methyl-butyl-amino]methyl]-2-pyridyl]carbamate**

tert-butyl N-[6-(iodomethyl)-2-pyridyl]carbamate (1.49 g, 4.46 mmol) was dissolved in dry DMF (30 ml) and n-butylamine (0.18 ml, 1.78 mmol) was added. DIPEA was added and the reaction mixture was stirred at 70 °C over night. The solvent was removed under reduced pressure and the crude liquid was purified using flash chromatography to afford the product (0.52 g, 1.08 mmol) in 60 % yield with a r.f-value of 0.28 in Et_2O/Hexane (50/50).

^{1}H NMR (400 MHz, $CDCl_3$) δ 7.90 (s, 2H, N*H*Boc), 7.76 (d, *J* = 8.2 Hz, 2H, Py-H), 7.59 (t, *J* = 7.9 Hz, 2H, Py-H), 7.15 (d, *J* = 7.2 Hz, 2H, Py-H), 3.66 (s, 4H, Py-C*H*$_2$), 2.46 (m, 2H, C*H*$_2$N(CH$_2$Py)$_2$), 1.47 (m, 20H, C*H*$_2$CH$_2$N(CH$_2$Py)$_2$ & (C*H*$_3$)$_3$), 1.24 (m, 2H, C*H*$_2$CH$_2$CH$_2$CH$_2$N(CH$_2$Py)$_2$), 0.81 (t, *J* = 7.3 Hz, 2H, C*H*$_3$CH$_2$CH$_2$CH$_2$N(CH$_2$Py)$_2$)

^{13}C NMR (101 MHz, CDCl$_3$) δ 158.40 (*Py*-CH$_2$), 152.52 (NH*C*OOtBu), 151.27 (*Py*-NHBoc), 138.39 (Py-H), 117.36 (Py-H), 110.25 (Py-H), 80.61 *C*(CH$_3$)$_3$, 59.73 (CH$_3$CH$_2$CH$_2$CH$_2$N(*C*H$_2$Py)$_2$), 53.96 (CH$_3$CH$_2$CH$_2$*C*H$_2$N(CH$_2$Py)$_2$), 29.30 (CH$_3$CH$_2$*C*H$_2$CH$_2$N(CH$_2$Py)$_2$), 28.22 ((*C*H$_3$)$_3$), 20.44 (CH$_3$*C*H$_2$CH$_2$CH$_2$N(CH$_2$Py)$_2$), 14.00 (*C*H$_3$CH$_2$CH$_2$CH$_2$N(CH$_2$Py)$_2$)

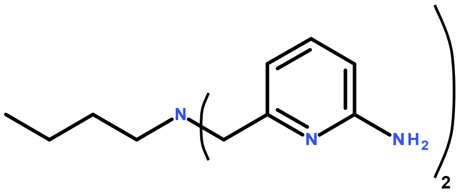

6-[[(6-amino-2-pyridyl)methyl-butyl-amino]methyl]pyridin-2-amine

tert-butylN-[6-[[[6-(*tert*-butoxycarbonylamino)-2-pyridyl]methyl-butyl-amino]methyl]-2-pyridyl]carbamate (0.52 g, 1.08 mmol) was dissolved in 10 ml DCM/TFA (10/90) and the reaction was stirred for 1 hour. The solvent was evaporated to yield the title compound as a brown liquid in quantitative yield.

^{1}H NMR (400 MHz, MeOD) δ 7.81 (dd, *J* = 8.9, 7.2 Hz, 2H, Py-H), 6.89 (d, *J* = 8.9 Hz, 2H, Py-H), 6.82 (d, *J* = 7.2 Hz, 2H, Py-H), 3.84 (s, 4H, Py-C*H*$_2$), 2.59 (m, 2H, C*H*$_2$N(CH$_2$Py)$_2$), 1.52 (m, 2H, C*H*$_2$CH$_2$N(CH$_2$Py)$_2$), 1.28 (m, 2H, C*H*$_2$CH$_2$CH$_2$CH$_2$N(CH$_2$Py)$_2$), 0.89 (t, *J* = 7.4 Hz, 2H, C*H*$_3$CH$_2$CH$_2$CH$_2$N(CH$_2$Py)$_2$).

^{13}C NMR (101 MHz, MeOD) δ 155.35 (*Py*-NH$_2$), 146.48 (*Py*-CH$_2$), 143.88 (Py-H), 112.17 (Py-H),111.64(Py-H),55.07(CH$_3$CH$_2$CH$_2$CH$_2$N(*C*H$_2$Py)$_2$),54.78 (CH$_3$CH$_2$CH$_2$*C*H$_2$N(CH$_2$Py)$_2$),27.82(CH$_3$CH$_2$*C*H$_2$CH$_2$N(CH$_2$Py)$_2$),20.00 (CH$_3$*C*H$_2$CH$_2$CH$_2$N(CH$_2$Py)$_2$), 12.70 (*C*H$_3$CH$_2$CH$_2$CH$_2$N(CH$_2$Py)$_2$)

HRMS (ESI-TOF) m/z: Calculated for $C_{16}H_{24}N_5$: 286.2032

Found: 286.2032 $[M+H]^+$

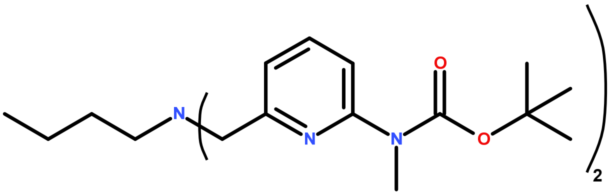

tert-butylN-[6-[[[6-[tert-butoxycarbonyl(methyl)amino]-2-pyridyl]methyl-butyl-amino]methyl]-2-pyridyl]-N-methyl-carbamate

tert-butyl N-[6-(iodomethyl)-2-pyridyl]-N-methyl-carbamate (0.50 g, 1.44 mmol) was dissolved in dry DMF (20 ml) and n-butylamine (0.06 ml, 0.57 mmol) was added. DIPEA was added and the reaction mixture was stirred at 70 °C over night. The solvent was removed under reduced pressure and the crude liquid was purified using flash chromatography to afford the product (0.15 g, 0.29 mmol) in 51 % yield.

^{1}H NMR (400 MHz, $CDCl_3$) δ 7.60 (dd, *J* = 8.1, 7.6 Hz, 2H, Py-H), 7.48 (d, *J* = 8.1 Hz, 2H, Py-H), 7.27 (d, *J* = 7.3 Hz, 2H, Py-H), 3.76 (s, 4H, Py-CH_2), 3.39 (s, 6H, $NHCH_3$), 2.56 (m, 2H, $CH_2N(CH_2Py)_2$), 1.52 (m, 20H, $CH_2CH_2N(CH_2Py)_2$ & $(CH_3)_3$)) 1.33 (m, 2H, $CH_2CH_2CH_2CH_2N(CH_2Py)_2$), 0.87 (t, *J* = 7.4 Hz, 3H, $CH_3CH_2CH_2CH_2N(CH_2Py)_2$)).

^{13}C NMR (101 MHz, $CDCl_3$) δ 158.30 (*Py*-CH_2), 154.50 (*Py*-NCH_3Boc), 154.38 ($NCH_3COOtBu$), 137.14 (Py-H), 117.96(Py-H), 117.13 (Py-H), 80.88 $C(CH_3)_3$, 60.01 ($CH_3CH_2CH_2CH_2N(CH_2Py)_2$) , 54.07 ($CH_3CH_2CH_2CH_2N(CH_2Py)_2$), 34.27 ($NHCH_3$), 29.52 ($CH_3CH_2CH_2CH_2N(CH_2Py)_2$), 28.33 (($CH_3)_3$), 20.50 ($CH_3CH_2CH_2CH_2N(CH_2Py)_2$), 14.06 ($CH_3CH_2CH_2CH_2N(CH_2Py)_2$)

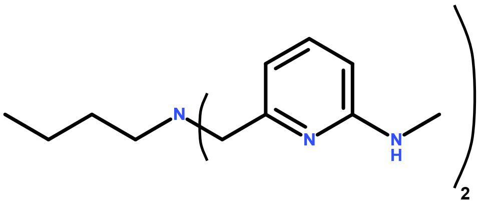

6-[[butyl-[[6-(methylamino)-2-pyridyl]methyl]amino]methyl]-N-methyl-pyridin-2-amine

tert-butylN-[6-[[[6-[*tert*-butoxycarbonyl(methyl)amino]-2-pyridyl]methyl-butyl-amino]methyl]-2-pyridyl]-N-methyl-carbamate (0.15 g, 0.29 mmol) was dissolved in 10 ml DCM/TFA (30/70) and the reaction was stirred for 1 hour. The solvent was evaporated to yield the title compound as a yellow liquid (0.082 g, 0.26 mmol) in 90 % yield.

^{1}H NMR (400 MHz, $CDCl_3$) δ 7.45 (dd, *J* = 8.2 Hz , *J* = 7.3 Hz, 2H, Py-H), 6.90 (d, *J* = 7.3 Hz, 2H, Py-H), 6.25 (d, *J* = 8.2 Hz, 2H, Py-H), 3.65 (s, 4H, Py-C*H*$_2$), 2.90 (d, *J* = 5.2 Hz, 6H, NHC*H*$_3$), 2.54 (m, 2H, C*H*$_2$N(CH_2Py)$_2$), 1.53 (m, 2H, C*H*$_2$$CH_2$N($CH_2$Py)$_2$)), 1.31 (m, 2H, C*H*$_2$$CH_2CH_2CH_2$N($CH_2$Py)$_2$), 0.87 (t, *J* = 7.4 Hz, 3H, C*H*$_3$$CH_2CH_2CH_2$N($CH_2$Py)$_2$)

^{13}C NMR (101 MHz, $CDCl_3$) δ 159.17 (*Py*-$NHCH_3$), 158.71 (*Py*-CH_2), 138.02 (Py-H), 111.55 (Py-H), 103.19 (Py-H), 60.28 ($CH_3CH_2CH_2CH_2$N(*C*H_2Py)$_2$), 54.08 ($CH_3CH_2CH_2$*C*H_2N(CH_2Py)$_2$) , 29.34 (CH_3CH_2*C*H_2CH_2N(CH_2Py)$_2$), 29.28 (NH*C*H_3), 20.57 (CH_3*C*$H_2CH_2CH_2$N(CH_2Py)$_2$), 14.11 (*C*$H_3CH_2CH_2CH_2$N(CH_2Py)$_2$)

HRMS (ESI-TOF) m/z: Calculated for $C_{18}H_{26}N_5Zn$: 376.1480

Found: 376.1486 $[M^-+Zn^{2+}]^+$

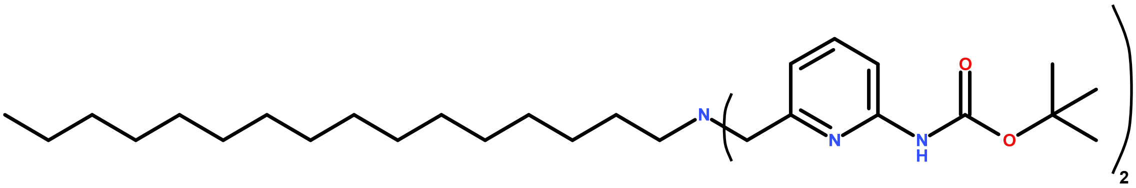

tert-butylN-[6-[[[6-(tert-butoxycarbonylamino)-2-pyridyl]methyl-hexadecyl-amino]methyl]-2-pyridyl]carbamate

tert-butyl N-[6-(iodomethyl)-2-pyridyl]carbamate (1.00 g, 2.99 mmol) was dissolved in 40 ml dry MeCN (alternatively dry DMF) and hexadecylamine (0.29 g, 1.20 mmol) was added. The alkylamine did not dissolve well in MeCN and the reaction was heated to encourage solubilisation. DIPEA (2.09 ml, 11.97 mmol) was added and the reaction was heated to 70 °C for 1 hour. The solvent was removed and the crude product was purified using flash chromatography to afford the title compound (0.43 g, 0.66 mmol) in 55 % yield with a r.f-value of 0.72 (in 100 % EtOAc).

^{1}H NMR (400 MHz, $CDCl_3$) δ 7.78 (d, *J* = 8.1 Hz, 2H, Py-H), 7.63 (t, *J* = 7.9 Hz, 2H, Py-H), 7.31 (s, 2H, N*H*Boc), 7.17 (d, *J* = 7.4 Hz, 2H, Py-H), 3.68 (s, 4H, Py-C*H*$_2$), 2.49 (m, 2H, $CH_3(CH_2)_{14}$C*H*$_2$N(CH_2)$_2$), 1.52 (s, 18H, (CH_3)$_3$), 1.25 (m, 28H, CH_3(C*H*$_2$)$_{14}$$CH_2$N($CH_2$)$_2$), 0.89 (t, *J* = 6.9 Hz, 3H, C*H*$_3$(CH_2)$_{14}$$CH_2$N($CH_2$)$_2$)

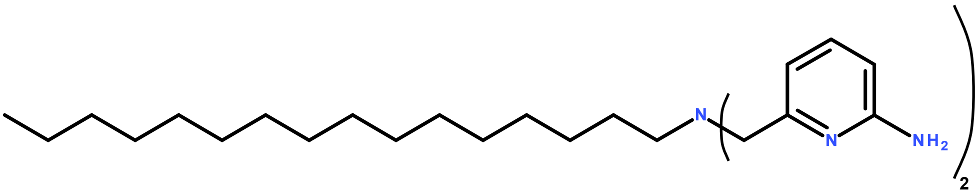

6-[[(6-amino-2-pyridyl)methyl-hexadecyl-amino]methyl]pyridin-2-amine

tert-butyl N-[6-[[[6-(*tert*-butoxycarbonylamino)-2-pyridyl]methyl-hexadecyl-amino]methyl]-2-pyridyl]carbamate (0.43 g, 0.66 mmol) was dissolved in 10 ml DCM/TFA (10/90) and the reaction was stirred for 1 hour. The solvent was evaporated to yield the title compound as a brown liquid in quantitative yield.

^{1}H NMR (400 MHz, MeOD) δ 7.82 (dd, J = 8.9, 7.2 Hz, 2H, Py-H), 6.89 (d, J = 8.9 Hz, 2H, Py-H), 6.82 (d, J = 7.2 Hz, 2H, Py-H), 3.84 (s, 4H, Py-$\mathrm{C}H_2$), 2.58 (m, 2H, $\mathrm{CH_3(CH_2)_{14}C}H_2\mathrm{N(CH_2)_2}$), 1.52 (m, 2H, $\mathrm{CH_3(CH_2)_{14}C}H_2\mathrm{N(CH_2)_2}$), 1.30 (m, 28H, $\mathrm{CH_3(C}H_2\mathrm{)_{14}CH_2N(CH_2)_2}$)), 0.92 (t, J = 6.8 Hz, 3H, $\mathrm{C}H_3\mathrm{(C}H_2\mathrm{)_{14}CH_2N(CH_2)_2}$)

^{13}C NMR (101 MHz, MeOD) δ 155.35 (*Py*-$\mathrm{NH_2}$), 146.56 (*Py*-$\mathrm{CH_2}$), 143.89 (Py-H), 112.15 (Py-H), 111.64 (Py-H), 55.18 $\mathrm{CH_3(CH_2)_{14}CH_2N(}C\mathrm{H_2)_2}$, 55.07 $\mathrm{CH_3(CH_2)_{14}}C\mathrm{H_2N(CH_2)_2}$, 31.66 ($\mathrm{CH_3CH_2}C\mathrm{H_2(CH_2)_{10}CH_2CH_2CH_2N(CH_2)_2}$),29.20$\mathrm{CH_3CH_2CH_2}$ ($C\mathrm{H_2)_{10}CH_2CH_2CH_2N(CH_2)_2}$), 26.85($\mathrm{CH_3CH_2CH_2(CH_2)_{10}}C\mathrm{H_2CH_2CH_2N(CH_2)_2}$),25.72 ($\mathrm{CH_3CH_2CH_2(CH_2)_{10}CH_2}C\mathrm{H_2CH_2N(CH_2)_2}$), 2.32 ($\mathrm{CH_3CH_2CH_2(CH_2)_{10}CH_2CH_2}C\mathrm{H_2N(CH_2)_2}$), 13.03 $C\mathrm{H_3(CH_2)_{14}CH_2N(CH_2)_2}$

HRMS (ESI-TOF) m/z: Calculated for $\mathrm{C_{28}H_{48}N_5}$: 454.3910

Found: 454.3913 $[\mathrm{M+H}]^+$

7.4 - Chapter 4 syntheses

7.4.1 - Peptide synthesis

The synthesis of the peptides was performed using standard Fmoc SPPS protocol was adhered to throughout the synthesis, see Chapter 8.9.2. The peptide sequence **Fmoc-*LENEVARLKKLVKQG*-OH** was purchased from Severn Biotech supplied on a polystyrene solid support with all the protecting groups intact. All couplings were performed at room temperature under N_2 atmosphere unless otherwise stated.

Ac-Y*LENEVARLKKLVKQG*-(L4-2)$_2$

The solid support attached sequence Fmoc-LENEVARLKKLVKQG was allowed to swell in DCM followed by DMF. The N-terminus was deprotected using 20% piperidine in DMF (agitated under nitrogen) followed by washing of the resin beads. A mixture containing Fmoc-Tyr(OtBu)-OH, HBTU and DIPEA in DMF was added to the resins and agitated for 3 hours. The resin was washed and Fmoc removed using the same procedure as above (20% piperidine in DMF). After washing the resin, mixture of Ac_2O, DIPEA and DMF was added to the resins and agitated for 1 hour followed by washing of the beads. The peptide sequence Ac-Y*LENEVARLKKLVKQG* was cleaved off the solid support under mildly acidic (1-5% TFA in DCM) conditions and the peptide was extracted from water using $CHCl_3$ and Et_2O and dried over $MgSO_4$. The crude mixture containing the peptide was used (0.46 g, 0.15 mmol) was dissolved with HBTU (0.06 g, 0.16 mmol) and DIPEA (0.15 ml, 0.88 mmol) in 5 ml DMF. *tert*-butylN-[6-[[3-aminopropyl-[[6-(*tert*-butoxycarbonylamino)-2-pyridyl]methyl]amino]methyl]-2-pyridyl]carbamate (0.21 g, 0.44 mmol) was dissolved in DMF and added to the reaction mixture and stirred over night. DMF was evaporated and the crude product was passed through a short silica plug. The resulting crude product was treated with TFA/TIS/H_2O (90/5/5) for 4 hours after which the TFA was removed by blowing nitrogen at the liquid. The peptide was purified using a 19 x 250 mm C-18 Waters X-bridge column with 25-60 % MeCN (0.1 % TFA), 20 min gradient, 254 nm detection, retention time 13.7 min. The peptide was freeze dried and obtained in 5 % yield (15 mg, 7 µmol) as a porous white solid.

LRMS (ES^+) *m/z* 1100 (MH^{2+})   Calculated *m/z* 1098.6424 (MH^{2+})

HRMS (ESI-TOF) m/z: Calculated for $C_{102}H_{169}N_{30}O_{24}$: 2198.2921

Found: 2198.2911 $[M+H]^+$

Ac-*CGYLENEVARLKKLVKQG*-OH

The peptide sequence was synthesised from Fmoc-LENEVARLKKLVKQG using standard Fmoc chemistry with HBTU, Fmoc-Tyr(OtBu)-OH, Fmoc-Gly-OH and Fmoc-Cys(trt)-OH.

LRMS (ES^+) *m/z* 1046 (MH^{2+})   Calculated *m/z* 1045.5677 (MH^{2+})

7.4.2 - Ligand synthesis

1,3-diazidopropane

1,3-dibromopropane (20.19 g, 100.00 mmol) was dissolved in DMF (100 ml) and NaN_3 (14.30 g, 220.00 mmol) was added. The reaction mixture was left stirring over night at 80 °C. The reaction mixture was added to H_2O (500 ml) and extracted with Et_2O (3 x 100 ml). The organic phases were pooled and washed with H_2O (3 x 250 ml) followed by drying over $MgSO_4$. The solvent was removed under reduced pressure to afford the title compound as a light yellow oil (11.34 g, 89.91 mmol) in 89% yield.

^{1}H NMR (400 MHz, $CDCl_3$) δ 3.44 (t, $J = 6.5$ Hz, 2H, $C\mathit{H}_2$), 1.85 (p, $J = 6.5$ Hz, 4H, $N_3C\mathit{H}_2$)

^{13}C NMR (101 MHz, $CDCl_3$) δ 48.43 (CH_2), 28.30 ($N_3\mathit{C}H_2$)

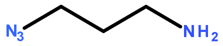

3-azidopropan-1-amine

1,3-dibromopropane (5.00 g, 39.64 mmol) was dissolved in 60 ml EtOAc/Et2O (50/50) and stirred in an ice bath. To the stirred solution 60 ml HCl (2 M) was added followed by the addition of triphenyl phosphine (10.40 g, 39.64 mmol) in small portions over 30 min then stirred vigorously over night. Et_2O was added and the organic layer was separated and discarded. The aqueous layer was washed thrice with Et_2O and the organic layer was discarded. The aqueous layer was basified (pH 12) which turned the solution cloudy and the basified aqueous layer was extracted thrice with Et_2O. The organic layer was dried over $MgSO_4$ the solvent was removed under reduced pressure to yield the product as a yellow liquid (1.65 g, 16.48 mmol) in 41 % yield.

Alternative synthesis:

3-Bromopropylamine hydrobromide (14.40 g, 65.78 mmol) dissolved in DMF (150 ml). NaN_3 (5.13 g, 78.94 mmol) was added and the reaction mixture was left stirring over night at 70 °C. The solvent was evaporated and H_2O was added followed by NaOH until solution was highly basic. DCM followed by Et_2O was used to extract the product followed by drying of the organic phase with $MgSO_4$. The solvent was removed under reduced pressure to afford the title compound as an orange liquid (6.48 g, 64.72 mmol) in 98% yield.

^{1}H NMR (400 MHz, $CDCl_3$) δ 3.32 (t, *J* = 6.7 Hz, 2H, N_3CH_2), 2.74 (t, *J* = 6.8 Hz, 2H, CH_2NH_2), 1.67 (p, *J* = 6.8 Hz, 2H, CH_2), 1.13 (s, 2H, NH_2)

^{13}C NMR (101 MHz, $CDCl_3$) δ 49.09 (N_3CH_2), 39.28 (NH_2CH_2), 32.41 (CH_2)

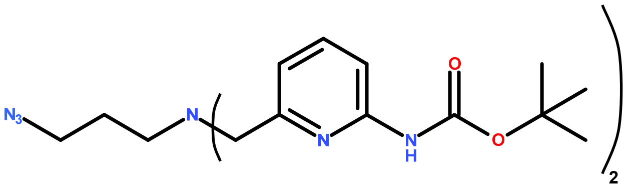

tert-butylN-[6-[[3-azidopropyl-[[6-(tert-butoxycarbonylamino)-2-pyridyl]methyl]amino]methyl]-2-pyridyl]carbamate

tert-butyl N-[6-(iodomethyl)-2-pyridyl]carbamate (1.50 g, 4.49 mmol) was dissolved in dry DMF and 3-azidopropan-1-amine (0.18 g, 1.80 mmol) was added. The reaction mixture was stirred and DIPEA (3.13 ml, 17.96 mmol) was added and the reaction was heated at 70 °C over night. The solvent was evaporated and the crude reaction mixture was purified using flash chromatography. The product was obtained as a porous light yellow solid in 37 % yield with a r.f-value of the 0.53 in EtOAc/Hexane (50/50).

^{1}H NMR (400 MHz, $CDCl_3$) δ 7.79 (d, *J* = 8.2 Hz, 2H, Py-H), 7.64 (t, *J* = 7.9 Hz, 2H, Py-H), 7.47 (s, 2H, N*H*Boc), 7.10 (d, *J* = 7.3 Hz, 2H, Py-H), 3.68 (s, 4H, Py-C*H*$_2$), 3.31 (t, *J* = 6.8 Hz, 2H, N_3C*H*$_2$CH$_2$), 2.60 (t, *J* = 6.9 Hz, 2H, C*H*$_2$N(CH$_2$Py)$_2$), 1.78 (p, *J* = 6.8 Hz, 2H, N_3CH_2C*H*$_2$), 1.52 (s, 18H, $(CH_3)_3$)

^{13}C NMR (101 MHz, $CDCl_3$) δ 157.69 (*Py*-CH$_2$), 152.37 (NH*C*OOtBu), 151.23 (*Py*-NHBoc), 138.53 (Py-H), 117.58 (Py-H), 110.35 (Py-H), 80.85 (*C*(CH$_3$)$_3$), 59.79 (Py-*C*H$_2$), 51.00 (*C*H$_2$N(CH$_2$Py)$_2$) , 49.44 (N_3*C*H$_2$CH$_2$), 28.26 ($(CH_3)_3$), 26.53 (N_3CH_2*C*H$_2$)

FT-IR (ATR solid, cm^{-1}): 2090.5 (N_3)

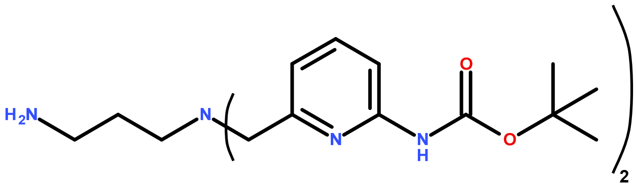

tert-butylN-[6-[[3-aminopropyl-[[6-(tert-butoxycarbonylamino)-2-pyridyl]methyl]amino]methyl]-2-pyridyl]carbamate

tert-butylN-[6-[[3-azidopropyl-[[6-(*tert*-butoxycarbonylamino)-2-pyridyl]methyl]amino]methyl]-2-pyridyl]carbamate (0.40 g, 0.78 mmol) was reduced to the corresponding amine compound using the ThalesNano H-Cube continuous-flow hydrogenation reactor. The compound was dissolved in the EtOAc (30 ml) and a few drops of AcOH were added to the reaction mixture. This was used in order to protonate the amine upon formation in order to minimise adhesion to the palladium in the catalyst. The catalyst used in the hydrogenation was Pd/C (10% on carbon) packed in a cartridge. The reaction solution was pumped through the cartridge at 1 ml/min (recirculation) with a $H_{2(g)}$ pressure of 30 bar and a temperature of 40 °C. After 2 hours the solvent was evaporated and to afford the title compound as a viscous yellow liquid in quantitative yield.

^{1}H NMR (400 MHz, $CDCl_3$) δ 7.77 (d, *J* = 8.4 Hz, 2H, Py-H), 7.60 (dd, *J* = 8.3, 7.4 Hz, 2H, Py-H), 7.07 (d, *J* = 7.2 Hz, 2H, Py-H), 3.64 (s, 4H, Py-CH_2), 2.71 (t, *J* = 6.6 Hz, 2H, $NH_2CH_2CH_2$), 2.54 (t, *J* = 6.8 Hz, 2H, $CH_2N(CH_2Py)_2$), 1.67 (p, *J* = 6.7 Hz, 2H, $NH_2CH_2CH_2$), 1.50 (s, 18H, $(CH_3)_3$)

^{13}C NMR (101 MHz, $CDCl_3$) δ 155.63 (*Py*-CH_2), 153.34 (NHCOOtBu), 153.16 (*Py*-NHBoc), 138.61 (Py-H), 118.14 (Py-H), 112.11 (Py-H), 80.61 ($C(CH_3)_3$), 59.52 (Py-CH_2), 53.37 ($CH_2N(CH_2Py)_2$), 40.36 ($NH_2CH_2CH_2$), 28.28 ($(CH_3)_3$), 22.99 ($NH_2CH_2CH_2$)

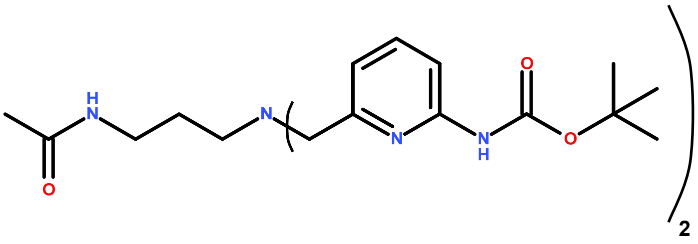

***tert*-butyl N-[6-[[3-acetamidopropyl-[[6-(*tert*-butoxycarbonylamino)-2-pyridyl]methyl]amino]methyl]-2-pyridyl]carbamate**

tert-butylN-[6-[[3-aminopropyl-[[6-(*tert*-butoxycarbonylamino)-2-pyridyl]methyl]amino]methyl]-2-pyridyl]carbamate (0.44 g, 0.90 mmol) was dissolved in DMF (10 ml) and DIPEA (1.59 ml, 8.96 mmol) was added. Acetic anhydride (0.85 ml, 8.96 mmol) was added and the reaction was allowed to stir over night under inert atmosphere. The solvent was removed and the crude reaction product was purified using flash chromatography to afford the title compound as a viscous liquid in 42 % yield (0.20 g, 0.38 mmol) with a r.f-value of 0.19 (in 100 % EtOAc).

^{1}H NMR (400 MHz, $CDCl_3$) δ 7.81 (d, *J* = 8.1 Hz, 2H, Py-H), 7.65 (dd, *J* = 8.3, 7.4 Hz, 2H, Py-H), 7.26 (s, 2H, N*H*Boc), 7.05 (d, *J* = 7.1 Hz, 2H, Py-H), 3.65 (s, 4H, Py-$C\mathit{H}_2$), 3.30 (dd, *J* = 12.0, 5.8 Hz, 2H, $CH_3CONC\mathit{H}_2CH_2$), 2.59 (t, *J* = 6.2 Hz, 2H, $C\mathit{H}_2N(CH_2Py)_2$), 1.89 (s, 3H, $C\mathit{H}_3CON$), 1.71 (p, *J* = 6.7 Hz, 2H, $NH_2CH_2C\mathit{H}_2$), 1.53 (s, 18H, $(CH_3)_3$)

^{13}C NMR (101 MHz, $CDCl_3$) δ 169.77 ($CH_3\mathit{C}ON$), 157.50 (*Py*-CH_2), 152.26 (NH*C*OOtBu), 151.36 (*Py*-NHBoc), 138.60 (Py-H), 117.91 (Py-H), 110.50 (Py-H), 81.06 ($\mathit{C}(CH_3)_3$), 59.71 (Py-$\mathit{C}H_2$), 52.44 ($\mathit{C}H_2N(CH_2Py)_2$), 38.50 ($CH_3CON\mathit{C}H_2CH_2$), 28.26 ($((CH_3)_3)$), 26.13 ($CH_3CONCH_2\mathit{C}H_2$), 23.20 ($\mathit{C}H_3CON$)

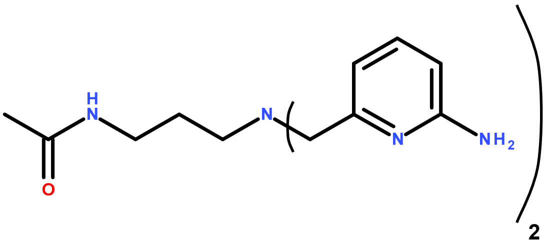

N-[3-[bis[(6-amino-2-pyridyl)methyl]amino]propyl]acetamide

tert-butylN-[6-[[3-acetamidopropyl-[[6-(*tert*-butoxycarbonylamino)-2-pyridyl]methyl]amino]methyl]-2-pyridyl]carbamate (0.20 g, 0.38 mmol) was placed in a flask and TFA/DCM (90/10) was added. The reaction was left to stir for 2 hours and the solvent was then evaporated by blowing $N_{2(g)}$ at the reaction solution. The work up consisted of adding $H_2O/CHCl_3$ to the crude reaction mixture to which NaOH was added to basify the aqueous solution and it was then extracted thrice with $CHCl_3$. The organic phase was dried over Na_2SO_4 and the solvent was removed under reduced pressure to yield the title compound (0.049 g, 0.15 mmol) as a viscous liquid in 39 % yield.

^{1}H NMR (400 MHz, $CDCl_3$) δ 7.40 (dd, *J* = 8.0, 7.3 Hz, 2H, Py-H), 6.77 (d, *J* = 7.3 Hz, 2H, Py-H), 6.39 (d, *J* = 8.0 Hz, 2H, Py-H), 4.52 (s, 4H, Py-N*H*$_2$), 3.58 (s, 4H, Py-C*H*$_2$), 3.31 (dd, *J* = 11.6, 5.7 Hz, 2H, CH$_3$CONC*H*$_2$CH$_2$), 2.59 (t, *J* = 6.0 Hz, 2H, C*H*$_2$N(CH$_2$Py)$_2$), 1.93 (s, 3H, C*H*$_3$CON), 1.68 (p, *J* = 6.7 Hz, 2H, CH$_3$CONCH$_2$C*H*$_2$).

^{13}C NMR (101 MHz, $CDCl_3$) δ 170.01 (CH$_3$*C*ON), 158.14 (*Py*-NH$_2$), 157.80 (*Py*-CH$_2$), 138.16 (Py-H), 113.22 (Py-H), 106.90 (Py-H), 60.21 (Py-*C*H$_2$), 52.77 (*C*H$_2$N(CH$_2$Py)$_2$), 38.60 (CH$_3$CON*C*H$_2$CH$_2$), 26.03 (CH$_3$CONCH$_2$*C*H$_2$), 23.23 (*C*H$_3$CON)

HRMS (ESI-TOF) m/z: Calculated for $C_{17}H_{25}N_6O$: 329.2090

Found: 329.2096 $[M+H]^+$

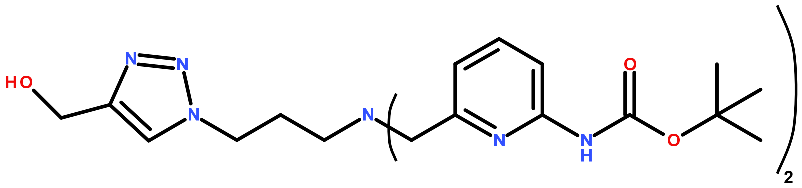

tert-butylN-[6-[[[6-(tert-butoxycarbonylamino)-2-pyridyl]methyl-[3-[4-(hydroxymethyl)triazol-1-yl]propyl]amino]methyl]-2-pyridyl]carbamate

tert-butylN-[6-[[3-azidopropyl-[[6-(*tert*-butoxycarbonylamino)-2-pyridyl]methyl]amino]methyl]-2-pyridyl]carbamate (0.42 g, 0.82 mmol) and prop-2-yn-1-ol (0.07 ml, 1.23 mmol) were dissolved in DCM (10 ml). CuSO4· 5 H2O (0.010 g, 0.04 mmol) and sodium ascorbate (0.024 g, 0.12 mmol) were dissolved in H_2O and added to the DCM solution. The biphasic reaction mixture was stirred vigorously for 7 hours and the organic phase was separated and dried over $MgSO_4$. The crude green reaction mixture was purified using flash chromatography to yield the title compound as a viscous liquid (0.22 g, 0.39 mmol) in 47 % yield with a r.f-value of 0.51 (in 10/90 MeOH/EtOAc).

^{1}H NMR (400 MHz, MeOD) δ 7.71 (m, 5H, Py-H & C*H*=CCH$_2$OH), 7.14 (dd, *J* = 6.8 Hz, *J* = 0.9 Hz, 2H), 4.64 (s, 2H, CH=CC*H*$_2$OH), 4.44 (t, *J* = 6.9 Hz, 2H,

$NCH_2CH_2CH_2N(CH_2Py)_2$), 3.70 (s, 4H, Py-C*H*$_2$), 2.56 (t, *J* = 6.8 Hz, 2H, $NCH_2CH_2CH_2N(CH_2Py)_2$), 2.14 (p, *J* = 6.7 Hz, 2H, $NCH_2CH_2CH_2N(CH_2Py)_2$), 1.54 (s, 18H, $(CH_3)_3$)

^{13}C NMR (101 MHz, MeOD) δ 157.47 (*Py*-CH_2) , 153.09 (NH*C*OOtBu), 151.73 (*Py*-NHBoc), 147.46 (CH=*C*CH_2OH), 138.31 (Py-H), 122.75 (*C*H=CCH_2OH), 117.69 (Py-H), 110.51 (Py-H), 80.17 (*C*$(CH_3)_3$), 59.34 (Py-*C*H_2), 55.06 ($NCH_2CH_2CH_2N(CH_2Py)_2$), 50.41 (CH=C*C*H_2OH), 47.85 ($NCH_2CH_2CH_2N(CH_2Py)_2$) , 27.34 ($NCH_2CH_2CH_2N(CH_2Py)_2$), 27.19 ($(CH_3)_3$)

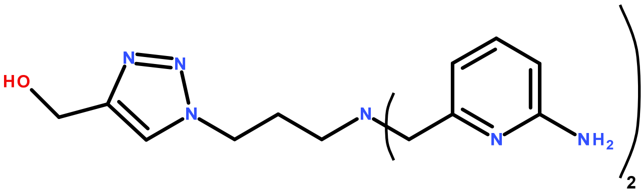

[1-[3-[bis[(6-amino-2-pyridyl)methyl]amino]propyl]triazol-4-yl]methanol

tert-butylN-[6-[[[6-(*tert*-butoxycarbonylamino)-2-pyridyl]methyl-[3-[4-(hydroxymethyl)triazol-1-yl]propyl]amino]methyl]-2-pyridyl]carbamate (0.22 g, 0.39 mmol) was dissolved in and TFA/DCM (90/10). The reaction was left to stir for 2 hours and the solvent was then evaporated by blowing $N_{2(g)}$ at the reaction solution. The work up consisted of adding H_2O/DCM to the crude reaction mixture to which NaOH was added to basify the aqueous solution and it was then extracted thrice with DCM. The organic phase was dried over $MgSO_4$ and the solvent was removed under reduced pressure to yield the title compound (0.046 g, 0.12 mmol) as a viscous liquid 32 % yield.

^{1}H NMR (400 MHz, MeOD) δ 7.75 (s, 1H, C*H*=CCH_2OH), 7.44 (dd, *J* = 8.2, 7.4 Hz, 2H, Py-H), 6.77 (d, *J* = 7.3 Hz, 1H, Py-H), 6.47 (d, *J* = 8.3 Hz, 1H, Py-H), 4.65 (s, 2H, CH=CC*H*$_2$OH), 4.42 (t, *J* = 6.9 Hz, 2H, $NCH_2CH_2CH_2N(CH_2Py)_2$), 3.59 (s, 4H, Py-C*H*$_2$), 2.55 (t, *J* = 6.8 Hz, 2H, $NCH_2CH_2CH_2N(CH_2Py)_2$), 2.10 (p, *J* = 6.8 Hz, 2H, $NCH_2CH_2CH_2N(CH_2Py)_2$)

^{13}C NMR (101 MHz, MeOD) δ 159.01 (*Py*-NH_2), 156.34 (*Py*-CH_2), 147.46 (CH=*C*CH_2OH), 138.45 (Py-H), 122.73 (*C*H=CCH_2OH), 111.86 (Py-H), 107.28 (Py-H), 59.59 (Py-*C*H_2), 55.05 ($NCH_2CH_2CH_2N(CH_2Py)_2$), 50.58 (CH=C*C*H_2OH), 47.91 ($NCH_2CH_2CH_2N(CH_2Py)_2$), 27.36 ($NCH_2CH_2CH_2N(CH_2Py)_2$)

HRMS (ESI-TOF) m/z: Calculated for $C_{18}H_{25}N_8O$: 369.2151

Found: 369.2145 $[M+H]^+$

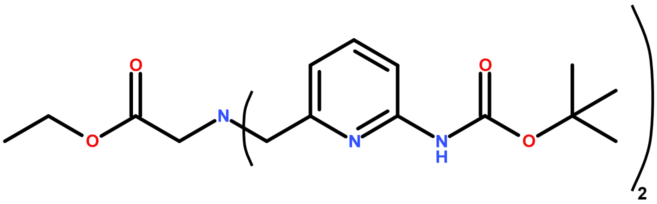

ethyl 2-[bis[[6-(*tert*-butoxycarbonylamino)-2-pyridyl]methyl]amino]acetate

tert-butyl N-[6-(iodomethyl)-2-pyridyl]carbamate (1.50 g, 4.49 mmol) was dissolved in dry DMF (100 ml). Glycine ethyl ester hydrochloride (0.25 g, 1.80 mmol) was added and the reaction mixture was stirred. DIPEA (3.13 ml, 17.96 mmol) was added and the reaction was heated in an oil bath to 70 °C over night. The DMF was evaporated under reduced pressure and the product was purified using flash chromatography to afford the title compound in 45% yield (0.42 g, 0.81 mmol).

^{1}H NMR (400 MHz, $CDCl_3$) δ 7.78 (d, J = 8.2 Hz, 2H, Py-H), 7.62 (t, J = 8.0 Hz, 2H, Py-H), 7.42 (s, 1H, N*H*Boc), 7.14 (d, J = 7.4 Hz, 2H, Py-H), 4.15 (q, J = 7.1 Hz, 2H, $COOCH_2CH_3$), 3.87 (s, 4H, Py-CH_2), 3.44 (s, 2H, $COCH_2$), 1.51 (s, 18H, $(CH_3)_3$), 1.26 (t, J = 7.1 Hz, 3H, $COOCH_2CH_3$)

^{13}C NMR (101 MHz, $CDCl_3$) δ 171.24 ($COOCH_2CH_3$), 157.28 (*Py*-CH_2), 152.37 (N*C*OOtBu), 151.28 (*Py*-NHBoc), 138.61 (Py-H), 117.80 (Py-H), 110.47 (Py-H), 80.82 ($C(CH_3)_3$), 60.38 ($COOCH_2CH_3$), 59.29 (Py-CH_2), 54.66 ($CH_2COOCH_2CH_3$), 28.25 ($(CH_3)_3$), 14.25 (CH_3)

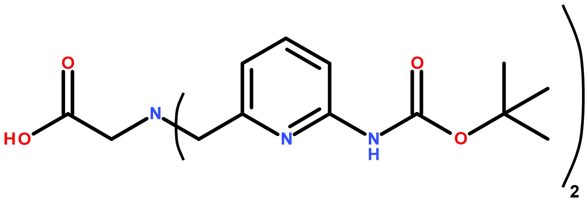

2-[bis[[6-(*tert*-butoxycarbonylamino)-2-pyridyl]methyl]amino]acetic acid

Ethyl 2-[bis[[6-(*tert*-butoxycarbonylamino)-2-pyridyl]methyl]amino]acetate (0.31 g, 0.61 mmol) was dissolved in 30 ml MeOH/EtOH (50/50) and stirred. After 5 min saturated NaOH (2 ml) was added dropwise and the reaction mixture was stirred. After 1 hour the solvent was evaporated. Water was added to the reaction mixture and the compound was extracted with $CHCl_3$ and dried over $MgSO_4$ and the solvent was evaporated under reduced pressure. The product was obtained as a viscous yellow liquid (0.31 g, 0.64 mmol) in quantitative yield.

^{1}H NMR (400 MHz, $CDCl_3$) δ 9.80 (s, 1H, COO*H*), 7.95 (d, *J* = 8.3 Hz, 2H, Py-H), 7.50 (dd, *J* = 8.4, 7.5 Hz, 2H, Py-H), 6.71 (d, *J* = 7.2 Hz, 2H, Py-H), 3.60 (dd, *J* = 72.6, 13.7 Hz, 4H, Py-C*H*$_2$), 3.33 (s, 2H, COC*H*$_2$), 1.51 (s, 18H, $(CH_3)_3$).

^{13}C NMR (101 MHz, $CDCl_3$) δ 179.92 (*C*OOH), 156.00 (*Py*-CH$_2$), 154.20 (N*C*OOtBu), 153.45 (*Py*-NHBoc), 138.51 (*Py*-H), 117.43 (*Py*-H), 111.94 (*Py*-H), 79.96 (*C*$(CH_3)_3$), 59.59 (*C*H$_2$COOH), 59.24 (Py-*C*H$_2$), 28.63 ((*C*H$_3$)$_3$)

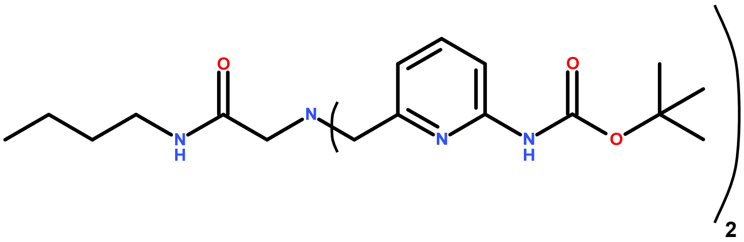

tert-butyl N-[6-[[[6-(_tert_-butoxycarbonylamino)-2-pyridyl]methyl-[2-(butylamino)-2-oxo-ethyl]amino]methyl]-2-pyridyl]carbamate

2-[bis[[6-(*tert*-butoxycarbonylamino)-2-pyridyl]methyl]amino]acetic acid (0.26 g, 0.54 mmol) was dissolved in DMF (25 ml), HBTU (0.23 g, 0.59 mmol) was added and the suspension was stirred. DIPEA (0.24 ml, 1.35 mmol) was added and the solution was stirred under inert atmosphere. After 1 hour n-butylamine (2.00 ml, 20.24 mmol) was added and the reaction mixture was stirred under inert atmosphere over night. The solvent was removed under reduced pressure and the crude brown liquid was analysed by LC-MS. The product peak is the major component according to the LC- trace, no further analyses were performed

7.5 - Chapter 5 syntheses

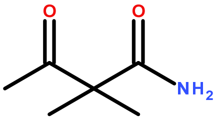

2,2-dimethyl-3-oxo-butanamide

Acetoacetamide (10.00 g, 98.91 mmol) and potassium carbonate (13.67 g, 98.91 mmol) were stirred in dry DMF (150 ml) for 30 min after which methyl iodide (6.16 ml, 98.91 mmol) was added. The reaction mixture was left to stir over night after which the solid was filtered off. To the supernatant was added potassium carbonate (13.67 g, 98.91 mmol) and stirred for 30 min followed by the addition of methyl iodide (6.16 ml, 98.91 mmol). The reaction mixture was stirred over night. The solid was filtered off and the DMF was evaporated. TLC revealed a spot with a r.f-value of 0.40 (in 100 % EtOAc) after staining with $KMnO_4$ that was different from the starting material. The brown liquid was left to crystallise in the fume hood over night. The solid filtered and washed with cold (-18 °C) EtOAc to afford the product as a white/yellow solid. After repeated crystallisations the product was obtained (9.74 g, 75.41 mmol) in 76% yield.

^{1}H NMR (400 MHz, MeOD) δ 4.91 (s, 2H, CON*H2*), 2.19 (s, 3H, C*H*$_3$CO), 1.36 (s, 6H, C(C*H*$_3$)$_2$).

^{13}C NMR (101 MHz, MeOD) δ 207.96 (CH$_3$*C*O), 177.25 (*C*ONH$_2$), 55.75 (*C*(CH$_3$)$_2$), 24.46 (*C*H$_3$CO), 21.25 (C(*C*H$_3$)$_2$)

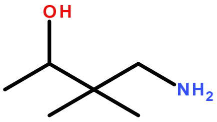

4-amino-3,3-dimethyl-butan-2-ol

Lithium aluminium hydride (7.05 g, 185.82 mmol) was charged under nitrogen into an oven dried flask and dry THF (200 ml) was slowly added. The flask was stirred under nitrogen at -78 °C. 2,2-dimethyl-3-oxo-butanamide (6.00 g, 46.45 mmol) was dissolved in dry THF (50 ml) and slowly added to the stirring $LiAlH_4$ suspension. The reaction was allowed to adapt room temperature over night. The reaction was then heated to reflux for 2 hours. The work up consisted of stirring the reaction in an ice bath and slowly adding H_2O (≈ 5ml) followed by 15 % NaOH solution (≈ 5ml). H_2O was then added until effervescence stopped. The solid was filtered off, washed with Et_2O and the organic phases were pooled and dried over $MgSO_4$. The solvent was removed under reduced pressure to afford the product as a clear liquid (5.18 g, 44.20 mmol) in 95 % yield.

^{1}H NMR (400 MHz, $CDCl_3$) δ 3.73 (q, *J* = 6.4 Hz, 1H, C*H*OH), 3.01 (br s, 2H, N*H*2), 2.75 (dd, *J* = 67.0, 12.4 Hz, 2H, C*H*$_2$NH$_2$), 1.10 (d, *J* = 6.4 Hz, 3H, C*H*$_3$CHOH), 0.86 (d, *J* = 34.1 Hz, 6H, *C*H$_3$)$_2$)

^{13}C NMR (101 MHz, $CDCl_3$) δ 76.44, 53.56, 36.93, 24.06, 18.18 (C(*C*H$_3$)$_2$), 17.90 (C(*C*H$_3$)$_2$)

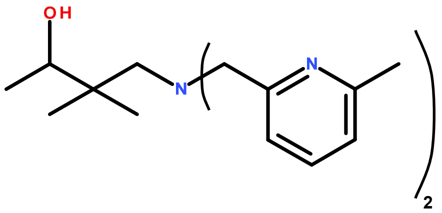

4-[bis[(6-methyl-2-pyridyl)methyl]amino]-3,3-dimethyl-butan-2-ol

2-(iodomethyl)-6-methyl-pyridine (4.00 g, 17.16 mmol) was dissolved in dry DMF (50 ml) and 4-amino-3,3-dimethyl-butan-2-ol (0.80 g, 6.87 mmol) was dissolved in dry DMF and added. DIPEA (4.78 g, 27.46 mmol) was added to the solution and the reaction was stirred at 70 °C over night. The solvent was evaporated and the crude reaction mixture was purified by flash chromatography. The product was obtained as a viscous brown liquid (1.86 g, 5.68 mmol) in 82 % yield.

^{1}H NMR (400 MHz, $CDCl_3$) δ 7.54 (t, *J* = 7.7 Hz, 2H, Py-H), 7.25 (d, *J* = 7.7 Hz, 2H, Py-H), 7.03 (d, *J* = 7.6 Hz, 2H, Py-H), 3.85 (dd, *J* = 81.0, 14.3 Hz, 4H, Py-C*H*$_2$), 3.49 (q, *J* = 6.4 Hz, 1H, C*H*OH), 2.68 (d, *J* = 4.4 Hz, 2H, C*H*$_2$N), 2.56 (s, 6H, Py-CH$_3$), 1.00 (d, *J* = 6.4 Hz, 3H, C*H*$_3$CHOH), 0.87 (d, *J* = 75.0 Hz, 6H, (C*H*$_3$)$_2$)

^{13}C NMR (101 MHz, $CDCl_3$) δ 155.41 (*Py*-CH$_3$), 152.42 (*Py*-CH$_2$), 144.45 (Py-H), 126.09 (Py-H), 123.75 (Py-H), 73.39 (*C*HOH), 66.00 (C(CH$_3$)$_2$*C*H$_2$), 57.48 (Py-*C*H$_2$), 39.35 (*C*(CH$_3$)$_2$), 24.68 (Py-CH$_3$), 20.13 ((*C*H$_3$)$_2$), 19.95 ((*C*H$_3$)$_2$), 17.98 (*C*H$_3$CHOH)

HRMS (ESI-TOF) m/z: Calculated for $C_{20}H_{30}N_3O$: 328.2389

Found: 328.2381 [M+H]$^+$

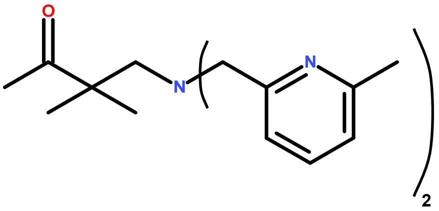

4-[bis[(6-methyl-2-pyridyl)methyl]amino]-3,3-dimethyl-butan-2-one

4-[bis[(6-methyl-2-pyridyl)methyl]amino]-3,3-dimethyl-butan-2-ol (0.36 g, 1.10 mmol) was dissolved in dry DCM and stirred in an ice bath. Dess-Martin periodinane (0.61 g, 1.43 mmol) was dissolved in dry DCM and added to the stirred reaction mixture which was stirred for an additional 2 hours at room temperature. To the clear reaction mixture was added one equivalent of H_2O (25 µL, 1.43 mmol) after which the solution turned cloudy and the reaction was stirred over night. The reaction mixture had turned green over night and excess H_2O was added. The organic phase was dried over $MgSO_4$ and purified using flash chromatography with MeOH/DCM (10/90) and a r.f-value of 0.55.

The product was obtained as yellow liquid (0.15 g, 0.46 mmol) in 42 % yield.

Alternative purification: HPLC (Waters Xbridge C18 column 5-58% MeCN 0.1% TFA, gradient 13 min, 254 nm) collected peak at 6.5 min. The fractions were pooled and MeCN was evaporated followed by treatment with dilute NaOH solution to neutralise the TFA. The product was extracted with $CHCl_3$ and EtOAc followed by drying over $MgSO_4$ to afford the product as a yellow liquid

^{1}H NMR (400 MHz, $CDCl_3$) δ 7.56 (t, *J* = 7.7 Hz, 2H, Py-H), 7.31 (d, *J* = 7.7 Hz, 2H, Py-H), 7.02 (d, *J* = 7.6 Hz, 2H, Py-H), 3.75 (s, 4H, Py-C*H*$_2$), 2.92 (s, 2H, C*H*$_2$N), 2.53 (s, 6H, Py-*C*H$_3$), 2.01 (s, 3H, C*H*$_3$CO), 1.08 (s, 6H, (C*H*$_3$)$_2$)

^{13}C NMR (101 MHz, $CDCl_3$) δ 213.75 (*C*=O), 159.01 (*Py*-CH$_3$), 157.46 (*Py*-CH$_2$), 136.60 (Py-H), 121.44 (Py-H), 120.11 (Py-H), 63.16 (*C*H$_2$N), 61.98 (Py-*C*H$_2$), 49.68 (*C*(CH$_3$)$_2$), 25.66 (*C*H$_3$CO), 24.43 (Py-*C*H$_3$), 23.43 ((*C*H$_3$)$_2$)

HRMS (ESI-TOF) m/z: Calculated for $C_{20}H_{28}N_3O$: 326.2227

Found: 326.2237 [M+H]$^+$; 388.1368 [M$^-$+Zn^{2+}]$^+$

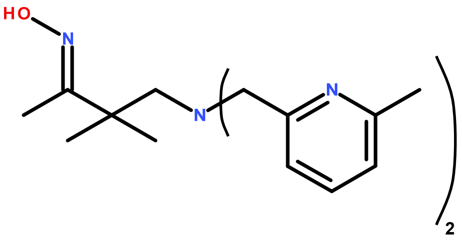

4-[bis[(6-methyl-2-pyridyl)methyl]amino]-3,3-dimethyl-butan-2-one oxime

4-[bis[(6-methyl-2-pyridyl)methyl]amino]-3,3-dimethyl-butan-2-one (0.076 g, 0.23 mmol) was dissolved in 50/50 H_2O/EtOH (5 ml). Hydroxylamine hydrochloride (0.018 g, 0.26 mmol) was added and after it had dissolved 1M NaOH (257 µL, 0.257 mmol) was added and the reaction was stirred for 2 hours. The EtOH was evaporated under reduced pressure and the crude mixture was extracted with $CHCl_3$ followed by EtOAc. The organic phase was dried over $MgSO_4$ and the solvent was removed under reduced pressure to yield the product as a viscous light yellow liquid (0.061 g, 0.18 mmol) in 77% yield. Alternatively, purification can be performed using flash chromatography with MeOH/DCM (10/90) and a r.f-value of 0.48.

^{1}H NMR (400 MHz, MeOD) δ 7.69 (t, *J* = 7.7 Hz, 2H, Py-H), 7.46 (d, *J* = 7.7 Hz, 2H, Py-H), 7.15 (d, *J* = 7.6 Hz, 2H Py-H), 3.76 (s, 4H, Py-C*H*$_2$), 2.78 (s, 2H, C(CH_3)$_2$C*H*$_2$N), 2.50 (s, 6H, Py-CH_3), 1.73 (s, 3H, C*H*$_3$C=NOH), 1.05 (s, 6H, (CH_3)$_2$).

^{13}C NMR (101 MHz, MeOD) δ 161.23 (*C*=NOH), 158.61 (*Py*-CH_3), 157.06 (*Py*-CH_2), 137.35 (Py-H), 121.79 (Py-H), 120.67 (Py-H), 62.98 (*C*H$_2$N), 60.96 (Py-C*H*$_2$), 41.46 (*C*(CH_3)$_2$), 23.78 (Py-*C*H$_3$), 22.32 ((*C*H$_3$)$_2$), 9.29 (*C*H$_3$C=NOH)

HRMS (ESI-TOF) m/z: Calculated for $C_{20}H_{27}N_4OZn$: 403.1476

Found: 403.1459 $[M^- + Zn^{2+}]^+$

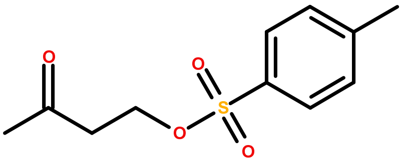

3-oxobutyl 4-methylbenzenesulfonate

4-hydroxybutan-2-one (15.00 g, 170.24 mmol) was weighed into a flask together with 4-toluenesulfonyl chloride (48.68 g, 255.36 mmol) and dissolved in dry DCM (250 ml) in an ice bath. Dry pyridine (41.14 ml, 255.36 mmol) was added to the solution and the reaction was stirred and allowed to adapt room temperature over night. The reaction was washed with H_2O (500 ml) and dried over Mg SO_4 and the solvent was removed under reduced pressure. The crude product was purified using flash chromatography with an r.f-value of 0.53 (in 100 % Et_2O) to afford the product as a viscous clear liquid (8.95 g, 36.94 mmol) in 21 % yield.

Note: The title compound is temperature sensitive (avoid temperatures exceeding 30 °C) and prolonged sonication may lead to the formation of a black liquid that when analysed indicated the presence of the elimination product but-3-en-2-one. The compound should preferably be purified as soon as possible after the work up. Once pure it should immediately be used in the subsequent reaction or stored under $N_{2(g)}$ at -18 °C.

^{1}H NMR (400 MHz, $CDCl_3$) δ 7.80 (d, *J* = 8.3 Hz, 2H, Ph-H), 7.37 (d, *J* = 8.5 Hz, 2H, Ph-H), 4.27 (t, *J* = 6.4 Hz, 2H, $COCH_2C\mathit{H}_2$), 2.84 (t, *J* = 6.3 Hz, 2H, $COC\mathit{H}_2CH_2$), 2.47 (s, 3H, Ph-$C\mathit{H}_3$), 2.16 (s, 2H, $C\mathit{H}_3CO$)

^{13}C NMR (101 MHz, $CDCl_3$) δ 204.34 (*C*=O), 145.00 (*Ph*-SO_3), 132.61 (*Ph*-CH_3), 129.90 (Ph-H), 128.02 (Ph-H), 64.98 ($COCH_2\mathit{C}H_2$), 42.18 ($CO\mathit{C}H_2CH_2$), 30.30 ($\mathit{C}H_3CO$), 21.67 (Ph-$\mathit{C}H_3$)

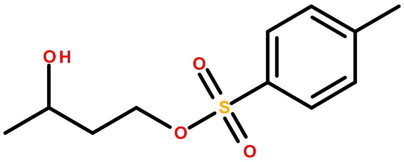

3-hydroxybutyl 4-methylbenzenesulfonate

3-oxobutyl 4-methylbenzenesulfonate (1.00 g, 4.13 mmol) was dissolved in EtOH (20 ml) and stirred in an ice bath. $NaBH_4$ (0.31 g, 8.25 mmol) was added to the stirred solution and the reaction was stirred for 1 hour at room temperature. H_2O was added and the reaction was extracted with DCM and then EtOAc. The organic phases were pooled and dried over $MgSO_4$ and the solvent was removed under reduced pressure to yield the title compound as a clear liquid (0.82 g, 3.36 mmol) in 81 % yield. The crude product did not require further purification and according to TLC the r.f-value of the compound was 0.45 (in 100 % Et_2O).

^{1}H NMR (400 MHz, $CDCl_3$) δ 7.81 (d, *J* = 8.2 Hz, 2H, Ph-H), 7.37 (d, *J* = 8.0 Hz, 2H, Ph-H), 4.20 (m, 2H, $CHOHCH_2C\mathit{H}_2$), 3.97 (s, 1H, Ph-$C\mathit{H}_3$), 2.47 (s, 3H,), 1.79 (m, 2H, $CHOHC\mathit{H}_2CH_2$), 1.21 (d, *J* = 6.2 Hz, 3H, $C\mathit{H}_3CHOH$)

^{13}C NMR (101 MHz, $CDCl_3$) δ 144.86 (*Ph*-SO_3), 132.99 (*Ph*-CH_3), 129.90 (Ph-H), 127.91 (Ph-H), 67.83 (*C*HOH), 64.13 (CHOHCH$_2$*C*H$_2$), 37.88 (CHOH*C*H$_2$CH$_2$), 23.63 (*C*H$_3$CHOH), 21.66 (Ph-*C*H$_3$)

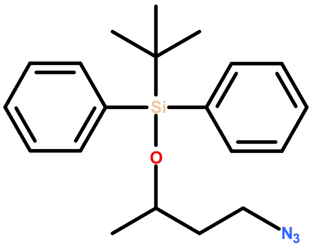

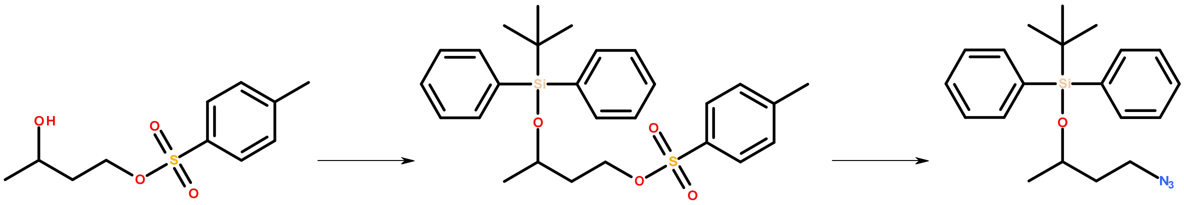

(3-azido-1-methyl-propoxy)-*tert*-butyl-diphenyl-silane

*t*BDPS-Cl (12.76 g, 46.43 mmol) was dissolved in dry THF (200 ml) and stirred in an ice bath. 3-hydroxybutyl 4-methylbenzenesulfonate (3.00 g, 12.28 mmol) was added to the reaction mixture followed by imidazole (8.62 g, 126.62 mmol) and the reaction was stirred over night. The precipitate that had formed overnight was filtered off and the solvent was evaporated. The crude mixture was dissolved in Et_2O and washed with H_2O. The organic phase was dried over $MgSO_4$ and the solvent was evaporated to afford 16 g of a clear liquid crude mixture consisting of product and excess starting material. The crude product mixture was used without further purification in the subsequent step.

Half the crude batch, 8 g, was used and it should consist of a given amount of 3-[*tert*-butyl(diphenyl)silyl]oxybutyl 4-methylbenzenesulfonate (2.96 g, 6.14 mmol). This crude liquid was dissolved in dry DMF (50 ml) and NaN_3 (2.73 g, 41.99 mmol) was added. The reaction was stirred at 70 °C over night. The solvent was evaporated, H_2O/DCM (50/50) was added and the aqueous layer was extracted twice with DCM and once with EtOAc. The organic phases were dried over $MgSO_4$ and the solvent was removed under reduced pressure. The obtained crude was a light yellow liquid amounting to 10 g and was purified using Et_2O/Hexane (25/75) with the title compound having an r.f-value of 0.72. The title compound was isolated using flash chromatography as a light yellow liquid (1.89 g, 5.35 mmol) corresponding to a yield of 87 % over 2 steps.

^{1}H NMR (400 MHz, $\mathrm{CDCl_3}$) δ 7.72 (m, 1H), 7.44 (m, 1H), 4.01 (m, 1H), 3.38 (t, *J* = 7.2 Hz, 1H), 1.75 (m, 1H), 1.11 (d, *J* = 6.2 Hz, 1H), 1.10 (s, 2H)

^{13}C NMR (101 MHz, $\mathrm{CDCl_3}$) δ 135.88 (Ph-H), 135.83 (Ph-H), 134.45 (Ph-Si), 133.93 (Ph-Si), 129.74 (Ph-H), 129.61(Ph-H), 127.68 (Ph-H), 127.52 (Ph-H), 67.07 ($\mathit{C}\mathrm{HOSi(Ph)_2(C(CH_3)_3)}$), 47.99 ($\mathrm{CH_2}\mathit{C}\mathrm{H_2N_3}$), 38.16 ($\mathit{C}\mathrm{H_2CH_2N_3}$), 27.04 ($\mathrm{C(}\mathit{C}\mathrm{H_3)_3}$), 23.45 ($\mathit{C}\mathrm{H_3CHOSi}$), 19.31 ($\mathit{C}\mathrm{(CH_3)_3}$)

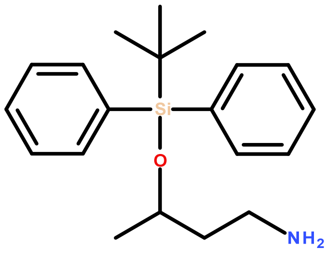

3-[*tert*-butyl(diphenyl)silyl]oxybutan-1-amine

(3-azido-1-methyl-propoxy)-*tert*-butyl-diphenyl-silane (1.81 g, 5.12 mmol) was reduced to the corresponding amine compound using the ThalesNano H-Cube continuous-flow hydrogenation reactor. The compound was dissolved in the EtOAc (50 ml) and a few drops of AcOH were added to the reaction mixture. This was used in order to protonate the amine upon formation in order to minimise adhesion to the palladium in the catalyst. The catalyst used in the hydrogenation was Pd/C (10% on carbon) packed in a cartridge. The reaction solution was pumped through the cartridge at 1 ml/min (recirculation) with a $\mathrm{H_{2(g)}}$ pressure of 40 bar and a temperature of 40 °C. After 2.5 hours the solvent was evaporated and to afford the title compound in quantitative yield as a viscous yellow liquid.

^{1}H NMR (400 MHz, $\mathrm{CDCl_3}$) δ 7.69 (m, 4H, Ph-H), 7.42 (m, 6H, Ph-H), 7.08 (s, 2H, $\mathrm{CH_2N}\mathit{H}_2$), 3.96 (m, 1H, $\mathit{C}\mathrm{H_3C}\mathit{H}\mathrm{OSi}$), 2.90 (m, 2H, $\mathrm{CH_2C}\mathit{H}_2\mathrm{NH_2}$), 1.80 (m, 2H, $\mathrm{C}\mathit{H}_2\mathrm{CH_2NH_2}$), 1.07 (d, *J* = 4.4 Hz, 2H, $\mathrm{C}\mathit{H}_3\mathrm{CO}$), 1.06 (s, 9H,$\mathrm{(C}\mathit{H}_3\mathrm{)_3}$)

^{13}C NMR (101 MHz, $\mathrm{CDCl_3}$) δ 135.86 (*Ph*-H), 135.81 (*Ph*-H), 134.36 (*Ph*-Si), 133.72 (*Ph*-Si), 129.77 (*Ph*-H), 129.62 (*Ph*-H), 127.72 (*Ph*-H), 127.52 (*Ph*-H), 67.67 ($\mathit{C}\mathrm{HOSi(Ph)_2(C(CH_3)_3)}$), 38.76 ($\mathit{C}\mathrm{H_2CH_2NH_2}$), 36.74 ($\mathrm{CH_2}\mathit{C}\mathrm{H_2NH_2}$), 27.01 ($\mathrm{((}\mathit{C}\mathrm{H_3)_3}$), 23.25 ($\mathit{C}\mathrm{H_3CHOSi}$), 19.23 ($\mathit{C}\mathrm{(CH_3)_3}$)

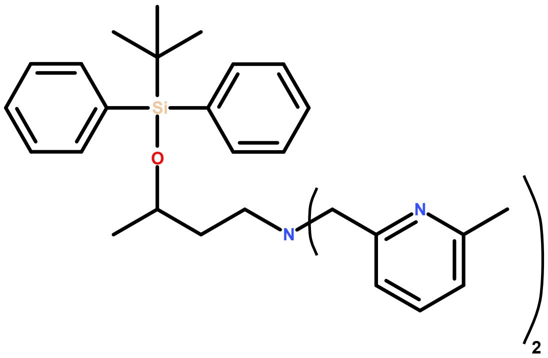

3-[*tert*-butyl(diphenyl)silyl]oxy-N,N-bis[(6-methyl-2-pyridyl)methyl]butan-1-amine

2-(iodomethyl)-6-methyl-pyridine(2.68 g, 11.50 mmol) was dissolved in dry DMF (50 ml) and 3-[*tert*-butyl(diphenyl)silyl]oxybutan-1-amine (1.50 g, 4.60 mmol) was added. The reaction mixture was stirred, DIPEA (3.20 ml, 18.40 mmol) was added and the reaction was stirred at 70 °C over night. The DMF was evaporated and the crude reaction mixture was dissolved in $CHCl_3$ and washed with 10 % $Na_2S_2O_3$ and extracted twice with $CHCl_3$ and once with EtOAc. The organic layer was dried over $MgSO_4$ and the solvent was removed under reduced pressure to afford a dark liquid that was purified using flash chromatography. The product was obtained as a viscous yellow liquid (0.77 g, 1.43 mmol) in 31 % yield.

^{1}H NMR (400 MHz, MeOD) δ 7.61 (m, 6H, Py-H & Ph-H), 7.36 (m, 8H, Py-H & Ph-H), 7.11 (d, *J* = 7.6 Hz, 2H, Py-H), 3.92 (m, 1H, $CH_3C\mathit{H}OSi$), 3.63 (dd, *J* = 44.9, 14.6 Hz, 4H, Py-$C\mathit{H}_2$), 2.55 (m, 2H, $CH_2C\mathit{H}_2N$), 2.49 (s, 6H, Py-CH_3), 1.70 (m, 2H, $C\mathit{H}_2CH_2N$), 0.98 (d, *J* = 6.1 Hz, 3H, $C\mathit{H}_3CHOSi$), 0.95 (s, 9H, $(C\mathit{H}_3)_3$)

^{13}C NMR (101 MHz, MeOD) δ 158.86 (*Py*-CH_3), 157.15 (*Py*-CH_2), 137.38 (*Py*-H), 135.56 (Ph-Si), 135.54 (Ph-Si), 134.23 (Ph-H), 133.92 (Ph-H), 129.39 (Ph-H), 129.34 (Ph-H), 127.27(Ph-H), 127.17 (Ph-H), 121.77 (*Py*-H), 120.09 (*Py*-H), 68.07 ($CH_3\mathit{C}HOSi$), 59.67 (Py-$\mathit{C}H_2$), 50.67 ($CH_2\mathit{C}H_2N$), 36.40 ($\mathit{C}H_2CH_2N$), 26.09 ($(\mathit{C}H_3)_3$), 22.36 (Py-$\mathit{C}H_3$), 22.24 ($\mathit{C}H_3CHOSi$), 18.56 ($\mathit{C}(\mathit{C}H_3)_3$)

LRMS (ES^+) *m/z* 538.8 (MH^+)   Calculated *m/z* 538.3248 (MH^+)

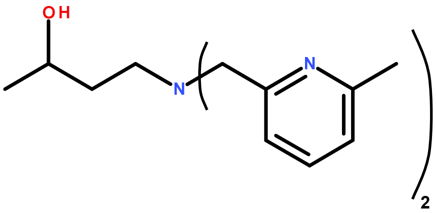

4-[bis[(6-methyl-2-pyridyl)methyl]amino]butan-2-ol

3-[*tert*-butyl(diphenyl)silyl]oxy-N,N-bis[(6-methyl-2-pyridyl)methyl]butan-1-amine (0.77 g, 1.43 mmol) was dissolved in dry THF (20 ml) and stirred in an ice bath. Solid TBAF hydrate (3.74 g, 14.32 mmol) was added in 10 equivalent excess and stirred under $N_{2(g)}$ over night. The solvent was evaporated to afford a clear viscous liquid that was purified by flash chromatography. The product was obtained as a light yellow viscous liquid (0.37 g, 1.25 mmol) in 87 % yield.

^{1}H NMR (400 MHz, MeOD) δ 7.67 (t, *J* = 7.7 Hz, 2H), 7.40 (d, *J* = 7.7 Hz, 2H), 7.14 (d, *J* = 7.6 Hz, 2H), 3.79 (m, 1H), 3.77 (dd, *J* = 43.8, 14.5 Hz, 4H), 2.69 (m, 2H, CH_2CH_2N), 2.52 (s, 3H, Py-CH_3), 1.68 (m, 2H, CH_2CH_2N), 1.10 (d, *J* = 6.3 Hz, 3H, CH_3CHOH)

^{13}C NMR (101 MHz, MeOD) δ 158.56 (*Py*-CH_3), 157.36 (*Py*-CH_2), 137.35 (Py-H), 121.78 (Py-H), 120.23 (Py-H), 66.37 (CH_3CHOH), 59.61 (Py-CH_2), 51.68 (CH_2CH_2N), 35.52 (CH_2CH_2N), 22.39 (Py-CH_3), 22.09 (CH_3CHOH)

HRMS (ESI-TOF) m/z: Calculated for $C_{18}H_{24}N_3OZn$: 326.1211

Found: 362.1207 $[M^{-}+Zn^{2+}]^{+}$

All the following oximes were synthesised according to this general procedure:

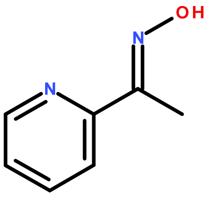

1-(2-pyridyl)ethanone oxime

1-(2-pyridyl)ethanone (0.93 ml, 8.25 mmol) was dissolved in 50 ml of H_2O/EtOH (50/50). Hydroxylamine hydrochloride (0.63 g, 9.08 mmol) was added and the solution was stirred in an ice bath. 1 M NaOH (9.08 ml, 9.08 mmol) was added and the reaction was stirred over night. The EtOH was removed under reduced pressure and the remaining aqueous solution was extracted with THF followed by EtOAc and lastly $CHCl_3$.The organic phases were pooled and the solvent was evaporated to remove the THF that might dissolve the drying agent ($MgSO_4$). The extracted product was dissolved in EtOAc and dried over $MgSO_4$. The solvent was evaporated and the product was isolated in 52% yield.

^{1}H NMR (400 MHz, $CDCl_3$) δ 9.12 (s, 1H, NO*H*), 8.66 (dd, *J* = 4.8, 0.9 Hz, 1H, Py-H), 7.86 (dd, *J* = 8.0 Hz, *J* = 0.8 Hz, 1H, Py-H), 7.72 (td, *J* = 7.8, 1.8 Hz, 1H, Py-H), 7.31 (m, 1H, Py-H), 2.43 (s, 3H, C*H*3)

^{13}C NMR (101 MHz, $CDCl_3$) δ 157.02 (*Py*-CNOH), 154.32 (Py-*C*NOH), 148.95 (Py-H), 136.40 (Py-H), 123.73 (Py-H), 120.56(Py-H), 10.70 (*C*H_3CNOH)

HRMS (ESI-TOF) m/z: Calculated for $C_6H_5N_2O$: 137.0709

Found: 137.0705 $[M+H]^+$

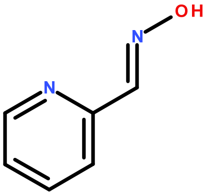

(2E)-pyridine-2-carbaldehyde oxime

Starting material pyridine-2-carbaldehyde

50 % yield

^{1}H NMR (400 MHz, MeOD) δ 8.53 (dd, *J* = 4.9, 1.0 Hz, 1H, Py-H), 8.12 (s, 1H, C*H*NOH), 7.87 (m, 2H, Py-H), 7.40 (td, *J* = 5.0, 1.7 Hz, 1H, Py-H).

^{13}C NMR (101 MHz, MeOD) δ 148.64 (*Py*-CNOH), 148.05 (Py-*C*NOH), 137.49 (Py-H), 137.16 (Py-H), 123.91 (Py-H), 120.50 (Py-H)

HRMS (ESI-TOF) m/z: Calculated for $C_6H_5N_2OZn$: 184.9693

Found: 123.0553 $[M+H]^+$; 184.9686 $[M^-+Zn^{2+}]^+$

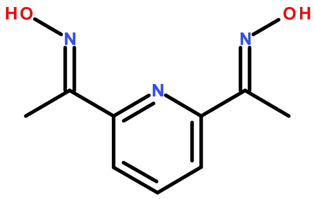

1-[6-[(E)-N-hydroxy-C-methyl-carbonimidoyl]-2-pyridyl]ethanone oxime

Starting material 1-(6-acetyl-2-pyridyl)ethanone

Quantitative yield

^{1}H NMR (400 MHz, MeOD) δ 7.85 (d, *J* = 7.9 Hz, 2H, Py-H), 7.70 (dd, *J* = 8.3, 7.3 Hz, 1H, Py-H), 2.34 (s, 6H, CH_3)

^{13}C NMR (101 MHz, MeOD) δ 155.37 (*Py*-CNOH), 153.86 (Py-*C*NOH), 136.00 (Py-H), 119.26 (Py-H), 8.93 (CH_3)

HRMS (ESI-TOF) m/z: Calculated for $C_9H_{12}N_3O_2$: 194.0930

Found: 194.0936 $[M+H]^+$

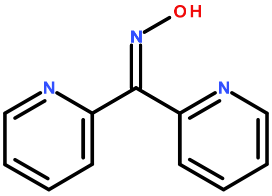

bis(2-pyridyl)methanone oxime

Was not successfully synthesised but instead purchased from Sigma Aldrich.

7.6 - Miscellaneous synthesis

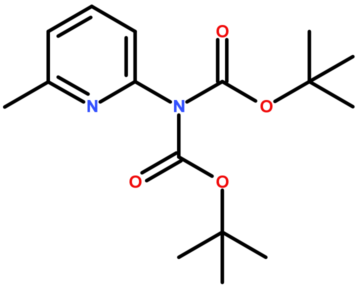

***tert*-butyl N-*tert*-butoxycarbonyl-N-(6-methyl-2-pyridyl)carbamate**

Byproduct from the synthesis of *tert*-butyl N-(6-methyl-2-pyridyl)carbamate.

^{1}H NMR (400 MHz, $CDCl_3$) δ 7.63 (t, *J* = 7.7 Hz, 1H, Py-H), 7.08 (d, *J* = 7.6 Hz, 1H, Py-H), 7.05 (d, *J* = 7.9 Hz, 1H, Py-H), 2.54 (s, 3H, CH_3), 1.46 (s, 18H, $(CH_3)_3$)

^{13}C NMR (101 MHz, $CDCl_3$) δ 157.82 (*Py*-CH_3), 151.58 (C=O), 151.40(*Py*-$N(Boc)_2$), 138.04 (*Py*-H), 121.68 (*Py*-H), 118.53 (*Py*-H), 82.87($\mathit{C}(CH_3)_3$), 27.90 (($\mathit{C}H_3)_3$), 24.06 (Py-$\mathit{C}H_3$)

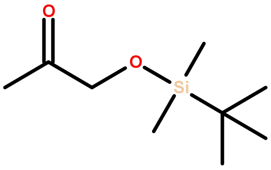

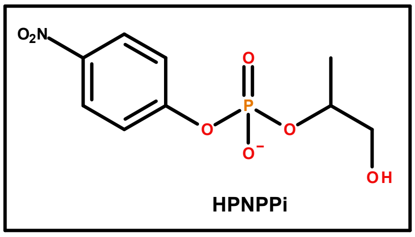

1-[*tert*-butyl(dimethyl)silyl]oxypropan-2-one (precursor for HPNPPi synthesis)

Imidazole (27.57 g, 404.97 mmol) and *tert*-Butyldimethylsilyl chloride (30.52 g, 202.48mmol mmol) were dissolved in dry DMF (200 ml) and stirred in an ice bath. 1-hydroxypropan-2-one (9.26 ml, 134.99 mmol) was added slowly and the reaction mixture was stirred over night at room temperature. H_2O was added to the reaction mixture followed by extraction with Et_2O. The volatile solvent was removed under reduced pressure and the residual DMF was removed with an additional extraction with Et_2O from H_2O. The solvent was removed under reduced pressure to afford the title compound as a clear liquid in quantitative yield.

^{1}H NMR (400 MHz, $CDCl_3$) δ 4.16 (s, 2H, $CH_3COC\mathit{H}_2$), 2.18 (s, 3H, $C\mathit{H}_3COCH_2$), 0.93 (s, 9H, $SiC(CH_3)_3$), 0.10 (s, 6H, $Si(CH_3)_2$)

^{13}C NMR (101 MHz, $CDCl_3$) δ 209.21 ($CH_3\mathit{C}OCH_2$), 69.56 ($CH_3CO\mathit{C}H_2$), 25.75 ($\mathit{C}H_3COCH_2$), 25.69 ($SiC(\mathit{C}H_3)_3$), 18.28 ($Si\mathit{C}(CH_3)_3$), -5.52 ($Si(\mathit{C}H_3)_2$)

Chapter 8 - Appendix

8.1 - Properties of 4-nitrophenol

At any given pH (this effect is negligible at very high pH-values) some of the PNP will not be visible at 400 nm (ArOH has a maximum absorbance around 320 nm) and thus only the deprotonated species is monitored (ArO$^-$ has a maximum absorbance around 400 nm). This can be solved by multiplying the absorbance at 400 nm with the corresponding factor for the invisible species at any given pH.

$$pH = pK_a + \log\left(\frac{[\mathrm{ArO^-}]}{[\mathrm{ArOH}]}\right)$$

$$10^{(pH - pK_a)} = \frac{[\mathrm{ArO^-}]}{[\mathrm{ArOH}]}$$

$$[\mathrm{ArOH}] = \frac{[\mathrm{ArO^-}]}{10^{(pH - pK_a)}}$$

$$\text{Fraction ArO}^- = \frac{[\mathrm{ArO^-}]}{[\mathrm{ArO^-}] + \frac{[\mathrm{ArO^-}]}{10^{(pH - pK_a)}}} = \mathrm{F(ArO^-)}$$

$$\mathrm{F(ArO^-)} = \frac{10^{(pH - pK_a)}}{1 + 10^{(pH - pK_a)}} = \frac{10^{pH}}{10^{pH} + 10^{pK_a}}$$

The total amount of released 4-nitrophenol, $[\mathrm{PNP}]_T$, at a given pH can be determined by measuring the absorbance at 400 nm and correcting for the protonation state (pK_a):

$$[\mathrm{PNP}]_T \propto \mathrm{Abs}_{\mathrm{ArO^-}} \times \frac{1}{\mathrm{F(ArO^-)}}$$

The pK_a for the 4-nitrophenol (PNP) was determined by measuring the absorbance at 400 nm under the same conditions used for the kinetic experiments. The PNP was dissolved in an aqueous solution containing 50 mM HEPES or CHES buffer with an ionic strength of 0.1 M ($NaNO_3$) at 25 °C.

The absorbance for 50 µM PNP was measured at 400 nm at various pH and the following equation was fitted to the data in Figure 8.1:

$$\mathrm{Abs}_{\mathrm{ArO^-}} \times \frac{10^{-pK_a}}{10^{-pK_a} + 10^{-\mathrm{pH}}}$$

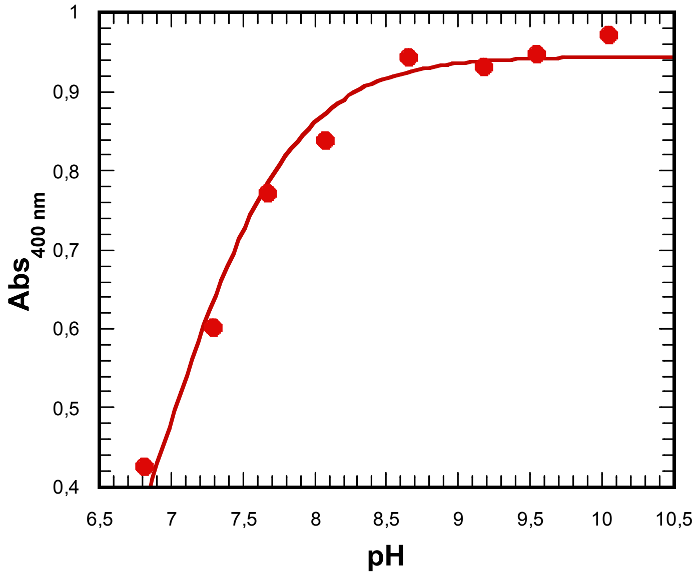

Figure 8.1. The absorbances at 400 nm versus pH plot for 50 µM PNP.

The data for the plot in Figure 8.1 is summarised in Table 8.1.

pH	Abs 400 nm
6.81	0.427
7.29	0.601
7.67	0.772
8.07	0.838
8.66	0.943
9.18	0.933
9.54	0.947
10.04	0.972

Table 8.1. The absorbances for 50 µM PNP at various pH.

The pK_a of PNP was determined to be 6.98 (± 0.05) which is in good agreement with literature (7.14).[211]

The absorbance for 50 µM PNP at 400 nm can be estimated for any pH from 6.8 upwards using the equation obtained from plot (solid line) in Figure 8.1:

$$\text{Abs}_{400nm} = 0.94439 \times \frac{(10^{-6.9801})}{(10^{-6.9801} + 10^{-pH})}$$

The absorbance at 400 nm versus the concentration of PNP (10, 20, 30, 40 and 50 µM) was measured at different pH and linear fitting yielded the extinction coefficient (ε) for each pH. A modified equation ($\text{Abs}_{(\text{ArO-})}$ replaced by ε) was fitted to a plot of the extinction coefficients versus pH to yield the limiting extinction coefficient at 400 nm (18503), see data in Table 8.2.

pH	[PNP] 10 µM	[PNP] 20 µM	[PNP] 30 µM	[PNP] 40 µM	[PNP] 50 µM	Extinction coefficient
6.81	0.1044	0.1701	0.2591	0.3424	0.427	8175
7.29	0.1341	0.2819	0.3723	0.5152	0.6006	11663
7.67	0.1764	0.3388	0.4697	0.6294	0.7723	14824
8.07	0.1625	0.3591	0.5142	0.6899	0.8383	16824
8.66	0.2105	0.3904	0.5715	0.7665	0.9434	18419
9.18	0.2136	0.3869	0.556	0.7773	0.9325	18282
9.54	0.2109	0.3887	0.5855	0.7595	0.9471	18432
10.04	0.2159	0.3848	0.5894	0.766	0.9724	18942

Table 8.2. The absorbance at 400nm of PNP at various pH and concentrations yielded the pH dependent extinction coefficients.

8.2 - Determining the purity and kinetic behavior of HPNPP

The synthesis of HPNPP[29] (see Chapter 7) yielded the desired compound but 10 % of the purified phosphate was methyl (4-nitrophenyl) phosphate (MPNPP), see Figure 8.2, according to the ratio obtained from NMR integration. The source of the MPNPP is most likely the work-up procedure and purification where the use of MeOH might lead to the esterification of residual unreacted phosphorodichloridate. The MPNPP doesn't contain an internal nucleophile and thus it hydrolyses at a slower rate (3200-fold slower in MeOH experiment)[212] and behaves more like a DNA analogue.

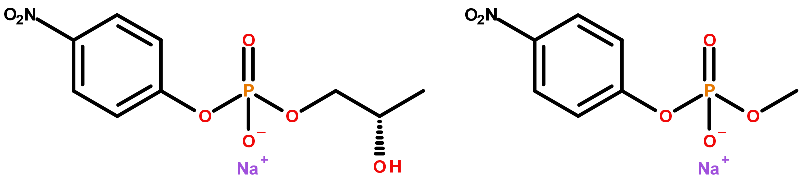

Figure 8.2. The HPNPP (left) and MPNPP (right) sodium salts.

In order to check whether or not the HPNPP product behaves as expected i.e. check the prediction that the MPNPP won't interfere, the transesterification was performed in NaOH (0.1 M) at 25 °C, see Figure 8.3.

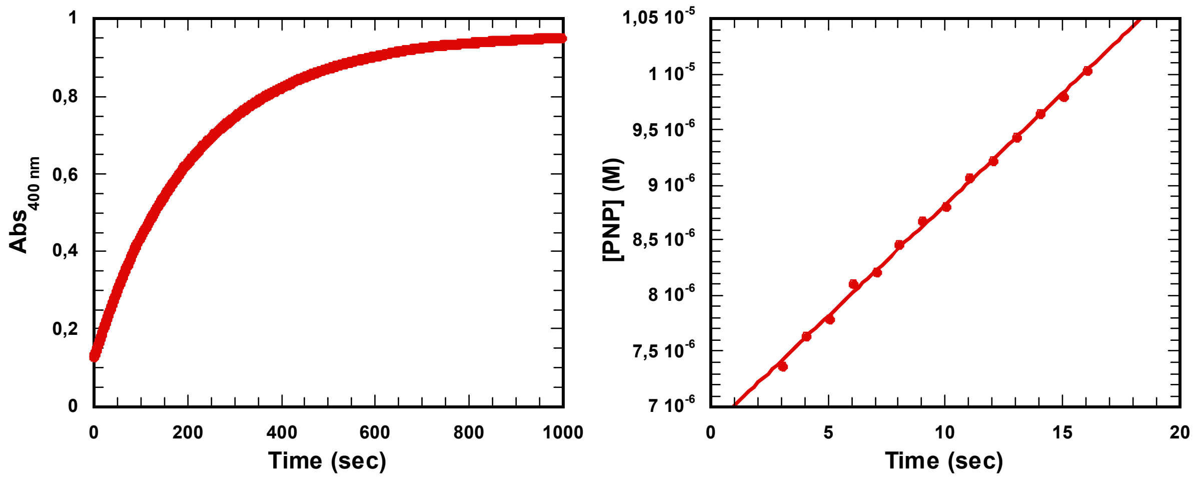

Figure 8.3. The absorbance (400 nm) versus time (left) was used to determine the pseudo-first-order rate and the concentration of released PNP versus time (right) was used to determine the initial rate for the transesterification of 50 µM HPNPP in 0.1 M NaOH.

The apparent second-order rate constants were (first-order fit 0.045 M^{-1} s^{-1} and initial rate fit 0.040 M^{-1} s^{-1}) determined and compared to the literature (0.065 M^{-1} s^{-1}).[65]

The initial rate for a reaction is followed within the time it takes for 10 % of the substrate to react. This initial phase is a linear relationship between time and amount of product formed. By following the complete reaction of a substrate one can obtain an accurate estimation of k_{obs} but the initial rate can be obtained when following the full reaction is not an option. The method of initial rates is utilised for very slow reactions and for reactions where the progression of the reaction makes accurate monitoring difficult (too high concentration of product). In order for accurate estimations of the reaction rates to be obtained the substrate needs to be of high purity since the presence of other compounds could interfere.

8.3 - Equations for kinetic experiments

Knowledge about the protonation state of a catalytic complex is of great importance for the determination of the optimal pH-range for a given reaction. The complexes that have been examined in previous chapters all display a pH-dependence with one or two deprotonations in the studied pH-range.

The relationship between the activity and protonation state can be expressed as a series of equations where ligand-Zn(II) complex is **C**, the total complex complex concentration is $[\mathbf{C}]_T$, the first and second acid dissociation constants are K_{a1} and K_{a2}, the second-order rate constant at a given pH is k_2^{pH} and the maxium second-order rate constant is k_2^{max}.

Sinlge-ionisation equation

$$[\boldsymbol{C}(\mathrm{OH_2})] \rightleftharpoons [\boldsymbol{C}(\mathrm{OH})] + [\mathrm{H^+}]$$

$$K_{a1} = \frac{[\boldsymbol{C}(OH)] \times [H^+]}{[\boldsymbol{C}(OH_2)]}$$

The total complex concentration is:

$$[\boldsymbol{C}]_T = [\boldsymbol{C}(OH_2)] + [\boldsymbol{C}(OH)]$$

Which can be expressed as:

$$[\boldsymbol{C}]_T = [\boldsymbol{C}(OH_2)] \times (1 + \frac{K_{a1}}{[H^+]})$$

Assuming that the monodeprotonated complex **C**(OH) is the active form, the percentage of the total amount of complex that is reactive can be expressed as:

$$\frac{[\boldsymbol{C}(OH)]}{[\boldsymbol{C}]_T} = \frac{[\boldsymbol{C}(OH_2)] \times \frac{K_{a1}}{[H^+]}}{[\boldsymbol{C}(OH_2)] \times (1 + \frac{K_{a1}}{[H^+]})} = \frac{K_{a1}}{[H^+] + K_{a1}}$$

Which yields the equation for the single-ionisation complex:

$$k_2^{max} = k_2^{pH} \times \frac{K_{a1}}{[H^+] + K_{a1}}$$

Dual-ionisation equation

$$[\boldsymbol{C}(OH_2)_2] \rightleftharpoons [\boldsymbol{C}(OHOH_2)] + [H^+]$$

$$K_{a1} = \frac{[\boldsymbol{C}(OHOH_2)] \times [H^+]}{[\boldsymbol{C}(OH_2)_2]}$$

$$[\boldsymbol{C}(OHOH_2)] \rightleftharpoons [\boldsymbol{C}(OH)_2] + [H^+]$$

$$K_{a2} = \frac{[\boldsymbol{C}(OHOH_2)] \times [H^+]}{[\boldsymbol{C}(OH)_2]}$$

The total complex concentration is:

$$[\boldsymbol{C}]_T = [\boldsymbol{C}(OH_2)_2] + [\boldsymbol{C}(OHOH_2)] + [\boldsymbol{C}(OH)_2]$$

Which can be expressed as:

$$[\boldsymbol{C}]_T = [\boldsymbol{C}(OH_2)] \times (1 + \frac{K_{a1}}{[H^+]} + \frac{K_{a2} \times K_{a1}}{[H^+]^2})$$

Assuming that the monodeprotonated complex **C**(OHOH2) is the active form, the percentage of the total amount of complex that is reactive can be expressed as:

$$\frac{[\boldsymbol{C}(OHOH_2)]}{[\boldsymbol{C}]_T} = \frac{[\boldsymbol{C}(OH_2)_2] \times \frac{K_{a1}}{[H^+]}}{[\boldsymbol{C}(OH_2)_2] \times (1 + \frac{K_{a1}}{[H^+]} + \frac{K_{a2} \times K_{a1}}{[H^+]^2})}$$

Which yields the equation for the two-fold ionisation complex:

$$k_2^{max} = k_2^{pH} \times \frac{K_{a1} \times [H^+]}{[H^+]^2 + [H^+]K_{a1} + K_{a1}K_{a2}}$$

8.4 - Conditions for kinetic experiments

The initial kinetic experiments surveying the reactivity of the complexes were performed on Varian UV spectrophotometers (Cary 1, Cary 3 or Cary 300 bio) using temperature controlled cell blocks. Quartz cuvettes (1 ml or 3 ml) were used for UV-scans and experiments carried out below 350 nm. For experiments at 400 nm, mainly plastic cuvettes (1 ml or 3 ml) were used. All experiments were carried out in 50 mM (HEPES or CHES) buffered aqueous solutions at 25 °C and the ionic strength was kept at 0.1 M ($NaNO_3$) unless stated otherwise. The pH of the experiments in 1 ml and 3 ml cuvettes were measured after completion of the reaction. The substrate HPNPP was synthesised according to the procedure in Chapter 7.2.1 and bis-(4-nitrophenyl) phosphate (BNPP) was purchased from Sigma-Aldrich and used without further purification.

The indicator displacement assays were performed using the Varian Cary 50 UV-Vis spectrophotometer with a fiber optic probe in a 5 ml solution containing 50 mM HEPES at pH 7.4 and 0.1 M ionic strength ($NaNO_3$). Each complex was used in 50 μM concentration and incubated with 50 μM pyrocatechol Violet (PV) prior to addition of phosphate. The substrate disodium hydrogenphosphate was added to the solution in 0.2 equivalent portions and stirred after each addition followed by a UV-scan (200-800 nm).

The main body of the DMP inhibition experiments was performed using a BMG Polarstar plate reader using Greiner flat bottom 96 well plates under the same conditions used for the previous kinetic experiments unless otherwise stated.

8.5 - Plate reader experiments

The plate reader experiments were performed on BMG Polarstar plate reader using Greiner Bio One 96-well black μClear flat bottom plates. The plate reader was set to 20 flashes per well at 25 °C and the standard volume used for each experiment was 200 μL. The pH of the experiments were not measured for each individual well but rather for a representative sample.

The absorbance of the solutions in the wells needs to be adjusted for the solution since the detector reading is vertical therefore the path length varies with the volume of the solution although this cancels out since the concentration increases accordingly. Based on the dimensions of the wells reported by the manufacturer, the theoretical volume of each well is 392 µL. The depth of each well is 10.9 mm and a 10 mm path length equals approximately 360 µL. The experiments were performed in 200 µL volume which equals a path length of approximately 5.6 mm. A series of experiments were performed using the Greiner plates with 200 µL of 50 µM 4-nitrophenol at pH 13, see Table 8.3.

Well	Abs $_{400nm}$	Well	Abs$_{400nm}$
1	0.5280	9	0.5266
2	0.5098	10	0.5308
3	0.5292	11	0.5327
4	0.5214	12	0.5252
5	0.5139	13	0.5332
6	0.5148	14	0.5232
7	0.5150	15	0.4887
8	0.5202	16	0.5273
	Average	0.5213	

Table 8.3. The absorbance at 400 nm for 50 µM 4-nitrophenol with 0.1 M NaOH in 200 µL. The measurements were performed in 16 different wells and the absorbances were averaged to yield a representative value.

The expected absorbance for 50 µM 4-nitrophenol at pH 13 for a 10 mm path length is 0.944, see Figure 8.1, which equates to a factor of 1.8-fold lower absorption for the plate reader experiments. The data obtained from the plate reader experiments were corrected for the discrepancy in path length.

It is worth keeping in mind that the wells of the plate are small which can affect the path length since the meniscus intrinsically displaces some of the liquid from the path of the beam. Additionally, the path length can be reduced by negligent deposition of the liquid leading to some drops clinging to the side of the well.

8.6 - The lability of the tBDMS protecting group

The synthesis of HPNPP highlighted some issues regarding the stability of the tertButyldimethylsilane protecting (tBDMS) group. The tBDMS protecting group was stable in the synthesis leading up to the attachment to the phosphate and showed no indication of being prone to spontaneous deprotection.

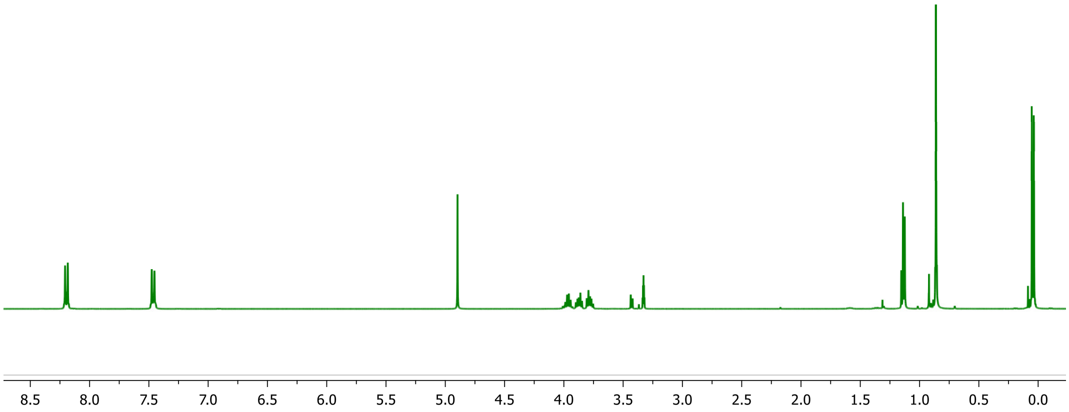

Figure 8.4. The ^{1}H-NMR spectrum (δ ppm) for the tBDMS protected HPNPP in MeOD-d_4.

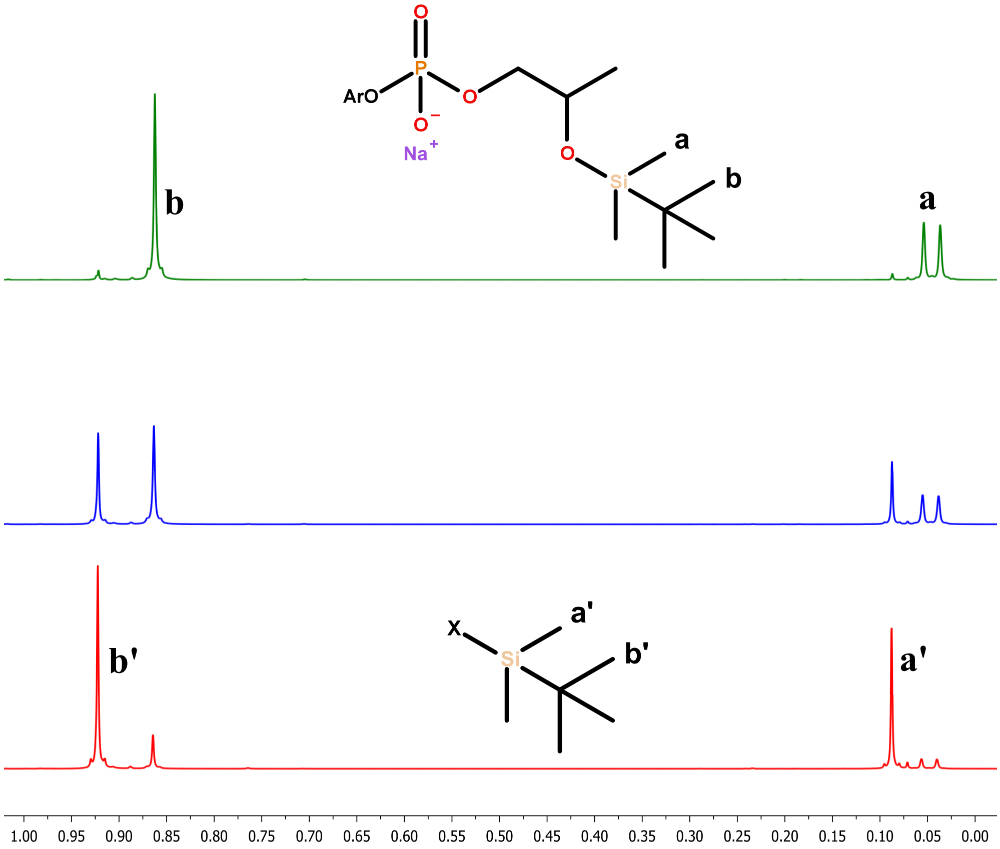

Figure 8.5. The partial ^{1}H-NMR spectra (δ ppm) showing the tBDMS group detaching over time (60 hours) in MeOD-d_4. Since the mechanism is not know, the functionality attached to the silicone of the free tBDMS is designated X.

The instability was discovered after NMR analysis where the protected diester seemed to lose the tBDMS group in MeOD-d4 over time with no external addition of reagent. The ^{1}H-NMR spectra for tBDMS protected HPNPP, see Figure 8.4, indicated spontaneous loss of the protecting group over time, see Figure 8.5.The relative ^{1}H-NMR integrals plotted over time yielded an apparent zeroth order reaction rate for the deprotection of tBDMS, see Figure 8.6.

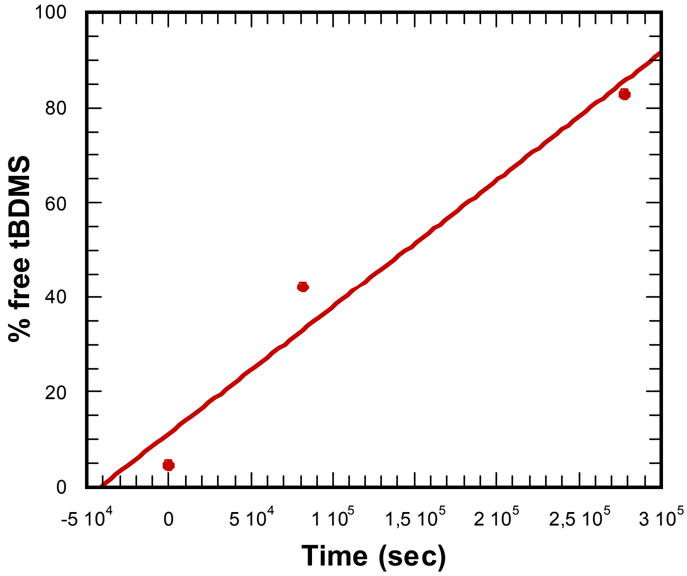

Time (sec)	% free tBDMS
0	5
81240	42
2.78×10^5	83

Figure 8.6. The percentage of free tBDMS versus time. The table represents the data points obtained from ^{1}H-NMR integration

Interestingly, the equivalent non-phosphorylated diol, see Figure 8.7, did not display similar tBDMS lability.

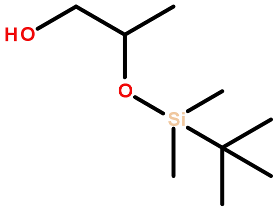

Figure 8.7. The stable tBDMS protected diol.

8.7 - Appendix for Chapter 2

8.7.1 - Compound structures

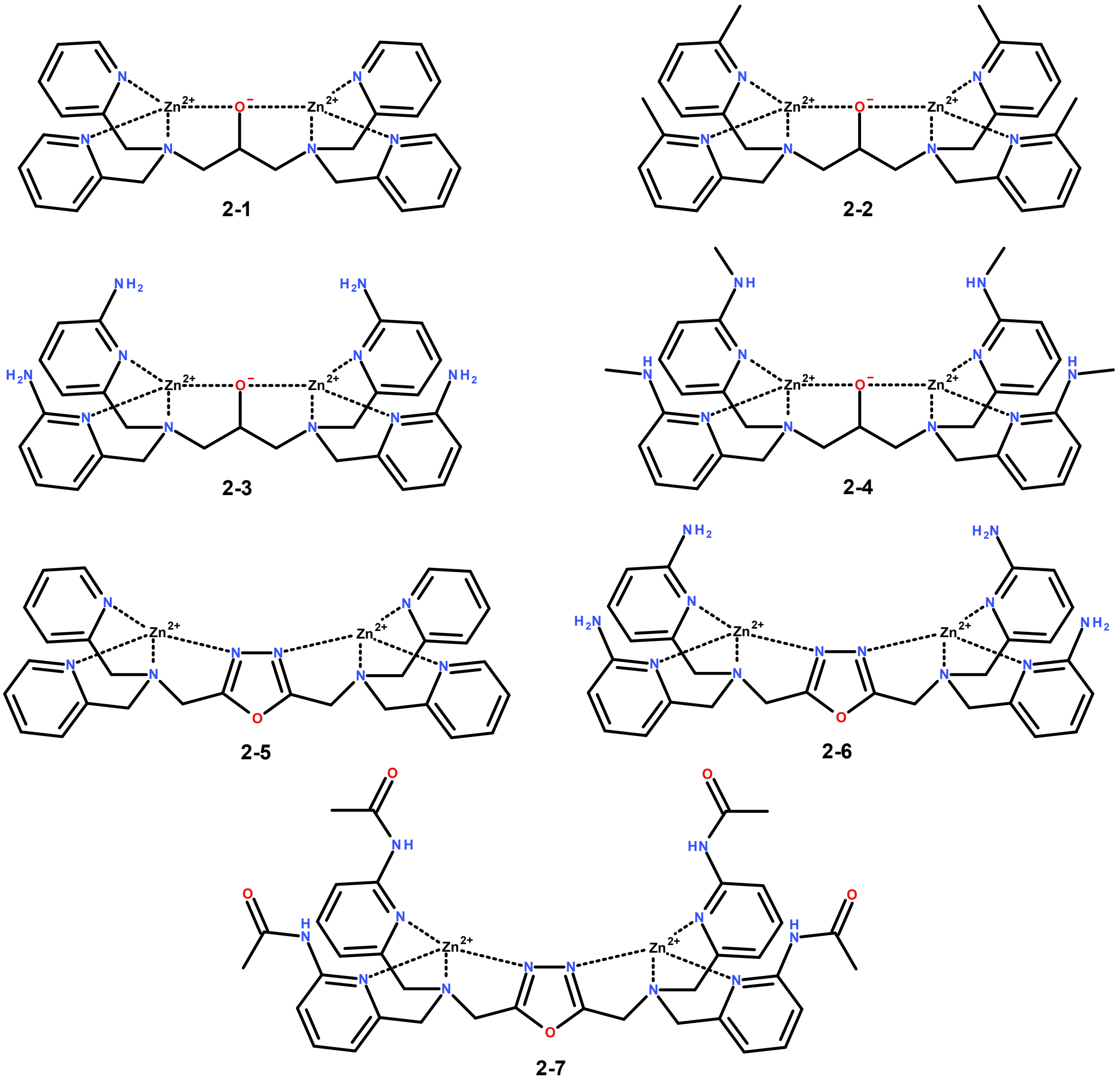

2-1

2-2

2-3

2-4

2-5

2-6

2-7

Figure 8.8. The structures of the dinuclear complexes studied in Chapter 2.

8.7.2 - Data for Chapter 2

	2-1		**2-2**	
pH	k_{obs} (× 10^{-4}) (s^{-1})	log k_{obs}	k_{obs} (× 10^{-5}) (s^{-1})	log k_{obs}
6.81	1.13 (± 0.001)	-3.95	2.10 (± 0.004)	-4.68
7.27	1.61 (± 0.001)	-3.79	2.84 (± 0.003)	-4.55
7.66	1.93 (± 0.001)	-3.71	3.73 (± 0.003)	-4.43
8.04	2.19 (± 0.002)	-3.66	5.14 (± 0.005)	-4.29
8.40	2.45 (± 0.002)	-3.61	4.13 (± 0.002)	-4.38
8.95	2.23 (± 0.002)	-3.65	3.99 (± 0.003)	-4.40
9.36	2.03 (± 0.001)	-3.69	3.93 (± 0.003)	-4.41
9.77	2.09 (± 0.001)	-3.68	4.00 (± 0.002)	-4.40

	2-3		**2-4**	
pH	k_{obs} (× 10^{-3}) (s^{-1})	log k_{obs}	k_{obs} (× 10^{-2}) (s^{-1})	log k_{obs}
6.81	4.01 (± 0.04)	-2.40	1.26 (± 0.005)	-1.90
7.27	4.23 (± 0.05)	-2.37	-	-
7.66	5.28 (± 0.02)	-2.28	-	-
8.04	4.19 (± 0.08)	-2.38	-	-
8.40	-	-	-	-
8.95	-	-	-	-
9.36	-	-	-	-
9.77	-	-	-	-

Table 8.4. The pseudo-first-order rate constants for 2 mM 2-1, 2 mM 2-2, 0.2 mM 2-3 and 0.2 mM 2-4 with 50 µM HPNPP and 50 mM HEPES or CHES with 0.1 M ionic strength ($NaNO_3$).

	2-1		**2-2**	
pH	k_2 (M^{-1} s^{-1}) (× 10^{-2})	log k_2	k_2 (M^{-1} s^{-1}) (× 10^{-2})	log k_2
6.83	2.7144 (± 0.06)	-1.57	0.53128 (± 0.06)	-2.27
7.28	4.1778 (± 0.04)	-1.38	0.87866 (± 0.09)	-2.06
7.67	5.1226 (± 0.03)	-1.29	1.31424 (± 0.14)	-1.88
8.11	5.9836 (± 0.08)	-1.22	1.70868 (± 0.20)	-1.77
8.7	5.6176 (± 0.10)	-1.25	1.32304 (± 0.41)	-1.88
9.14	6.0886 (± 0.36)	-1.22	0.9052 (± 0.51)	-2.04
9.5	4.5962 (± 0.39)	-1.34	1.87872 (± 0.36)	-1.73
9.95	5.3368 (± 1.04)	-1.27	1.85596 (± 0.90)	-1.73

Table 8.5. The second-order rate constants for 2-1 and 2-2 in 50 mM HEPES or CHES at 0.1 M ionic strength ($NaNO_3$) at various pH.

pH 6.9		pH 6.9		pH 7.4		pH 7.4	
$NaNO_3$		$NaNO_3$		$NaNO_3$		$NaNO_3$	
[DMP] mM	**2-1** k/k_0	[DMP] mM	**2-2** k/k_0	[DMP] mM	**2-1** k/k_0	[DMP] mM	**2-2** k/k_0
0	1	0	1	0	1	0	1
2	0.70683	5	0.83836	8	0.54429	5	0.91369
4	0.53721	10	0.71018	15	0.39939	10	0.80043
6	0.44439	20	0.65625	20	0.32796	15	0.79699
8	0.36755	30	0.50907			20	0.75309
12	0.30365	40	0.42751			30	0.70349
15	0.26647	50	0.37704			40	0.62864
20	0.20267	60	0.35831				
30	0.17106						
40	0.13283						
50	0.088535						

Table 8.6. The normalised rate k/k_0 for the inhibition studies with DMP for 1 mM 2-1 and 2-2 with 0.5 mM HPNPP at pH 6.9 and 7.4. The experimental conditions were 50 mM HEPES and 0.1 M ionic strength ($NaNO_3$)

pH 8.1	
$NaNO_3$	
[DMP] mM	**2-3** k/k_0
0	1
0.5	0.76237
1	0.6773
2.5	0.43514
5	0.29172
10	0.15438

Table 8.7. The normalised rate k/k_0 for the inhibition studies with DMP for 0.2 mM 2-3 with 50 µM HPNPP using DMP at pH 8.1. The experimental conditions were 50 mM HEPES and 0.1 M ionic strength ($NaNO_3$)

pH 6.9		pH 6.9		pH 6.9		pH 6.9	
NaCl		NaCl		NaCl		NaCl	
[DMP] mM	**2-1** k/k_0	[DMP] mM	**2-2** k/k_0	[DMP] mM	**2-3** k/k_0	[DMP] mM	**2-4** k/k_0
0	1	0	1	0	1	0	1
2	0.88741	5	0.87474	5	0.11903	5	0.11228
4	0.81601	10	0.7405	10	0.048574	10	0.054833
6	0.73002	20	0.60575	20	0.022369	20	0.024802
8	0.68555	30	0.52433	30	0.010513	30	0.011846
12	0.58365	40	0.45124	40	0.006831	40	0.006872
15	0.52859	50	0.40606	50	0.004032	50	0.003776
20	0.44647	60	0.36144	60	0.002086	60	0.002466
30	0.34095						
40	0.25516						
50	0.24442						

Table 8.8. The normalised rate k/k_0 for the inhibition studies with DMP for 1 mM 2-1 and 2-2 with 0.5 mM HPNPP as well as 0.2 mM 2-3 and 2-4 with 50 µM HPNPP using DMP at pH 6.9. The experimental conditions were 50 mM HEPES and 0.1 M ionic strength (NaCl).

Complex	$\Delta G^{\ddagger}$ kcal/mol	$\Delta\Delta G^{\ddagger}_{cat}$ kcal/mol	$\Delta\Delta G^{\circ}_{bind}$ kcal/mol	$\Delta G^{\ddagger}_{stab}$ (%)	ΔG°_{stab} (%)
2-1	20.01736	8.728752	2.440496	72	28
2-2	20.24175	8.504359	2.028539	76	24
2-3	15.84049	12.90563	4.393468	66	34
2-4	15.15542	13.59069	4.403421	68	32
HPNPP$_{uncat}$	28.74611	-	-	-	-

Table 8.9. The contribution of interactions in the ground state versus the transition state are estimated using the kinetic data obtained for the complexes at pH 6.9 for 1 mM 2-1 and 2-2 with 0.5 mM HPNPP and for 0.2 mM 2-3 and 2-4 with 50 µM HPNPP.

pH 6.9		
$NaNO_3$		
$[Na_2CO_3]$ mM	**2-1** k/k_0	**2-2** k/k_0
0	1	1
1	0.61279	0.91653
2	0.35043	0.80025
5	0.13719	0.66053
10	0.084117	0.56847

Table 8.10. The normalised rate k/k_0 for the inhibition studies with DMP for 1 mM 2-1 and 2-2 with 0.5 mM HPNPP at pH 6.9 in 50 mM HEPES and 0.1 M ionic strength ($NaNO_3$).

	2-5		**2-6**	
pH	k_{obs} (× 10^{-5}) (s^{-1})	log k_{obs}	k_{obs} (× 10^{-4}) (s^{-1})	log k_{obs}
6.87	0.20 (± 0.01)	-5.6914	1.60 (± 0.05)	-3.7947
7.33	0.97 (± 0.006)	-5.0121	1.61 (± 0.02)	-3.7919
7.74	1.68 (± 0.003)	-4.7734	-	-
8.14	2.20 (± 0.01)	-4.6566	-	-
8.65	-	-	-	-
9.15	-	-	-	-
9.54	-	-	-	-
9.91	-	-	-	-
	2-7		**L2-6-Co(II)**	
pH	k_{obs} (× 10^{-5}) (s^{-1})	log k_{obs}	k_{obs} (× 10^{-4}) (s^{-1})	log k_{obs}
6.87	0.62 (± 0.004)	-5.2067	0.76 (± 0.0004)	-4.1167
7.33	1.30 (± 0.001)	-4.8868	1.10 (± 0.001)	-3.9592
7.74	2.07 (± 0.001)	-4.6843	1.22 (± 0.002)	-3.9121
8.14	2.82 (± 0.002)	-4.5494	1.29 (± 0.002)	-3.8898
8.65	4.56 (± 0.05)	-4.3410	-	-
9.15	4.35 (± 0.05)	-4.3619	-	-
9.54	6.02 (± 0.06)	-4.2202	-	-
9.91	7.61 (± 0.08)	-4.1186	-	-

Table 8.11. The observed rate constants for 0.4 mM oxazole-bridged complex in 50 mM HEPES or CHES and 0.1 M ionic strength ($NaNO_3$) at various pH.

8.8 - Appendix for Chapter 3

8.8.1 - Compound structures

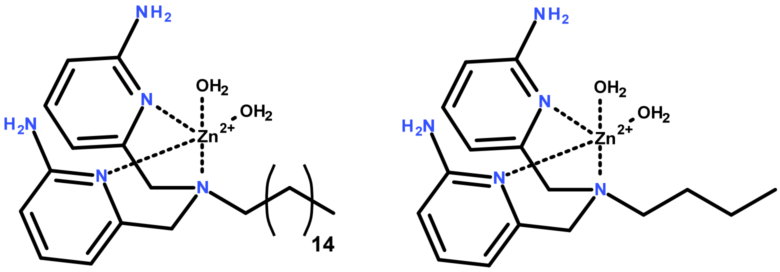

3-1 **3-2**

Figure 8.9. The structures of the mononuclear complexes studied in Chapter 3.

8.8.2 - Data for Chapter 3

	Complex **3-1**		Complex **3-2**	
pH	k_2 (M^{-1} s^{-1})	log k_2	k_2 (M^{-1} s^{-1})	log k_2
6.83	0.9648 (± 0.02)	-0.0156	0.0232 (± 0.0004)	-1.6342
7.28	1.7007 (± 0.08)	0.2306	0.0425 (± 0.0003)	-1.3718
7.67	2.4632 (± 0.17)	0.3915	0.0668 (± 0.0002)	-1.1752
8.11	3.6224 (± 0.16)	0.5590	0.1028 (± 0.0003)	-0.9881
8.7	-	-	0.1572 (± 0.0007)	-0.8035
9.14	-	-	0.1908 (± 0.003)	-0.7194
9.5	-	-	0.1550 (± 0.001)	-0.8096
9.95	-	-	0.1404 (± 0.002)	-0.8528

Table 8.12. The second-order rate constants for 3-1 and 3-2 at 1 mM with 100 µM HPNPP at various pH in 50 mM HEPES and 25 °C. The highest observed k_2 is highlighted (green) for each complex.

The apparent second-order rate constants, see Table 8.12, for **3-1** and **3-2** show the highest k_2 is at pH 8.11 (3.38 ± 0.16 M^{-1} s^{-1}) and pH 9.14 (0.19 ± 0.003 M^{-1} s^{-1}), respectively.

The listed second-order rate constants in Table 8.12 indicate that there is approximately an order of magnitude difference in reactivity in favor of **3-1**. The data seem to indicate a decrease in activity for **3-1** at pH 8.7 but this can be misleading given the unreliability of measurements at high pH due to precipitation.

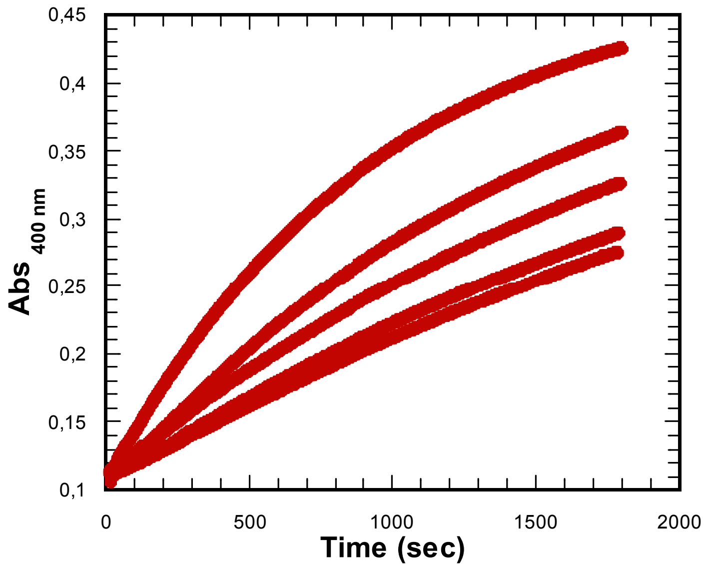

Figure 8.10. The absorbance at 400 nm versus time for Na_2CO_3 treated 1 mM 3-2 and 50 µM HPNPPi in 50 mM HEPES at pH 7.4 in 0.1 M ionic strength ($NaNO_3$).

$[Na_2CO_3]$ mM	k_{obs} (× 10^{-3}) (s^{-1})	k/k_0
0	1.065 (± 0.0005)	1
0.5	0.614 (± 0.0014)	0.575958
1	0.45 (± 0.0007)	0.422634
1.5	0.34 (± 0.0013)	0.318729
2	0.255 (± 0.0014)	0.239579

Table 8.13. The observed rates and normalised rate for Na_2CO_3 with 1 mM 3-2 and 50 µM HPNPPi in 50 mM HEPES at pH 7.4 in 0.1 M ionic strength ($NaNO_3$).

8.9 - Appendix for Chapter 4

8.9.1 - SPPS chemistry

The standard mechanism for activation of carboxyl groups in organic using *N,N'*-dicyclohexylcarbodiimide (DCC). The byproduct of the reaction with DCC is dicyclohexylurea that precipitates out of most organic solution and is therefore not appropriate for use in solid phase peptide synthesis.

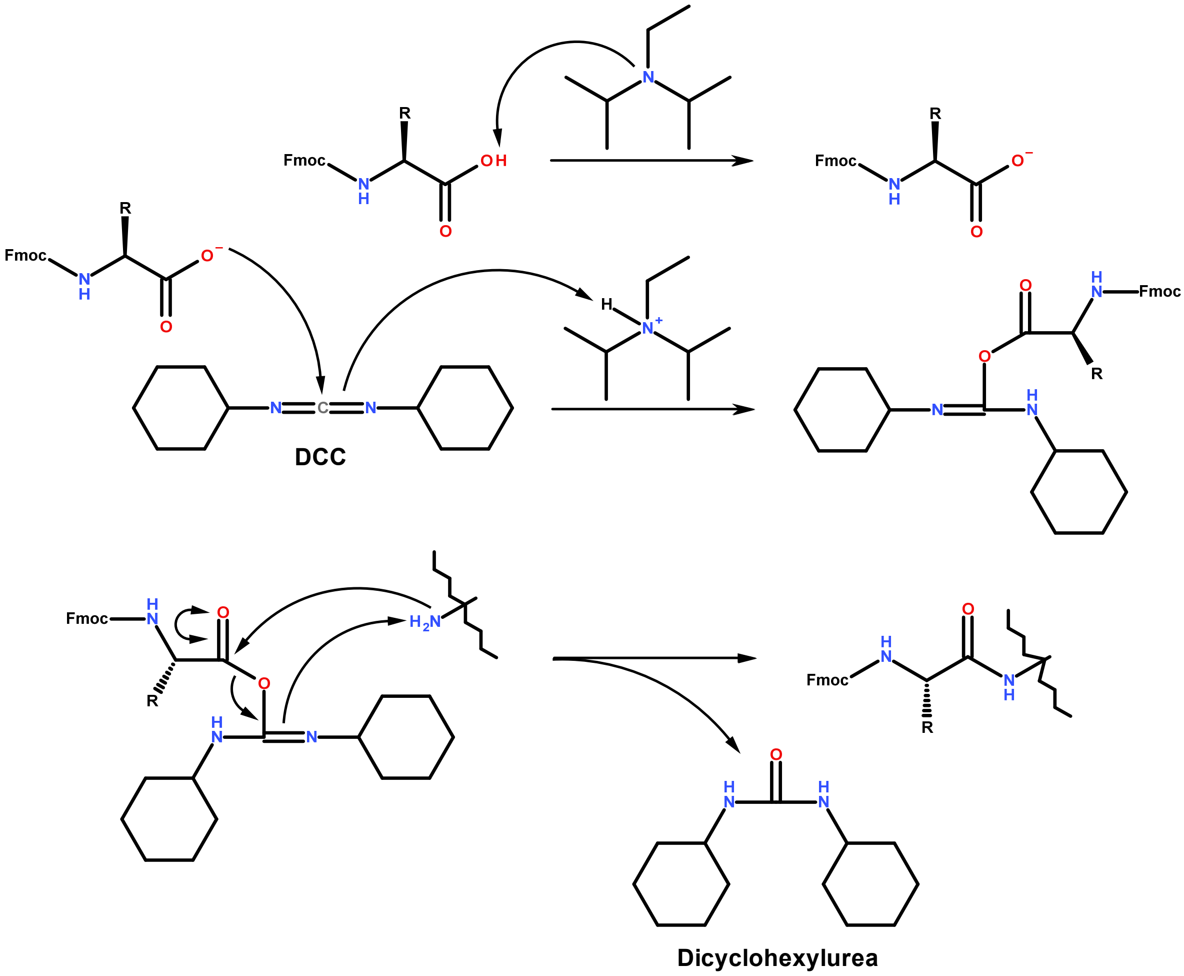

Figure 8.11. The activation and coupling of an amino acid using DCC.

For SPPS purposes *N,N'*-diisopropylcarbodiimide (DIC) is a better alternative since it follows the same mechanism but the by-product diisopropylurea is more soluble in organic solvent and thus doesn't interfere with the solid support. Unfortunately the usage of DCC and DIC lead to significant racemisation of the amino acid which could be attributed to the fact that both these compounds are prone to form oxazolone species.[169] For this reason DCC and

DIC were usually employed together with HOBt (1-hydroxybenzotriazol) which formed a less reactive activated ester and reduced the risk of racemisation.[213] For Fmoc peptide synthesis the standard activating agent is HBTU which incorporates a carbodiimide and benzotriazole in one molecular entity.

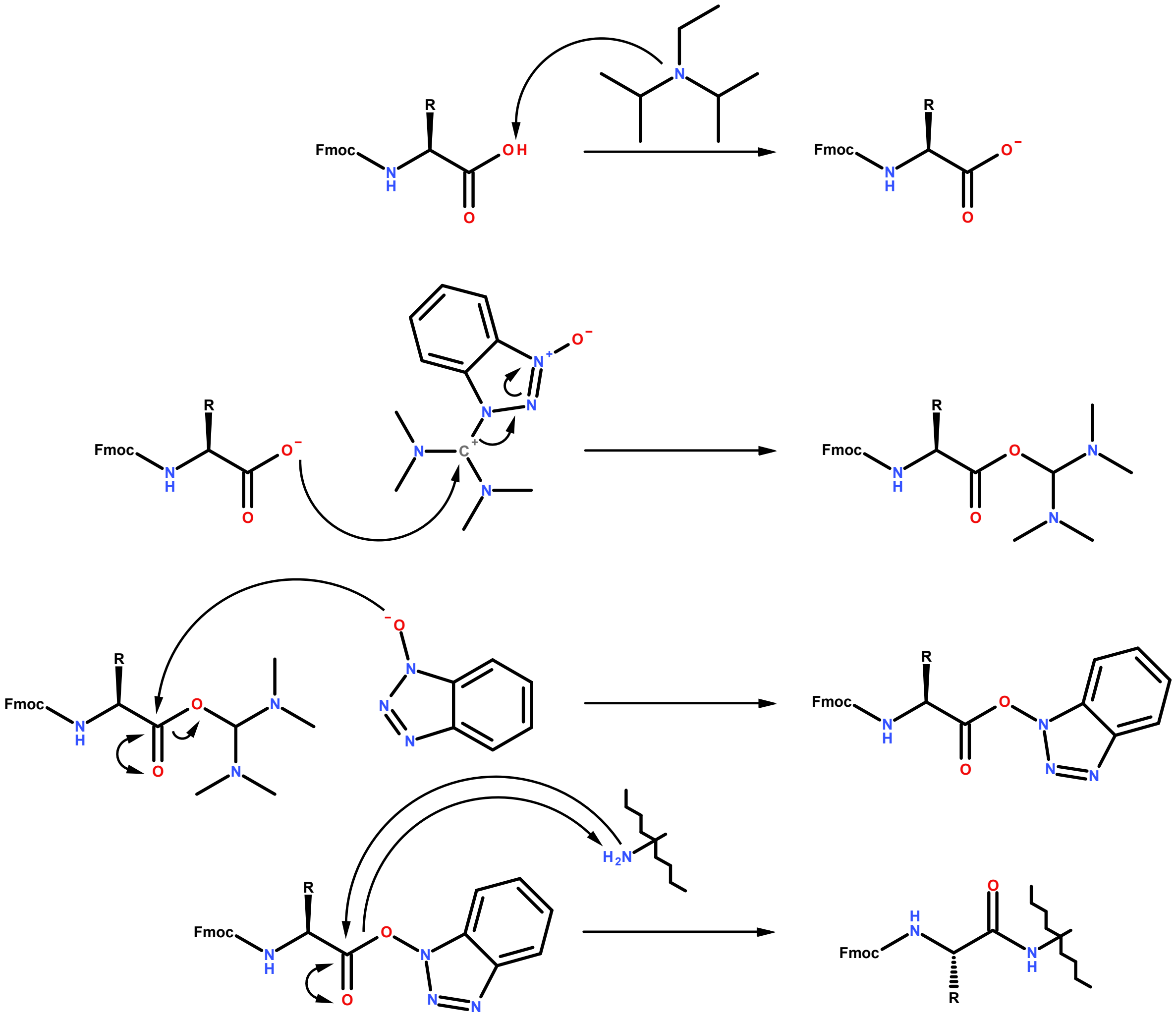

Figure 8.12. The activation and coupling of an amino acid using HBTU.

8.9.2 - SPPS protocol

The following protocol has been devised for 2-chlorotrityl chloride (2-CTC) functionalised resins although most of the steps are applicable for any general Fmoc peptide synthesis. The added advantage of 2-CTC, apart from allowing for mild cleavage, is that it is reusable and can be activated with relative ease.[214]

***i*)** Put the unloaded resins in the reaction vessel with the sintered filter bottom of appropriate porosity for the polymer beads and allow them to swell without agitation in 5 ml DCM, enough to cover the resin, for approximately 15 min. Wash out the DCM and add 5 ml DMF and allow the resins to swell for approximately 30 min without agitation.

***ii*)** Wash out the DMF and add the first reaction mixture by first dissolving the amino acid in DMF and then adding DIPEA. Agitate the mixture together with the resins for 4 hours preferably over night since the addition of the first amino acid is one of the most critical steps in solid phase peptide synthesis. The first amino acid is used in a 6-fold excess and DIPEA is used in a 6.6-fold excess compared to the unloaded resin.

***iii*)** Wash the resins (agitate) with approximately 5 ml of each solvent in the following order:

DMF:	5 times (approx. 1 min each)
MeOH:	2 times (approx. 1 min each)
DCM:	5 times (approx. 1 min each)

The linkers that have not attached the amino acid must be capped This can be achieved by washing the resins with MeOH for a longer period of time.

MeOH:	2 times (approx. 10 min each)

OPTIONAL In this step it is possible to get an estimation of the actual loading for the attachment of the first the amino acid (see subappendix below).

***iv*)** Wash resins with 5 ml each time:

DCM:	5 times (approx. 1 min each)
DMF:	3 times (approx. 1 min each)

***v*)** In order to attach the subsequent amino acid in the peptide the N-terminal must be deprotected i.e. the Fmoc group must be cleaved off. The mixture used to cleave off Fmoc is a solution of 20 percent piperidine in DMF (30 percent piperidine in DMF is preferred). Store the piperidine solution in dark colored glassware.

Wash with approximately 5 ml of:

Piperidine/DMF: 1 time (approx. 20 min)

Piperidine/DMF: 2 times (approx. 10 min each)

***vi*)** Wash the resins with approximately 5 ml of:

DMF: 5 times (approx. 1 min each)

MeOH: 2 times (approx. 1 min each)

DCM: 5 times (approx. 1 min each)

DMF: 3 times (approx. 1 min each)

***vii*)** Add the reaction mixture **2** by first dissolving the amino acid and coupling reagent in DMF and then adding DIPEA. Agitate the mixture together with the resins for 1.5 to 2 hours or longer if there are no time constraints. The second amino acid like the other remaining amino acids are used in a 4-fold excess and DIPEA is used in a 4.4-fold excess compared to the unloaded resins.

***viii*)** Wash as described in step vi.

ix) Deprotect as described in v.

***x*)** Wash as described in step vi.

Repeat step *vii* through *x* until all amino acids are coupled to the peptide.

***xi*)** Skip this step if acetylation is not required. Use a 50-fold excess of acetic anhydride and a 50-fold excess of DIPEA dissolved in DMF. Add the mixture to the resin and agitate for 1 hour. Wash the resin according to step vi and proceed.

xii) Before cleaving off the peptide from the beads they must be washed in order to remove all DMF because DMF can cleave the peptide in the presence of TFA.

Wash resins with approximately 5ml of:

MeOH: 2 times (approx. 1 min each)

DCM: 5 times (approx. 1 min each)

It is essential that DMF is thoroughly removed from the resins and reaction vessel prior to addition of cleavage mixture. Dry the resins by blowing nitrogen at them and place them in a vacuum desiccator over night. If the fully protected peptide is desired, use 1% TFA in DCM, otherwise follow the procedure below.

Add the cleavage mixture containing TFA /TIS/H_2O in the ratio 90/5/5.

Cleave with 3 times the volume of the resin each time:

TFA/TIS/H_2O: 3 times (approx. 60 min each)

Collect the fractions and evaporate the solvent in the rotary evaporator.

Subappendix

Wash the resins with approximately 5ml of:

DCM: 5 times (approx. 1 min each)

Et_2O: 3 times (approx. 1 min each)

Dry the resins by gently blowing nitrogen at the resins. Place the resins in a vacuum desiccator over night. Weigh approximately 1 mg of the resins and place them in a 1 ml UV-cuvette and add 1 ml of 20 or 30 percent piperidine in DMF. Leave the resins together with the piperidine solution (with occasional agitation) for 2-3 h. Set the UV detection to 290 nm and don't forget to zero with the piperidine solution. The loading can then be estimated using the following equation:

Loading = Abs_{290nm} / (mg resin * 1.75) [in the unit mmol/g]

8.9.3 - Compound structures

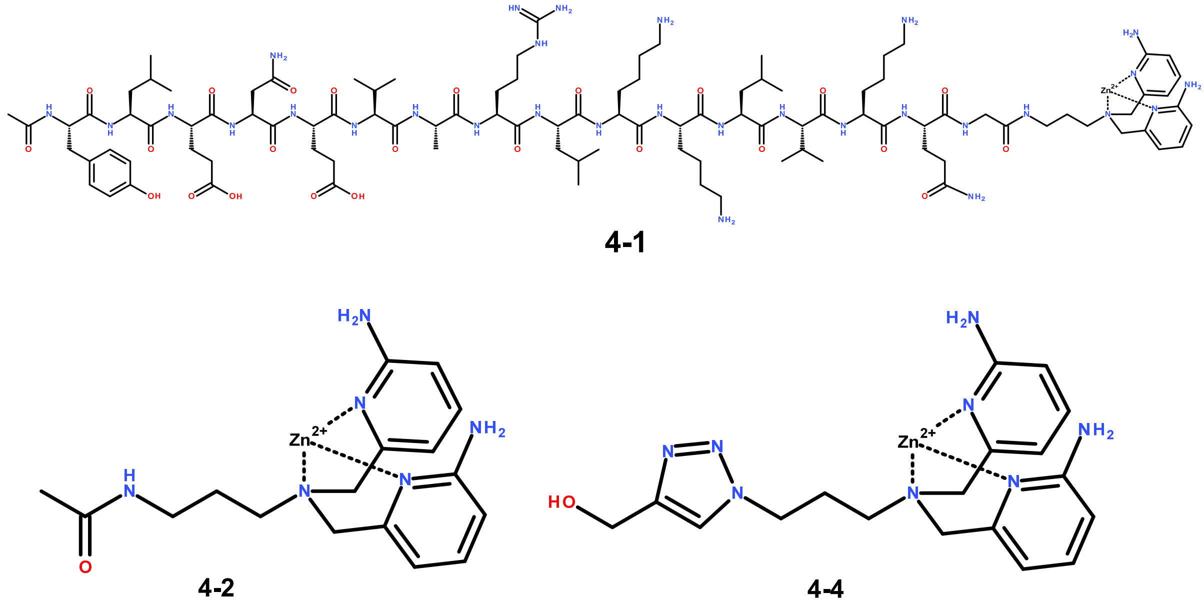

4-1

4-2

4-4

Figure 8.13. The structures of the mononuclear peptide based complexes studied in Chapter 4.

8.9.4 - Data for Chapter 4

[**L4-2**] mM	Abs_{295nm}
0.00625	0.059
0.0125	0.12
L4-1	0.13
0.025	0.23
0.05	0.46
0.1	0.92
0.2	1.84

Table 8.14. The spectrophotometric concentration calibration measurements for L4-2 and the interpolated measurement for L4-1 (green).

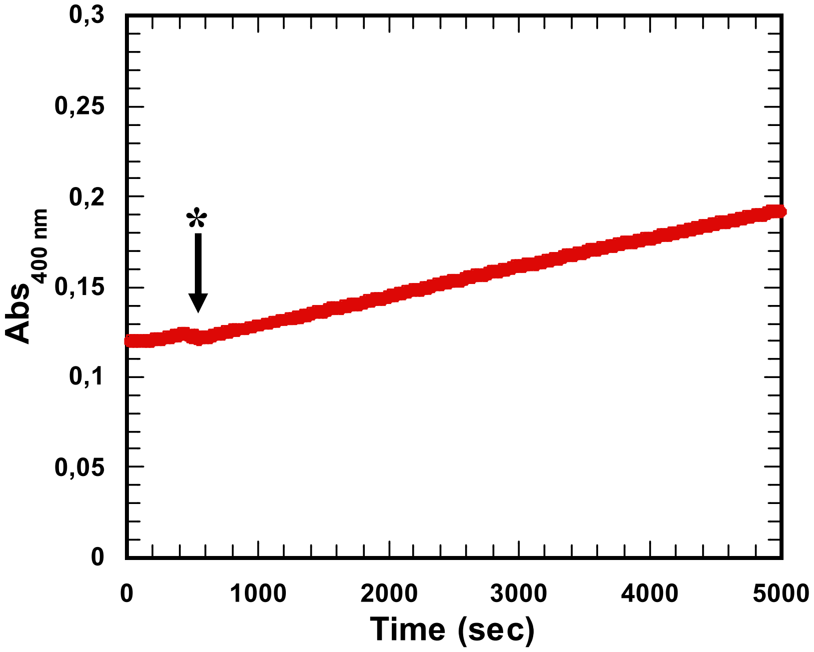

Figure 8.14. The absorbance was monitored at 400 nm for the transesterification of 50 µM HPNPP using 0.4 mM 4-1 at pH 7.4 in 50 mM HEPES and 0.1 M ionic strength (NaNO3). No activity was seen during the initial 7 minutes of the experiment therefore 6 equivalents of $Zn(OTf)_2$ were added at 450 seconds (*). The experiment was monitored over 10 h in order to obtain a well defined first-order curvature.

The reactivity observed after the addition of excess Zn(II) hints that potential allosteric binding of Zn(II) could be the cause, see Figure 8.14 The addition of excess $Zn(OTf)_2$ can be seen in light of the x-ray crystallographic data of the trihelical structure studied by Pecoraro *et al.* (PDB code: 3PBJ), see Figure 8.15, that show multiple Zn(II) ions coordinated to other residues (glutamic acid) than histidine in the peptide sequence.[161]

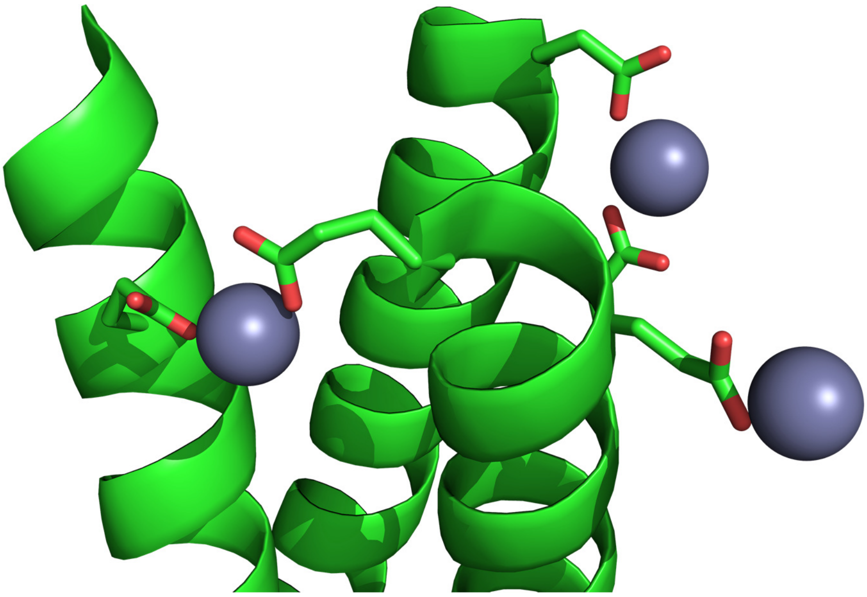

Figure 8.15. Additional Zn(II) coordination by glutamic acid in the trihelical structure studied by Pecoraro *et al.* (PDB code: 3PBJ). [45]

pH	k_{obs} (× 10^{-5}) (s^{-1})	log k_{obs}
6.87	3.12 (± 0.003)	-4.5059
7.32	6.8 (± 0.004)	-4.1677
7.36	7.56 (± 0.003)	-4.1214
7.68	11.70 (± 0.005)	-3.9296
8.11	19.51 (± 0.009)	-3.7097
8.73	30.05 (± 0.008)	-3.4808
9.18	34.54 (± 0.02)	-3.4617
9.52	30.95 (± 0.006)	-3.4617
9.93	34.54 (± 0.008)	-3.5093

Table 8.15.The observed rates for 1 mM 4-2 and 4-1 (green) with 50 µM HPNPP and 50 mM HEPES or CHES in 0.1 M ionic strength ($NaNO_3$) at various pH.

Addition	pH	Addition	pH	Addition	pH
0	3.25	17	7.00	34	10.82
1	3.33	18	7.27	35	10.86
2	3.43	19	7.47	36	10.90
3	3.57	20	7.66	37	10.94
4	3.76	21	7.83	38	10.97
5	4.04	22	8.06	39	11.01
6	4.38	23	8.29	40	11.04
7	4.71	24	8.65	41	11.06
8	4.98	25	9.23	42	11.08
9	5.20	26	9.80	43	11.11
10	5.38	27	10.13	44	11.14
11	5.57	28	10.45	45	11.16
12	5.74	29	10.45	46	11.18
13	5.95	30	10.56	47	11.20
14	6.17	31	10.64	48	11.22
15	6.43	32	10.71	49	11.23
16	6.72	33	10.77	50	11.25

Table 8.16. The titration of L4-2 using 50 mM NaOH added in 0.1 equivalents per addition (10 µL).

Addition	pH	Addition	pH	Addition	pH
0	3.12	17	5.06	34	8.53
1	3.19	18	5.14	35	8.71
2	3.27	19	5.23	36	8.96
3	3.36	20	5.32	37	9.23
4	3.48	21	5.43	38	9.57
5	3.64	22	5.56	39	9.79
6	3.86	23	5.73	40	9.96
7	4.09	24	5.97	41	10.09
8	4.27	25	6.28	42	10.2
9	4.4	26	6.71	43	10.3
10	4.51	27	7.09	44	10.38
11	4.6	28	7.41	45	10.45
12	4.68	29	7.67	46	10.52
13	4.76	30	7.88	47	10.58
14	4.83	31	8.06	48	10.64
15	4.91	32	8.21	49	10.69
16	4.97	33	8.37	50	10.74

8.17. The titration of 4-2 using 50 mM NaOH added in 0.1 equivalents per addition (10 µL).

The Zn(OH) and $Zn(OH)_2$ formation constants were obtained from literature.[215]

pH	k_{obs} ($\times 10^{-4}$) (s^{-1})	log k_{obs}
6.88	2.46 (± 0.004)	-3.6084
7.31	3.47 (± 0.007)	-3.4603
7.33	6.31 (± 0.004)	-3.1999
7.71	11.96 (± 0.006)	-2.9223
8.15	21.08 (± 0.008)	-2.6762
8.77	31.28 (± 0.022)	-2.4571
9.23	35.60 (± 0.027)	-2.4205
9.58	37.97 (± 0.029)	-2.4485
9.97	34.91 (± 0.020)	-2.5047

Table 8.18. The observed pseudo-first-order rate constants for 0.4 mM 4-4 and for comparison 0.4 mM 3-2 (green) towards the transesterification of 50 µM HPNPPi in 50 mM HEPES/CHES at various pH with 0.1 M ionic strength ($NaNO_3$).

8.10 - Appendix for Chapter 5

8.10.1 - Compound structures

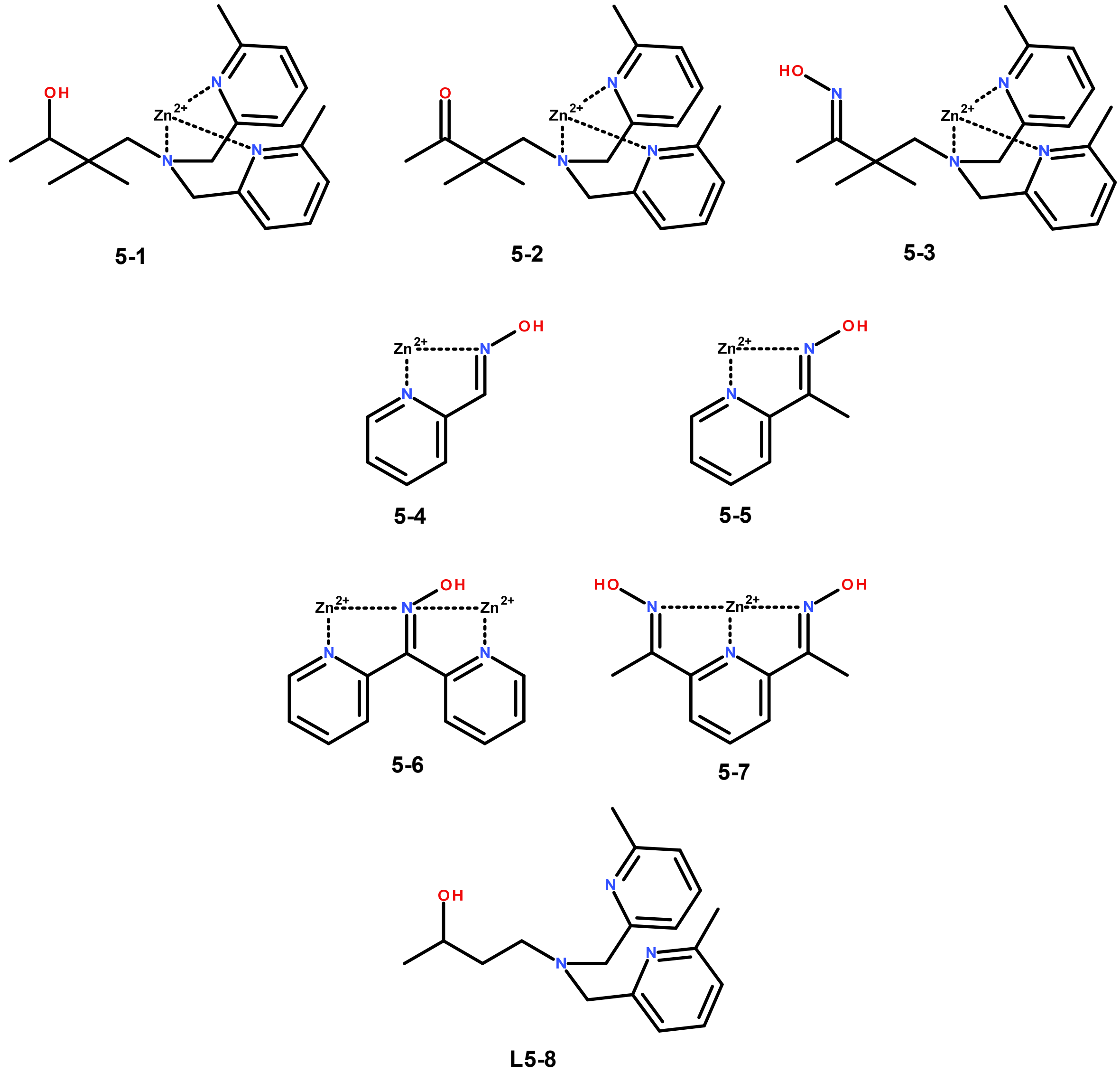

Figure 8.16. The structures of the nucleophilic complexes studied in Chapter 5.

8.10.2 - Data for Chapter 5

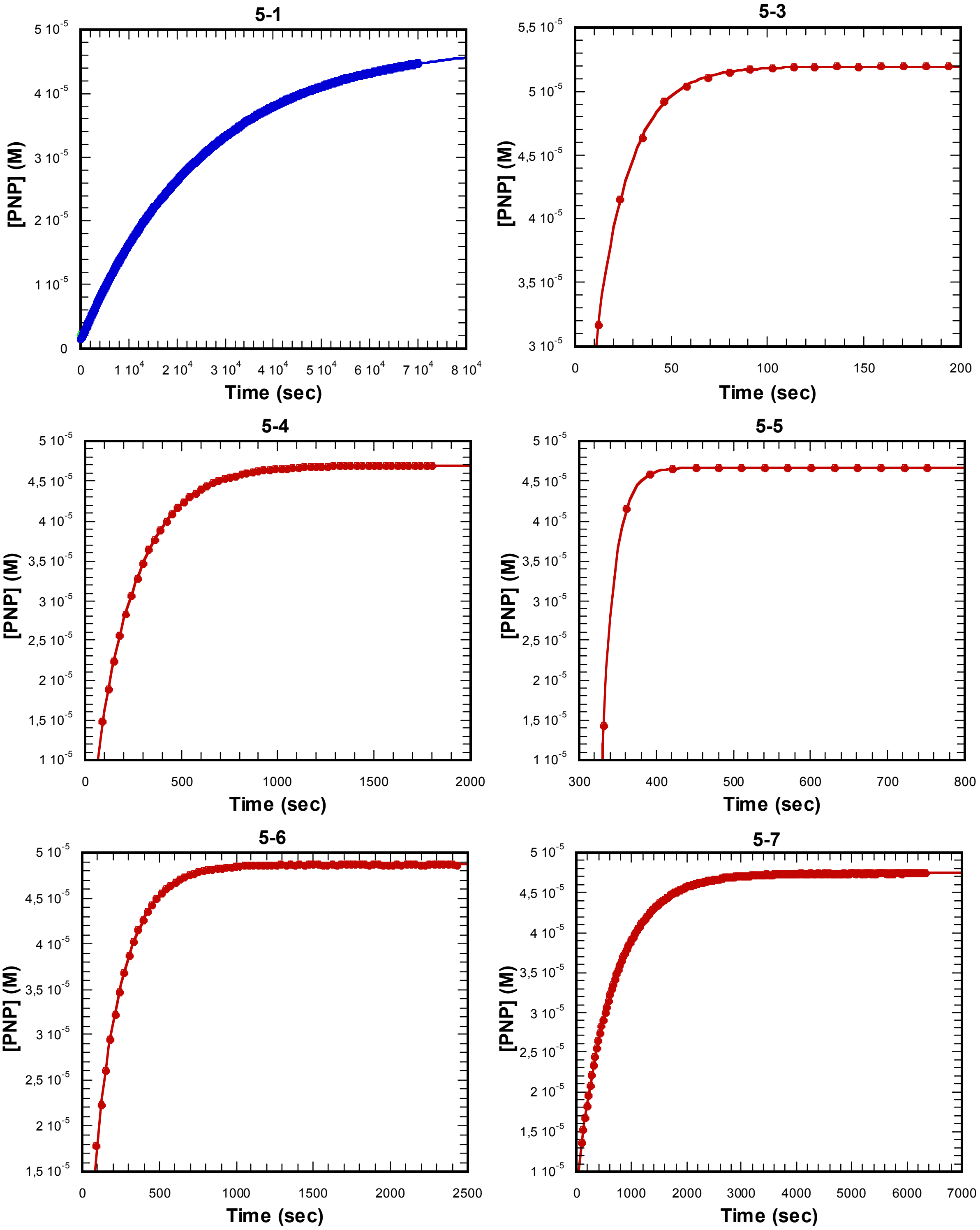

Figure 8.17. The observed reaction rates for 1 mM of the nucleophilic complexes in 50 mM HEPES (pH 7.4) with 0.1 M ionic strength (NaNO$_3$) and 50 µM pNPA.

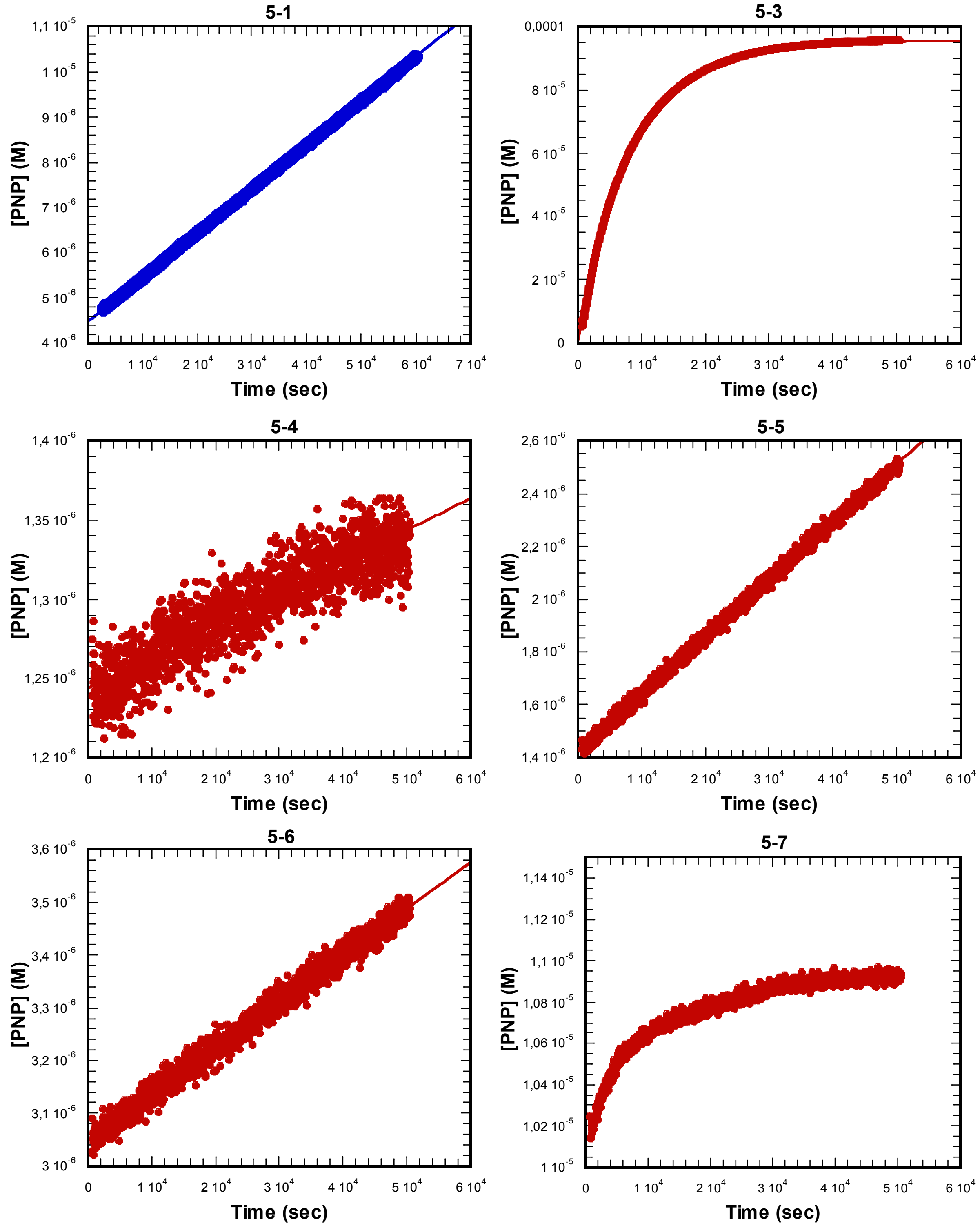

Figure 8.18. The observed reaction rates for 1 mM of the nucleophilic complexes in 50 mM HEPES (pH 7.4) with 0.1 M ionic strength (NaNO$_3$) and 50 µM BNPP. Complex 5-6 was used with 2 mM Zn(NO$_3$)$_2$ and kinetic experiment for 5-7 was performed in 24 % EtOH as reported in literature.[197]

[**5-1**] mM	pH 6.82	pH 7.28	pH 7.65	pH 7.92	pH 8.10
0.2	2.39×10^{-13}	1.04×10^{-11}	2.62×10^{-11}	5.59×10^{-11}	1.88×10^{-12}
0.4	8.15×10^{-12}	2.88×10^{-11}	6.36×10^{-11}	1.36×10^{-10}	5.93×10^{-12}
0.6	1.53×10^{-11}	4.97×10^{-11}	1.09×10^{-10}	2.30×10^{-10}	9.61×10^{-12}
0.8	2.36×10^{-11}	7.24×10^{-11}	1.58×10^{-10}	3.30×10^{-10}	1.38×10^{-11}
1	3.42×10^{-11}	9.75×10^{-11}	2.03×10^{-10}	4.12×10^{-10}	1.84×10^{-11}

Table 8.19. Initial rate (M s^{-1}) for the hydrolysis 1 mM BNPP (50 µM BNPP at pH 8.1) at various 5-1 concentrations and pH in 50 mM HEPES (pH 8.1 in EPPS) with 0.1 M ionic strength ($NaNO_3$).

At higher pH the data became unreliable due to precipitation. This was initially observed using CHES at pH 8.59 which further deteriorated with increasing pH. The initial rates were measured up to pH 8.1 in 50 mM EPPS and 0.1 M ionic strength ($NaNO_3$).

pH	k_{obs} (× 10^{-8}) (s^{-1})	k_2 (× 10^{-5}) (M^{-1} s^{-1})	log k_2
6.82	4.17 (± 0.18)	4.17 (± 0.18)	-4.38
7.28	10.89 (± 0.37)	10.89 (± 0.37)	-3.96
7.65	22.40 (± 0.58)	22.40 (± 0.58)	-3.65
7.92	45.31 (± 0.97)	45.31 (± 0.97)	-3.34
8.10	2.05 (± 0.05)	40.91 (± 0.05)	-3.39

Table 8.20. The linear fit of initial rate versus complex concentration yielded observed rate constants (s^{-1}) and apparent second-order rate constants (M^{-1} s^{-1}) for 5-1 with 1 mM BNPP (50 µM BNPP at pH 8.1).

[**5-3**] mM	pH 6.72	pH 7.21	pH 7.58	pH 8.00
0.2	1.32×10^{-8}	3.06×10^{-8}	4.17×10^{-8}	5.24×10^{-8}
0.4	3.87×10^{-8}	7.21×10^{-8}	9.50×10^{-8}	1.09×10^{-7}
0.6	6.53×10^{-8}	1.2×10^{-7}	1.49×10^{-7}	1.65×10^{-7}
0.8	9.93×10^{-8}	1.61×10^{-7}	2.20×10^{-7}	2.25×10^{-7}
1	1.23×10^{-7}	2.1×10^{-7}	2.44×10^{-7}	2.72×10^{-7}

Table 8.21. Initial rate (M s^{-1}) for the hydrolysis 1 mM BNPP at various 5-3 concentrations and pH in 50 mM HEPES with 0.1 M ionic strength ($NaNO_3$).

[**5-3**] mM	pH 8.54	pH 9.10	pH 9.45	pH 9.86
0.2	5.45×10^{-8}	4.34×10^{-8}	3.46×10^{-8}	1.91×10^{-8}
0.4	1.16×10^{-7}	9.24×10^{-8}	7.22×10^{-8}	4.36×10^{-8}
0.6	1.60×10^{-7}	1.37×10^{-7}	1.11×10^{-7}	6.78×10^{-8}
0.8	2.67×10^{-7}	1.85×10^{-7}	1.47×10^{-7}	9.20×10^{-8}
1	2.14×10^{-7}	2.32×10^{-7}	1.86×10^{-7}	1.21×10^{-7}

Figure 8.19. Initial rate (M s^{-1}) for the hydrolysis 1 mM BNPP at various 5-3 concentrations and pH in 50 mM HEPES with 0.1 M ionic strength ($NaNO_3$).

pH	k_{obs} ($\times 10^{-4}$) (s^{-1})	k_2 (M^{-1} s^{-1})	log k_2
6.72	1.40 (± 0.04)	0.14(± 0.04)	-0.85
7.21	2.24 (± 0.04)	0.22 (± 0.04)	-0.64
7.58	2.65 (± 0.19)	0.26 (± 0.19)	-0.58
8.00	2.78 (± 0.06)	0.28 (± 0.06)	-0.56
8.54	2.62 (± 0.06)	0.26 (± 0.06)	-0.58
9.10	2.34 (± 0.01)	0.23 (± 0.01)	-0.63
9.45	1.89 (± 0.01)	0.19 (± 0.01)	-0.72
9.86	1.26 (± 0.02)	0.13(± 0.02)	-0.90

Figure 8.20. The linear fit of initial rate versus complex concentration yielded observed rate constants (s^{-1}) and apparent second-order rate constants (M^{-1} s^{-1}) for 5-3 with 1 mM BNPP.

Chapter 9 - References

1. Westheimer, F. Why nature chose phosphates. *Science (80-.).* **235,** 1173–1178 (1987).

2. Kamerlin, S. C. L., Sharma, P. K., Prasad, R. B. & Warshel, A. Why nature really chose phosphate. *Q. Rev. Biophys.* **46,** 1–132 (2013).

3. Urban, P. L. Compartmentalised chemistry: from studies on the origin of life to engineered biochemical systems. *New J. Chem.* **38,** 5135–5141 (2014).

4. Luisi, P. L., Walde, P. & Oberholzer, T. Lipid vesicles as possible intermediates in the origin of life. *Curr. Opin. Colloid Interface Sci.* **4,** 33–39 (1999).

5. Monnard, P.-A. & Walde, P. Current Ideas about Prebiological Compartmentalization. *Life (Basel, Switzerland)* **5,** 1239–63 (2015).

6. Davis, B. D. On the importance of being ionized. *Arch. Biochem. Biophys.* **78,** 497–509 (1958).

7. Lindahl, T. & Nyberg, B. Rate of depurination of native deoxyribonucleic acid. *Biochemistry* **11,** 3610–3618 (1972).

8. Schroeder, G. K., Lad, C., Wyman, P., Williams, N. H. & Wolfenden, R. The time required for water attack at the phosphorus atom of simple phosphodiesters and of DNA. *Proc. Natl. Acad. Sci. U. S. A.* **103,** 4052–5 (2006).

9. Serpersu, E. H., Shortle, D. & Mildvan, A. S. Kinetic and magnetic resonance studies of active-site mutants of staphylococcal nuclease: factors contributing to catalysis. *Biochemistry* **26,** 1289–1300 (1987).

10. Wolfenden, R., Ridgway, C. & Young, G. Spontaneous Hydrolysis of Ionized Phosphate Monoesters and Diesters and the Proficiencies of Phosphatases and Phosphodiesterases as Catalysts. *J. Am. Chem. Soc.* **120,** 833–834 (1998).

11. Williams, N. H. & Wyman, P. Base catalysed phosphate diester hydrolysis. *Chem. Commun.* 1268–1269 (2001). doi:10.1039/b103317b

12. Kamerlin, S. C. L., Williams, N. H. & Warshel, A. Dineopentyl phosphate hydrolysis: evidence for stepwise water attack. *J. Org. Chem.* **73,** 6960–9 (2008).

13. Chin, J., Banaszczyk, M., Jubian, V. & Zou, X. Cobalt(III) complex-promoted hydrolysis of phosphate diesters: comparison in reactivity of rigid cis-diaquo(tetraaza)cobalt(III) complexes. *J. Am. Chem. Soc.* **111,** 186–190 (1989).

14. Livieri, M., Mancin, F., Saielli, G., Chin, J. & Tonellato, U. Mimicking enzymes: cooperation between organic functional groups and metal ions in the cleavage of phosphate diesters. *Chem. Eur. J.* **13,** 2246–56 (2007).

15. Yatsimirsky, A. K. Metal ion catalysis in acyl and phosphoryl transfer: Transition states as ligands. *Coord. Chem. Rev.* **249,** 1997–2011 (2005).

16. Lassila, J. K., Zalatan, J. G. & Herschlag, D. Biological phosphoryl-transfer reactions: understanding mechanism and catalysis. *Annu. Rev. Biochem.* **80,** 669–702 (2011).

17. Levene, P. A. The structure of yeast nucleic acid. IV. Ammonia hydrolysis. *J. Biol. Chem.* **40,** 415–424 (1919).

18. Cohn, W. E. Heterogeneity in pyrimidine nucleotides. *J. Am. Chem. Soc.* **72,** 2811–2812 (1950).

19. Loring, H. S., Luthy, N. G., Bortner, H. W. & Levy, L. W. The isolation of an isomeric cytidylic acid from hydrolysates of yeast ribonucleic acid. *J. Am. Chem. Soc.* **72,** 2811–2811 (1950).

20. Carter, C. E. Paper Chromatography of Purine and Pyrimidine Derivatives of Yeast Ribonucleic Acid. *J. Am. Chem. Soc.* **72,** 1466–1471 (1950).

21. Kirby, A. J. Effective Molarities for Intramolecular Reactions. *Adv. Phys. Org. Chem.* **17,** 183 (1980).

22. Lönnberg, H. Cleavage of RNA phosphodiester bonds by small molecular entities: a mechanistic insight. *Org. Biomol. Chem.* **9,** 1687–703 (2011).

23. Westheimer, F. H. Pseudo-Rotation in the Hydrolysis of Phosphate Esters. *Acc. Chem. Res.* **1,** 70–78 (1968).

24. Oivanen, M., Kuusela, S. & Lönnberg, H. Kinetics and Mechanisms for the Cleavage and Isomerization of the Phosphodiester Bonds of RNA by Brønsted Acids and Bases. *Chem. Rev.* **98,** 961–990 (1998).

25. Jarvinen, P., Oivanen, M. & Lonnberg, H. Interconversion and phosphoester hydrolysis of 2’,5'- and 3',5'-dinucleoside monophosphates: kinetics and mechanisms. *J. Org. Chem.* **56,** 5396–5401 (1991).

26. Kuusela, S. & Lönnberg, H. Metal ions that promote the hydrolysis of nucleoside phosphoesters do not enhance intramolecular phosphate migration. *J. Phys. Org. Chem.* **6,** 347–356 (1993).

27. Korhonen, H., Mikkola, S. & Williams, N. H. The mechanism of cleavage and isomerisation of RNA promoted by an efficient dinuclear Zn2+ complex. *Chemistry* **18,** 659–70 (2012).

28. Tsang, W. Y. *et al.* Dinuclear Zn(II) complex promotes cleavage and isomerization of 2-hydroxypropyl alkyl phosphates by a common cyclic phosphate intermediate. *J. Am. Chem. Soc.* **131,** 4159–66 (2009).

29. Humphry, T. *et al.* Altered transition state for the reaction of an RNA model catalyzed by a dinuclear zinc(II) catalyst. *J. Am. Chem. Soc.* **130,** 17858–66 (2008).

30. Yang, M., Iranzo, O., Richard, J. P. & Morrow, J. R. Solvent deuterium isotope effects on phosphodiester cleavage catalyzed by an extraordinarily active Zn(II) complex. *J. Am. Chem. Soc.* **127,** 1064–5 (2005).

31. Dupureur, C. M. Roles of metal ions in nucleases. *Curr. Opin. Chem. Biol.* **12,** 250–5 (2008).

32. Fedor, M. J. The role of metal ions in RNA catalysis. *Curr. Opin. Struct. Biol.* **12,** 289–95 (2002).

33. Komiyama, M., Takeda, N. & Shigekawa, H. Hydrolysis of DNA and RNA by lanthanide ions: mechanistic studies leading to new applications. *Chem. Commun.* 1443–1451 (1999). doi:10.1039/a901621j

34. Cowan, J. a. Chemical nucleases. *Curr. Opin. Chem. Biol.* **5,** 634–42 (2001).

35. Franklin, S. J. Lanthanide-mediated DNA hydrolysis. *Curr. Opin. Chem. Biol.* **5,** 201–208 (2001).

36. Mitić, N. *et al.* The catalytic mechanisms of binuclear metallohydrolases. *Chem. Rev.* **106,** 3338–63 (2006).

37. Bobyr, E. *et al.* High-resolution analysis of Zn(2+) coordination in the alkaline phosphatase superfamily by EXAFS and x-ray crystallography. *J. Mol. Biol.* **415,** 102–17 (2012).

38. Williams, N. H. Models for biological phosphoryl transfer. *Biochim. Biophys. Acta* **1697,** 279–87 (2004).

39. Liu, C., Wang, M., Zhang, T. & Sun, H. DNA hydrolysis promoted by di- and multi-nuclear metal complexes. *Coord. Chem. Rev.* **248,** 147–168 (2004).

40. Parkin, G. Synthetic analogues relevant to the structure and function of zinc enzymes. *Chem. Rev.* **104,** 699–767 (2004).

41. Sigel, H. & Martin, R. B. The colourless "chameleon" or the peculiar properties of Zn2+ in complexes in solution. Quantification of equilibria involving a change of the coordination number of the metal ion. *Chem. Soc. Rev.* **23,** 83 (1994).

42. Dudev, T. & Lim, C. Tetrahedral vs Octahedral Zinc Complexes with Ligands of Biological Interest: A DFT/CDM Study. *J. Am. Chem. Soc.* **122,** 11146–11153 (2000).

43. Vallee, B. L. & Auld, D. S. Cocatalytic zinc motifs in enzyme catalysis. *Proc. Natl. Acad. Sci. U. S. A.* **90,** 2715–8 (1993).

44. Vallee, B. L. & Auld, D. S. Active-site zinc ligands and activated H2O of zinc enzymes. *Proc. Natl. Acad. Sci. U. S. A.* **87,** 220–4 (1990).

45. The PyMOL Molecular Graphics System, Version 1.3 Schrödinger, LLC. (2010).

46. Vallee, B. L. & Auld, D. S. Zinc coordination, function, and structure of zinc enzymes and other proteins. *Biochemistry* **29,** 5647–5659 (1990).

47. Vallee, B. L. & Auld, D. S. New perspective on zinc biochemistry: Cocatalytic sites in multi-zinc enzymes. *Biochemistry* **32,** 6493–6500 (1993).

48. Mikkola, S. *et al.* The mechanism of the metal ion promoted cleavage of RNA phosphodiester bonds involves a general acid catalysis by the metal aquo ion on the departure of the leaving group. *J. Chem. Soc. Perkin Trans. 2* 1619–1626 (1999). doi:10.1039/a903691a

49. Sträter, N., Lipscomb, W. N., Klabunde, T. & Krebs, B. Two-Metal Ion Catalysis in Enzymatic Acyl- and Phosphoryl-Transfer Reactions. *Angew. Chemie Int. Ed. English* **35,** 2024–2055 (1996).

50. Wilcox, D. E. Binuclear Metallohydrolases. *Chem. Rev.* **96,** 2435–2458 (1996).

51. Feng, G., Natale, D., Prabaharan, R., Mareque-Rivas, J. C. & Williams, N. H. Efficient phosphodiester binding and cleavage by a ZnII complex combining hydrogen-bonding interactions and double Lewis acid activation. *Angew. Chem. Int. Ed. Engl.* **45,** 7056–9 (2006).

52. Zalatan, J. G., Fenn, T. D., Brunger, A. T. & Herschlag, D. Structural and functional comparisons of nucleotide pyrophosphatase/phosphodiesterase and alkaline phosphatase: implications for mechanism and evolution. *Biochemistry* **45,** 9788–803 (2006).

53. Zalatan, J. G., Fenn, T. D. & Herschlag, D. Comparative enzymology in the alkaline phosphatase superfamily to determine the catalytic role of an active-site metal ion. *J. Mol. Biol.* **384,** 1174–89 (2008).

54. Miller, B. G. & Wolfenden, R. Catalytic proficiency: the unusual case of OMP decarboxylase. *Annu. Rev. Biochem.* **71,** 847–85 (2002).

55. Stroppolo, M. E., Falconi, M., Caccuri, A. M. & Desideri, A. Superefficient enzymes. *Cell. Mol. Life Sci.* **58,** 1451–1460 (2001).

56. Radzicka, A. & Wolfenden, R. A proficient enzyme. *Science* **267,** 90–3 (1995).

57. Bar-Even, A. *et al.* The moderately efficient enzyme: evolutionary and physicochemical trends shaping enzyme parameters. *Biochemistry* **50,** 4402–10 (2011).

58. Feng, G., Mareque-Rivas, J. C., Torres Martín de Rosales, R. & Williams, N. H. A highly reactive mononuclear Zn(II) complex for phosphodiester cleavage. *J. Am. Chem. Soc.* **127,** 13470–1 (2005).

59. Alkherraz, A. *et al.* Phosphate ester analogues as probes for understanding enzyme catalysed phosphoryl transfer. *Faraday Discuss.* **145,** 281–299 (2010).

60. Korhonen, H. J., Conway, L. P. & Hodgson, D. R. W. Phosphate analogues in the dissection of mechanism. *Curr. Opin. Chem. Biol.* **21,** 63–72 (2014).

61. Westheimer, F. H. & Shookhoff, M. W. The Electrostatic Influence of Substituents on the Dissociation Constants of Organic Acids. III. *J. Am. Chem. Soc.* **61,** 555–560 (1939).

62. Jameson, G. W. & Lawlor, J. M. Aminolysis of N-phosphorylated pyridines. *J. Chem. Soc. B Phys. Org.* 53 (1970). doi:10.1039/j29700000053

63. Skoog, M. T. & Jencks, W. P. Reactions of pyridines and primary amines with N-phosphorylated pyridines. *J. Am. Chem. Soc.* **106,** 7597–7606 (1984).

64. Buchholz, R. R. *et al.* A structural and catalytic model for zinc phosphoesterases. *Dalton Trans.* 6045–54 (2008). doi:10.1039/b806391e

65. Feng, G., Mareque-Rivas, J. C. & Williams, N. H. Comparing a mononuclear Zn(II) complex with hydrogen bond donors with a dinuclear Zn(II) complex for catalysing phosphate ester cleavage. *Chem. Commun. (Camb).* **2,** 1845–7 (2006).

66. Iranzo, O., Elmer, T., Richard, J. P. & Morrow, J. R. Cooperativity between metal ions in the cleavage of phosphate diesters and RNA by dinuclear Zn(II) catalysts. *Inorg. Chem.* **42,** 7737–46 (2003).

67. Iranzo, O., Kovalevsky, A. Y., Morrow, J. R. & Richard, J. P. Physical and kinetic analysis of the cooperative role of metal ions in catalysis of phosphodiester cleavage by a dinuclear Zn(II) complex. *J. Am. Chem. Soc.* **125,** 1988–93 (2003).

68. Diez-Castellnou, M., Mancin, F. & Scrimin, P. Efficient phosphodiester cleaving nanozymes resulting from multivalency and local medium polarity control. *J. Am. Chem. Soc.* **136,** 1158–61 (2014).

69. Neverov, A. A. *et al.* Combination of a dinuclear Zn2+ complex and a medium effect exerts a 10(12)-fold rate enhancement of cleavage of an RNA and DNA model system. *J. Am. Chem. Soc.* **128,** 16398–405 (2006).

70. Motherwell, W. B., Bingham, M. J. & Six, Y. Recent progress in the design and synthesis of artificial enzymes. *Tetrahedron* **57,** 4663–4686 (2001).

71. Morrow, J. R. & Iranzo, O. Synthetic metallonucleases for RNA cleavage. *Curr. Opin. Chem. Biol.* **8,** 192–200 (2004).

72. Mancin, F., Scrimin, P. & Tecilla, P. Progress in artificial metallonucleases. *Chem. Commun. (Camb).* **48,** 5545–59 (2012).

73. Bonfá, L., Gatos, M., Mancin, F., Tecilla, P. & Tonellato, U. The ligand effect on the hydrolytic reactivity of Zn(II) complexes toward phosphate diesters. *Inorg. Chem.* **42,** 3943–9 (2003).

74. Piątek, A. M., Gray, M. & Anslyn, E. V. Guanidinium Groups Act as General-Acid Catalysts in Phosphoryl Transfer Reactions: A Two-Proton Inventory on a Model System. *J. Am. Chem. Soc.* **126,** 9878–9879 (2004).

75. Meyer, F. Clues to Dimetallohydrolase Mechanisms from Studies on Pyrazolate-Based Bioinspired Dizinc Complexes – Experimental Evidence for a Functional Zn–O2H3–Zn Motif. *Eur. J. Inorg. Chem.* **2006,** 3789–3800 (2006).

76. Kimura, E., Shiota, T., Koike, T., Shiro, M. & Kodama, M. A zinc(II) complex of 1,5,9-triazacyclododecane ([12]aneN3) as a model for carbonic anhydrase. *J. Am. Chem. Soc.* **112,** 5805–5811 (1990).

77. Mitra, M. *et al.* A Bis(μ-phenoxo)-Bridged Dizinc Complex with Hydrolytic Activity. *Zeitschrift für Anorg. und Allg. Chemie* **639,** 1534–1542 (2013).

78. Arca, M. *et al.* Coordination properties of new bis(1,4,7-triazacyclononane) ligands: a highly active dizinc complex in phosphate diester hydrolysis. *Inorg. Chem.* **42,** 6929–39 (2003).

79. Fry, F. H. *et al.* Binuclear copper(II) complexes of xylyl-bridged bis(1,4,7-triazacyclononane) ligands. *Inorg. Chem.* **42,** 5594–603 (2003).

80. Montagner, D., Gandin, V., Marzano, C. & Erxleben, A. Phosphate Diester Cleavage, DNA Interaction and Cytotoxic Activity of a Bimetallic Bis(1,4,7-triazacyclononane) Zinc Complex. *Eur. J. Inorg. Chem.* **2014,** 4084–4092 (2014).

81. Cao, R., Müller, P. & Lippard, S. J. Tripodal tris-tacn and tris-dpa platforms for assembling phosphate-templated trimetallic centers. *J. Am. Chem. Soc.* **132,** 17366–9 (2010).

82. Kawahara, S. & Uchimaru, T. Dinucleotide Hydrolysis Promoted by Dinuclear Zn Complexes − The Effect of the Distance between Zn Ions in the Complexes on the Hydrolysis Rate. *Eur. J. Inorg. Chem.* **2001,** 2437–2442 (2001).

83. Molenveld, P. *et al.* Dinuclear and Trinuclear Zn(II) Calix[4]arene Complexes as Models for Hydrolytic Metallo-Enzymes. Synthesis and Catalytic Activity in Phosphate Diester Transesterification. *J. Org. Chem.* **64,** 3896–3906 (1999).

84. Molenveld, P., Engbersen, J. F. J. & Reinhoudt, D. N. Dinuclear metallo-phosphodiesterase models: application of calix[4]arenes as molecular scaffolds. *Chem. Soc. Rev.* **29,** 75–86 (2000).

85. Scarso, A., Zaupa, G., Houillon, F. B., Prins, L. J. & Scrimin, P. Tripodal, cooperative, and allosteric transphosphorylation metallocatalysts. *J. Org. Chem.* **72,** 376–85 (2007).

86. Fritsky, I. O., Ott, R. & Krämer, R. Allosteric Regulation of Artificial Phosphoesterase Activity by Metal Ions. *Angew. Chem. Int. Ed. Engl.* **39,** 3255–3258 (2000).

87. Takebayashi, S., Shinkai, S., Ikeda, M. & Takeuchi, M. Metal ion induced allosteric transition in the catalytic activity of an artificial phosphodiesterase. *Org. Biomol. Chem.* **6,** 493–9 (2008).

88. Urry, D. W., Gowda, D. C., Peng, S. Q., Parker, T. M. & Harris, R. D. Design at nanometric dimensions to enhance hydrophobicity-induced pKa shifts. *J. Am. Chem. Soc.* **114,** 8716–8717 (1992).

89. Kövári, E. & Krämer, R. Zink(II)-Komplexe des Ammonium-funktionalisierten 2,2′-Bipyridins [6,6′-{Me2N(H)CH2C≡C}2bpy](ClO4)2 und des verwandten Liganden 6,6′-(CH3CH2CH2C≡C)2bpy. *Chem. Ber.* **127,** 2151–2157 (1994).

90. Kövári, E. & Krämer, R. Rapid Phosphodiester Hydrolysis by an Ammonium-Functionalized Copper(II) Complex. A Model for the Cooperativity of Metal Ions and NH-Acidic Groups in Phosphoryl Transfer Enzymes. *J. Am. Chem. Soc.* **118,** 12704–12709 (1996).

91. Krämer, R. Bioinorganic models for the catalytic cooperation of metal ions and functional groups in nuclease and peptidase enzymes. *Coord. Chem. Rev.* **182,** 243–261 (1999).

92. Dalby, K. N., Kirby, A. J. & Hollfelder, F. Simple but efficient models for nuclease catalysis. *Pure Appl. Chem.* **66,** 687–694 (1994).

93. Mohamed, M. F. & Brown, R. S. Cleavage of an RNA model catalyzed by dinuclear Zn(II) complexes containing rate-accelerating pendants. Comparison of the catalytic benefits of H-bonding and hydrophobic substituents. *J. Org. Chem.* **75,** 8471–7 (2010).

94. Morgan, B. P., He, S. & Smith, R. C. Dizinc enzyme model/complexometric indicator pairs in indicator displacement assays for inorganic phosphates under physiological conditions. *Inorg. Chem.* **46,** 9262–6 (2007).

95. Ngo, H. T., Liu, X. & Jolliffe, K. a. Anion recognition and sensing with Zn(II)-dipicolylamine complexes. *Chem. Soc. Rev.* **41,** 4928–65 (2012).

96. England, A. H. *et al.* On the hydration and hydrolysis of carbon dioxide. *Chem. Phys. Lett.* **514,** 187–195 (2011).

97. Hatch, M. D. Carbonic anhydrase assay: strong inhibition of the leaf enzyme by CO2 in certain buffers. *Anal. Biochem.* **192,** 85–9 (1991).

98. Kinoshita, E., Takahashi, M., Takeda, H., Shiro, M. & Koike, T. Recognition of phosphate monoester dianion by an alkoxide-bridged dinuclear zinc(II) complex. *Dalton Trans.* 1189–93 (2004). doi:10.1039/b400269e

99. Håkansson, K., Carlsson, M., Svensson, L. a & Liljas, a. Structure of native and apo carbonic anhydrase II and structure of some of its anion-ligand complexes. *J. Mol. Biol.* **227,** 1192–204 (1992).

100. Paddock, R. L., Hiyama, Y., McKay, J. M. & Nguyen, S. T. Co(III) porphyrin/DMAP: an efficient catalyst system for the synthesis of cyclic carbonates from CO2 and epoxides. *Tetrahedron Lett.* **45,** 2023–2026 (2004).

101. Zhang, X. & van Eldik, R. A functional model for carbonic anhydrase: thermodynamic and kinetic study of a tetraazacyclododecane complex of zinc(II). *Inorg. Chem.* **34,** 5606–5614 (1995).

102. Nakata, K. *et al.* Kinetic study of catalytic CO2 hydration by water-soluble model compound of carbonic anhydrase and anion inhibition effect on CO2 hydration. *J. Inorg. Biochem.* **89,** 255–266 (2002).

103. Koziol, L. *et al.* Toward a small molecule, biomimetic carbonic anhydrase model: theoretical and experimental investigations of a panel of zinc(II) aza-macrocyclic catalysts. *Inorg. Chem.* **51,** 6803–12 (2012).

104. Wong, S. E. *et al.* Designing small-molecule catalysts for CO2 capture. *Energy Procedia* **4,** 817–823 (2011).

105. Liu, X., Du, P. & Cao, R. Trinuclear zinc complexes for biologically relevant μ3-oxoanion binding and carbon dioxide fixation. *Nat. Commun.* **4,** 2375 (2013).

106. Walkup, G. K., Burdette, S. C., Lippard, S. J. & Tsien, R. Y. A New Cell-Permeable Fluorescent Probe for Zn 2+. *J. Am. Chem. Soc.* **122,** 5644–5645 (2000).

107. Williams, N. H., Cheung, W. & Chin, J. Reactivity of Phosphate Diesters Doubly Coordinated to a Dinuclear Cobalt(III) Complex: Dependence of the Reactivity on the Basicity of the Leaving Group. *J. Am. Chem. Soc.* **120,** 8079–8087 (1998).

108. Yu, F. *et al.* Protein design: toward functional metalloenzymes. *Chem. Rev.* **114,** 3495–578 (2014).

109. Ely, F. *et al.* The organophosphate-degrading enzyme from Agrobacterium radiobacter displays mechanistic flexibility for catalysis. *Biochem. J.* **432,** 565–73 (2010).

110. Arora, H., Barman, S. K., Lloret, F. & Mukherjee, R. Isostructural dinuclear phenoxo-/acetato-bridged manganese(II), cobalt(II), and zinc(II) complexes with labile sites: kinetics of transesterification of 2-hydroxypropyl-p-nitrophenylphosphate. *Inorg. Chem.* **51,** 5539–53 (2012).

111. Linjalahti, H., Feng, G., Mareque-Rivas, J. C., Mikkola, S. & Williams, N. H. Cleavage and isomerization of UpU promoted by dinuclear metal ion complexes. *J. Am. Chem. Soc.* **130,** 4232–3 (2008).

112. Weston, J. Mode of action of bi- and trinuclear zinc hydrolases and their synthetic analogues. *Chem. Rev.* **105,** 2151–74 (2005).

113. Gale, P. A. & Steed, J. W. Supramolecular Chemistry: From Molecules to Nanomaterials. *Wiley Sons* (2012).

114. Van Meer, G., Voelker, D. R. & Feigenson, G. W. Membrane lipids: where they are and how they behave. *Nat. Rev. Mol. Cell Biol.* **9,** 112–24 (2008).

115. Doyle, E. L., Hunter, C. a, Phillips, H. C., Webb, S. J. & Williams, N. H. Cooperative binding at lipid bilayer membrane surfaces. *J. Am. Chem. Soc.* **125,** 4593–9 (2003).

116. Menger, F. M. & Fei, Z. X. Fast Amide Cleavage under Mild Conditions: An Evolutionary Approach to Bioorganic Catalysis. *Angew. Chemie Int. Ed. English* **33,** 346–348 (1994).

117. Mancin, F., Scrimin, P., Tecilla, P. & Tonellato, U. Amphiphilic metalloaggregates: Catalysis, transport, and sensing. *Coord. Chem. Rev.* **253,** 2150–2165 (2009).

118. Bhattacharya, S. & Kumari, N. Metallomicelles as potent catalysts for the ester hydrolysis reactions in water. *Coord. Chem. Rev.* **253,** 2133–2149 (2009).

119. Jiang, F. *et al.* Metallomicellar catalysis. *Colloids Surfaces A Physicochem. Eng. Asp.* **254,** 91–97 (2005).

120. Moss, R. A. & Ragunathan, K. G. Metal Cation Micelle Mediated Hydrolysis of Phosphonic Acid Esters. *Langmuir* **15,** 107–110 (1999).

121. Poznik, M. & König, B. Cooperative hydrolysis of aryl esters on functionalized membrane surfaces and in micellar solutions. *Org. Biomol. Chem.* **12,** 3175–80 (2014).

122. Gruber, B., Kataev, E., Aschenbrenner, J., Stadlbauer, S. & König, B. Vesicles and micelles from amphiphilic zinc(II)-cyclen complexes as highly potent promoters of hydrolytic DNA cleavage. *J. Am. Chem. Soc.* **133,** 20704–7 (2011).

123. Manea, F., Houillon, F. B., Pasquato, L. & Scrimin, P. Nanozymes: gold-nanoparticle-based transphosphorylation catalysts. *Angew. Chem. Int. Ed. Engl.* **43,** 6165–9 (2004).

124. Guarise, C. *et al.* Cooperative nanosystems. *J. Pept. Sci.* **14,** 174–83 (2008).

125. Zaupa, G., Mora, C., Bonomi, R., Prins, L. J. & Scrimin, P. Catalytic self-assembled monolayers on Au nanoparticles: the source of catalysis of a transphosphorylation reaction. *Chemistry* **17,** 4879–89 (2011).

126. Bonomi, R. *et al.* Phosphate diester and DNA hydrolysis by a multivalent, nanoparticle-based catalyst. *J. Am. Chem. Soc.* **130,** 15744–5 (2008).

127. Wimley, W. C. & Thompson, T. E. Transbilayer and interbilayer phospholipid exchange in dimyristoylphosphatidylcholine/dimyristoylphosphatidylethanolamine large unilamellar vesicles. *Biochemistry* **30,** 1702–1709 (1991).

128. Gurtovenko, A. A. & Vattulainen, I. Molecular mechanism for lipid flip-flops. *J. Phys. Chem. B* **111,** 13554–9 (2007).

129. Smith, B. A. *et al.* Enhanced cell death imaging using multivalent zinc(II)-bis(dipicolylamine) fluorescent probes. *Mol. Pharm.* **10,** 3296–303 (2013).

130. DiVittorio, K. M. *et al.* Synthetic peptides with selective affinity for apoptotic cells. *Org. Biomol. Chem.* **4,** 1966–76 (2006).

131. Ganesh, V. *et al.* Effective binding and sensing of lipopolysaccharide: combining complementary pattern recognition receptors. *Angew. Chem. Int. Ed. Engl.* **48,** 356–60 (2009).

132. Tirel, E. Y. *et al.* Catalytic zinc complexes for phosphate diester hydrolysis. *Angew. Chem. Int. Ed. Engl.* **53,** 8246–50 (2014).

133. Pengo, P., Baltzer, L., Pasquato, L. & Scrimin, P. Substrate modulation of the activity of an artificial nanoesterase made of peptide-functionalized gold nanoparticles. *Angew. Chem. Int. Ed. Engl.* **46,** 400–4 (2007).

134. Vriezema, D. M. *et al.* Self-assembled nanoreactors. *Chem. Rev.* **105,** 1445–89 (2005).

135. Chadha, G. & Zhao, Y. Environmental control of nucleophilic catalysis in water. *Chem. Commun. (Camb).* **50,** 2718–20 (2014).

136. Zastrow, M. L. & Pecoraro, V. L. Designing hydrolytic zinc metalloenzymes. *Biochemistry* **53,** 957–78 (2014).

137. Boyle, A. L. & Woolfson, D. N. De novo designed peptides for biological applications. *Chem. Soc. Rev.* **40,** 4295–306 (2011).

138. Woolfson, D. N. *et al.* De novo protein design: how do we expand into the universe of possible protein structures? *Curr. Opin. Struct. Biol.* **33,** 16–26 (2015).

139. Yuen, K. K. Y. & Jolliffe, K. a. Bis[zinc(II)dipicolylamino]-functionalised peptides as high affinity receptors for pyrophosphate ions in water. *Chem. Commun. (Camb).* **49,** 4824–6 (2013).

140. Serpell, L. C. Alzheimer's amyloid fibrils: structure and assembly. *Biochim. Biophys. Acta* **1502,** 16–30 (2000).

141. Hamley, I. W. The amyloid beta peptide: a chemist's perspective. Role in Alzheimer's and fibrillization. *Chem. Rev.* **112,** 5147–92 (2012).

142. Matsumoto, M., Lee, S. J., Waters, M. L. & Gagné, M. R. A catalyst selection protocol that identifies biomimetic motifs from β-hairpin libraries. *J. Am. Chem. Soc.* **136,** 15817–20 (2014).

143. Yamada, K. *et al.* Phosphodiester bond cleavage mediated by a cyclic β-sheet peptide-based dinuclear zinc(ii) complex. *Chem. Commun.* **2,** 1315–1316 (2000).

144. Rossi, P. *et al.* A Bimetallic Helical Heptapeptide as a Transphosphorylation Catalyst in Water. *J. Am. Chem. Soc.* **121,** 6948–6949 (1999).

145. Baltzer, L. Crossing borders to bind proteins--a new concept in protein recognition based on the conjugation of small organic molecules or short peptides to polypeptides from a designed set. *Anal. Bioanal. Chem.* **400,** 1653–64 (2011).

146. Ślósarczyk, A. T. & Baltzer, L. The molecular recognition of phosphorylated proteins by designed polypeptides conjugated to a small molecule that binds phosphate. *Org. Biomol. Chem.* **9,** 7697–704 (2011).

147. Scarso, A. *et al.* A peptide template as an allosteric supramolecular catalyst for the cleavage of phosphate esters. *Proc. Natl. Acad. Sci. U. S. A.* **99,** 5144–9 (2002).

148. Baltzer, L., Nilsson, H. & Nilsson, J. De novo design of proteins--what are the rules? *Chem. Rev.* **101,** 3153–63 (2001).

149. Allert, M. & Baltzer, L. Noncovalent binding of a reaction intermediate by a designed helix-loop-helix motif-implications for catalyst design. *Chembiochem* **4,** 306–18 (2003).

150. Allert, M. & Baltzer, L. Setting the stage for new catalytic functions in designed proteins--exploring the imine pathway in the efficient decarboxylation of oxaloacetate by an Arg-Lys site in a four-helix bundle protein scaffold. *Chemistry* **8,** 2549–60 (2002).

151. Andersson, L. K., Dolphin, G. T. & Baltzer, L. Multifunctional folded polypeptides from peptide synthesis and site-selective self-functionalization--practical scaffolds in aqueous solution. *Chembiochem* **3,** 741–51 (2002).

152. Baltzer, L., Broo, K. S., Nilsson, H. & Nilsson, J. Designed four-helix bundle catalysts--the engineering of reactive sites for hydrolysis and transesterification reactions of p-nitrophenyl esters. *Bioorg. Med. Chem.* **7,** 83–91 (1999).

153. Broo, K. S., Brive, L., Ahlberg, P. & Baltzer, L. Catalysis of Hydrolysis and Transesterification Reactions of p -Nitrophenyl Esters by a Designed Helix - Loop - Helix Dimer. **7863,** 11362–11372 (1997).

154. Broo, K. S., Nilsson, H., Nilsson, J., Flodberg, A. & Baltzer, L. Cooperative Nucleophilic and General-Acid Catalysis by the HisH + −His Pair and Arginine Transition State Binding in Catalysis of Ester Hydrolysis Reactions by Designed Helix−Loop−Helix Motifs. *J. Am. Chem. Soc.* **120,** 4063–4068 (1998).

155. Olofsson, S., Johansson, G. & Baltzer, L. Design, synthesis and solution structure of a helix-loop-helix dimer--a template for the rational design of catalytically active polypeptides. *J. Chem. Soc. Perkin Trans. 2* 2047 (1995). doi:10.1039/p29950002047

156. Razkin, J., Lindgren, J., Nilsson, H. & Baltzer, L. Enhanced complexity and catalytic efficiency in the hydrolysis of phosphate diesters by rationally designed helix-loop-helix motifs. *Chembiochem* **9,** 1975–84 (2008).

157. Razkin, J., Nilsson, H. & Baltzer, L. Catalysis of the cleavage of uridine 3'-2,2,2-trichloroethylphosphate by a designed helix-loop-helix motif peptide. *J. Am. Chem. Soc.* **129,** 14752–8 (2007).

158. Rossi, P., Tecilla, P., Baltzer, L. & Scrimin, P. De novo metallonucleases based on helix-loop-helix motifs. *Chem. Eur. J.* **10,** 4163–70 (2004).

159. Copeland, K. D., Fitzsimons, M. P., Houser, R. P. & Barton, J. K. DNA Hydrolysis and Oxidative Cleavage by Metal-Binding Peptides Tethered to Rhodium Intercalators †. *Biochemistry* **41,** 343–356 (2002).

160. Zastrow, M. L. & Pecoraro, V. L. Influence of active site location on catalytic activity in de novo-designed zinc metalloenzymes. *J. Am. Chem. Soc.* **135,** 5895–903 (2013).

161. Zastrow, M. L., Peacock, A. F. A., Stuckey, J. A. & Pecoraro, V. L. Hydrolytic catalysis and structural stabilization in a designed metalloprotein. *Nat. Chem.* **4,** 118–23 (2012).

162. Cangelosi, V. M., Deb, A., Penner-Hahn, J. E. & Pecoraro, V. L. A de novo designed metalloenzyme for the hydration of CO2. *Angew. Chem. Int. Ed. Engl.* **53,** 7900–3 (2014).

163. Steinmetz, M. O. *et al.* Molecular basis of coiled-coil formation. *Proc. Natl. Acad. Sci. U. S. A.* **104,** 7062–7 (2007).

164. Parry, D. a D., Fraser, R. D. B. & Squire, J. M. Fifty years of coiled-coils and alpha-helical bundles: a close relationship between sequence and structure. *J. Struct. Biol.* **163,** 258–69 (2008).

165. Ellenberger, T. E., Brandl, C. J., Struhl, K. & Harrison, S. C. The GCN4 basic region leucine zipper binds DNA as a dimer of uninterrupted alpha helices: crystal structure of the protein-DNA complex. *Cell* **71,** 1223–37 (1992).

166. Merrifield, R. B. Solid Phase Peptide Synthesis. I. The Synthesis of a Tetrapeptide. *J. Am. Chem. Soc.* **85,** 2149–2154 (1963).

167. Carpino, L. A. & Han, G. Y. 9-Fluorenylmethoxycarbonyl amino-protecting group. *J. Org. Chem.* **37,** 3404–3409 (1972).

168. Amblard, M., Fehrentz, J., Martinez, J. & Subra, G. Methods and Protocols of Modern Solid Phase Peptide Synthesis. **33,** (2006).

169. Chan, W. C. & White, P. D. Fmoc Solid phases peptide synthesis: A Practical Approach. *Oxford Univ. Press* (2000).

170. Carpino, L. A. *et al.* The uronium/guanidinium Peptide coupling reagents: finally the true uronium salts. *Angew. Chem. Int. Ed. Engl.* **41,** 441–5 (2002).

171. Baslé, E., Joubert, N. & Pucheault, M. Protein chemical modification on endogenous amino acids. *Chem. Biol.* **17,** 213–27 (2010).

172. Guzman, F., Barberis, S. & Illanes, A. Peptide synthesis: chemical or enzymatic. *Electron. J. Biotechnol.* **10,** (2007).

173. Greenfield, N. J. Using circular dichroism spectra to estimate protein secondary structure. *Nat. Protoc.* **1,** 2876–90 (2006).

174. Kelly, S. M. & Price, N. C. The use of circular dichroism in the investigation of protein structure and function. *Curr. Protein Pept. Sci.* **1,** 349–84 (2000).

175. Bunagan, M. R., Cristian, L., DeGrado, W. F. & Gai, F. Truncation of a cross-linked GCN4-p1 coiled coil leads to ultrafast folding. *Biochemistry* **45,** 10981–6 (2006).

176. O'Shea, E. K., Klemm, J. D., Kim, P. S. & Alber, T. X-ray structure of the GCN4 leucine zipper, a two-stranded, parallel coiled coil. *Science* **254,** 539–44 (1991).

177. Zitzewitz, J. a, Ibarra-Molero, B., Fishel, D. R., Terry, K. L. & Matthews, C. R. Preformed secondary structure drives the association reaction of GCN4-p1, a model coiled-coil system. *J. Mol. Biol.* **296,** 1105–16 (2000).

178. Kammerer, R. A. *et al.* An autonomous folding unit mediates the assembly of two-stranded coiled coils. *Proc. Natl. Acad. Sci. U. S. A.* **95,** 13419–24 (1998).

179. Missimer, J. H., Dolenc, J., Steinmetz, M. O. & van Gunsteren, W. F. Exploring the trigger sequence of the GCN4 coiled-coil: biased molecular dynamics resolves apparent inconsistencies in NMR measurements. *Protein Sci.* **19,** 2462–74 (2010).

180. Avogadro: an open-source molecular builder and visualization tool. Version 1.1.1. http://avogadro.openmolecules.net/.

181. Accelrys Discovery Studio Visualizer (Accelrys Software Inc., 2014 Accelrys Discovery Studio Visualiser v 4.1.0. Accelrys Software Inc., San Diego). (2014).

182. Zhou, N. E., Kay, C. M. & Hodges, R. S. Disulfide bond contribution to protein stability: positional effects of substitution in the hydrophobic core of the two-stranded alpha-helical coiled-coil. *Biochemistry* **32,** 3178–87 (1993).

183. Betz, S. F. Disulfide bonds and the stability of globular proteins. *Protein Sci.* **2,** 1551–8 (1993).

184. Zavodszky, M. *et al.* Disulfide bond effects on protein stability: designed variants of Cucurbita maxima trypsin inhibitor-V. *Protein Sci.* **10,** 149–60 (2001).

185. McAuley, A. *et al.* Contributions of a disulfide bond to the structure, stability, and dimerization of human IgG1 antibody CH3 domain. *Protein Sci.* **17,** 95–106 (2008).

186. Bulaj, G. Formation of disulfide bonds in proteins and peptides. *Biotechnol. Adv.* **23,** 87–92 (2005).

187. Vogler, R., Gelinsky, M., Guo, L. F. & Vahrenkamp, H. Solution behaviour and zinc complexation of di- and tripeptides with two cysteine units. *Inorganica Chim. Acta* **339,** 1–8 (2002).

188. Lombardo, V., Bonomi, R., Sissi, C. & Mancin, F. Phosphate diesters and DNA hydrolysis by dinuclear Zn(II) complexes featuring a disulfide bridge and H-bond donors. *Tetrahedron* **66,** 2189–2195 (2010).

189. Peacock, A. F. a *et al.* Gold-phosphine binding to de novo designed coiled coil peptides. *J. Inorg. Biochem.* **117,** 298–305 (2012).

190. Meier, M., Lustig, A., Aebi, U. & Burkhard, P. Removing an interhelical salt bridge abolishes coiled-coil formation in a de novo designed peptide. *J. Struct. Biol.* **137,** 65–72 (2002).

191. Urankar, D., Steinbücher, M., Kosjek, J. & Košmrlj, J. N-(Propargyl)diazenecarboxamides for “click” conjugation and their 1,3-dipolar cycloadditions with azidoalkylamines in the presence of Cu(II). *Tetrahedron* **66,** 2602–2613 (2010).

192. Lee, B.-Y., Park, S. R., Jeon, H. B. & Kim, K. S. A new solvent system for efficient synthesis of 1,2,3-triazoles. *Tetrahedron Lett.* **47,** 5105–5109 (2006).

193. Yu, M. *et al.* Copper, nickel, and zinc cyclam-amino acid and cyclam-peptide complexes may be synthesized with “click” chemistry and are noncytotoxic. *Inorg. Chem.* **50,** 12823–35 (2011).

194. Lumb, K. J., Carr, C. M. & Kim, P. S. Subdomain Folding of the Coiled Coil Leucine Zipper from the bZIP Transcriptional Activator GCN4. *Biochemistry* **33,** 7361–7367 (1994).

195. Livieri, M., Mancin, F., Tonellato, U. & Chin, J. Multiple functional group cooperation in phosphate diester cleavage promoted by Zn(II) complexes. *Chem. Commun. (Camb).* 2862–3 (2004). doi:10.1039/b412111b

196. Kirby, A. J. *et al.* Reactions of alpha-nucleophiles with a model phosphate diester. *Ark. 2009* 28–38 (2009).

197. Yatsimirsky, A. K., Gómez-Tagle, P., Escalante-Tovar, S. & Ruiz-Ramírez, L. Kinetics and mechanism of ester hydrolysis by metal complexes of 2,6-diacetylpyridine dioxime. *Inorganica Chim. Acta* **273,** 167–174 (1998).

198. Gómez-Tagle, P., Lugo-González, J. C. & Yatsimirsky, A. K. Oximate metal complexes breaking the limiting esterolytic reactivity of oximate anions. *Chem. Commun. (Camb).* **49,** 7717–9 (2013).

199. Breslow, R. & Chipman, D. Mixed Metal Complexes as Enzyme Models. I. Intracomplex Nucleophilic Catalysis by an Oxime Anion. *J. Am. Chem. Soc.* **87,** 4195–4196 (1965).

200. Hsu, C. & Cooperman, B. S. Metal-Ion Catalysis of Phosphoryl Transfer via a Ternary Complex. Effects of Changes in Leaving Group, Metal Ion, and Attacking Nucleophile. *J. Am. Chem. Soc.* **98,** 5657–5663 (1976).

201. Hsu, C.-M. & Cooperman, B. S. Metal ion and nucleophilic catalysis of pyridine-2-carbaldoximyl phosphate hydrolysis. *J. Am. Chem. Soc.* **98,** 5652–5657 (1976).

202. G. J. Lloyd , Barry S. Cooperman. Nucleophilic Attack by Zinc (II)-Pyridine-2-carbaldoxine Anion on Phosphorylimidazole. A Model for Enzymatic Phosphate Transfer. *J. Am. Chem. Soc.* **93,** 4883–4889 (1971).

203. Tirel, E. Y. & Williams, N. H. Enhancing Phosphate Diester Cleavage by a Zinc Complex through Controlling Nucleophile Coordination. *Chemistry* **21,** 7053–6 (2015).

204. Mancin, F., Tecilla, P. & Tonellato, U. Activation of Oximic Nucleophiles by Coordination of Transition Metal Ions. *European J. Org. Chem.* **2000,** 1045–1050 (2000).

205. Orama, M. *et al.* Formation, Redox and Structural Properties of Nickel Complexes of Pyridine-2-aldoxime. *Acta Chem. Scand.* **43,** 407–412 (1989).

206. Saarinen, H. *et al.* Equilibrium and Structural Studies on Metal Complexes of Oxime Ligands. Formation of Nickel(II) Complexes of Two Methyl-Substituted Pyridine Oxime Ligands in Aqueous Solution. *Acta Chem. Scand.* **52,** 1209–1213 (1998).

207. Milios, C. J., Stamatatos, T. C. & Perlepes, S. P. The coordination chemistry of pyridyl oximes. *Polyhedron* **25,** 134–194 (2006).

208. Pu, W. T. & Struhl, K. The leucine zipper symmetrically positions the adjacent basic regions for specific DNA binding. *Proc. Natl. Acad. Sci. U. S. A.* **88,** 6901–5 (1991).

209. Åström, H. & Strömberg, R. Synthesis of new OBAN's and further studies on positioning of the catalytic group. *Org. Biomol. Chem.* **2,** 1901–7 (2004).

210. Åström, H., Williams, N. H. & Strömberg, R. Oligonucleotide based artificial nuclease (OBAN) systems. Bulge size dependence and positioning of catalytic group in cleavage of RNA-bulges. *Org. Biomol. Chem.* **1,** 1461–1465 (2003).

211. Davis, A. M., Hall, A. D. & Williams, A. Charge description of base-catalyzed alcoholysis of aryl phosphodiesters: a ribonuclease model. *J. Am. Chem. Soc.* **110,** 5105–5108 (1988).

212. Lu, Z., Liu, C. T., Neverov, A. A. & Brown, R. S. Rapid three-step cleavage of RNA and DNA model systems promoted by a dinuclear Cu(II) complex in methanol. energetic origins of the catalytic efficacy. *J. Am. Chem. Soc.* **129,** 11642–52 (2007).

213. Carpino, L. A., El-Faham, A. & Albericio, F. Racemization studies during solid-phase peptide synthesis using azabenzotriazole-based coupling reagents. *Tetrahedron Lett.* **35,** 2279–2282 (1994).

214. García-Martín, F., Bayó-Puxan, N., Cruz, L. J., Bohling, J. C. & Albericio, F. Chlorotrityl Chloride (CTC) Resin as a Reusable Carboxyl Protecting Group. *QSAR Comb. Sci.* **26,** 1027–1035 (2007).

215. Reichle, R. A., McCurdy, K. G. & Hepler, L. G. Zinc Hydroxide: Solubility Product and Hydroxy-complex Stability Constants from 12.5–75 °C. *Can. J. Chem.* **53,** 3841–3845 (1975).